

Structural and magnetic properties of Low-dimensional quantum Antiferromagnets

Von der Fakultät Chemie der Universität Stuttgart
zur Erlangung der Würde eines Doktors der Naturwissenschaften
(Dr. rer. nat.) genehmigte Abhandlung

Vorgelegt von

Aleksandr Golubev

aus Moskau (Russische Föderation)

Hauptberichter:	Prof. Dr. Robert Dinnebier
Mitberichter:	Prof. Dr. Rainer Niewa
Prüfungsvorsitzender:	Prof. Dr. Joris van Slageren

Tag der mündlichen Prüfung: 29.05.2020

Max-Planck-Institut für Festkörperforschung

Universität Stuttgart

2020

This thesis is dedicated to my family and friends for their understanding, patience, and support, my beloved wife and daughter who were always in my mind every moment of this work.

Erklärung über die Eigenständigkeit der Dissertation

Ich versichere, dass ich die vorliegende Arbeit mit dem Titel
Structural and magnetic properties of Low-dimensional quantum Antiferromagnets
selbständig verfasst und keine anderen als die angegebenen Quellen und Hilfsmittel benutzt
habe; aus fremden Quellen entnommene Passagen und Gedanken sind als solche kenntlich
gemacht.

Declaration of Authorship

I hereby certify that the dissertation entitled
Structural and magnetic properties of Low-dimensional quantum Antiferromagnets
is entirely my own work except where otherwise indicated. Passages and ideas from other
sources have been clearly indicated.

Name/Name: Aleksandr Golubev

Unterschrift/Signed: _____

Datum/Date: _____

Abstract

In this thesis, I investigated low-dimensional quantum antiferromagnets. The chemical systems in question all contain Cu ions in the oxidation state +2 with one hole in the 3d electron shell and a magnetic moment, which can be described by a spin $S=1/2$. The compounds I prepared and investigated with respect to their chemical, magnetic, structural, optical and lattice properties were the ternary cuprates CuTa_2O_6 , $\alpha\text{-CuV}_2\text{O}_6$ and a set of rare-earth copper hydroxoarsenates with the composition $RE\text{Cu}_6(\text{OH})_6(\text{AsO}_4)_3 \cdot n\text{H}_2\text{O}$ ($RE = \text{Y, Bi, La, Lu}$; $n \approx 3$) from the mixite and agardite mineral family.

Early attempts to synthesize CuTa_2O_6 from a $\text{CuO} - \text{Cu}_2\text{O}$ flux, by solid state reaction or high pressure synthesis resulted in phases with either a cubic tetragonal, or a pseudo-cubic orthorhombic defective perovskite-like crystal structure. It had been shown by Krabbes and collaborators that a trirutile-type polycrystalline sample of CuTa_2O_6 can be synthesized by thermal decomposition of a freeze-dried Cu-Ta-oxalate precursor at 700°C . X-ray and neutron powder diffraction studies carried out in this thesis confirm phase purity of the sample. A slight monoclinic distortion similar to that found in CuSb_2O_6 is observed at room temperature. Detailed high-temperature X-ray and neutron powder diffraction investigations, as well as Raman scattering spectroscopy, revealed a structural phase transition at $503(3)$ K from the monoclinic to the tetragonal trirutile-type structure. GGA+ U density functional calculations of the spin-exchange parameters, as well as magnetic susceptibility and isothermal magnetization measurements, reveal that CuTa_2O_6 is a new 1D Heisenberg magnet with predominant antiferromagnetic nearest-neighbor intra-chain spin-exchange interaction of ~ 50 K. Inter-chain exchange is about a factor of five smaller. Heat capacity and low-temperature high-intensity neutron powder diffraction studies could not detect long-range order down to 0.45 K.

In several preceding reports, the magnetic properties of the low-dimensional quantum antiferromagnet $\alpha\text{-CuV}_2\text{O}_6$ had been analyzed in terms of a one-dimensional Heisenberg model with uniform nearest-neighbor spin-exchange

interaction. However, new extensive DFT+ U calculations proposed that a correct spin-exchange-model is rather an anisotropic square planar spin $S=1/2$ Heisenberg antiferromagnet with $J_x \neq J_y$. These results have been contested against angular dependent magnetic susceptibility and electron paramagnetic resonance measurements and found in best agreement with the experimental findings. α -CuV₂O₆ exhibits antiferromagnetic long-range order below the Néel temperature of ~ 22.5 K to a collinear magnetic structure. Using the results of neutron powder diffraction, the magnetic structure was resolved. A comparison with quantum Monte Carlo simulations of the magnetic susceptibilities for an anisotropic square lattice Heisenberg antiferromagnet indicated an anisotropy ratio J_x/J_y of ~ 0.7 being in good agreement with the DFT calculations. The results of the Monte Carlo simulations have been encoded into a Padé approximant enabling fits of experimental data of related antiferromagnetic two-dimensional systems.

The structural, vibrational and especially the magnetic properties of natural and synthetic polycrystalline samples of the minerals mixite with the composition BiCu₆(OH)₆(AsO₄)₃ · nH₂O ($n \approx 3$), goudeyite with the composition YCu₆(OH)₆(AsO₄)₃ · nH₂O ($n \approx 3$), La-Agardite with the composition LaCu₆(OH)₆(AsO₄)₃ · nH₂O ($n \approx 3$) and Lu-Agardite with the composition LuCu₆(OH)₆(AsO₄)₃ · nH₂O ($n \approx 3$) have been investigated. Polycrystalline powders of synthetic mixite, goudeyite and agardite were precipitated from stoichiometric aqueous solutions of M(NO₃)₃·5H₂O (M = Bi, Y, La, Lu), Na₂HAsO₄ · 7H₂O and Cu(NO₃)₂ · 2.5H₂O and compared with natural mixite samples from different origins. The investigated systems crystallize in the space group $P6_3/m$ (no. 176) with a hexagonal structure, which contains CuO₂ ribbons interconnected via (AsO₄)³⁻ groups. They form hexagonal tubes of about a 10 Å inner diameter. These tubes host zeolite-type water molecules, which can be reversibly removed at moderate temperatures of $\sim 100^\circ\text{C}$. The temperature dependence of the magnetic susceptibilities is dominated by short-range antiferromagnetic correlations evidenced by the characteristic broad maximum. It reflects the low-dimensional character of the spin-lattice in the mixite crystal structure. Long-range magnetic ordering could not be detected down to 0.4 K. The magnetic properties of the

samples are determined by a substantial antiferromagnetic spin-exchange between the magnetic moments of the Cu^{2+} cations. A first model approach of the magnetic properties in terms of an alternating $S=1/2$ Heisenberg model is proposed in this thesis, which describes the magnetic susceptibilities rather well. The nearest-neighbor spin-exchanges range between 200 K and 130 K for natural and synthetic samples, respectively. The alternation parameters, i.e., the ratios of nearest and next-nearest neighbor spin-exchange range between ~ 0.52 for natural mixite and ~ 0.75 for synthetic mixite and Y-Agardite, respectively. The experimentally observed spin-exchange parameters are consistent with the results of density functional calculations.

Kurzfassung

In dieser Arbeit werden niedrigdimensionale Quantenantiferromagnete untersucht. Die betreffende chemischen Systeme enthalten alle Cu-Ionen in der Oxidationsstufe +2 mit einem Loch in der 3d Elektronenhülle und einem magnetischen Moment, das durch einen Spin $S = 1/2$ beschrieben werden kann. Die Verbindungen, die im Rahmen dieser Arbeit hergestellt und hinsichtlich ihrer chemischen, magnetischen, strukturellen, optischen und Gittereigenschaften untersucht werden, sind die ternären Cuprate CuTa_2O_6 , $\alpha\text{-CuV}_2\text{O}_6$ und eine Reihe von Seltenerd-Kupfer-Hydroxide-Arsenaten aus der Familie der Mixit- und Agardit-Mineralien mit der Zusammensetzung $\text{RECu}_6(\text{OH})_6(\text{AsO}_4)_3 \cdot n\text{H}_2\text{O}$ ($\text{RE} = \text{Y, Bi, La, Lu}$; $n \approx 3$)

Frühe Versuche, CuTa_2O_6 aus Schmelzlösung von $\text{CuO} - \text{Cu}_2\text{O}$ durch Festkörperreaktion oder Hochdrucksynthese zu synthetisieren, führten zu Entstehung von Phasen mit entweder einer kubischen tetragonalen oder einer pseudokubischen orthorhombischen defekten perowskitartigen Kristallstruktur. Krabbes et al. hatten gezeigt, dass eine polykristalline Trirutil-Typ Probe von CuTa_2O_6 durch thermische Zersetzung eines gefriergetrockneten Cu-Ta-Oxalat-Vorläufers bei 700°C synthetisiert werden kann. In dieser Arbeit durchgeführte Röntgen- und Neutronenpulverbeugungsstudien bestätigen die Phasenreinheit der Probe. Bei Raumtemperatur wird eine leichte monokline Verzerrung ähnlich der in CuSb_2O_6 beobachtet. Detaillierte Hochtemperatur-Röntgen- und Neutronenpulverbeugungsuntersuchungen sowie Raman-Streuspektroskopie zeigten einen strukturellen Phasenübergang bei $503(3)\text{K}$ von der monoklinen zur tetragonalen Trirutil-Struktur. GGA+U-Dichtefunktionsberechnungen der Spinaustauschparameter sowie Messungen der magnetischen Suszeptibilität und der isothermen Magnetisierung zeigen, dass CuTa_2O_6 ein neuer 1D-Heisenberg-Magnet mit einer vorherrschenden antiferromagnetischen Intra-Ketten-Spin-Austausch-Wechselwirkung zwischen den Nachbarn von $\sim 50\text{K}$ ist. Der Austausch zwischen Ketten ist um den Faktor fünf kleiner. Wärmekapazität und

hochintensive Neutronenpulverbeugungsstudien bei niedriger Temperatur konnten keine magnetische Fernordnung bis zu 0,45 K nachweisen.

In mehreren vorhergehenden Berichten wurden die magnetischen Eigenschaften des niedrigdimensionalen Quantenantiferromagneten α - CuV_2O_6 im Hinblick auf ein eindimensionales Heisenberg-Modell mit einheitlicher Spin-Austausch-Wechselwirkung zum nächsten Nachbarn analysiert. Neue umfangreiche DFT+U-Berechnungen deuten jedoch darauf hin, dass ein korrektes Spin-Austausch-Modell eher ein anisotroper quadratischer planarer Spin $S = 1/2$ Heisenberg-Antiferromagnet mit $J_x \neq J_y$ ist. Dieser Vorschlag wird mittels winkelabhängigen Messungen der magnetischen Suszeptibilität und der elektronenparamagnetischen Resonanz überprüft und es wird beste Übereinstimmung mit den theoretischen Vorhersagen gefunden. α - CuV_2O_6 zeigt eine antiferromagnetische Fernordnung unterhalb der Néel-Temperatur von $\sim 22,5$ K zu einer kollinearen magnetischen Struktur. Anhand der Ergebnisse der Neutronenpulverbeugung wurde die magnetische Struktur aufgelöst. Ein Vergleich mit Quanten-Monte-Carlo-Simulationen der magnetischen Suszeptibilitäten für einen anisotropen Heisenberg-Antiferromagneten mit quadratischem Gitter ergibt, dass ein Anisotropieverhältnis J_x / J_y von $\sim 0,7$ gut mit den DFT-Berechnungen übereinstimmt. Die Ergebnisse der Monte-Carlo-Simulationen werden in einen Padé-Approximanten codiert, der Anpassungen experimenteller Daten verwandter antiferromagnetischer zweidimensionaler Systeme ermöglicht.

Die strukturellen, gittedynamischen und insbesondere magnetischen Eigenschaften natürlicher und synthetischer polykristalliner Proben der Mixite-Mineralien mit der Zusammensetzung $\text{BiCu}_6(\text{OH})_6(\text{AsO}_4)_3 \cdot n\text{H}_2\text{O}$ ($n \approx 3$), Goudeyit mit der Zusammensetzung $\text{YCu}_6(\text{OH})_6(\text{AsO}_4)_3 \cdot n\text{H}_2\text{O}$ ($n \approx 3$), La-Agardit mit der Zusammensetzung $\text{LaCu}_6(\text{OH})_6(\text{AsO}_4)_3 \cdot n\text{H}_2\text{O}$ ($n \approx 3$) und Lu-Agardit mit der Zusammensetzung $\text{LuCu}_6(\text{OH})_6(\text{AsO}_4)_3 \cdot n\text{H}_2\text{O}$ ($n \approx 3$) werden untersucht. Polykristalline Pulver aus synthetischem Mixit, Goudeyit und Agardit werden aus stöchiometrischen wässrigen Lösungen von $\text{M}(\text{NO}_3)_3 \cdot 5\text{H}_2\text{O}$ ($\text{M} = \text{Bi}, \text{Y}, \text{La}, \text{Lu}$), $\text{Na}_2\text{HAsO}_4 \cdot 7\text{H}_2\text{O}$ und $\text{Cu}(\text{NO}_3)_2 \cdot 2,5\text{H}_2\text{O}$ ausgefällt und mit natürliche

Mixitproben unterschiedlicher Herkunft verglichen. Die untersuchten Systeme kristallisieren in der Raumgruppe $P6_3/m$ (Nr. 176) mit einer hexagonalen Struktur, die CuO_2 Bänder enthält, die über $(\text{AsO}_4)^{3-}$ Gruppen miteinander verbunden sind. Sie bilden sechseckige Röhren mit einem Innendurchmesser von etwa 10 Å. Diese Röhren enthalten Wassermoleküle vom Zeolithtyp, die bei moderaten Temperaturen von $\sim 100^\circ\text{C}$ reversibel entfernt werden können. Die Temperaturabhängigkeit der magnetischen Suszeptibilitäten wird von kurzreichweitigen antiferromagnetischen Korrelationen dominiert, die durch das charakteristische breite Maximum belegt werden. Es spiegelt den niedrigdimensionalen Charakter des Spin-Gitters in der Mixit-Kristallstruktur wider. Eine magnetische Fernordnung konnte bis zu 0,4 K nicht nachgewiesen werden. Die magnetischen Eigenschaften der Proben werden durch einen dominanten antiferromagnetischen Spinaustausch zwischen den magnetischen Momenten der Cu^{2+} Kationen bestimmt. In dieser Arbeit wird ein erster Modellansatz der magnetischen Eigenschaften in Form eines alternierenden $S = 1/2$ Heisenberg-Modells vorgeschlagen, der die magnetischen Suszeptibilitäten ziemlich gut beschreibt. Der Spin-Austausch zum nächsten Nachbarn liegt zwischen 200 K und 130 K für natürliche bzw. synthetische Proben. Die Alternierungsparameter, d. h. Die Verhältnisse des Spinaustauschs zum nächsten und übernächsten nächsten Nachbarn, liegen zwischen $\sim 0,52$ für natürlichen Mixit und $\sim 0,75$ für synthetischen Mixit bzw. Y-Agardit. Die experimentell beobachteten Spinaustauschparameter stimmen mit den Ergebnissen von Dichtefunktionsberechnungen gut überein.

List of Publications

1. A. Golubev, R. E. Dinnebier, A. Schulz, R. K. Kremer, H. Langbein, A. Senyshyn, J. M. Law, T. C. Hansen, H.-J. Koo, M.-H. Whangbo, *Structural and Magnetic Properties of the Trirutile-type 1D-Heisenberg Anti-Ferromagnet $CuTa_2O_6$* , Inorg. Chem. **56(11)**, 6318-6329 (2017)
DOI: 10.1021/acs.inorgchem.7b00421
2. A. Golubev, J. Nuss, R. K. Kremer, E.E. Gordon, M.-H. Whangbo, C. Ritter, L. Weber, S. Wessel, *Two-Dimensional Magnetism in α - CuV_2O_6* , in preparation
3. A. Golubev, E. Bruecher, A. Schulz, R. K. Kremer, F. X. Schmidt, E.E. Gordon, M.-H. Whangbo, *Low-Dimensional Magnetic Properties of Natural and Synthetic Mixite $(Bi,Ca)Cu_6(OH)_6(AsO_4)_3 \cdot n H_2O$ ($n \approx 3$) and Goudeyite $YCu_6(OH)_6(AsO_4)_3 \cdot n H_2O$ ($n \approx 3$)*, ZAAC 644(24), 1782-1790 (2018)
DOI: 10.1002/zaac.201800344
4. A. Golubev, E. Bruecher, A. Schulz, R. K. Kremer, R. Glaum, *La- and Lu-agardite – preparation, crystal structure, vibrational and magnetic properties*, Zeitschrift für Naturforschung B, Volume 75, Issue 1-2, Pages 191–199, ISSN (Online) 1865-7117, ISSN (Print) 0932-0776

Contents

Abstract	4
Kurzfassung.....	7
List of Publications	10
List of the Figures.....	13
List of the Tables.....	21
1. Introduction.....	24
2. Theory	27
2.1. X-ray and neutron diffraction	27
2.2. Density Functional Theory	29
3. Experimental methods.....	34
3.1. Powder diffraction.....	34
3.2. Magnetic property measurements	40
3.3. Electronic paramagnetic resonance.....	42
3.4. Heat capacity measurements	46
3.5. Raman spectroscopy.....	51
3.6. Differential thermal analysis.....	55
3.7. Thermal gravimetric analysis	58
4. CuTa_2O_6	59
4.1. Introduction.....	59
4.2. Preparation.....	61
4.3. Sample characterization	62
4.4. Crystal structure	64
4.5. Spin-exchange parameters	77
4.6. Raman Scattering	80
4.7. Magnetic properties	83

4.8	Electron paramagnetic resonance	88
4.9	Specific heat capacity	92
5.	CuV_2O_6	95
5.1.	Introduction.....	95
5.2.	Preparation.....	97
5.3.	Sample characterization	98
5.4.	Crystal structure	101
5.5.	Spin-exchange parameters	107
5.6.	Magnetic properties	112
5.7.	Magnetic structure	117
5.8.	Quantum Monte Carlo calculations	125
5.9.	Electron paramagnetic resonance	130
6.	Rare-earth mixite and agardite minerals	133
6.1.	Introduction.....	133
6.2.	Preparation.....	137
6.3.	Sample characterization	138
6.4.	Thermal gravimetric analysis	147
6.5.	Spin-exchange parameters	149
6.6.	Raman Scattering	152
6.7.	UV-VIS spectroscopy.....	158
6.8.	Magnetic properties	161
7.	Summary and Conclusion	169
7.	Zusammenfassung und Schlussfolgerung	172
	Bibliography.....	176
	Curriculum Vitae	188
	Acknowledgements	189

List of the Figures

1. Introduction

2. Theory

Figure 2-1. Bragg diffraction 28

3. Experimental methods

Figure 3-1. Comparison of scattering strength between X-Rays and neutrons (left) and interaction of x-rays and neutrons with the atoms (right) 35

Figure 3-2. STOE STADI P (right) and Bruker D8 ADVANCE (left) diffractometers 36

Figure 3-3. Capillary sample prepared for STOE STADI P diffractometer (right) and scheme of Debye-Scherrer diffractometer 37

Figure 3-4. Thin-film sample prepared for the Oxford PheniX cryocooler (right) and the scheme of Bragg Brentano diffractometer. 38

Figure 3-5. SPODI and D20 neutron powder diffractometers 38

Figure 3-6. Principal scheme of the two-axis high-resolution powder diffractometer SPODI 39

Figure 3-7. Quantum Design MPMS XL7 SQUID magnetometer (left) and schematic scheme of the probe component 40

Figure 3-8. Principal scheme of a RF SQUID magnetometer 41

Figure 3-9. Principal scheme of a EPR spectrometer 43

Figure 3-10. The Bruker X-band EPR spectrometer 44

Figure 3-11. An oriented crystal of α - CuV_2O_6 mounted in a quartz glass tube for EPR measurements..	44
Figure 3-12. λ -type anomaly in the heat capacity of GdCl_3 at the FM ordering.....	47
Figure 3-13. Construction of the PPMS calorimeter sample puck..	48
Figure 3-14. Heat-flow diagram for a conventional thermal-relaxation calorimeter.....	49
Figure 3-15. Different possibilities of light scattering.....	52
Figure 3-16. Intensities of the Stokes, anti-Stokes Raman and Rayleigh peaks at low temperatures	53
Figure 3-17. Principal scheme of the Raman spectrometer.....	54
Figure 3-18. Principal scheme of the DTA setup.....	55
Figure 3-19. Schematic representation of TGA setup(left) and its principal scheme(right).....	58

4. CuTa_2O_6

Figure 4-1. Perspective view of the room temperature crystal structure of CuTa_2O_6	59
Figure 4-2. (left) Typical SEM scan across a polycrystalline CuTa_2O_6 sample and (right) result of the EDX analysis..	62
Figure 4-3. Room temperature X-ray powder diffraction pattern (Cu $K_{\alpha 1}$ radiation) of a polycrystalline sample of CuTa_2O_6	63
Figure 4-4. X-ray powder diffraction pattern (Mo $K_{\alpha 1}$ radiation) of a polycrystalline sample of CuTa_2O_6 at 293K and 500K.....	65

Figure 4-5. Splitting of the $(123)_{\text{tet}}$ Bragg reflection around the critical temperature $T_C = 503 \pm 3$ K.....	66
Figure 4-6. Neutron powder diffraction patterns collected at the instrument SPODI (MLZ) at the wavelength 1.548 Å of a polycrystalline sample of CuTa_2O_6 at 293 K and 573 K.	70
Figure 4-7. The relative difference of the lattice parameters a and b , $(b - a)/(b + a)$, and the monoclinic angle β versus temperature as derived from the refinement of the neutron powder diffraction patterns..	71
Figure 4-8. Lattice parameter c versus temperature as derived from the refinement of the neutron powder diffraction patterns.	72
Figure 4-9. Group – subgroup relationship between the space groups $P4_2/mnm$ (no. 136) and $P 2_1/n$ (no. 14).....	74
Figure 4-10. (top) Difference between neutron powder diffraction patterns of CuTa_2O_6 collected at 1.86 K and 5.7 K at a wavelength of 1.88 Å. (main frame) Contour plot of the neutron powder diffraction patterns between 1.86 K and 5.7 K	76
Figure 4-11. Ordered spin arrangements of (a) FM, (b) AF1, (c) AF2, (d) AF3, (e) AF4, (f) AF5, (g) AF6 and (h) AF7 states of CuTa_2O_6 at 293 K.....	77
Figure 4-12. Relevant spin-exchange paths in CuTa_2O_6	78
Figure 4-13. (upper panel) Raman spectra of CuTa_2O_6 at various temperatures (middle panel) Raman spectrum of NiTa_2O_6 (lower panel) Raman spectrum of CuSb_2O_6	81
Figure 4-14. Contour map of the temperature dependence of the Raman spectra of CuTa_2O_6	82
Figure 4-15 Temperature dependence of the magnetic susceptibility of CuTa_2O_6 together with the fit of the experimental..	83

Figure 4-16. Isothermal magnetization of polycrystalline CuTa_2O_6 at 2 K measured with the pulsed field magnetometer.....	86
Figure 4-17. EPR absorption spectrum of polycrystalline sample of CuTa_2O_6 measured at room temperature at a microwave frequency of 9.478 GHz..	89
Figure 4-18. (main frame) g -factor of the EPR line for CuTa_2O_6 versus temperature. (inset) Integrated intensity of the EPR line.....	90
Figure 4-19. Specific heat capacity of CuTa_2O_6	92

5. CuV_2O_6

Figure 5-1. Crystal structure of $\alpha\text{-CuV}_2\text{O}_6$: (a) VO_3 chain of corner-sharing VO_4 tetrahedra (b) CuV_2O_6 layer made up of stacks of CuO_4 square planes corner-shared with VO_3 chains (c) Stacking of CuV_2O_6 layers in $\alpha\text{-CuV}_2\text{O}_6$..	95
Figure 5-2. Neutron powder diffraction pattern of $\alpha\text{-CuV}_2\text{O}_6$ collected at 1.5 K using neutrons with a wavelength of $\lambda = 1.594 \text{ \AA}$ (ILL D2B).....	100
Figure 5-3. The DTA trace of $\alpha\text{-CuV}_2\text{O}_6$	101
Figure 5-4. Contour plot of X-ray diffraction patterns of $\alpha\text{-CuV}_2\text{O}_6$ sample collected with $\text{Mo K}_{\alpha 1}$ radiation between $500 \text{ }^\circ\text{C}$ and $660 \text{ }^\circ\text{C}$	102
Figure 5-5. Splitting of $(1,1,0)_{C 2/m}$ and $(1,1,1)_{C 2/m}$ Bragg's peaks of $\alpha\text{-CuV}_2\text{O}_6$ below $\sim 615 \text{ }^\circ\text{C}$	103
Figure 5-6. X-ray diffraction patterns ($\text{Mo K}_{\alpha 1}$ radiation) of $\alpha\text{-CuV}_2\text{O}_6$ collected between $615 \text{ }^\circ\text{C}$ and $635 \text{ }^\circ\text{C}$	103
Figure 5-7. X-ray diffraction patterns ($\text{Mo K}_{\alpha 1}$ radiation) of $\alpha\text{-CuV}_2\text{O}_6$ collected at high temperatures.....	106
Figure 5-8. Spin-exchange paths of $\alpha\text{-CuV}_2\text{O}_6$	107

Figure 5-9. Ordered spin states of α -CuV₂O₆ employed to extract the values of $J_1 - J_4$ by the energy-mapping analysis based on DFT+U calculations. .. 108

Figure 5-10. (a) Magnetic orbital of a CuO₄ square plane containing a Cu²⁺ (d⁹, S = 1/2) ion. (b) Interactions between two magnetic orbitals associated with a Cu-O · · · O-Cu spin-exchange. 111

Figure 5-11. Anisotropy of the magnetic susceptibilities of a crystal of an α -CuV₂O₆ observed with magnetic field applied parallel [100] and perpendicular.. 112

Figure 5-12. Heat capacity versus magnetic field of flux grown and a CVT grown crystal near the Néel temperature..... 114

Figure 5-13. Magnetization of an α -CuV₂O₆ crystal at 1.85 K with the magnetic field applied parallel and perpendicular the crystal needle 115

Figure 5-14. Derivative of the isothermal magnetization versus the magnetic field indicating the position of the spin-flop..... 116

Figure 5-15. Neutron powder diffraction pattern of α -CuV₂O₆ collected at 1.5 K using neutrons with a wavelength of $\lambda = 2.424 \text{ \AA}$ (D20) together with a Rietveld profile refinement..... 117

Figure 5-16. Integrated intensities of the magnetic Bragg reflection at $2\theta = 16.14^\circ$ 118

Figure 5-17. Magnetic Bragg reflections. The difference pattern of neutron powder diffraction patterns collected at D20 ($\lambda = 2.424 \text{ \AA}$)..... 119

Figure 5-18. Rietveld profile refinement of the difference pattern $I(1.5 \text{ K}) - I(30 \text{ K})$ 120

Figure 5-19. Magnetic structure of α -CuV₂O₆..... 121

Figure 5-20. Three extra antiferromagnetic spin lattices, AFM5, AFM6, AFM7, used for a consistency check of the DFT+U results. 122

Figure 5-21. Temperature dependence of the unit cell volume relative to its value at 50K. 123

Figure 5-22. Temperature dependence of the lattice parameters relative to their values at 50 K. 124

Figure 5-23. Reduced magnetic susceptibility, $\chi^* = \frac{\chi J_x}{N_A g^2 \mu_B^2}$, of the anisotropic square planar Heisenberg lattice with nearest-neighbour spin-exchange interaction, J_x and J_y for ratios $0.5 \leq \alpha = J_y/J_x \leq 1$ 125

Figure 5-24. Magnetic susceptibility of a crystal of α -CuV₂O₆ measured with a field of 0.1 Tesla applied parallel to the crystal needle (a-axis in P-1 setting). 128

Figure 5-25. Angular dependence of the g-factor of an α -CuV₂O₆ needle-shaped crystal at room temperature. 130

Figure 5-26. Temperature of the g-factor of α -CuV₂O₆ measured at a microwave frequency of 9.4803 GHz with the external magnetic field along the needle axis (a-axis in P-1 setting). 132

6. *Rare-earth mixite and agardite minerals*

Figure 6-1. Crystal structure of mixite (space group P6₃/m (no. 176)) projected along [0001]. 134

Figure 6-2. Chain of edge-sharing CuO₅ square-pyramids with the (AsO₄)³⁻ groups attached to oxygen atoms O1, O2, and O3. 135

Figure 6-3. SEM image of a piece of natural mixite sample from Wittichen 138

Figure 6-4. EDX spectrum of our natural mixite sample originating from Wittichen 139

Figure 6-5. X-ray powder diffraction patterns of mixite and goudeyite $\text{Mo K}_{\alpha 1}$ radiation ($\lambda = 70.9300 \text{ pm}$) in comparison with the patterns obtained from the Rietveld profile refinement	141
Figure 6-6. X-ray diffraction patterns of $\text{RECu}_6(\text{OH})_6(\text{AsO}_4)_3 \cdot n\text{H}_2\text{O}$ ($\text{RE} = \text{Y, La, Lu}; n \approx 3$).....	143
Figure 6-7. Tri-capped trigonal oxygen atom coordination of the RE atoms in $\text{RECu}_6(\text{OH})_6(\text{AsO}_4)_3 \cdot n\text{H}_2\text{O}$ ($\text{RE} = \text{Y, La, Lu}; n \approx 3$).....	144
Figure 6-8. Lattice parameters of $\text{RECu}_6(\text{OH})_6(\text{AsO}_4)_3 \cdot n\text{H}_2\text{O}$ ($\text{RE} = \text{Y, La, Lu}; n \approx 3$) as a function of the ionic radii of the RE ions in a 9-fold coordination	145
Figure 6-9. Cu- O – Cu bonding angles as a function of the ionic radii of the RE atoms as indicated.....	146
Figure 6-10. TGA analysis of dehydration of mixite.....	147
Figure 6-11. Definition of the various exchange parameters J_i used to map the total energies for the DFT + U calculations	150
Figure 6-12. Reduced spin-exchange coupling scheme of an ‘unfolded’ six-ring..	151
Figure 6-13. Comparison of the Raman spectra of natural mixite, the synthetic mixite, and the synthetic goudeyite samples.....	153
Figure 6-14. Raman spectra of natural and synthetic mixite and synthetic goudeyite in the energy range where $(\text{AsO}_4)^{3-}$ related stretching vibrations are expected.....	155
Figure 6-15. Raman spectra of $\text{RECu}_6(\text{OH})_6(\text{AsO}_4)_3 \cdot n\text{H}_2\text{O}$ ($\text{RE} = \text{Y, La, Lu}; n \approx 3$) collected at room temperature.	157
Figure 6-16. Powder reflectance spectrum of $\text{LaCu}_6(\text{OH})_6(\text{AsO}_4)_3 \cdot 3 \text{H}_2\text{O}$.	159

Figure 6-17. Comparison of the magnetic susceptibilities of (a) natural and (b) synthetic mixite and (c) synthetic goudeyite.. 162

Figure 6-18. Comparison of the magnetic susceptibilities of natural ((Bi,Ca)Cu₆(OH)₆(AsO₄)₃ · 3H₂O) and synthetic (BiCu₆(OH)₆(AsO₄)₃ · 3H₂O) mixite and synthetic goudeyite (YCu₆(OH)₆(AsO₄)₃ · 3H₂O) corrected for magnetic impurities in comparison to the results of the fits to the theoretical susceptibilities of an alternating Heisenberg S=1/2 spin chain.. 165

Figure 6-19. Specific heat capacity of LaCu₆(OH)₆(AsO₄)₃ · 3 H₂O..... 167

Figure 6-20. Magnetic susceptibilities of RECu₆(OH)₆(AsO₄)₃ · 3 H₂O corrected for a temperature independent contribution and a Curie-tail at low temperatures due to single-ion magnetic species.. 168

List of the Tables

1. Introduction

2. Theory

3. Experimental methods

4. CuTa_2O_6

Table 4-1. Comparison of atom fractional coordinates of CuTa_2O_6 , CuSb_2O_6 , NiTa_2O_6 and CoTa_2O_6 at room temperature (RT) and at 300 °C 65

Table 4-2. Crystal structure data of CuTa_2O_6 as refined from X-ray powder diffraction data at RT and 500 K..... 67

Table 4-3. Lattice parameters, cell volume, isotropic displacement factor and R factors resulting from the profile refinement of the neutron powder diffraction patterns collected at instrument SPODI between room temperature and 300 °C 69

Table 4-4. Atom positional parameters resulting from the refinement of the neutron powder diffraction patterns of CuTa_2O_6 versus temperature 71

Table 4-5. Results of the neutron powder diffraction patterns of CuTa_2O_6 collected at 150°C..... 72

Table 4-6. Results of the neutron powder diffraction patterns of CuTa_2O_6 collected at 200°C..... 73

Table 4-7. Relative energies and spin-exchange parameters obtained from the GGA+*U* calculations for CuTa_2O_6 at 293 K 77

5. CuV_2O_6

Table 5-1. Structural parameters of $\alpha\text{-CuV}_2\text{O}_6$ as obtained from the Rietveld profile refinement of the XRD pattern collected with Mo $K_{\alpha 1}$ radiation and high-resolution NPD patterns ($\lambda = 1.594\text{\AA}$) at $T = 1.5\text{ K}$	96
Table 5-2. Positions of the small Bragg peaks not indexable in $C2/m$	102
Table 5-3. Lattice parameters and atom positions of $\alpha\text{-CuV}_2\text{O}_6$ between $615\text{ }^\circ\text{C}$ and $635\text{ }^\circ\text{C}$	102
Table 5-4. $\text{Cu}\cdots\text{Cu}$ and $\text{O}\cdots\text{O}$ distances and $\text{Cu-O}\cdots\text{O}$ and $\text{O}\cdots\text{O-Cu}$ angles associated with the $\text{Cu-O}\cdots\text{O-Cu}$ spin-exchange paths of $\alpha\text{-CuV}_2\text{O}_6$	105
Table 5-5. Relative energies of the five collinear spin configurations used in the DFT+U calculations..	108
Table 5-6. Magnetic moments on the Cu, V and O atoms in the FM states of $\alpha\text{-CuV}_2\text{O}_6$ from the DFT+U calculations	108
Table 5-7. $J_1 - J_4$ spin-exchange parameters of $\alpha\text{-CuV}_2\text{O}_6$ determined by the energy-mapping analyses based on the DFT+U calculations	108
Table 5-8. Total energies for the three extra antiferromagnetic collinear test configurations.....	121
Table 5-9. Coefficients of the polynomial used to calculate the Padé coefficients	125

6. *Rare-earth mixite and agardite minerals*

Table 6-1. Results of the EDX analysis of the mixite samples from Wiitichen and Jáchymov.	137
Table 6-2. Room-temperature lattice parameters of the mixite and goudeyite samples.....	138

Table 6-3. Lattice parameters and cell volumes of $RECu_6(OH)_6(AsO_4)_3 \cdot nH_2O$ ($RE = Y, La, Lu; n \approx 3$).....	140
Table 6-4. Positional parameters of the Cu and As atoms, at the Wyckoff position 12i and 6h in $RECu_6(OH)_6(AsO_4)_3 \cdot nH_2O$ ($RE = Y, La, Lu; n \approx 3$).....	142
Table 6-5. Distances between the Cu atoms within and between the hexagonal rings.....	148
Table 6-6. Spin-exchange parameters J_i obtained from the total energies DFT calculations.....	148
Table 6-7. Results of the deconvolution of the As – O stretching bands observed in the Raman spectra between 800 and 900 cm^{-1} of natural and synthetic mixite and synthetic goudeyite.....	154
Table 6-8. Relevant fit parameters of the magnetic susceptibility data ...	162
Table 6-9. Spin exchange parameters of $RECu_6(OH)_6(AsO_4)_3 \times 3 H_2O$ and Curie-Weiss temperature Θ_{CW}	165

1. Introduction

Inspired by the discovery of high-Tc superconductivity in two-dimensional oxycuprates [1-1] low-dimensional quantum antiferromagnets and their unique properties attracted much interest in the past few decades. In such low-dimensional systems, a strong intra-chain (intra-plane) spin-exchange coupling is being prevalent. Inter-chain (inter-plane) spin-exchange coupling is significantly weaker and becomes relevant only at low temperatures. Ideal low-dimensional systems like isolated chains or planes exhibit some fascinating properties (e.g. spin-liquid behavior).

In 1925, Ernst Ising proposed a mathematical model for a ferromagnet, that consisted of discrete magnetic moments +1 and -1 (or spin up and spin down).[1-2] These moments are coupled by nearest-neighbor interaction along a chain. The energy of the system with this spin configuration is given by the following Hamiltonian (“Ising chain“):

$$\mathcal{H} = -J \sum_i S_i^z S_{i+1}^z - \mu_B H \sum_i S_i^z, \quad (1-1)$$

where:

S_i^z is the z component of the spin angular momentum;

J is the spin-exchange interaction between two adjacent sites;

$i, i+1$ represents the nearest-neighbor sites i and $i+1$;

$\mu_B = \frac{e\hbar}{2m_e}$ is the Bohr magnetron;

H is the external field interacting with the spin moments.

To his surprise, Ising could find a long-range magnetic order for the chain model only at T=0K. [1-2]

Later in 1944, Lars Onsager studied the two-dimensional Ising model on a square lattice with no external magnetic field applied. [1-3] From an analytical solution, he showed that the Ising square lattice exhibits a long-range magnetic order with

a logarithmic singularity in the heat capacity at the finite temperature $T_c = \frac{2J}{k_B \ln(1+\sqrt{2})}$.

Historically, the next step in the investigation of low-dimensional systems was done by studying the one-dimensional Heisenberg chain model. In this model, the exchange energy depends on the relative orientation of the spin moments with no reference to a special direction in the crystal, as assumed in the Ising model. The energy of the system is given by this Hamiltonian function:

$$\mathcal{H} = -J \sum_i \vec{S}_i \vec{S}_{i+1} - \mu_B H \sum_i \vec{S}_i, \quad (1-2)$$

where:

$\vec{S}_i = (S_i^x, S_i^y, S_i^z)$ is the spin moment.

In 1964 Bonner and Fisher calculated the magnetic susceptibility and the heat capacity of $S = 1/2$ finite Heisenberg chains with ferro- and antiferromagnetic nearest-neighbor spin exchange coupling. [1-4] Later they extrapolated the results for finite chain fragments to infinite systems. These results have since been used frequently to analyze experimental data.

In the 1990s, modern calculational methods such as quantum Monte Carlo or Density Matrix Renormalization Group calculations were applied to obtain the magnetic susceptibility and the heat capacity e.g., of $S = 1/2$ chains with nearest-neighbor Heisenberg spin-exchange coupling. [1-5, 1-6, 1-7] High precision Padé approximations of these results have been published, enabling more precise comparisons with experimental data. [1-8] Recently, a similar treatment for systems with spins $S > 1/2$ systems was published by Law et al. [1-9] It has been shown that, for antiferromagnetic Heisenberg chains, the magnetic susceptibility and the heat capacity are both characterized by a broad maximum at temperatures comparable to the spin-exchange coupling constant. These maxima originate from short-range antiferromagnetic correlation. Similar to Ising chains, long-range ordering in Heisenberg chains is not observed at finite temperatures. These findings were put into a more general theoretical perspective (Mermin-Wagner theorem) by Mermin and Wagner in 1966 and Berezinskii in 1971. [1-10, 1-11] The Heisenberg chains realize a spin-liquid state. Excitations in Heisenberg chains are not of the usual magnon type with $\Delta S=1$, they rather have an $\Delta S=1/2$ spinon character with a continuous range for excitation energies given by: [1-12]

$$\hbar\omega = \pi|J\sin(qa)|, \quad (1-3)$$

where:

a is the lattice constant;

q is the wave vector.

In this thesis, I have investigated the low-dimensional spin $S=1/2$ Heisenberg chain systems CuTa_2O_6 , $\alpha\text{-CuV}_2\text{O}_6$, and RE-mixites (RE= non-magnetic rare earth) with composition $\text{RECu}_6(\text{OH})_6(\text{AsO}_4)_3 \cdot n\text{H}_2\text{O}$ (RE = Bi, Y, La, Lu; $n \approx 3$) by various experimental and theoretical techniques. The magnetism of these compounds originates from Cu^{2+} ($3d^9$ electronic configuration, $S=1/2$) cations. Exposed to the ligand field of the surrounding anions as it is given, for example, when Cu^{2+} cation is placed in the center of an octahedron of anions (e.g. O^{2-} anions), the doubly degenerate e_g state is unstable with respect to a lattice distortion. The most common effect is an elongation of the anion octahedra (Jahn-Teller elongation), substantially pushing the anions at apical positions further away. This lifts the degeneracy of the e_g state, leaving a hole in the x^2-y^2 orbitals. The interaction with orbitals of neighboring cations also has to be taken into consideration resulting in further and often more complex distortion patterns and lower symmetry. Decreasing the orbital degeneracy by distortions generally implies a distinct directionality of the spin-exchange interaction to neighboring cations via intermediate anions, which often results in low dimensional quantum magnetism with dominant spin-exchange along chains or within layers. The pronounced orbital directionality makes it challenging to guess the spin-exchange pathway from sheer structural motifs only. Modern electronic density functional theory (DFT) calculations provide helpful advice to identify the dominant spin-exchange pathways.

2. Theory

In this chapter, a short overview of the diffraction theory and DFT is provided. This basic knowledge is required for better understanding of methods used in this work.

2.1. X-ray and neutron diffraction

In order to characterize the crystal structure of the compounds and to check for phase purity, I have used X-ray and neutron powder diffraction experiments. The X-ray diffraction experiments were carried out employing laboratory-based powder diffractometers using monochromated X-rays of wavelength $\lambda = 1.5406 \text{ \AA}$ (Cu $K_{\alpha 1}$) and $\lambda = 0.7093 \text{ \AA}$ (Mo $K_{\alpha 1}$). Neutron powder diffraction studies were done using the high-resolution diffractometer SPODI at the Heinz Maier-Leibnitz Zentrum (MLZ) neutron center at TU Munich [2-1] and the high-intensity medium-resolution powder diffractometer D20 at the Institut Laue-Langevin (ILL). [2-2]

X-ray and neutron diffraction are based on Bragg's law. In 1913, Lawrence and William Bragg studied diffraction patterns of NaCl, ZnS, and diamond crystals. They found that very strong reflected intensities observed on a film (Bragg's peaks) have a certain unique position for different crystals. A simple equation (Bragg's law) to describe this condition for constructive interference was proposed:

$$2d \sin\theta = n\lambda, \quad (2-1)$$

where

d is the inter-planar distance, depending on the lattice parameters;

θ is the scattered angle;

λ is the wavelength of the incident X-rays and neutrons.

Bragg's law can be derived from simple geometrical considerations shown in Figure 2-1.

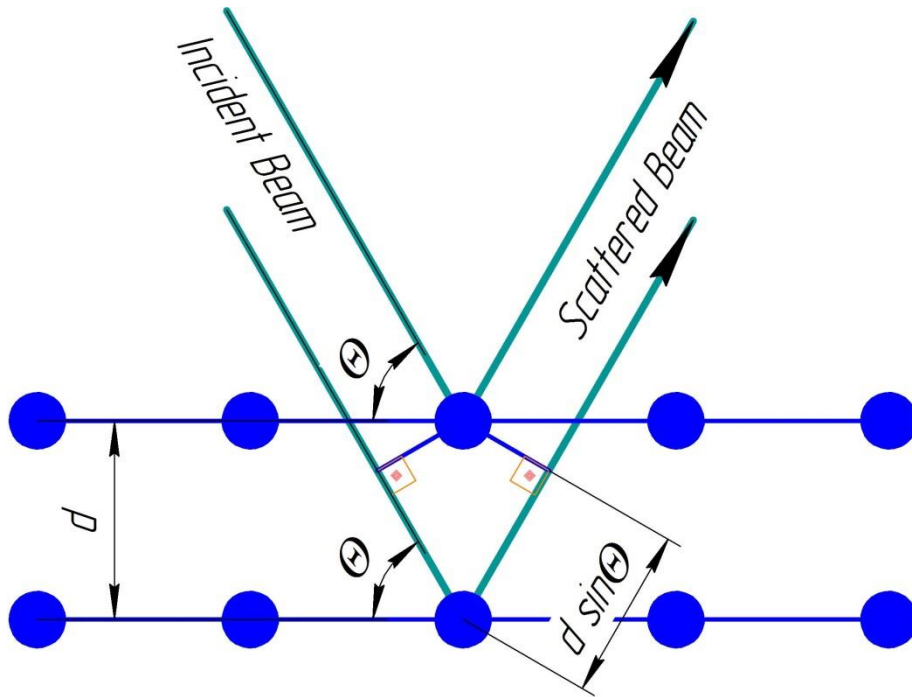


Figure 2-1. Bragg diffraction

X-ray diffraction is particularly sensitive to the heavy elements in a compound [2-3], whereas neutron scattering is also able to trace light elements like e.g. oxygen. [2-4]

Since neutrons carry a spin $S=1/2$, the neutron scattering cross-section is sensitive to the magnetic structure of a compound. Neutron diffraction is the prime technique to establish the magnetic structure of a compound.

2.2. Density Functional Theory

Density functional theory (DFT) is a computational quantum mechanical method used for the calculation of the electronic structure of a many-electrons systems. These calculations are based on using functionals (a function of another function) of the electronic density.

The DFT method was developed by Walter Kohn and Pierre Hohenberg in the framework of the two Hohenberg–Kohn theorems (H–K) in 1964. [2-5] The first H–K theorem postulates that an electron density uniquely determines the ground state properties of a many-electron system. Three spatial coordinates uniquely determine this electron density function. Applying the first H-K theorem to a many-body problem of n electrons with $3n$ spatial coordinates, it is possible to reduce the problem to 3 spatial coordinates. The second H–K theorem defines the energy functional and the ground state of the system. It proves that the ground state has the lowest energy functional.

Kohn together with Sham, further developed the H–K theorems and proposed the Kohn–Sham DFT (KS DFT) in 1965. [2-6] Their idea was to replace the intractable many-body problem of interacting electrons in a static external potential to a tractable problem of non-interacting electrons moving in an effective potential. The effective potential consists of the external potential and the effects of the Coulomb interactions between the electrons (exchange and correlation interactions). The Born–Oppenheimer approximation can be applied. The nuclei of atoms are supposed to be fixed. They generate a static external potential V_{ext} in which the electrons are moving. A stationary electronic state is described by a wave-function $\Psi(\vec{r}_1, \vec{r}_2, \dots, \vec{r}_N)$ satisfying the many-electron time-independent Schrödinger equation given by:

$$\begin{aligned} \mathcal{H}\Psi &= [\hat{T} + \hat{V} + \hat{U}]\Psi = \left[\sum_i^N \left(-\frac{\hbar}{2m_i} \nabla_i^2 \right) + \sum_i^N V(\vec{r}_i) + \sum_{i<j}^N U(\vec{r}_i, \vec{r}_j) \right] \Psi \\ &= E\Psi \end{aligned} \quad (2-2)$$

where:

N is the number of electrons in the system;

\mathcal{H} is the Hamiltonian;

E is the total energy;

\hat{T} , \hat{V} , \hat{U} are the kinetic energy, the potential energy from the external field due to positively charged nuclei and electron-electron interaction energy, respectively.

The operators \hat{T} , and \hat{U} are universal operators, i.e. they are the same for any N -electron system. \hat{V} is a system-dependent operator. By replacing electron positions \vec{r}_i by the electron density functional $n(\vec{r})$, DFT provides a way to solve a many-body problem, with electron-electron interaction energy \hat{U} , as a single-body problem without \hat{U} . The electronic density is given by:

$$n(\vec{r}) = N \int d^3r_2 \dots \int d^3r_N \Psi^*(\vec{r}_1, \vec{r}_2, \dots, \vec{r}_N) \Psi(\vec{r}_1, \vec{r}_2, \dots, \vec{r}_N) \quad (2-3)$$

This relation can be reversed. For a given ground-state density $n_0(\vec{r})$ the corresponding ground-state wavefunction $\Psi_0(\vec{r}_1, \vec{r}_2, \dots, \vec{r}_N)$ can be derived. [2-5] The ground-state expectation value can be written as:

$$O(n_0) = \langle \Psi(n_0) | \hat{O} | \Psi(n_0) \rangle \quad (2-4)$$

The ground state energy is given by:

$$E_0 = E(n_0) = \langle \Psi(n_0) | \hat{T} + \hat{V} + \hat{U} | \Psi(n_0) \rangle \quad (2-5)$$

The contribution of the external potential $\langle \Psi(n) | \hat{V} | \Psi(n) \rangle$ can be written in terms of the electron density $n(\vec{r})$:

$$V(n) = \int V(\vec{r}) n(\vec{r}) d^3r \quad (2-6)$$

The total energy of the system is then given by:

$$E[n] = T[n] + U[n] + \int V(\vec{r}) n(\vec{r}) d^3r \quad (2-7)$$

The variational problems of minimizing the energy functional $E[n]$ is solved by applying the Lagrangian method of undetermined multipliers.[2-6] The external effective potential in which the particles are moving can be written as:

$$V_s(\vec{r}) = V(\vec{r}) + \int \frac{e^2 n(\vec{r}')}{|\vec{r} - \vec{r}'|} d^3\vec{r}' + V_{xc}(n(\vec{r})), \quad (2-8)$$

where:

V_{xc} is the exchange-correlation potential, which includes all many-particle interactions.

The second term of Eq. (2-8) $\int \frac{e^2 n(\vec{r}')}{|\vec{r} - \vec{r}'|} d^3\vec{r}'$ is called the Hartree term. It describes electron-electron Coulomb repulsion.

The Kohn–Sham equation Eq. (2-8) has to be solved in a self-consistent iterative manner. The exact value of the exchange and correlation functionals can be found only for the free electron gas. Therefore many different approximations have been proposed to calculate these functionals for real systems. For example, the Local-Density Approximation (LDA) is one of the simplest and the most commonly used approach. It is based on the exact exchange energy obtained from the Thomas–Fermi model and fits the correlation energy for a uniform electron gas. In each point in space \vec{r} with electron density $n(\vec{r})$, an electron has the same interactions with other electrons, as in the system with uniform density $n(\vec{r})$. For non-interacting systems, the wave-function can be represented as a Slater determinant of orbitals. The functional in LDA depends only on the density at the coordinate where the functional is evaluated. The kinetic energy functional for

such a system can be found exactly. The exchange-correlation energy can be written as:

$$E_{XC}^{LDA}(n) = \int \varepsilon_{XC}(n) n(\vec{r}) dr^3, \quad (2-9)$$

where:

$\varepsilon_{XC} = \varepsilon_X + \varepsilon_C$ is the exchange-correlation energy.

The exchange-correlation energy is usually divided into the exchange part ε_X and the correlation part ε_C . The exchange part is called the Dirac exchange. It takes the form $\varepsilon_X \propto n(\vec{r})^{1/3}$.

From Quantum Monte Carlo simulations of the jellium, in 2005, Perdew et al. proposed an improved approximation for the correlation energy density $\varepsilon_C(n_\uparrow, n_\downarrow)$. [2-7]

In the LDA approximation, as described above, the same electron density is assumed to be present everywhere. That is why this approximation tends to underestimate the exchange energy and over-estimate the correlation energy. [2-8] The errors occur from the tendency of exchange and correlation parts, which may compensate each other to a certain degree. To correct this problem, the generalized gradient approximations (GGA) has been proposed. In order to account for the non-homogeneity of the true electron density, the GGA density was expanded in terms of the gradient of the electron density. It takes into account corrections based on the variation of the electron density away from the coordinate.

The exchange-correlation energy within GGA approximation can be written as [2-9, 2-10, 2-11]:

$$E_{XC}^{GGA}(n_\uparrow, n_\downarrow) = \int \varepsilon_{XC}(n_\uparrow, n_\downarrow, \nabla n_\uparrow, \nabla n_\downarrow) n(\vec{r}) dr^3 \quad (2-10)$$

Total energy calculations including the spin moments can be used to differentiate between various magmatic structures. Mapping the total energy on an exchange

Hamiltonian enables to derive the spin-exchange parameters between the magnetic moments in a magnetic compound.

3. Experimental methods

In this chapter, a short description of the different experimental techniques used in the investigations of the magnetic and structural properties of CuTa_2O_6 , CuV_2O_6 , and RE mixite samples is provided.

3.1. Powder diffraction

Powder X-ray, neutron, or electron diffractions are techniques used for the structural characterization and phase identification of materials.

The central equation for the diffraction method is Bragg's law described in Chapter Two. Different methods use different incident rays, like X-rays or neutrons. Due to the different nature of the incident rays, different information about the sample is obtained. X-rays are electromagnetic waves. They interact with the electron shells. This implies that, in the presence of heavy atoms with many electrons, it may be difficult to detect light atoms by X-ray diffraction. Neutrons are neutral particles with the mass of $1839m_e$ (where m_e is the mass of the electron). They interact with the cores of the atoms via a strong interaction. The neutron scattering lengths differ from X-ray scattering lengths and do not depend on the number of electrons (see Figure 3-1). Therefore neutron diffraction can, fortunately, be used to detect light elements such as oxygen or hydrogen in a combination with heavy atoms. Since neutrons carry no electrical charge, they are able to penetrate into the investigated sample and, therefore, sometimes provide more information about the bulk of a sample.

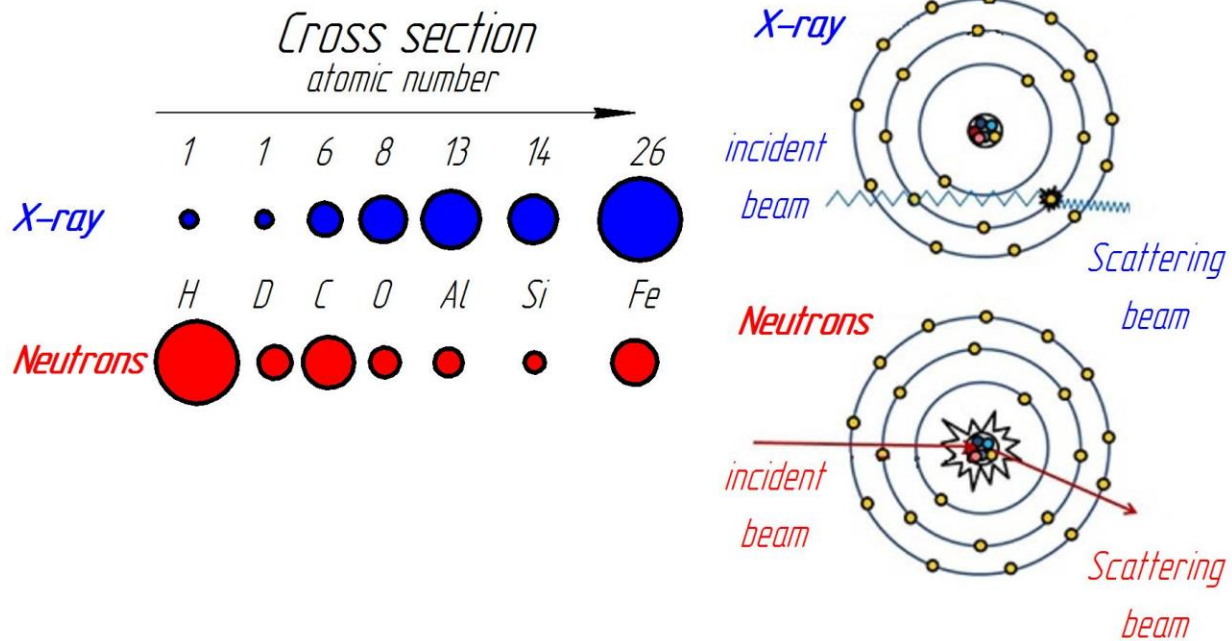


Figure 3-1. Comparison of scattering strength between X-Rays and neutrons for few elements (left) and interaction of x-rays and neutrons with the atoms (right). Adopted from [3-1].

The diffraction pattern of the powder sample consists of a series of Debye-Scherrer rings. These rings result from the superposition of the individual single-crystal diffraction patterns from averaged over a very large number of randomly oriented crystallites. The intensities in the Debye-Scherrer rings are integrated to obtain the intensity of a Bragg reflection. The background intensity and peak widths provide information about the crystallinity of the sample. Peak positions and intensities can be used in Rietveld profile refinements to detect the phase composition, the crystal structure, and microstructural parameters. Shifts in the diffraction peak positions and changes in their intensities (for example by temperature changes or by applying external pressure) allow to extract changes in lattice parameters and the atom positions. The appearance of new peaks and the disappearance of peaks indicated may hint at phase transitions.

In contrast to X-rays, neutrons carry a magnetic moment ($S=1/2$), and they are scattered from other magnetic moments, thus allowing to use them in order to study the magnetic structure. At a temperature above the ordering point of the

magnetic moments, materials behave as a paramagnetic. Only the crystallographic structure will be seen in a neutron diffraction pattern. Paramagnetic scattering typically gives a broad diffusive-like background at low scattering angles. Below the ordering point (the Néel temperature of an antiferromagnet (AF) or the Curie-point T_c of a ferromagnet (FM)), the neutrons will also experience scattering from the ordered magnetic moments, and new superstructure peaks and/or intensity changes of the Bragg reflections will be observed. The diffraction pattern can be refined in the same manner as the nuclear structure to obtain the magnetic structure of the material.

X-ray powder diffraction measurements presented in this work were performed with the STOE STADI P and the Bruker D8 ADVANCE X-ray powder diffractometers shown in Figure 3-2.



Figure 3-2. STOE STADI P (right) and Bruker D8 ADVANCE (left) diffractometers. [3-2, 3-3]

The STOE STADI P diffractometer is equipped with a high-precision two circle goniometer and can be used in Debye-Scherrer or Bragg-Brentano geometry. The principal scheme is shown in Figure 3-3. The divergent beam from the X-ray source is focused not onto the sample but beyond onto the 2θ measuring circle of the position-sensitive detector (PSD). This geometry has several advantages: no height displacement corrections have to be applied and a wide 2θ range is accessible. The STOE STADI P diffractometer can be equipped with different X-ray

sources (Fe, Co, Cu, Mo or Ag) and attachments for high- and low-temperature measurements.

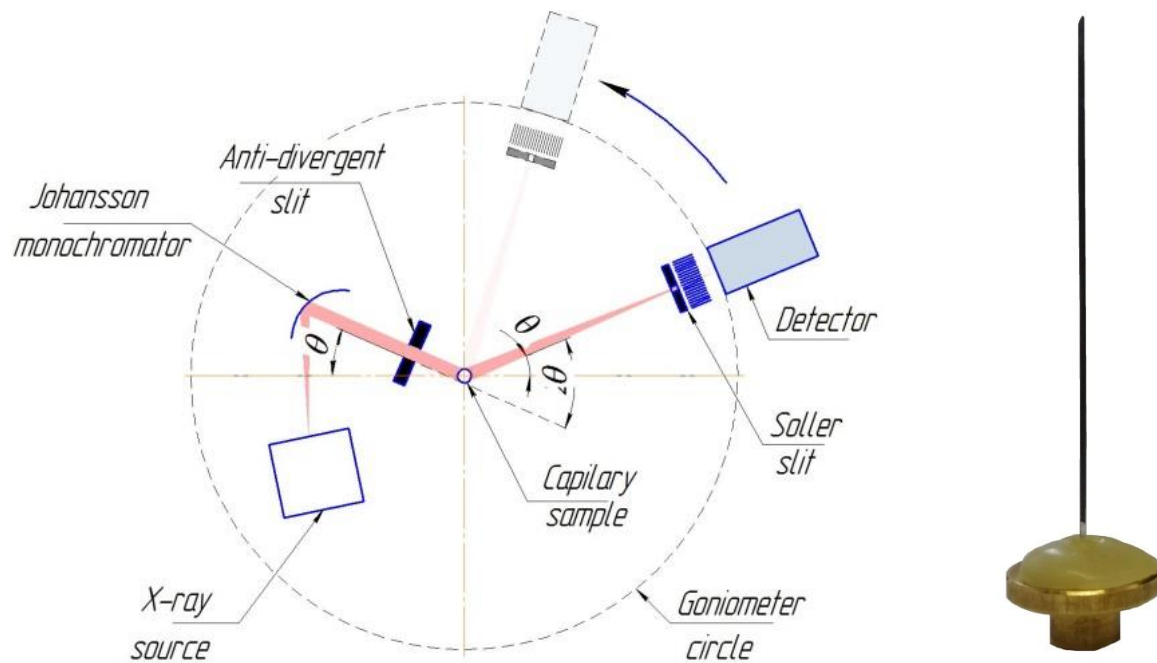


Figure 3-3. Capillary sample prepared for STOE STADI P diffractometer (right) and scheme of Debye-Scherrer diffractometer (left). [3-4]

The Bruker D8 ADVANCE powder diffractometer is a full-sized goniometer class diffractometer operating in Bragg Brentano geometry. The principal scheme is sketched in Figure 3-4. It also can be equipped with attachments for measurement under ambient and non-ambient conditions, and different X-ray sources can be installed.

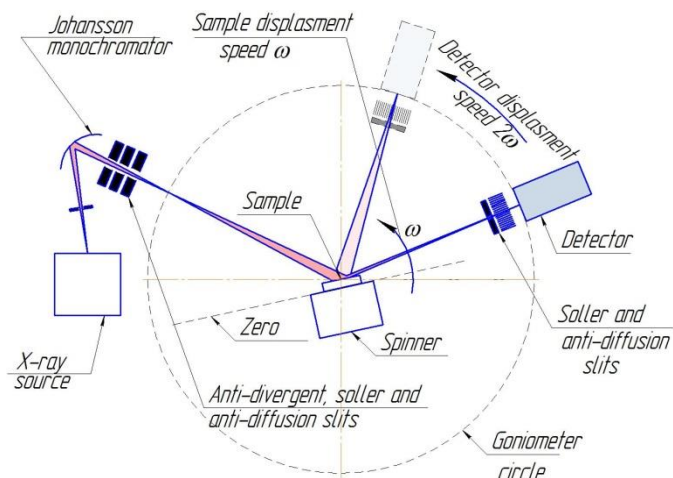


Figure 3-4. Thin-film sample prepared for the Oxford Phenix cryocooler (right) and the scheme of Bragg Brentano diffractometer (left). [3-4]

Neutron powder diffraction measurements were performed with the high-intensity medium-resolution diffractometer D20 at ILL, Grenoble, and the high-resolution diffractometer SPODI at MLZ, Garching (Figure 3-5). Both instruments are two axis powder diffractometers. The principal scheme is shown below in Figure 3-6. They are designed to study crystal and magnetic structures under ambient and non-ambient conditions.

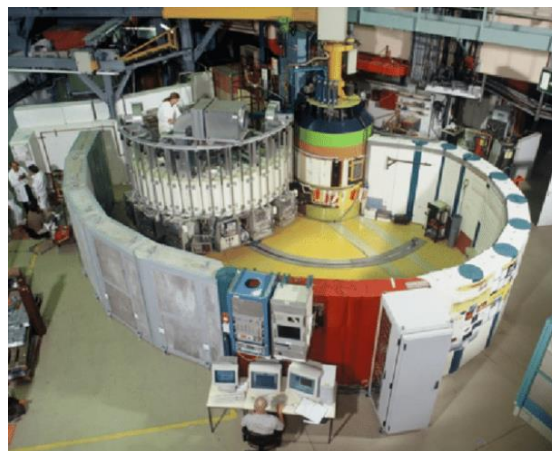


Figure 3-5. SPODI (left) and D20(right) neutron powder diffractometers. [3-5, 3-6]

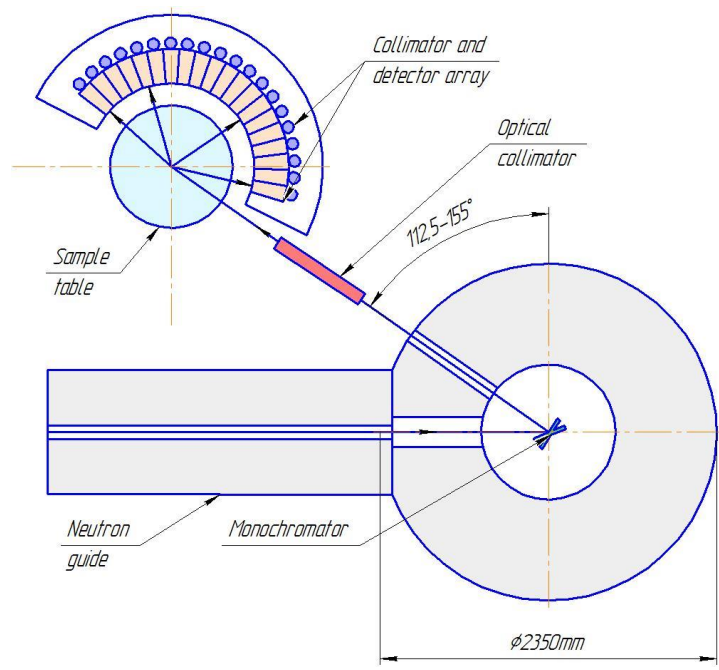


Figure 3-6. Principal scheme of the two-axis high-resolution powder diffractometer SPODI. [3-6]

3.2 Magnetic property measurements

Magnetization measurements were performed with the MPMS-XL7 magnetometer (see Figure 3-7) using a radio frequency (RF) SQUID (Superconducting Quantum Interference Device) detector. It enables to apply magnetic fields of up to 7 Tesla and it can measure magnetic moments of the order of 1×10^{-7} emu.

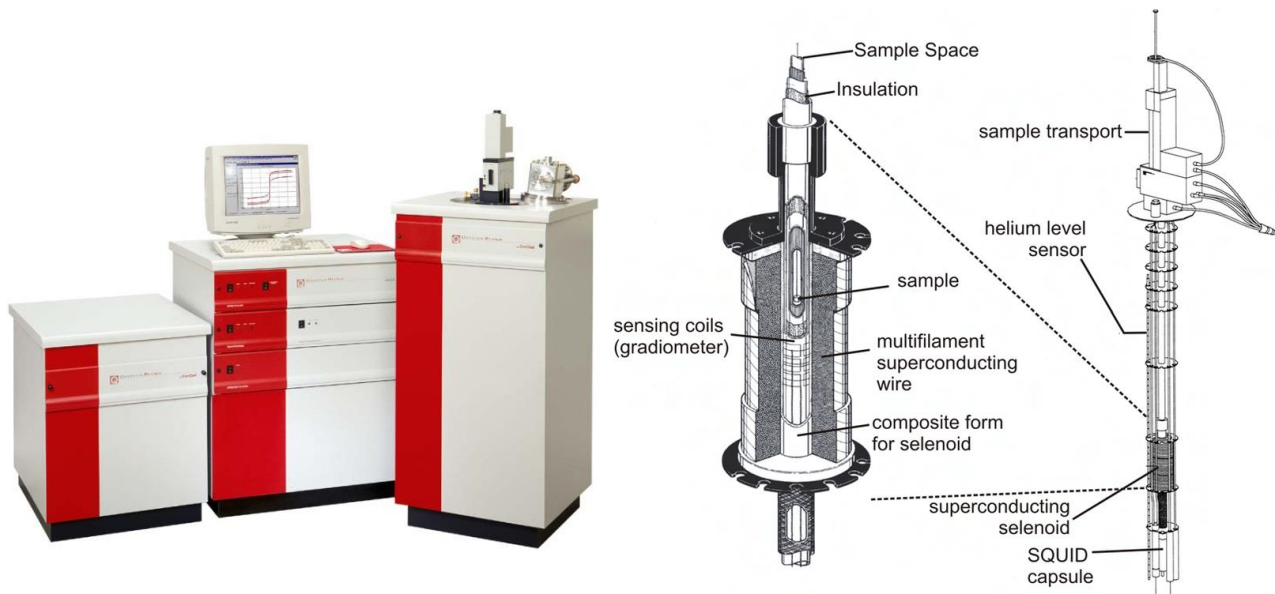


Figure 3-7. Quantum Design MPMS XL7 SQUID magnetometer (left) and schematic scheme of the probe component (right). [3-7, 3-8]

During the measurement, a sample is scanned over a set of distances through the superconducting detection input coil (see Figure 3-8). Magnetic flux is inductively coupled to the SQUID detector. Any changes in the input coil current will induce a change in the current flowing in the SQUID ring. The principal scheme of the RF SQUID magnetometer is represented in Figure 3-8. The flux transformer is connected to the input coil. The second coil, called “RF” coil, is coupled to a high-quality resonant circuit. It is used to read out the flux changes in the SQUID loop.

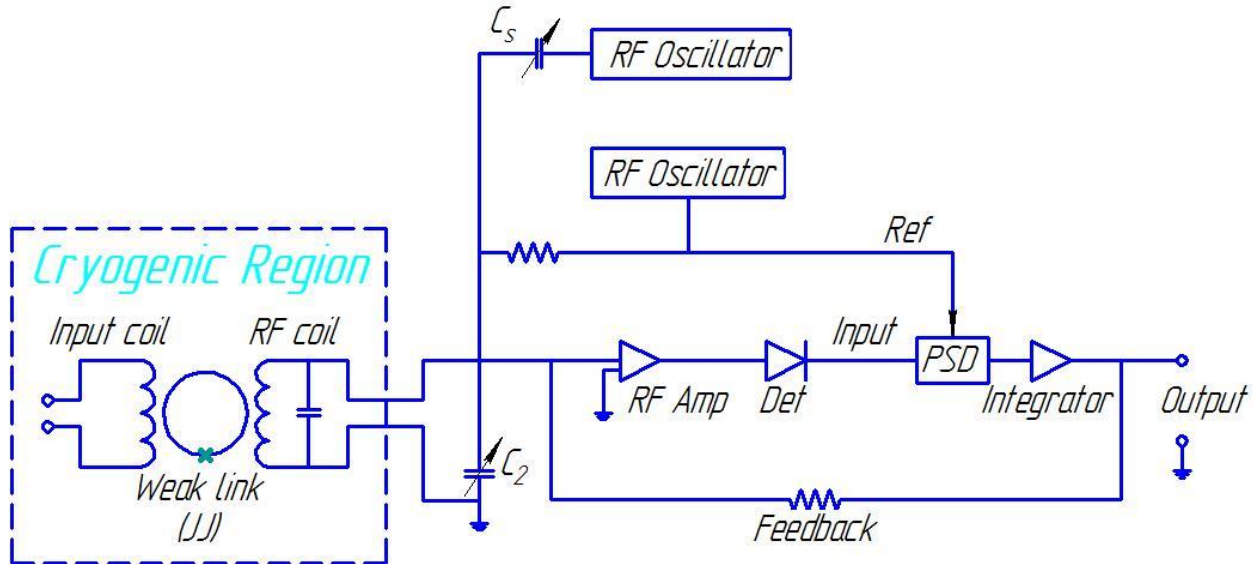


Figure 3-8. Principal scheme of a RF SQUID magnetometer. [3-10]

The magnetization per unit mass of the sample $M(T, H)$ is calculated from the magnetic moment read out by SQUID magnetometer using the following equation:

$$M(T, H) = \frac{M_s}{m_s}, \quad (3-1)$$

where:

M_s is the magnetic moment in $\text{cm}^{-3}(\text{emu})$,
 m_s is the mass of the sample in g.

The molar susceptibility of the sample is calculated using the following equation:

$$\chi_{mol} = \frac{M_s M_{mol}}{m_s H}, \quad (3-2)$$

where:

M_{mol} is the molar mass in g/mol,
 H is the applied magnetic field in Ørsted .

3.3 Electronic paramagnetic resonance

Electron paramagnetic resonance (EPR) is a spectroscopy method to study materials with unpaired electrons. When an external magnetic field H is applied on a sample, the energy of the unpaired electron splits (Zeeman splitting). The energy difference between $m_s=1/2$ and $m_s=-1/2$ (for a spin $S=1/2$ moment) can be described as

$$\Delta E = g_e \mu_B H, \quad (3-3)$$

where:

$g_e=2.0023$ is the electron g-factor,
 μ_B is the Bohr magneton.

The energy difference between the Zeeman levels can be detected by absorbing or emitting a photon of energy $h\nu$. Thus, the resonance conditions can be written as

$$h\nu = g\mu_B H_{res} \quad (3-4)$$

Deviations of the g-factor from 2.0023 can be related to internal fields, e.g. spin-exchange interaction to neighboring spin moments or ligand field effect. Hyperfine coupling with the nucleus can also influence on g . [3-11] Moreover, additional ligand field splitting due to electric fields from neighboring charges acting on the electron orbits can be measured.

Modern EPR developments use pulsed magnetic fields operating in microwave frequencies to several hundred GHz-THz. [3-12, 3-14] Laboratory-based EPR spectrometers use microwave frequencies ranging between 1 and 100 GHz resulting in resonance magnetic fields between 0.035 to 3.5 Tesla. [3-15] Usually these spectrometers operate at constant microwave frequency in a continuous-wave mode. The principal scheme of an EPR spectrometer is outlined in Figure 3-9.

The microwave resonance frequency can be detected by sweeping the external magnetic field. In order to get a higher sensitivity, a small effect AC modulation of the external field (typical frequency of 100 kHz) is employed. This allows to

improve the signal-to-noise ratio. The resulting signal from the microwave detection diode is filtered and amplified using a phase sensitive amplifier (lock-in amplifier). The modulation of the slowly varying external magnetic field combined with the phase sensitive detection technique provides the first derivative of the microwave absorption P_{abs} . [3-16, 3-17]

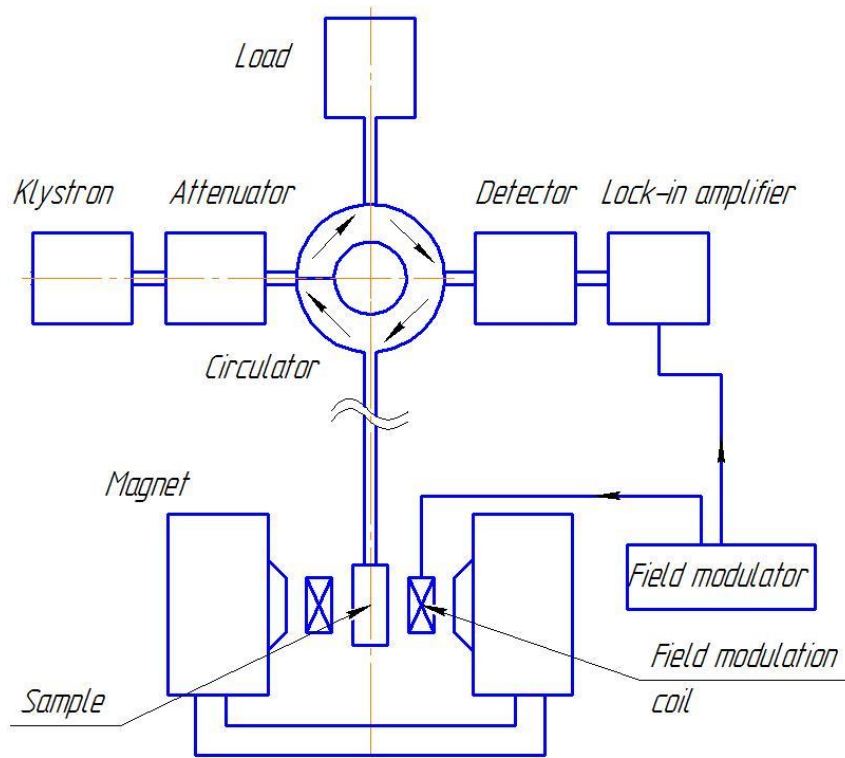


Figure 3-9. Principal scheme of a EPR spectrometer [3-16]

The measured EPR spectra can generally be well described in terms of a Lorentzian resonance line according to:

$$\frac{dP_{abs}}{dH} \propto \frac{d}{dH} \left(\frac{\Delta H + C(H - H_{res})}{(H - H_{res})^2 + \Delta H^2} + \frac{\Delta H + C(H - H_{res})}{(H + H_{res})^2 + \Delta H^2} \right), \quad (3-5)$$

where:

P_{abs} is the absorbed microwave power,

ΔH is the half-width at half-maximum (HWHM),

H_{res} is the resonance field,

C is a degree of the mixture of the absorption and the dispersion signals.

For a narrow EPR spectrum ($H_{res} \gg \Delta H$), only the first term (ω^+ resonance) is required. Relaxation effects and internal fields can result in a broadening of the resonance line ($H_{res} \approx \Delta H$) and the second term in Eq (3-5) (ω^- resonance) resulting from the opposite precession of the spin has to be taken into account.

For the fitting of the spectra, an offset and a linear variation of the background signal with the field also have to be considered.[3-18]

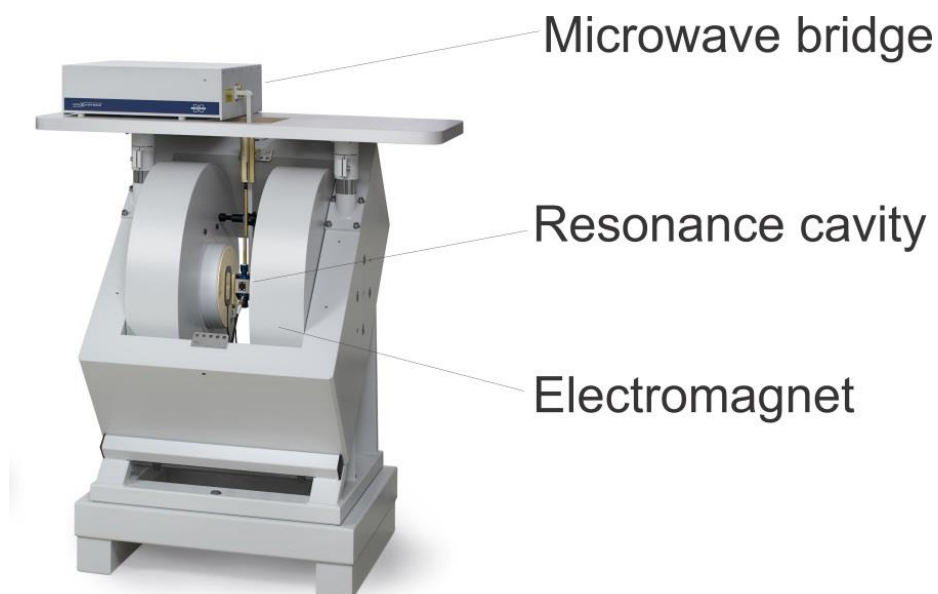


Figure 3-10. The Bruker X-band EPR spectrometer [3-19].

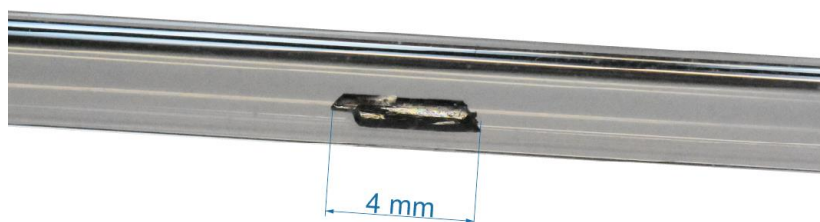


Figure 3-11. An oriented crystal of α - CuV_2O_6 mounted in a quartz glass tube for EPR measurements.

In this thesis, the Bruker ER 040XK EPR spectrometer shown in Figure 3-10 was used. It is a spectrometer operating at ~ 9.5 GHz (X-band). Magnetic fields are generated by a Bruker iron core ER73 electromagnet, which is controlled by a Bruker BH-015 field controller calibrated against the resonance of 2,2-diphenyl-1-picrylhydrazyl (DPPH). The EPR spectra can be measured at temperatures

between 2.5 K and 300 K using an Oxford continuous flow cryostat. A typical sample mounting of a crystal (α -CuV₂O₆) is shown in Figure 3-11.

3.4 Heat capacity measurements

Specific heat capacity measurements are a powerful tool to study phase transitions. The heat capacity is the amount of heat ΔQ required to raise the temperature of the sample by ΔT under constant conditions (e.g. constant pressure or volume). [3-20, 3-21]:

$$C_x = \lim_{\Delta T \rightarrow 0} \left(\frac{\Delta Q}{\Delta T} \right)_x, \quad (3-6)$$

where:

ΔQ is the heat input;

ΔT is the temperature change;

\square_x the subscript x stands for constant pressure or constant volume conditions.

Heat capacity at constant volume and constant pressure are connected by the following equation:

$$C_v = C_p - \frac{\beta^2 VT}{k_T}, \quad (3-7)$$

where:

C_v and C_p are the heat capacities at constant volume and at constant pressure, accordingly;

β is the volumetric coefficient of thermal expansion;

V is the molar volume;

k_T is the isothermal compressibility or the reverse bulk modulus.

At low temperatures, the difference of the specific heat capacities at constant volume and constant pressure is small ($\propto T$). In a first approximation, the Debye model can describe the lattice heat capacity. In addition, electron and magnetic excitations may contribute to the heat capacity. Lattice vibrations at low temperatures are proportional to T^3 , whereas electron contributions have a linear

($\propto T$) dependence (Sommerfeld term). For magnetic materials, an additional contribution from magnon excitations is observed. For low temperatures magnon excitations are proportional to $T^{\frac{d}{n}}$, where d is the dimensionality of the lattice and n is the exponent of the magnetic dispersion relation. For AFM and FM magnons n is equal to 1 (linear magnon dispersion) and 2 (parabolic magnon dispersion), respectively. Thus for three-dimensional compounds, the magnetic contribution of the heat capacities will be proportional to $T^{\frac{3}{2}}$ and T^3 for FM and AFM compounds, accordingly. For one-dimensional AF compound the magnon contribution is proportional to T ($n=1, d=1$). [3-21, 3-22, 3-23, 3-24, 3-25, 3-26, 3-27]

Magnetic phase transitions generally give rise to so-called λ -type anomalies in the heat capacities, as is exemplified for the FM ordering of GdCl_3 at ≈ 2.2 K (see Figure 3-12).

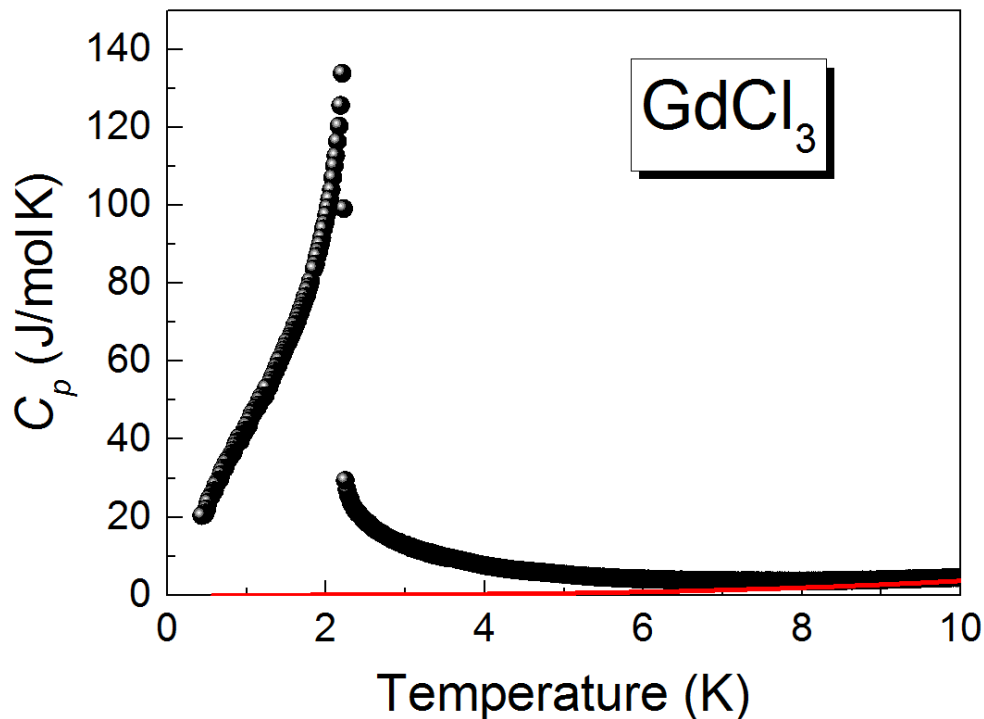


Figure 3-12. λ -type anomaly in the heat capacity of GdCl_3 at the FM ordering.

Heat capacity experiments were done in the Quantum Design Physical Property Measurement System (PPMS). The sample is placed on a platform shown in

Figure 3-13, which is connected with the electronic controller by eight wires. The platform itself is a sapphire chip with a heater and a calibrated thermometer attached to the bottom of the chip. The sample is thermally anchored to the platform using vacuum grease (e.g. Apiezon N). To protect the sample and the platform from thermal radiation and guarantee thermal equilibrium, a thermal radiation shield is placed on top of the sample puck. [3-28]

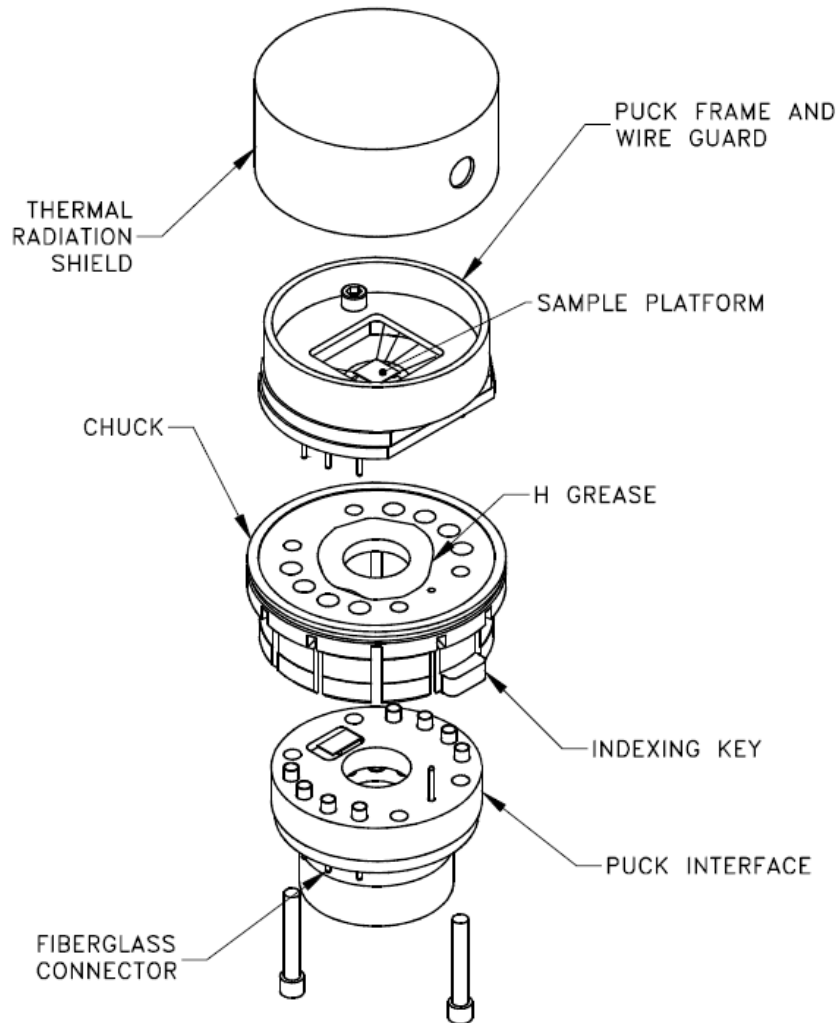


Figure 3-13. Construction of the PPMS calorimeter sample puck. [3-28]

The measurements are performed under high vacuum for temperatures ranging from 1.8 K to 300 K with magnetic fields up to 9 Tesla. The thermal relaxation calorimetric method was used. It is designed for fast measurements of small samples (10-20mg). The heat flow diagram is presented in Figure 3-14. After the

temperature stabilization, short heat pulses are sent into the sample to raise the temperature. Temperature changes *versus* time are recorded by the electronic controller system. The individual temperatures of the sample and the platform *versus* time are fitted to the solution of two coupled linear differential Eqns (3-8) and (3-9), [3-29] by varying two relaxation times (internal: from the platform to the sample; external: from platform and sample to the environment), the heat capacity of the sample and the starting temperature.

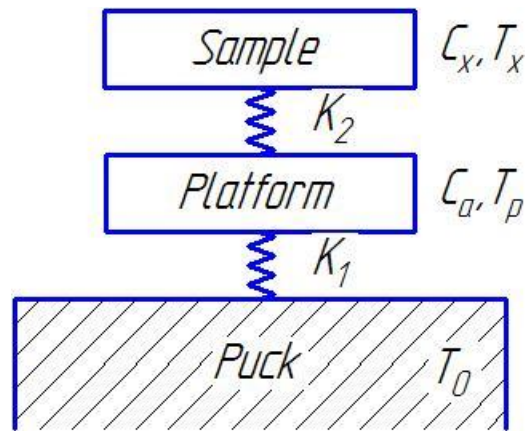


Figure 3-14. Heat-flow diagram for a conventional thermal-relaxation calorimeter.

$$P = C_a \frac{dT_p}{dt} + K_2(T_p - T_x) + K_1(T_p - T_0), \quad (3-8)$$

$$0 = C_x \frac{dT_x}{dt} + K_2(T_x - T_p), \quad (3-9)$$

where:

T_x, T_p, T_0 are the temperatures of the sample, the platform, and the puck, respectively;

C_x and C_a are the heat capacities of the sample and the platform respectively;

K_2 and K_1 are the thermal conductance between the sample and the platform, the platform, and the puck via wires, respectively.

When the thermal connection between the sample and the platform is very strong ($K_2 \gg K_1$) then $T_x = T_p$. The heat-balance condition (Eq.3-8 and Eq.3-9) can be written as

$$P = (C_a + C_x) \frac{dT_p}{dt} + K_1(T_p - T_0), \quad (3-10)$$

where:

P is a power applied to the heater.

If the supply of the heat power P is suspended, we can find the temperature of the sample as:

$$T_p(t) = T_0 + \Delta T e^{-\frac{t}{\tau}}, \quad (3-11)$$

where:

$\tau = \frac{C_{tot}}{K_1} = \frac{C_a + C_x}{K_1}$ is the time constant, gained from fitting the temperature relaxation curve versus time.

The PPMS software uses a specific curve fitting algorithm developed by Hwang et al. in 1997. [3-30] The addenda heat capacity C_a includes the heat capacities of the platform, the vacuum grease, the wires, the heater, and the thermometer. Generally, the addenda heat capacity is determined before the sample measurements in order to subtract it from the total heat capacity. The normalized heat capacities of the sample can be written as [3-28]:

$$C_{nx}(T) = C_x \frac{M_{molar}}{m_x}, \quad (3-12)$$

where:

C_{nx} is the normalized heat capacity of the sample;

M_{molar} is the molar mass of the sample;

M_x is a mass of the sample.

3.5 Raman spectroscopy

Raman spectroscopy is an optical spectroscopic technique used for the determination of the vibrational modes of molecules and solids. It is often employed to provide a fingerprint by which, for example, molecules can be identified. Vibrational modes are usually in the center of interest in Raman spectroscopy, however rotational and other low-frequency modes of systems, for example, electronic excitation, may also be observed. [3-31] Raman spectroscopy is a nondestructive method and requires little or no sample preparation. Solids, powder samples, or aqueous solutions can be analyzed. Raman spectroscopy is sensitive to the samples anisotropy. It provides information on the crystal structure, such as short- and long-range ordering, strain, temperature influence, doping and phase transitions.

Raman spectroscopy is based on inelastic scattering of photons. Lasers in the visible, near-infrared or near-ultraviolet ranges are commonly used as a source of monochromatic light. For some applications, X-rays can be used as well. When light from the source is scattered by a sample, most of the photons diffuse elastically (without any changes in energy). This is also called Rayleigh scattering. However, there is a small fraction of the photons that are scattered with a slightly different energy (inelastic scattering). These energy (frequency) changes are called “Raman shift” and they correspond to the energy of characteristic excited vibrations.

Raman shifts are typically reported in wavenumbers. Conversion from spectral wavelength to wavenumbers of shift in the Raman spectrum can be done with the following equation:

$$\Delta\tilde{\nu} = \frac{1}{\lambda_0} - \frac{1}{\lambda_1}, \quad (3-13)$$

where:

$\Delta\tilde{\nu}$ is the Raman shift expressed in wavenumber;

λ_0 and λ_1 are the excitation wavelength and the Raman spectrum wavelength, respectively.

Depending of the sign of Raman shift $\Delta\tilde{\nu}$ Stokes (negative, energy gain) and anti-Stokes (positive, energy loss) Raman scattering are defined. Stokes and anti-Stokes peaks in the pattern are located symmetrically around the Rayleigh line. The Raman shift corresponds to the energy difference between ground state and 1st excited state. (see Figure 3-15).

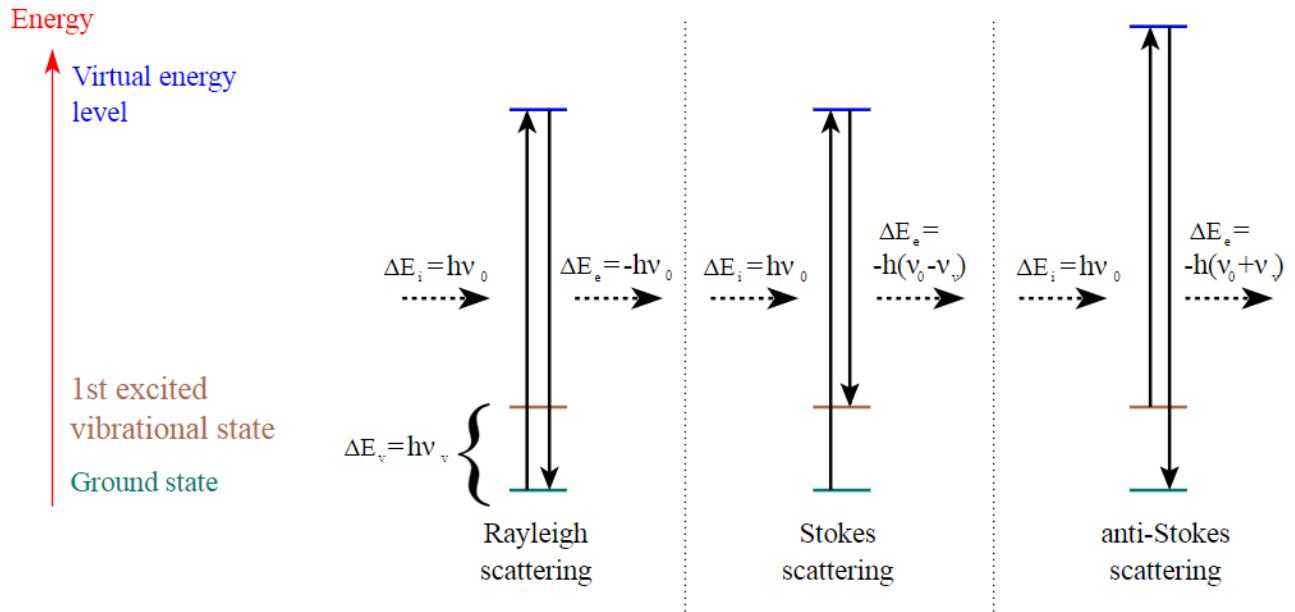


Figure 3-15. Different possibilities of light scattering [3-32]

The intensities of the Stokes and anti-Stokes Raman peaks depend on the number of the initial states (i.e. from the temperature). In thermodynamic equilibrium, the lower states will be more populated and Stokes Raman scattering peaks will be stronger than anti-Stokes. The ratio between them can be described by following equations:

$$\frac{I_{Stokes}}{I_{anti-Stokes}} = \left(\frac{\tilde{\nu}_0 - \tilde{\nu}_v}{\tilde{\nu}_0 + \tilde{\nu}_v} \right)^4 \exp\left(\frac{hc\tilde{\nu}_v}{kT}\right) \quad (3-14)$$

where:

$\tilde{\nu}_0, \tilde{\nu}_v$ are the wavenumber of incident beam and 1st excited state.

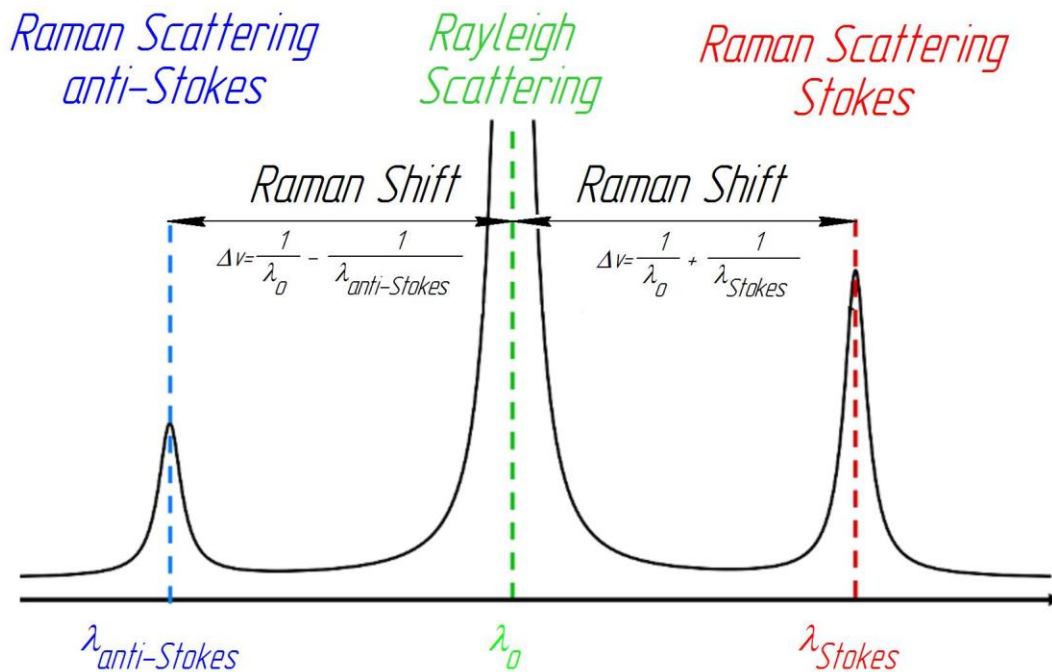


Figure 3-16. Intensities of the Stokes, anti-Stokes Raman and Rayleigh peaks at low temperatures.

The principal scheme of a Raman spectrometer is sketched in Figure 3-17. Raman spectroscopy and infrared (IR) absorption spectroscopy are complementary light scattering techniques. Both techniques study lattice vibrations and therefore provide similar information. However, there are significant differences. The selection rules are different. In IR spectroscopy, only vibrations that change the polarization vector are active. In Raman spectroscopy, the vibrations affect the polarizability tensor. As a consequence, modes that are observed by IR are very weak or vanish for Raman spectroscopy and vice versa.

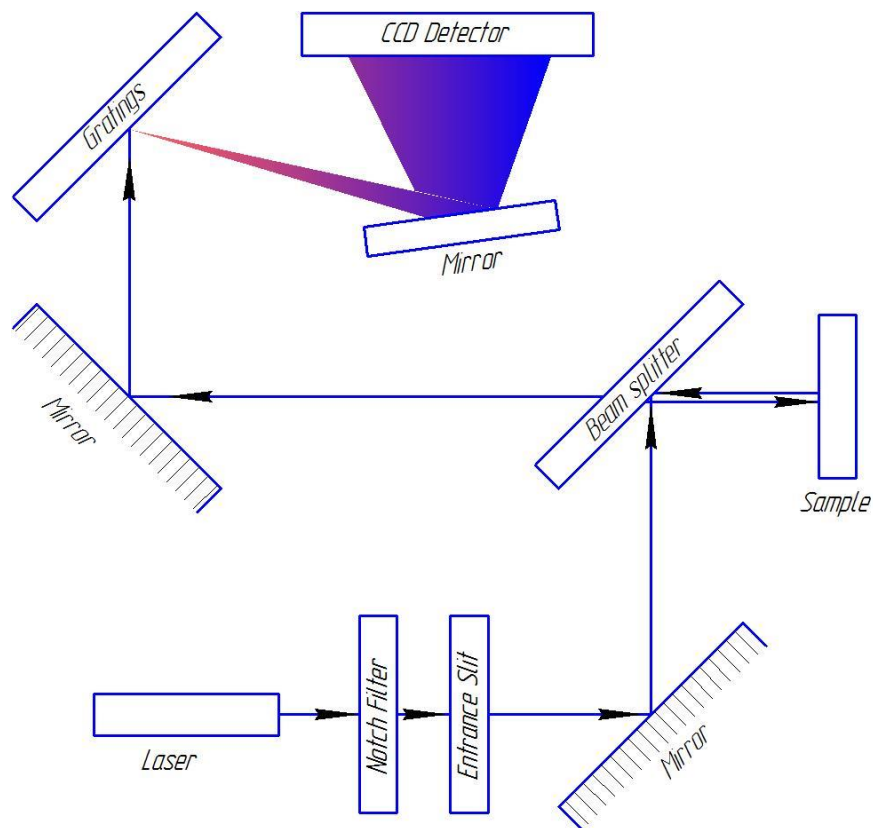


Figure 3-17. Principal scheme of the Raman spectrometer.[3-33]

In this work, a Horiba LabRAM HR Evolution Raman spectrometer was used. It is compatible with a wide range of lasers and detectors allowing to work in a range from 50 cm^{-1} (200000 nm) to 5000 cm^{-1} (2000 nm). The spectrometer setup included a double super razor edge filter, a Peltier cooled CCD camera and a Mikrocryo cryostat with a copper cold finger. [3-34] Measurements were performed with linearly polarized laser light of 532 nm wavelength. The power of the laser was typically less than 1 mW in order to avoid deterioration of the sample. The light beam was typically focused to a $10 \mu\text{m}$ spot on the top surface of the sample using a microscope.

3.6 Differential thermal analysis

Differential thermal analysis (DTA) is a powerful tool in the investigation of phase transformations and chemical reactions. DTA combines the measurement of heating or cooling curves with the quantitative features of calorimetry. Figure 3-18 schematically represents a principal scheme of the DTA setup.

The temperature of the two thermocouples is continuously monitored while heating or cooling the sample. The difference temperature measurement is based on the calculation of the heat flow difference between reference and studied specimens, which are kept as closely as possible in identical environments in the DTA furnace.

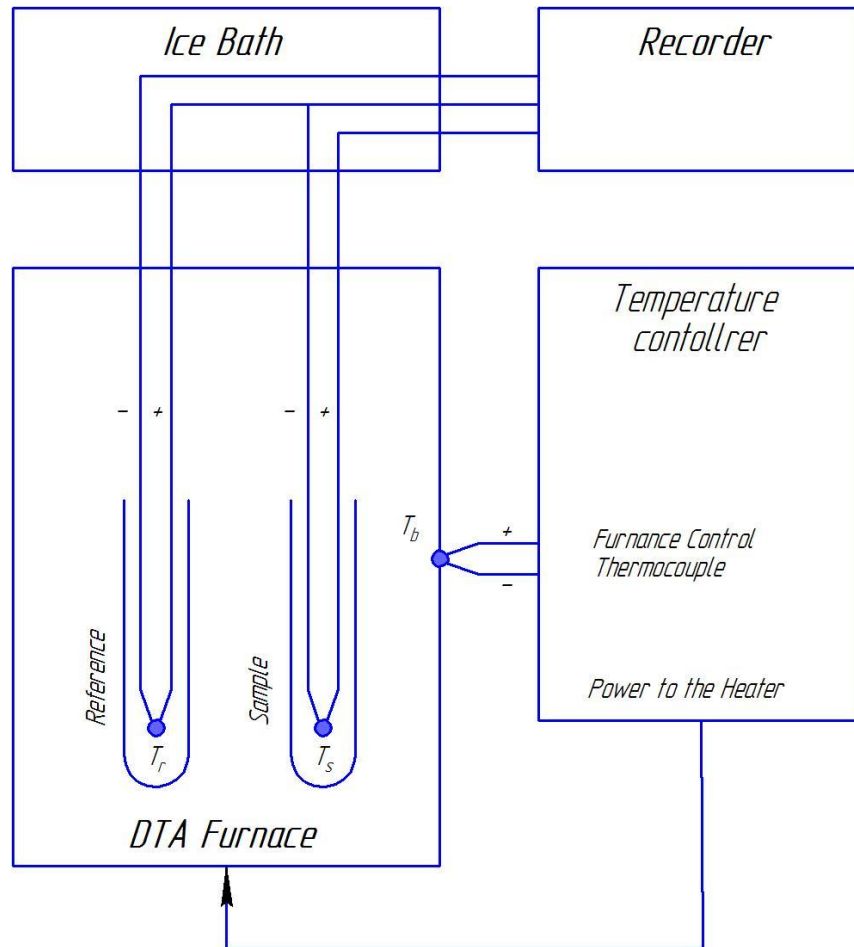


Figure 3-18. Principal scheme of the DTA setup.

The temperature controller provides a linear increase of the furnace temperature. If the temperature gradient within the sample is small, the effect of sample heat conductivity on the sample temperature itself can be eliminated. Heat flows, in this case, can be calculated from temperature measurements [3-35]:

$$\frac{dQ_r}{dt} = K(T_b - T_r), \quad (3-15)$$

$$\frac{dQ_s}{dt} = K(T_b - T_s), \quad (3-16)$$

where:

Q_r and Q_s are the heat flows into the reference and the sample respectively

K is the thermal conductivity, which is dependent on geometry and material of the cell but is independent of the sample. It is assumed that the sample plus the container and the reference have the same K ;

T_b , T_r , and T_s are the temperatures of the furnace, the reference, and the sample respectively.

By assuming a linear increase of T_b and assuming that all heat flow to the sample is used to increase the sample temperature, the heat flow equation can be derived from Eqns. (3-15) and (3-16):

$$\frac{dQ_s}{dt} = K \left(qt - \frac{Q_s}{c_p} \right), \quad (3-17)$$

where:

q is the heating rate,

c_p is the sample heat capacity.

By applying the following initial conditions:

$t=0$	$T_b=T_s=T_0=0$ $Q=0$
-------	--------------------------

The heat flow and the sample temperature equations can be written as:

$$Q_s = qC_p t - \frac{qC_p^2}{K} \left(1 - e^{-\frac{Kt}{C_p}} \right), \quad (3-18)$$

$$Q_s = qC_p t - \frac{qC_p^2}{K} \left(1 - e^{-\frac{Kt}{C_p}} \right), \quad (3-19)$$

$$T_s = qt - \frac{qC_p}{K} \left(1 - e^{-\frac{Kt}{C_p}} \right). \quad (3-20)$$

3.7 Thermal gravimetric analysis

Thermal gravimetric analysis (TGA) is the method used following mass change of the sample on heating or cooling. TGA provides information about phase transitions, absorption, adsorption, and desorption processes. During the TGA analysis, the mass of the sample is continuously recorded as a function of temperature. Mass, temperature, and time are considered the base quantities in the thermogravimetric analysis from which many additional parameters are derived.

A typical thermogravimetric analyzer (like our NETZSCH STA 449 F5 Jupiter) setup consists of a precision balance with a sample pan located inside a furnace with a programmable temperature controller. The temperature is raised at a constant rate to induce thermal reactions. Different sample environments (e.g. gases or vacuum) can be applied. Figure 3-19 schematically represents a typical TGA setup and its principal scheme.

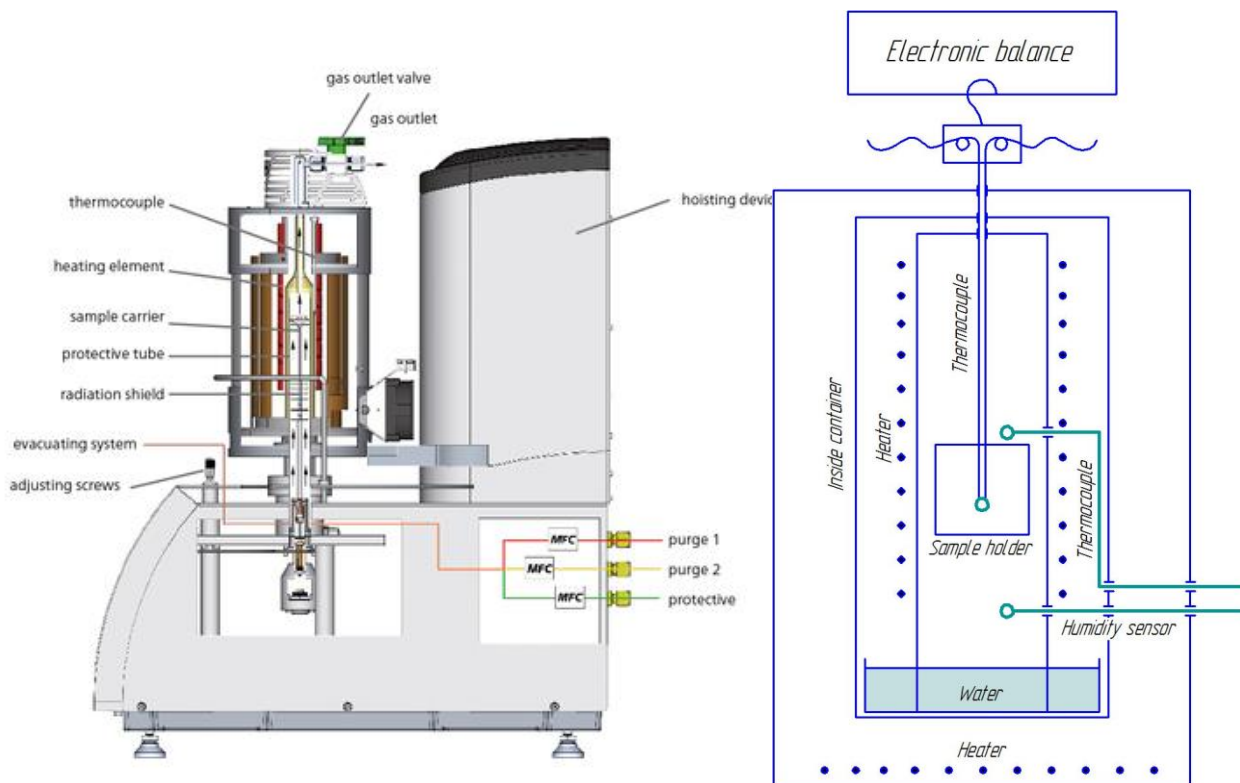


Figure 3-19. Schematic representation of TGA setup(left) and its principal scheme(right).[3-36]

4. CuTa_2O_6 ¹

4.1. Introduction

Compounds of the composition MX_2O_6 (M = divalent 3d transition metal cation, X = pentavalent transition metal cation) often crystallize with the trirutile structure-type shown in Figure 4-1 in which the divalent transition metal cations M are arranged in square planar layers separated by neighboring double layers of edge connected XO_6 octahedra. [4-1, 4-2]

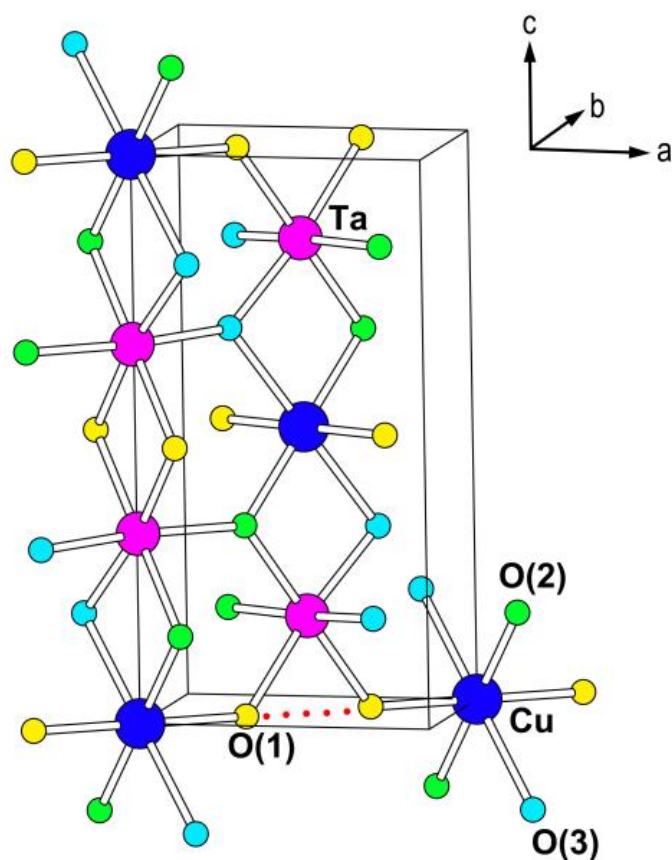


Figure 4-1. Perspective view of the room temperature crystal structure of CuTa_2O_6 where the blue, pink, yellow, green and cyan circles represent Cu, Ta, O(1), O(2) and O(3) atoms, respectively.

Reprinted (adapted) with permission from A. Golubev, R. E. Dinnebier, A. Schulz, R. K. Kremer, H. Langbein, A. Senyshyn, J. M. Law, T. C. Hansen, H.-J. Koo, M.-H. Whangbo, *Structural and Magnetic Properties of the Trirutile-type 1D-Heisenberg Anti-Ferromagnet CuTa_2O_6* , *Inorg. Chem.* **56(11)**, 6318-6329 (2017). Copyright (2017) American Chemical Society.

¹ This work has been published in *Inorg. Chem.* 56(11), 6318-6329 (2017)
DOI: 10.1021/acs.inorgchem.7b00421

The crystal structure and the physical properties of trirutile-type tantalates of most of the 3d transition metals have been intensively investigated before. [4-1, 4-2, 4-3]

The physical properties of trirutile-type CuTa_2O_6 have not been studied thus far. Early attempts to synthesize CuTa_2O_6 from a $\text{CuO} - \text{Cu}_2\text{O}$ flux, by solid state reaction or high-pressure synthesis resulted in perovskite-like phases with either a cubic or a pseudo-cubic orthorhombic crystal structure. [4-4, 4-5, 4-6, 4-7]

A detailed overview of early endeavors into the Cu-Ta-O systems is given by Longo and Sleight in 1975. [4-8] In 1996, Krabbes and Langbein obtained phase pure samples of the trirutile-type CuTa_2O_6 by employing thermal decomposition of the freeze-dried Cu-Ta-oxalate precursor at 700°C . [4-9, 4-10]

By choosing such relatively mild synthesis conditions, the formation of stable Cu(I) species is prevented. In their reports, the crystal structure was described in the tetragonal trirutile type. A characteristic splitting of the (123) Bragg reflection was observed and ascribed to the onset of a transformation into the perovskite phase. [4-9]

4.2. Preparation²

Polycrystalline samples were prepared by decomposing a freeze-dried Cu-Ta-oxalate precursor at 700°C following the procedure described in literature. [4-9, 4-10]

The carboxylate solution precursor was prepared by mixing solutions of ammonium-oxo-tris-oxalato-tantalate and ammonium-oxalato-cuprate with metal/oxalate in a ratio of 1/3 with a total metal concentration $\leq 0.01 \text{ mol l}^{-1}$. An additional presence of 0.3 mol/l H_2O_2 is required to prevent the formation of tantalum-containing solutions. The resulting solution was immediately frozen with liquid nitrogen and freeze dried in an Alpha 2-4 LSCbasic drier from Martin Christ.

Subsequently, the freeze-dried Cu-Ta-oxalate precursor with Cu/Ta ratio of 4/1 was decomposed in the oven. In the beginning, it was put at 250 °C for 17 hrs. This procedure released water, CO, CO_2 , NH_3 , HCOOH, and HCN. Hydrochloric acid in concentration in 1.2mol/l was added to completely remove the CuO surplus. Then for the next 50 hrs, the temperature was held at 700°C to anneal our sample.

² I thank H. Langbein for providing the polycrystalline samples for this study.

4.3. Sample characterization

The composition of the products was determined by microprobe analysis employing a TESCAN TS5130MM scanning electron microscope (SEM) equipped with an INCA crystal spectrometer. Figure 4-2 displays a typical SEM picture and energy-dispersive X-ray spectroscopy (EDX) analysis of the sample. According to the EDX analysis, the composition of the heavy atoms amounted to 11.2(1) atom-% for the Cu content and 20.8(4) atom-% for the Ta content corresponding to a composition ratio of 1:1.8(5). The sample particles exhibit a fluffy morphology with typical particle sizes of 20 - 30 μm .

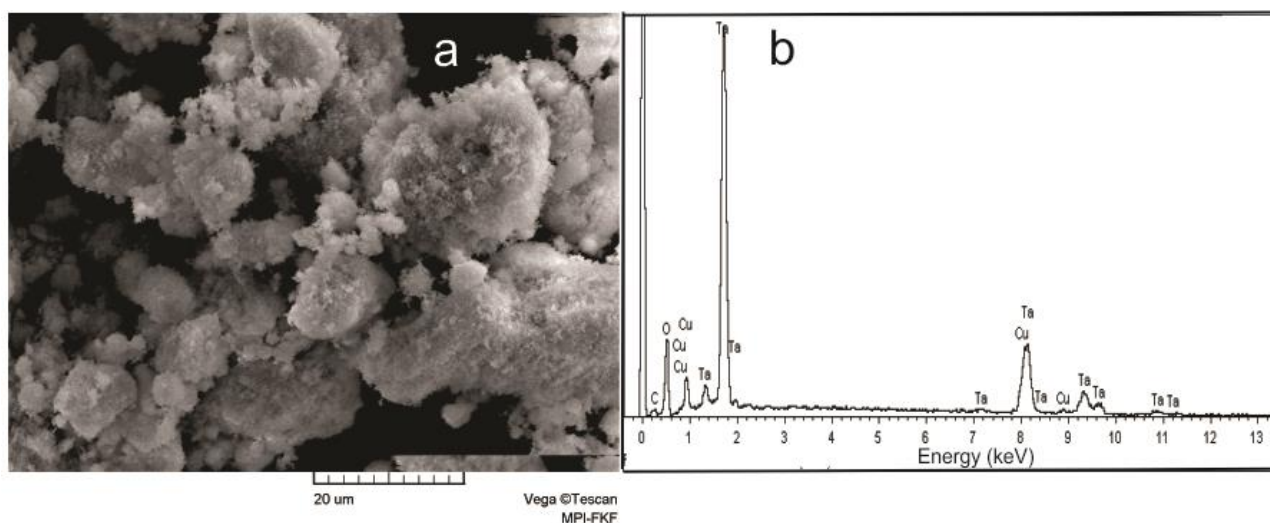


Figure 4-2. (left) Typical SEM scan across a polycrystalline CuTa_2O_6 sample and (right) result of the EDX analysis.

Reprinted (adapted) with permission from A. Golubev, R. E. Dinnebier, A. Schulz, R. K. Kremer, H. Langbein, A. Senyshyn, J. M. Law, T. C. Hansen, H.-J. Koo, M.-H. Whangbo, *Structural and Magnetic Properties of the Trirutile-type 1D-Heisenberg Anti-Ferromagnet CuTa_2O_6* , *Inorg. Chem.* **56(11)**, 6318-6329 (2017). Copyright (2017) American Chemical Society.

The phase purity of the products was checked deploying the X-ray powder diffraction using $\text{Cu K}\alpha_1$ radiation in Debye-Scherrer geometry (capillary diameter 0.3 mm) on the STOE STADI P diffractometer. Figure 4-3 represents a room temperature diffraction pattern.

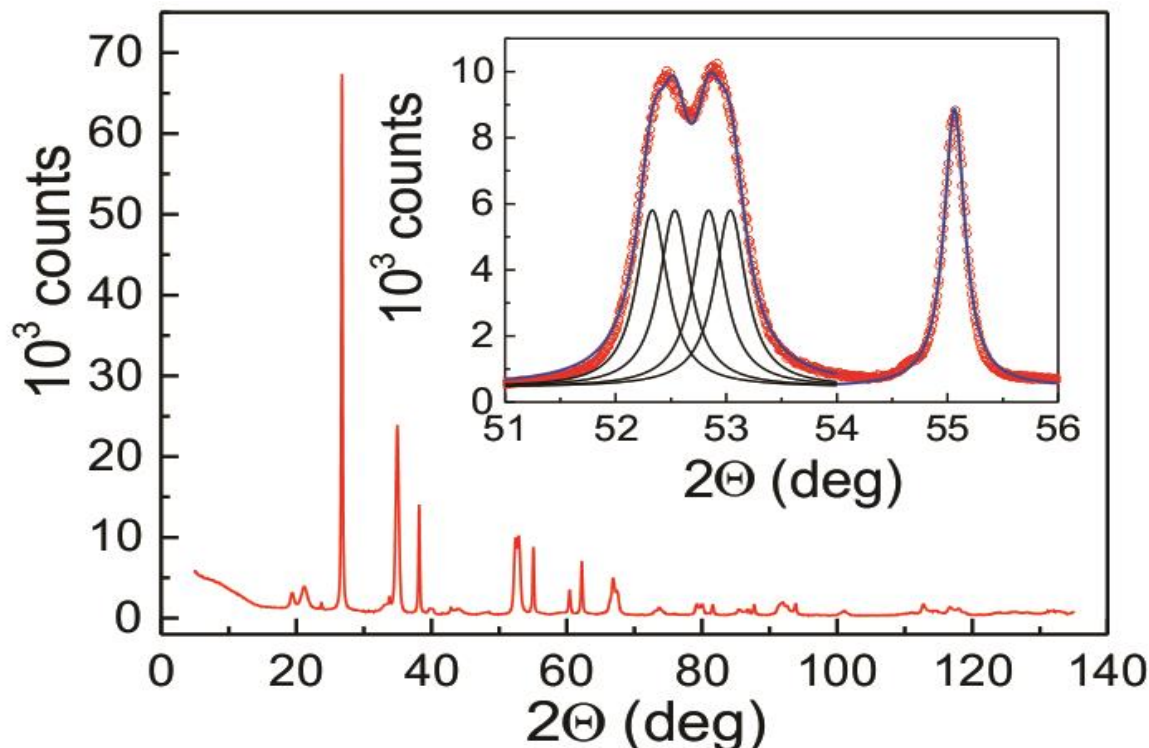


Figure 4-3. Room temperature X-ray powder diffraction pattern (Cu $K_{\alpha 1}$ radiation) of a polycrystalline sample of CuTa_2O_6 . The inset shows the angular region near the $(123)_{\text{tet}}$ and the $(220)_{\text{tet}}$ Bragg reflection with fits of Lorentzian lines (blue) and the deconvolution of the split doublet at $2\theta=52.7^\circ$ into four separate lines of equal intensity (black solid lines).

Reprinted (adapted) with permission from A. Golubev, R. E. Dinnebier, A. Schulz, R. K. Kremer, H. Langbein, A. Senyshyn, J. M. Law, T. C. Hansen, H.-J. Koo, M.-H. Whangbo, *Structural and Magnetic Properties of the Trirutile-type 1D-Heisenberg Anti-Ferromagnet CuTa_2O_6* , *Inorg. Chem.* **56(11)**, 6318-6329 (2017). Copyright (2017) American Chemical Society.

A splitting of the characteristic Bragg reflections around $2\theta=52.7^\circ$ was found. This splitting was noted before by Krabbes, Langbein and Bremer in 1996 and 1997. [4-9, 4-10]

The $(123)_{\text{tet}}$ Bragg reflection at $d = 1.74 \text{ \AA}$ ($2\theta=52.7^\circ$) splits into two reflections of equal intensity with a distance between the two reflections of about 0.5° . Considering the width of the nearby $(220)_{\text{tet}}$ Bragg reflection at $2\theta=55^\circ$ as a single reflection, a broadening of these two reflections was derived. It can be a result of an $\sim 0.2^\circ$ additional splitting. The inset in Figure 4-3 displays fits of the $(220)_{\text{tet}}$ and $(123)_{\text{tet}}$ Bragg reflections assuming a Lorentzian profile of the Bragg reflections resulting with a FWHM of $\sim 0.25^\circ$.

4.4. Crystal structure

Room temperature and high-temperature crystal structures were determined from powder diffraction patterns collected on a Bruker D8 ADVANCE X-ray powder diffractometer (see Figure 3-2) with Mo $K\alpha_1$ radiation and the high-resolution neutron powder diffractometer SPODI at MLZ, Munich (see Figure 3-6). A thin-walled Nb tubular container of 8 mm outer diameter filled with ~9 g sample was used for the neutron studies. Glass capillaries with the outer diameter of about 0.3 mm were used for the X-ray measurements. By raising the temperature to >500 K, a structural phase transition from the monoclinic room temperature structure to the tetragonal trirutile-type high-temperature structure was detected.

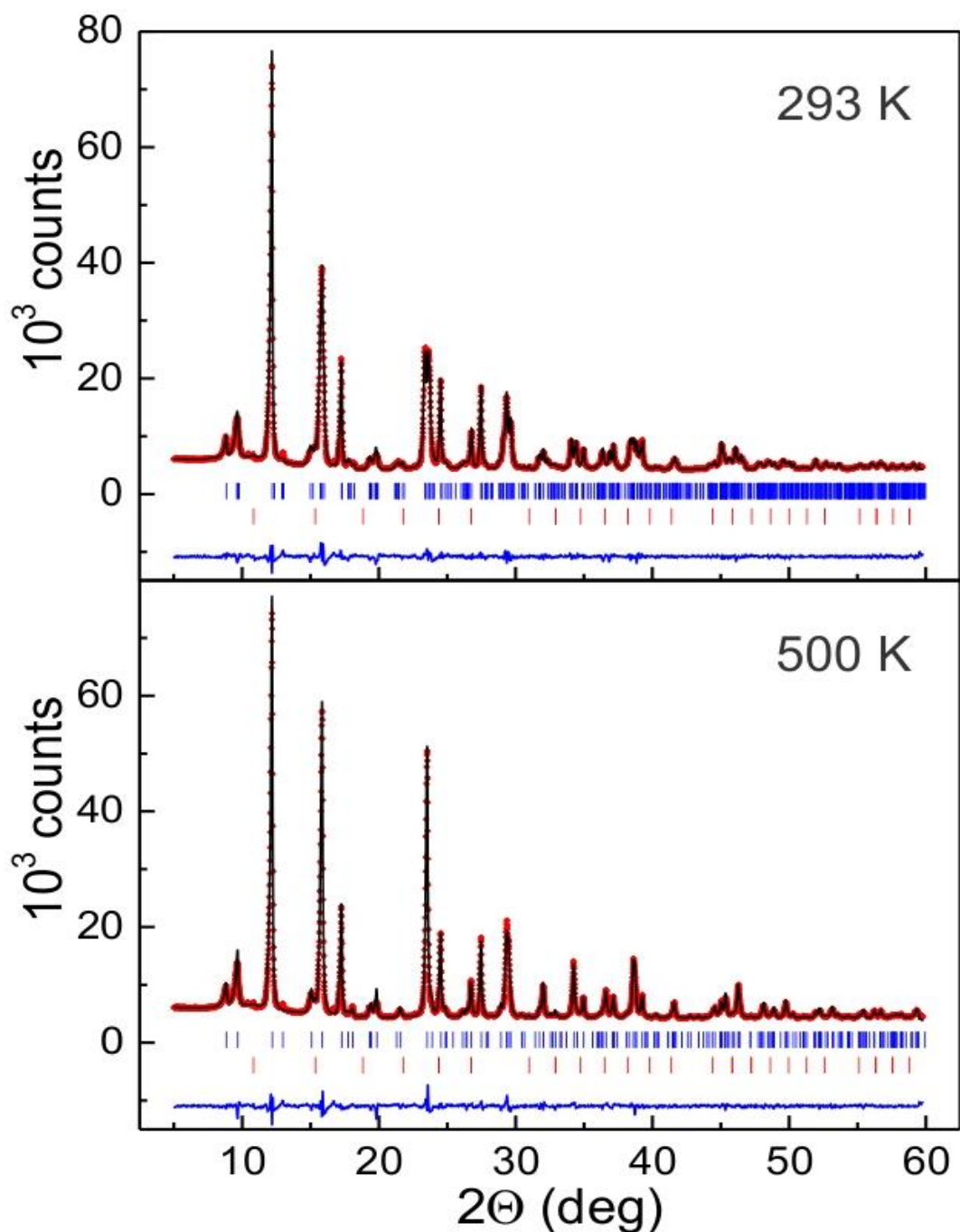


Figure 4-4. X-ray powder diffraction pattern (Mo $K\alpha_1$ radiation) of a polycrystalline sample of CuTa_2O_6 at 293K and 500K as indicated. Red circles mark the data points, the black solid line represents the result of the Rietveld profile refinement, The blue and red vertical bars mark the positions of the Bragg reflections used to simulate the theoretical pattern (blue: trirutile CuTa_2O_6 ; red: cubic $\text{Cu}_{0.5}\text{TaO}_3$). The blue solid lines beneath give the difference between the measured and calculated patterns. Reprinted (adapted) with permission from A. Golubev, R. E. Dinnebier, A. Schulz, R. K. Kremer, H. Langbein, A. Senyshyn, J. M. Law, T. C. Hansen, H.-J. Koo, M.-H. Whangbo, *Structural and Magnetic Properties of the Trirutile-type 1D-Heisenberg Anti-Ferromagnet CuTa_2O_6* , *Inorg. Chem.* **56(11)**, 6318-6329 (2017). Copyright (2017) American Chemical Society.

In a series of X-ray powder diffraction experiments at different temperatures in a range from room temperature to 600 K, the splitting of the $(123)_{\text{tet}}$ Bragg reflection was followed in detail. Figure 4-5 displays the splitting of $(123)_{\text{tet}}$ Bragg reflection as a function of the temperature together with a critical power law calculated assuming a mean field critical exponent $\beta = 1/2$ and $T_C = 503(3)$ K according to:

$$\begin{aligned} (\Delta 2\theta)_{123} &= I_0 t^{\frac{1}{2}} + a_0 + a_1 T, & \text{for } T < T_C \\ (\Delta 2\theta)_{123} &= a_0 + a_1 T, & \text{for } T > T_C. \end{aligned} \quad (4-1)$$

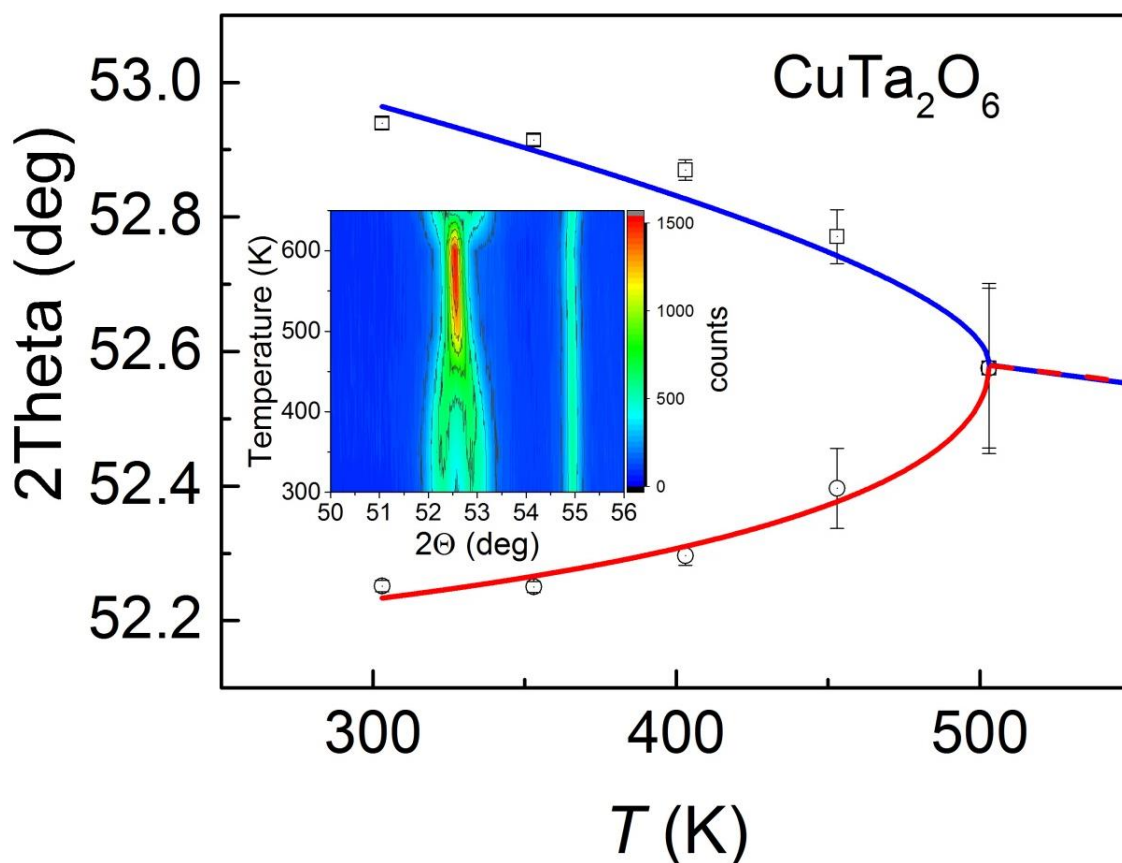


Figure 4-5. Splitting of the $(123)_{\text{tet}}$ Bragg reflection around the critical temperature $T_C = 503 \pm 3$ K. The red and blue solid lines are calculated using Eq. (4-1) assuming a critical exponent $\beta = 1/2$ and a background linearly varying with the temperature. The inset shows a color-coded plot of the $(123)_{\text{tet}}$ and the $(220)_{\text{tet}}$ Bragg reflections versus temperature.

Reprinted (adapted) with permission from A. Golubev, R. E. Dinnebier, A. Schulz, R. K. Kremer, H. Langbein, A. Senyshyn, J. M. Law, T. C. Hansen, H.-J. Koo, M.-H. Whangbo, *Structural and Magnetic Properties of the Trirutile-type 1D-Heisenberg Anti-Ferromagnet CuTa_2O_6* , *Inorg. Chem.* **56(11)**, 6318-6329 (2017). Copyright (2017) American Chemical Society.

The crystal structure of CuTa_2O_6 at room temperature was refined in the space group $P2_1/n$ (space group no. 14). The refinement converged to Bragg R -factor of 2.06 % (R_f -factor 2.44 %). As input parameters for the Rietveld refinement for CuTa_2O_6 atom fractional coordinates and lattice parameters reported for CuSb_2O_6 by Nakua *et al.* in 1991 [4-11] were assumed as starting parameters. Table 4-1 summarizes the results of the refinements compared with published data for other NiTa_2O_6 and CoTa_2O_6 [4-12 ,4-13].

Table 4-1. Comparison of atom fractional coordinates of CuTa_2O_6 , CuSb_2O_6 , NiTa_2O_6 and CoTa_2O_6 at room temperature (RT) and at 300 °C, as indicated.

Reprinted (adapted) with permission from A. Golubev, R. E. Dinnebier, A. Schulz, R. K. Kremer, H. Langbein, A. Senyshyn, J. M. Law, T. C. Hansen, H.-J. Koo, M.-H. Whangbo, *Structural and Magnetic Properties of the Trirutile-type 1D-Heisenberg Anti-Ferromagnet CuTa_2O_6* , Inorg. Chem. **56(11)**, 6318-6329 (2017). Copyright (2017) American Chemical Society.

	CuTa_2O_6		CuSb_2O_6	NiTa_2O_6	CoTa_2O_6
	RT	300 °C	RT	RT	RT
Cu	2a	2a	2a	2a	2a
(Ni,Co)	x	0	0	0	0
	y	0	0	0	0
	z	0	0	0	0
Ta	4e	4e	4e	4e	4e
	x	0.0015(3)	0	0.0011(9)	0
	y	0.0170(3)	0	0.0080(10)	0
	z	0.3329(1)	0.3329(1)	0.3338(6)	0.3316(3)
O1	4e	4f	4e	4f	4f
	x	0.3241(31)	0.2940(16)	0.3130(9)	0.307(8)
	y	0.2627(30)	0.2940(16)	0.2983(8)	0.307(8)
	z	0.0022(28)	0	0.0017(4)	0
O2	4e	8j	4e	8j	8j
	x	0.3222 (44)	0.3074(10)	0.2991(8)	0.297(6)
	y	0.3017(44)	0.3074(10)	0.3176(7)	0.297(6)
	z	0.3355(19)	0.3245(11)	0.3291(4)	0.327(4)
O3	4e		4e		
	x	-0.2808(46)	-	-0.3012(8)	-
	y	-0.3083(48)	-	-0.2915(9)	-
	z	0.3184(18)	-	0.3248(4)	-

In the Rietveld profile refinements equal displacement factors for all atoms and a Thompson-Cox-Hastings pseudo Voigt profile of the reflections (FullProf, NPR = 7)

were assumed. The resolution function of the diffractometer (IRF file) determined from a diffraction pattern of a LaB₆ standard sample measured with the same instrumental and capillary parameters was utilized. Apparent broadening of the Bragg reflections of CuTa₂O₆ was subsequently modeled by expanding the particle size and shape contributions into spherical harmonics, $c_{mn}Y_{mn}$, with $m = 0, 2, 4$, and even $\pm n$; $|n| \leq m$ appropriate for Laue class $2/m$ (FullProf, size model no. 15) and fitting the expansion coefficients c_{mn} . The average particle size amounted to 32(8) nm consistent with the SEM results. The background was constructed by superposing Chebychev polynomials of a higher degree. A first attempt to refine the pattern collected at 500 K was made by refining the Ta atom parameters but fixing the oxygen positional parameters and assuming monoclinic structure as starting parameters. The refinement converged (Bragg R -factor 2.5 %) to lattice parameters $a \approx b$ and a monoclinic angle $\beta \approx 90^\circ$ indicating tetragonal symmetry of the crystal structure. The refinement can be slightly improved (Bragg R -factor 2.34 % (R_f -factor 2.32 %) with the assumption of the tetragonal trirutile structure and the space group $P4_2/mnm$ (no. 136). The refined structural parameters are summarized in Table 2 and Table 3. A small additional Bragg reflection was detected at $d \sim 3.75 \text{ \AA}$ in both patterns which can be ascribed to a trace (< 1%) of the orthorhombic defect perovskite Cu_{0.5}TaO₃. [4-4]

Neutron powder diffraction patterns collected between room temperature and 573K were refined in an analogous manner. The diffraction patterns together with the Rietveld refinement are presented in Figure 4-6. The error bars for the oxygen position parameters could be reduced by a factor of 2 to 3 compared to the X-ray data. No dramatic changes of the atom positional parameters could be observed. Table 3 compiles the lattice parameters and the cell volumes *versus* temperature.

Table 4-2. Crystal structure data of CuTa₂O₆ as refined from X-ray powder diffraction data at RT and 500 K. Reprinted (adapted) with permission from A. Golubev, R. E. Dinnebier, A. Schulz, R. K. Kremer, H. Langbein, A. Senyshyn, J. M. Law, T. C. Hansen, H.-J. Koo, M.-H. Whangbo, *Structural and Magnetic Properties of the Trirutile-type 1D-Heisenberg Anti-Ferromagnet CuTa₂O₆*, Inorg. Chem. **56(11)**, 6318-6329 (2017). Copyright (2017) American Chemical Society.

Empirical formula	CuTa ₂ O ₆	CuTa ₂ O ₆
Formula weight (g/mol)	521.44	521.44
Temperature (K)	293(2)	500(5)
Wavelength(Å)	0.70932	0.70932
Crystal system	monoclinic	tetragonal
Space group	<i>P</i> 2 ₁ / <i>n</i>	<i>P</i> 4 ₂ / <i>mnm</i>
<i>a</i> (Å)	4.7190(7)	4.7219(3)
<i>b</i> (Å)	4.7238(7)	4.7219(3)
<i>c</i> (Å)	9.188(1)	9.1970(6)
β (deg)	91.085(1)	90
Volume (Å ³)	204.79(5)	205.06(2)
<i>Z</i>	4	4
Density _{calc} (g cm ⁻³)	8.456	8.446
Reflections collected	5° < 2 θ < 60°	5° < 2 θ < 60°
χ^2	8.55	8.69
Bragg factor <i>R</i> _B (%)	2.06	2.34
<i>R</i> _F factor (%)	2.44	2.32

Atoms	Wyckoff sites and atom coordinates	
Cu	2a	2a
x	0	0
y	0	0
z	0	0
Ta	4e	4e
x	0.0015(3)	0
y	0.0170(3)	0
z	0.3329(1)	0.3329(1)
O1	4e	4f
x	0.3241(31)	0.2940(16)
y	0.2627(30)	0.2940(16)
z	0.0022(28)	0
O2	4e	8j
x	0.3222(44)	0.3074(10)
y	0.3017(44)	0.3074(10)
z	0.3355(19)	0.3245 (11)
O3	4e	
x	-0.2808 (46)	
y	-0.3083(48)	
z	0.3184(18)	

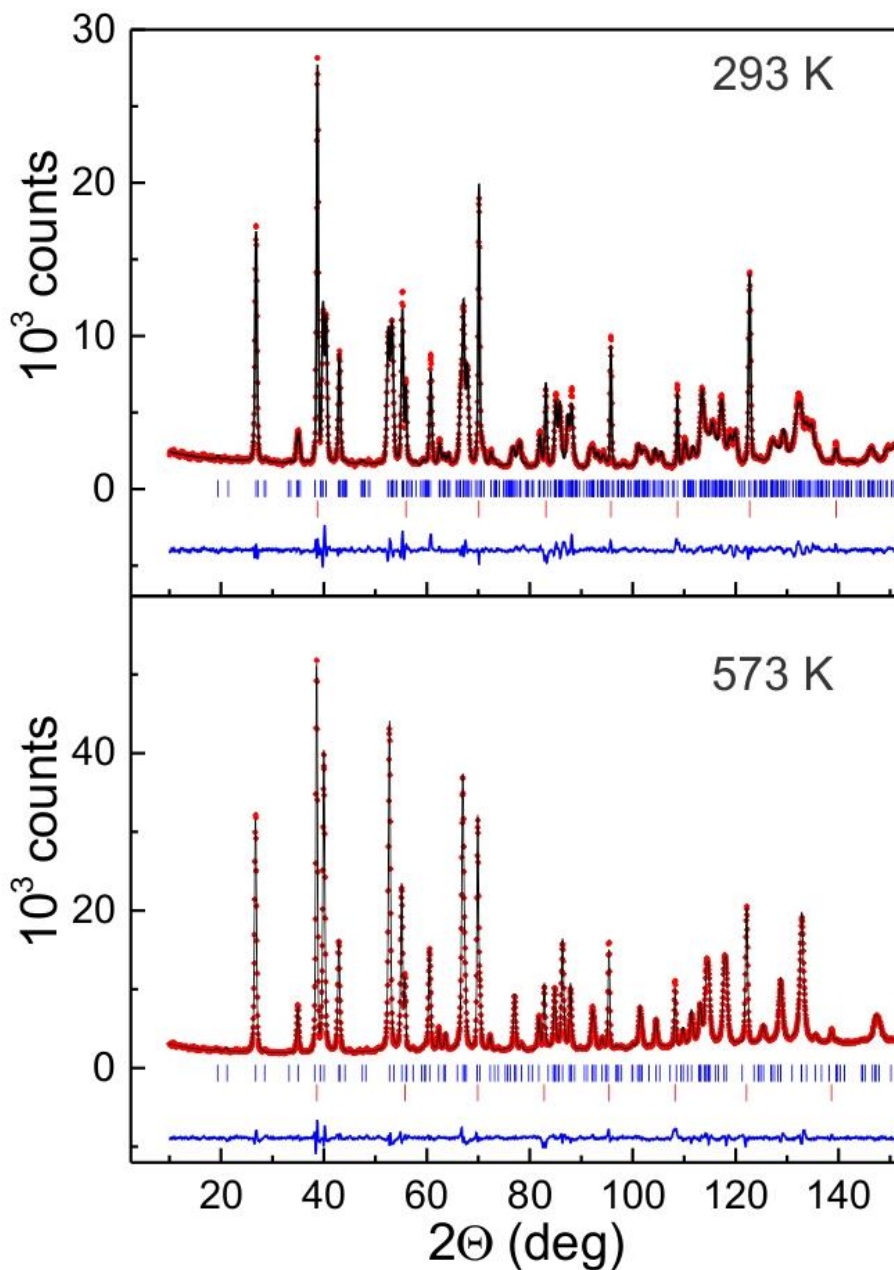


Figure 4-6. Neutron powder diffraction patterns collected at the instrument SPODI (MLZ) at the wavelength 1.548 Å of a polycrystalline sample of CuTa_2O_6 at 293 K and 573 K as indicated. Red circles mark the data points, the black solid lines represent the result of the profile refinements. The blue and red vertical bars indicate the positions of the Bragg reflections used to simulate the theoretical pattern. (blue: trirutile CuTa_2O_6 ; red: Nb sample container. The blue solid lines beneath give the difference between measured and calculated patterns.

Reprinted (adapted) with permission from A. Golubev, R. E. Dinnebier, A. Schulz, R. K. Kremer, H. Langbein, A. Senyshyn, J. M. Law, T. C. Hansen, H.-J. Koo, M.-H. Whangbo, *Structural and Magnetic Properties of the Trirutile-type 1D-Heisenberg Anti-Ferromagnet CuTa_2O_6* , *Inorg. Chem.* **56**(11), 6318-6329 (2017). Copyright (2017) American Chemical Society.

Table 4-3. Lattice parameters, cell volume, isotropic displacement factor (identical for all atoms) and R factors resulting from the profile refinement of the neutron powder diffraction patterns collected at instrument SPODI between room temperature and 300 °C as indicated.

Reprinted (adapted) with permission from A. Golubev, R. E. Dinnebier, A. Schulz, R. K. Kremer, H. Langbein, A. Senyshyn, J. M. Law, T. C. Hansen, H.-J. Koo, M.-H. Whangbo, *Structural and Magnetic Properties of the Trirutile-type 1D-Heisenberg Anti-Ferromagnet CuTa_2O_6* , *Inorg. Chem.* **56(11)**, 6318-6329 (2017). Copyright (2017) American Chemical Society.

	25 °C	80 °C	150 °C	200 °C	250 °C	300 °C
Space group	$P 2_1/n$ (no. 14)	$P 2_1/n$ (no. 14)	$P 2_1/n$ (no. 14)	$P 2_1/n$ (no. 14)	$P 2_1/n$ (no. 14)	$P 4_2/mnm$ (no. 136)
a , Å	4.7236(1)	4.7248(1)	4.7261(1)	4.7278(1)	4.7299(1)	4.7313(1)
b , Å	4.7234(1)	4.7252(1)	4.7268(1)	4.7288(1)	4.7306(1)	4.7313(1)
c , Å	9.1922(15)	9.1968(2)	9.2032(2)	9.2066(2)	9.2100(2)	9.2136(1)
β , deg	91.1550(16)	90.774(23)	90.2242(30)	90.1694(35)	90.1571(37)	90
Volume, Å ³	205.050(4)	205.305(6)	205.589(6)	205.830(6)	206.089(4)	206.248(2)
Bragg R-factor R_B , %	2.55	3.86	3.72	4.02	3.90	2.53
B , Å ²	0.97(2)	1.19(3)	1.18(2)	1.16(2)	1.32(2)	1.40(1)
Z	4	4	4	4	4	4

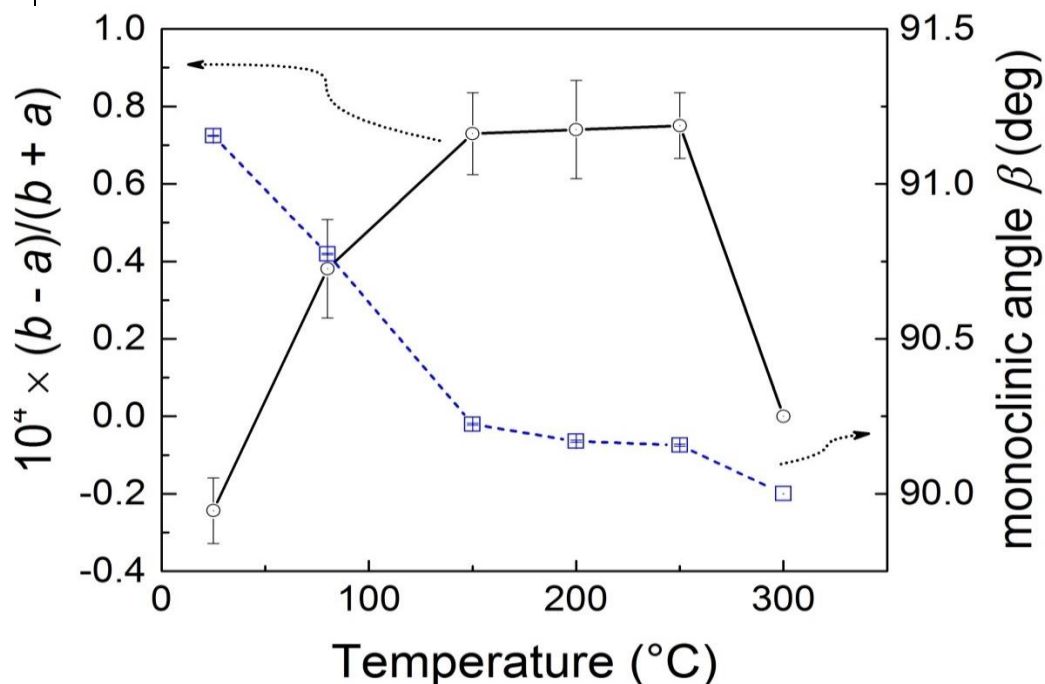


Figure 4-7. The relative difference of the lattice parameters a and b , $(b - a)/(b + a)$, and the monoclinic angle β versus temperature as derived from the refinement of the neutron powder diffraction patterns. Powder patterns below 250 °C were refined assuming space group $P 2_1/n$, patterns above 250 °C with space group $P 4_2/mnm$. Lattice parameters are listed in Table 4-3.

Reprinted (adapted) with permission from A. Golubev, R. E. Dinnebier, A. Schulz, R. K. Kremer, H. Langbein, A. Senyshyn, J. M. Law, T. C. Hansen, H.-J. Koo, M.-H. Whangbo, *Structural and Magnetic Properties of the Trirutile-type 1D-Heisenberg Anti-Ferromagnet CuTa_2O_6* , *Inorg. Chem.* **56(11)**, 6318-6329 (2017). Copyright (2017) American Chemical Society.

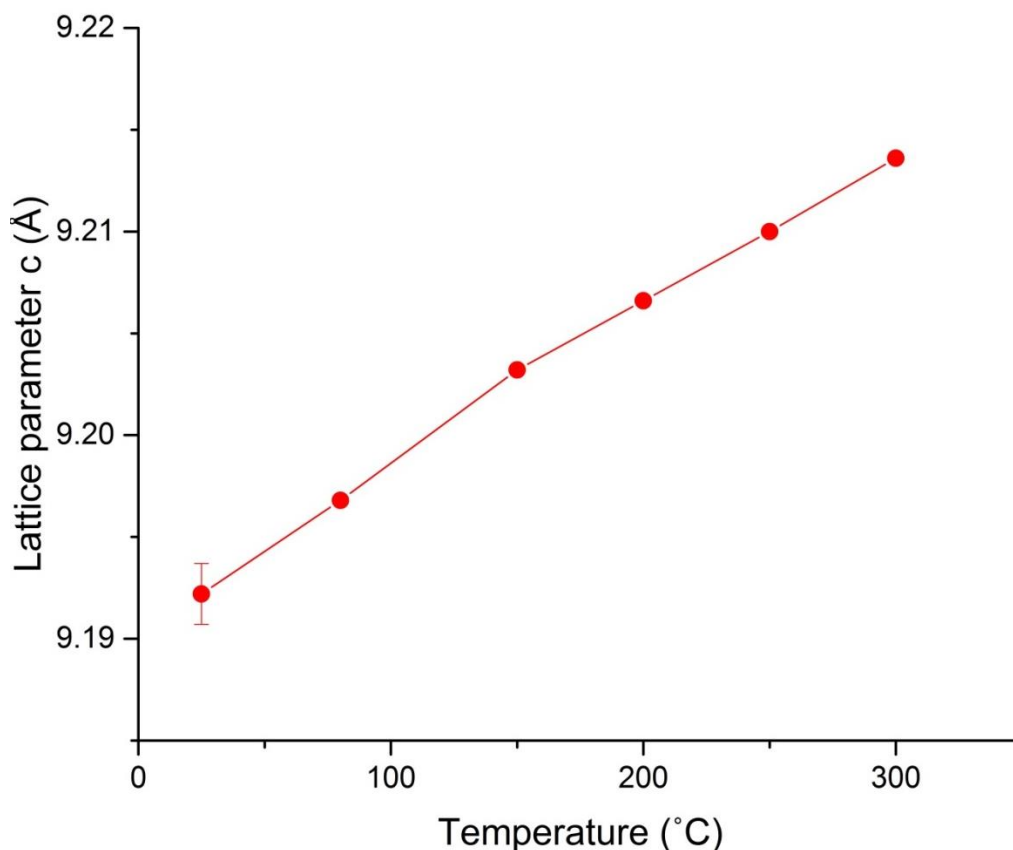


Figure 4-8. Lattice parameter c versus temperature as derived from the refinement of the neutron powder diffraction patterns. Powder patterns below 250 °C were refined assuming space group $P 2_1/n$, patterns above 250 °C with space group $P 4_2/mnm$. Lattice parameters are listed in Table 4-3. Reprinted (adapted) with permission from A. Golubev, R. E. Dinnebier, A. Schulz, R. K. Kremer, H. Langbein, A. Senyshyn, J. M. Law, T. C. Hansen, H.-J. Koo, M.-H. Whangbo, *Structural and Magnetic Properties of the Trirutile-type 1D-Heisenberg Anti-Ferromagnet CuTa_2O_6* , *Inorg. Chem.* **56(11)**, 6318-6329 (2017). Copyright (2017) American Chemical Society.

The atom positional parameters are summarized in Table 4-4. The monoclinic angle β decreases monotonically with an increased temperature whereas the quantity $(b - a)/(b + a)$ passes through a broad maximum and levels off before the phase becomes tetragonal (see Figure 4-7).

Table 4-4. Atom positional parameters resulting from the refinement of the neutron powder diffraction patterns of CuTa_2O_6 versus temperature.

Reprinted (adapted) with permission from A. Golubev, R. E. Dinnebier, A. Schulz, R. K. Kremer, H. Langbein, A. Senyshyn, J. M. Law, T. C. Hansen, H.-J. Koo, M.-H. Whangbo, *Structural and Magnetic Properties of the Trirutile-type 1D-Heisenberg Anti-Ferromagnet CuTa_2O_6* , *Inorg. Chem.* **56(11)**, 6318-6329 (2017). Copyright (2017) American Chemical Society.

Space group		25 °C	80 °C	150 °C	200 °C	250 °C	300 °C
		$P 2_1/n$	$P 2_1/n$	$P 2_1/n$	$P 2_1/n$	$P 4_2/mnm$	$P 4_2/mnm$
Cu	x	0	0	0	0	0	0
	y	0	0	0	0	0	0
	z	0	0	0	0	0	0
Ta	x	0.0013(13)	-0.0074(19)	-0.0045(29)	-0.0036(28)	0	0
	y	0.0148(10)	0.0108(17)	0.0038(26)	0.0052(25)	0	0
	z	0.3312(8)	0.3322(10)	0.3323(9)	0.3327 (9)	0.3336(11)	0.3335(6)
O1	x	0.2981(18)	0.2935(23)	0.3092(23)	0.3081(23)	0.2947(13)	0.2971(8)
	y	0.3012(16)	0.3100(21)	0.3108(33)	0.3124(35)	0.2947(13)	0.2971(8)
	z	-0.0004(8)	-0.0026(12)	-0.0010(19)	-0.0012(19)	0	0
O2	x	0.3049(14)	0.2996(21)	0.2842(26)	0.2807(23)	0.3048(7)	0.3040(4)
	y	0.3206(13)	0.3133(20)	0.3135 (21)	0.3144(22)	0.3048(7)	0.3040(4)
	z	0.3267(7)	0.3269(9)	0.3268(11)	0.3262(12)	0.3404(4)	0.3418(2)
O3	x	-0.3030(14)	-0.3071(18)	-0.2935(28)	-0.2947(26)		
	y	-0.2818(12)	-0.2821(17)	-0.2967(25)	-0.2985(27)		
	z	0.3177(6)	0.3189(7)	0.3230(12)	0.3239(11)		

The lattice parameter c increases linearly with temperature (see Table 4-3). For the temperatures of 150°C and 200°C, the monoclinic angle within error bars amounted to 90°, and the relative difference of the lattice parameters $(b - a)/(b + a)$ is reduced to less than 10^{-4} . This indicates that a description with the tetragonal unit cell is appropriate. Inspection of group - subgroup relationship of the space groups $P4_2/mnm$ and $P 2_1/n$ reveals a two-step transformation of index 4 via the space group $Pnmm$ as an intermediate (see Figure 4-9).

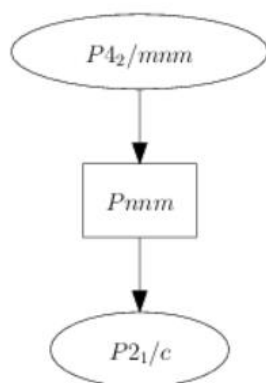


Figure 4-9. Group – subgroup relationship between the space groups $P4_2/mnm$ (no. 136) and $P 2_1/n$ (no. 14).

Table 4-5. Results of the neutron powder diffraction patterns of CuTa_2O_6 collected at 150°C , assuming various space groups as indicated.

Reprinted (adapted) with permission from A. Golubev, R. E. Dinnebier, A. Schulz, R. K. Kremer, H. Langbein, A. Senyshyn, J. M. Law, T. C. Hansen, H.-J. Koo, M.-H. Whangbo, *Structural and Magnetic Properties of the Trirutile-type 1D-Heisenberg Anti-Ferromagnet CuTa_2O_6* , *Inorg. Chem.* **56(11)**, 6318-6329 (2017). Copyright (2017) American Chemical Society.

Space group		$P 2_1/n$ (no. 14)	$P nmm$ (no. 58)	$P 4_2/mnm$ (no. 136)
$a, \text{Å}$		4.7261(5)	4.732(13)	4.7264(4)
$b, \text{Å}$		4.7268(5)	4.721(12)	4.7264(4)
$c, \text{Å}$		9.203(21)	9.202(16)	9.204(16)
β, deg		90.22(30)	90	90
Volume, Å^3		205.59(6)	205.58(9)	205.60(4)
Bragg R-factor $R_B, \%$		3.72	4.20	3.74
$B, \text{Å}^2$		1.18 (2)	1.11(2)	1.30(2)
Cu	x	0	0	0
	y	0	0	0
	z	0	0	0
Ta	x	-0.0045(29)	0	0
	y	0.0038(26)	0	0
	z	0.3323 (9)	0.3371(8)	0.3333(11)
O1	x	0.3092(23)	0.2859(20)	0.2944(13)
	y	0.3108(33)	0.2853(20)	0.2944(13)
	z	-0.0010(19)	0	0
O2	x	0.2842(26)	0.3331(34)	0.3051(7)
	y	0.3135(21)	0.2931(34)	0.3051(7)
	z	0.3268(11)	0.3393(5)	0.3403(5)
O3	x	-0.2935(28)	-0.2982(34)	
	y	-0.2967(25)	-0.3182(34)	
	z	0.3230(12)	0.3393(5)	

Refining the diffraction patterns in the space group $Pn\bar{m}$ (no. 58) decreases the R -factors by about 10 to 15% (see Table 4-5 and Table 4-6). However, minor changes in the lattice parameters and the atomic coordinates do not allow to conclusively define which space group is preferred at high temperatures.

Table 4-6. Results of the neutron powder diffraction patterns of CuTa_2O_6 collected at 200°C assuming various space groups as indicated.

Reprinted (adapted) with permission from A. Golubev, R. E. Dinnebier, A. Schulz, R. K. Kremer, H. Langbein, A. Senyshyn, J. M. Law, T. C. Hansen, H.-J. Koo, M.-H. Whangbo, *Structural and Magnetic Properties of the Trirutile-type 1D-Heisenberg Anti-Ferromagnet CuTa_2O_6* , *Inorg. Chem.* **56(11)**, 6318-6329 (2017). Copyright (2017) American Chemical Society.

Space group		$P 2_1/n$ (no. 14)	$P n\bar{m}$ (no. 58)	$P 4_2/mnm$ (no. 136)
$a, \text{Å}$		4.7280(5)	4.733(15)	4.7282(4)
$b, \text{Å}$		4.728(7)	4.724(14)	4.7282(4)
$c, \text{Å}$		9.207(21)	9.206(15)	9.207(15)
β, deg		90.17(35)	90	90
Volume, Å^3		205.83(6)	205.81(1)	205.83(4)
Bragg R-factor $R_B, \%$		4.02	4.26	4.16
$B, \text{Å}^2$		1.16(2)	1.09(2)	1.28(2)
Cu	x	0	0	0
	y	0	0	0
	z	0	0	0
Ta	x	-0.0036(28)	0	0
	y	0.0052(25)	0	0
	z	0.3327(9)	0.33657(76)	0.3333(11)
O1	x	0.3081(23)	0.2878(22)	0.2947(13)
	y	0.3124 (35)	0.2844(23)	0.2947(13)
	z	-0.0012(19)	0	0
O2	x	0.2807(23)	0.3325 (43)	0.3051(6)
	y	0.3144(22)	0.2925(43)	0.3051(6)
	z	0.3262(12)	0.3394(5)	0.3405(4)
O3	x	-0.2947(26)	-0.2988(43)	
	y	-0.2985(27)	-0.3188(43)	
	z	0.3239(11)	0.3394(5)	

The medium resolution high-intensity neutron powder diffractometer D20 (ILL, Grenoble) was used for the long-range magnetic ordering investigations. Figure 4-10 displays a color contour plot of several powder patterns collected between

1.86 and 6 K. Apart from the nuclear Bragg reflections, the patterns revealed no additional Bragg reflections or intensity changes, which indicate an absence of long-range magnetic order. The top part of Figure 4-10 shows the difference between the patterns collected at 1.86 K and 5.7 K at the wavelength of 1.89 Å. The difference is featureless across the whole low angle regime where the magnetic scattering may have been expected.

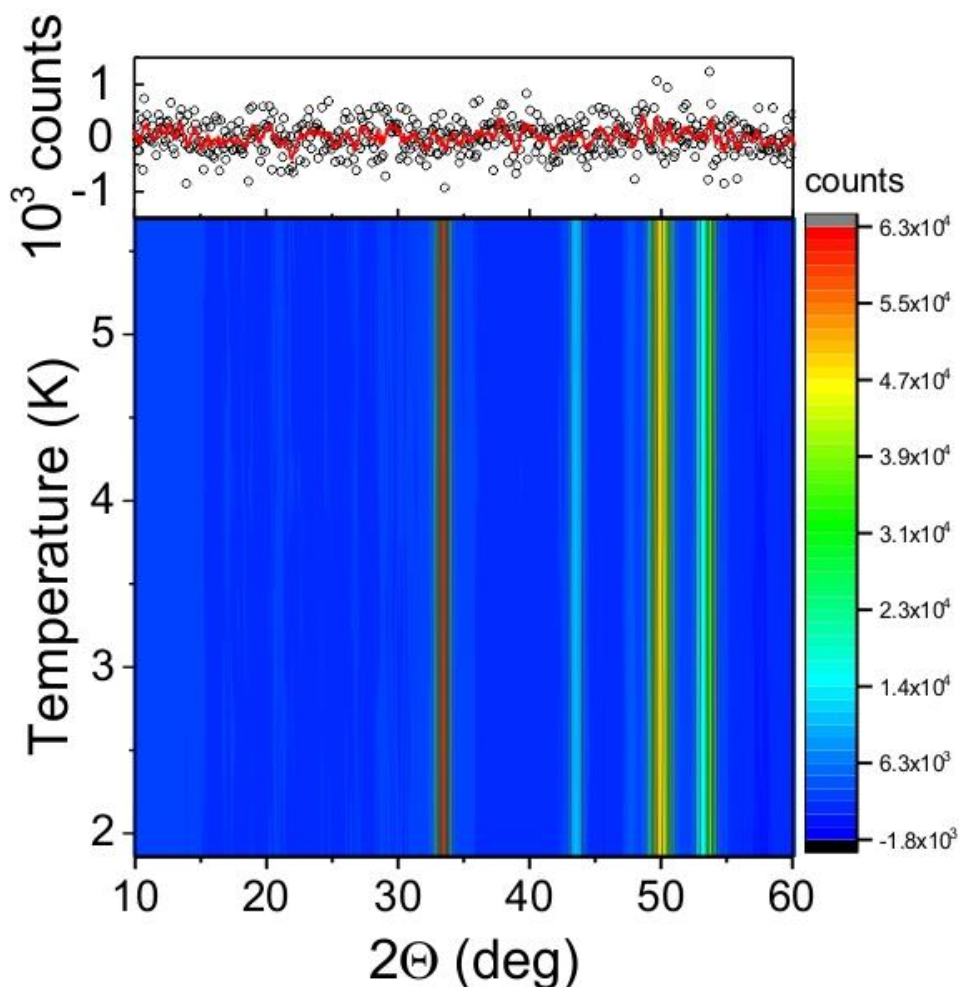


Figure 4-10. (top) Difference between neutron powder diffraction patterns of CuTa_2O_6 collected at 1.86 K and 5.7 K at a wavelength of 1.88 Å. (main frame) Contour plot of the neutron powder diffraction patterns between 1.86 K and 5.7 K with intensities given by the vertical bar on the right. Reprinted (adapted) with permission from A. Golubev, R. E. Dinnebier, A. Schulz, R. K. Kremer, H. Langbein, A. Senyshyn, J. M. Law, T. C. Hansen, H.-J. Koo, M.-H. Whangbo, *Structural and Magnetic Properties of the Trirutile-type 1D-Heisenberg Anti-Ferromagnet CuTa_2O_6* , *Inorg. Chem.* **56(11)**, 6318-6329 (2017). Copyright (2017) American Chemical Society.

4.5. Spin-exchange parameters³

The structural parameters determined in Chapter 4.4. were used as input parameters for the spin-exchange calculations. The mapping analysis of the total energy was calculated by the DFT method assuming several ordered spin structures displayed in Figure 4-11. [4-14]

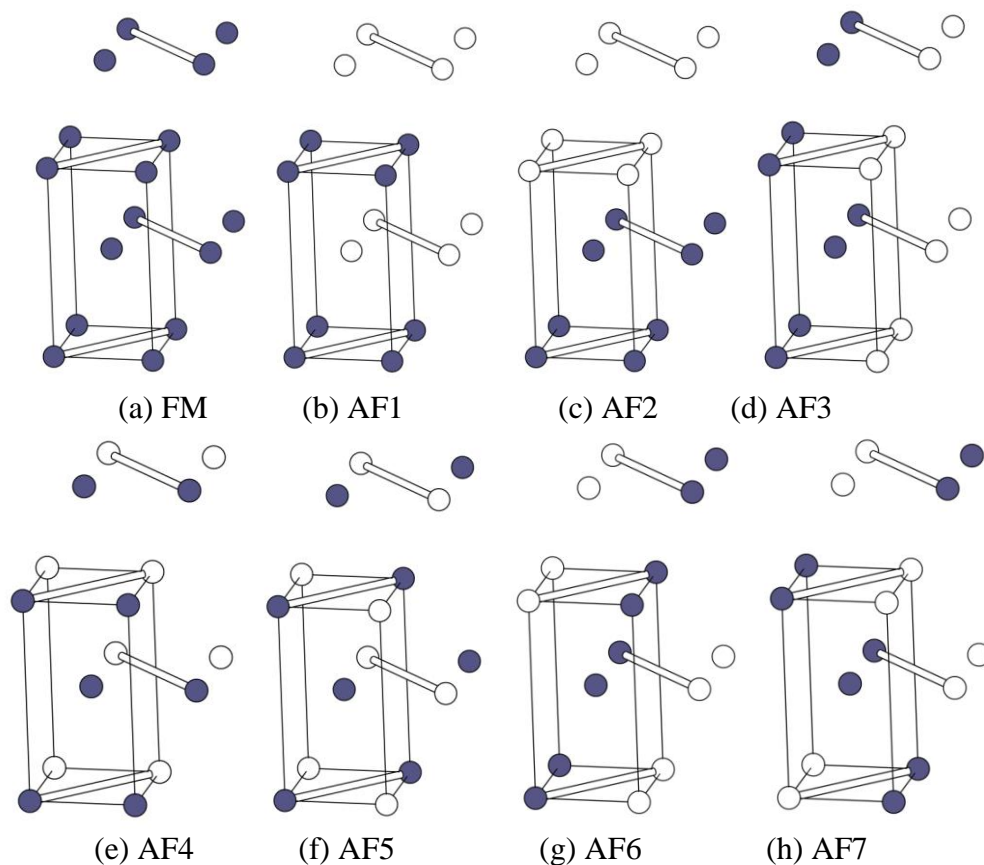


Figure 4-11. Ordered spin arrangements of (a) FM, (b) AF1, (c) AF2, (d) AF3, (e) AF4, (f) AF5, (g) AF6 and (h) AF7 states of CuTa_2O_6 at 293 K. The blue and empty circles represent the up and down spin sites of Cu^{2+} cation, respectively.

Reprinted (adapted) with permission from A. Golubev, R. E. Dinnebier, A. Schulz, R. K. Kremer, H. Langbein, A. Senyshyn, J. M. Law, T. C. Hansen, H.-J. Koo, M.-H. Whangbo, *Structural and Magnetic Properties of the Trirutile-type 1D-Heisenberg Anti-Ferromagnet CuTa_2O_6* , *Inorg. Chem.* **56(11)**, 6318-6329 (2017). Copyright (2017) American Chemical Society.

³ The DFT calculations were performed by Prof. Myung-Hwan Whangbo from North Carolina State University (Raleigh, North Carolina 27695-8204, USA) and Prof. Hyun-Joo Koo from Kyung Hee University (Seoul 130-701, Republic of Korea).

The mapping analysis was performed assuming the spin exchange pathways J_1 and $J_a - J_d$ according to Figure 4-12.

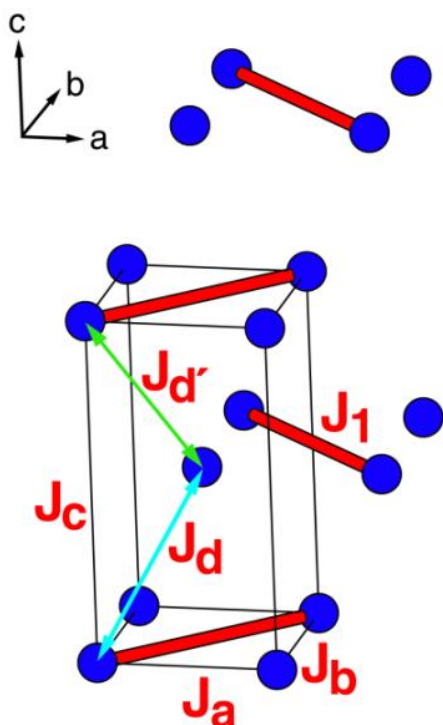


Figure 4-12. Relevant spin-exchange paths in CuTa_2O_6 . The dominant exchange across diagonals of the slightly distorted Cu squares in the $a - b$ planes is denoted by J_1 . Inter-chain exchange paths are J_{a-d} . Reprinted (adapted) with permission from A. Golubev, R. E. Dinnebier, A. Schulz, R. K. Kremer, H. Langbein, A. Senyshyn, J. M. Law, T. C. Hansen, H.-J. Koo, M.-H. Whangbo, *Structural and Magnetic Properties of the Trirutile-type 1D-Heisenberg Anti-Ferromagnet CuTa_2O_6* , *Inorg. Chem.* **56(11)**, 6318-6329 (2017). Copyright (2017) American Chemical Society.

The Vienna *ab initio* simulation package, with the projected augmented-wave method, the generalized gradient approximation (GGA) of Perdew, Burke and Ernzerhof for the exchange and the correlation functionals, a plane-wave cutoff energy of 400 eV, and a sampling of the irreducible Brillouin zone with 32 k points were employed. In order to account for an on-site repulsion, GGA+ U calculations were done. On-site repulsion energies $U = 4, 5,$ and 6 eV for Cu atom were assumed. The AF7 spin configuration (see Figure 4-11) was found to have the lowest energy. The relative energies of the eight ordered spin states obtained from our GGA+ U calculations with respect to the AF7 are summarized in Table 4-7. In order to determine the spin-exchange parameters, the energies of the eight

ordered spin states were expressed in terms of a Heisenberg type spin Hamiltonian according to Eq. (4-2)

$$H = - \sum_{i < j} J_{ij} \vec{S}_i \vec{S}_j, \quad (4-2)$$

where:

$J_{ij} = J_1, J_a - J_d$ are the parameters for the spin-exchange interaction between the spin sites i and j ,

\vec{S}_i and \vec{S}_j are the spin angular momentum operators at the spin sites i and j , respectively.

Table 4-7. Relative energies [in (meV/FU)] with respect to the AF7 state and spin-exchange parameters (in K) obtained from the GGA+ U calculations for CuTa_2O_6 (293 K).

Reprinted (adapted) with permission from A. Golubev, R. E. Dinnebier, A. Schulz, R. K. Kremer, H. Langbein, A. Senyshyn, J. M. Law, T. C. Hansen, H.-J. Koo, M.-H. Whangbo, *Structural and Magnetic Properties of the Trirutile-type 1D-Heisenberg Anti-Ferromagnet CuTa_2O_6* , *Inorg. Chem.* **56(11)**, 6318-6329 (2017). Copyright (2017) American Chemical Society.

State	$U = 4$ eV	$U = 5$ eV	$U = 6$ eV
FM	3.14	2.69	2.26
AF1	3.82	3.16	2.59
AF2	3.42	2.88	2.38
AF3	0.26	0.21	0.17
AF4	0.91	0.73	0.57
AF5	2.95	2.51	2.10
AF6	0.50	0.39	0.31
AF7	0	0	0
J_1	-60.5	-51.9	-43.5
J_a	-13.1	-10.4	-8.12
J_b	2.03	1.63	1.31
J_c	-0.15	-0.22	-0.29
J_d	1.01	0.43	0.11
$J_{d'}$	6.82	5.00	3.73

4.6. Raman Scattering

The temperature dependent Raman scattering measurements were performed to check for the structural phase transition observed in the diffraction experiments. According to a symmetry analyses [4-15], one expects 24 Raman active modes for CuTa_2O_6 in the monoclinic structure-type (space group no. 14) and 16 in the tetragonal structure-type (space group no. 136). For both cases, Cu at Wyckoff site 2a is not involved in Raman active vibrations. [4-16] Figure 4-13 shows the Raman spectra in the range of temperatures up to 773 K in comparison with the room temperature Raman spectrum of the well-crystallized polycrystalline sample of NiTa_2O_6 reported earlier by Haeuseler in 2013. [4-17] and CuSb_2O_6 spectrum reported by Gieré *et al.* in 1997 [4-18]. The Raman spectrum of CuTa_2O_6 is significantly more smeared out than that of NiTa_2O_6 . The broad band between 600 and 800 cm^{-1} of the CuTa_2O_6 spectrum corresponds to the two strong peaks at 650 cm^{-1} and 697 cm^{-1} observed for the NiTa_2O_6 spectrum. Merging of two split strong modes near $\sim 650 \text{ cm}^{-1}$ when crossing the structural phase transition as reported by Gieré *et al.* [4-18] for CuSb_2O_6 in 2013 is not seen for CuTa_2O_6 .

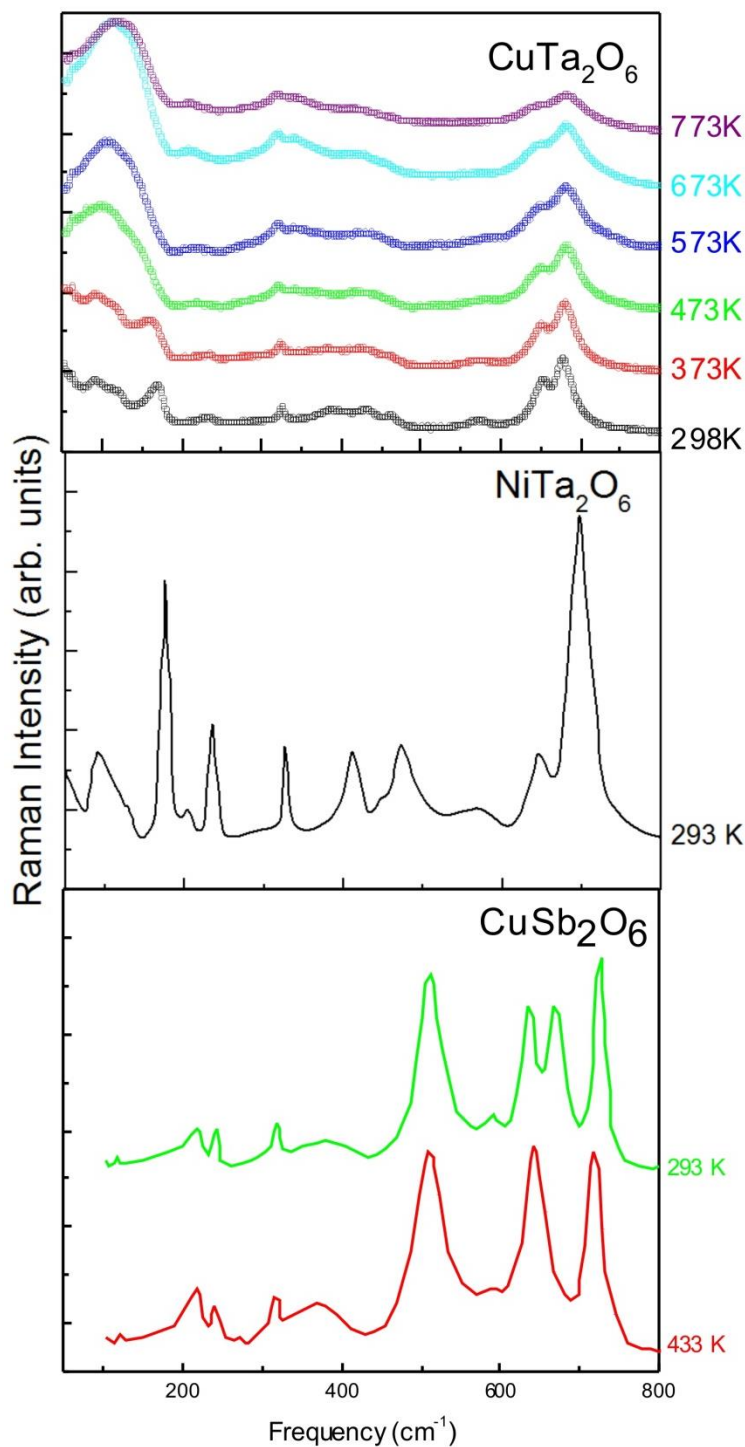


Figure 4-13. (upper panel) Raman spectra of CuTa_2O_6 at various temperatures as indicated. For clarity, each spectrum has been shifted by the same amount. (middle panel) Raman spectrum of NiTa_2O_6 taken from Haeuseler [4-17] (lower panel) Raman spectrum of CuSb_2O_6 taken from Giere *et al.* [4-18] Reprinted (adapted) with permission from A. Golubev, R. E. Dinnebier, A. Schulz, R. K. Kremer, H. Langbein, A. Senyshyn, J. M. Law, T. C. Hansen, H.-J. Koo, M.-H. Whangbo, *Structural and Magnetic Properties of the Trirutile-type 1D-Heisenberg Anti-Ferromagnet CuTa_2O_6* , *Inorg. Chem.* **56(11)**, 6318-6329 (2017). Copyright (2017) American Chemical Society.

The smeared ridge between $\sim 300\text{ cm}^{-1}$ and $\sim 500\text{ cm}^{-1}$ in the CuTa_2O_6 spectrum finds its counterpart in several resolved peaks in the NiTa_2O_6 spectrum. Only the mode at 330 cm^{-1} is seen as a small cusp in the CuTa_2O_6 spectrum. The strong peak at 180 cm^{-1} and other modes below 200 cm^{-1} merge to a structured continuum in the CuTa_2O_6 spectrum. This continuum shows the strongest changes when raising the temperature. At the higher temperatures, it collapses to the featureless bulge between 50 cm^{-1} and 180 cm^{-1} with no drastic modifications except the shift of the center of gravity to higher frequencies before passing through the phase transition from monoclinic to tetragonal. The latter, however, is clearly discernible in the color-coded contour map of the temperature dependence of the Raman spectra displayed in Figure 4-14.

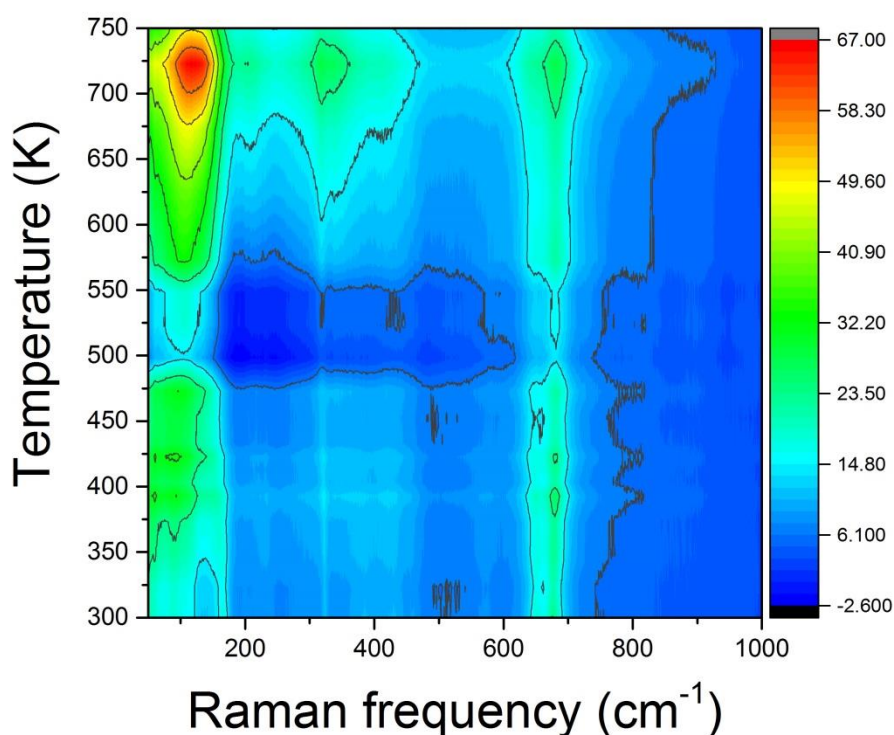


Figure 4-14. Contour map of the temperature dependence of the Raman spectra of CuTa_2O_6 . The monoclinic \rightarrow tetragonal structural phase transition takes place at 550 K
 Reprinted (adapted) with permission from A. Golubev, R. E. Dinnebier, A. Schulz, R. K. Kremer, H. Langbein, A. Senyshyn, J. M. Law, T. C. Hansen, H.-J. Koo, M.-H. Whangbo, *Structural and Magnetic Properties of the Trirutile-type 1D-Heisenberg Anti-Ferromagnet CuTa_2O_6* , *Inorg. Chem.* **56(11)**, 6318-6329 (2017). Copyright (2017) American Chemical Society.

4.7. Magnetic properties

The magnetic susceptibility of CuTa_2O_6 sample was measured in a MPMS SQUID magnetometer in a magnetic field of 0.1 T. The results are shown below in Figure 4-15.

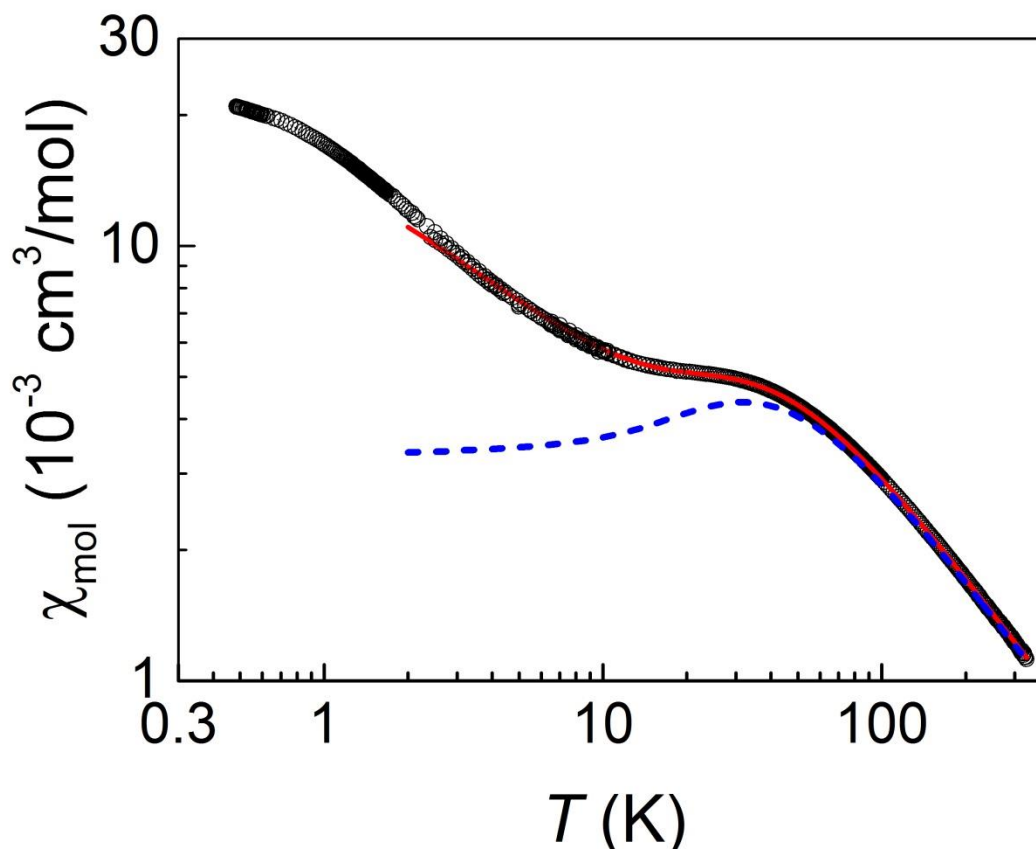


Figure 4-15. (circles) Temperature dependence of the magnetic susceptibility of CuTa_2O_6 shown together with the fit of the experimental data to Eq. (4-3) with parameters given in the text. The blue dashed line highlights the contribution from the $S = 1/2$ spins in the linear chain. The upturn at low temperatures, i.e. the difference between the solid red line and the dashed blue line is due to $\sim 7\%$ of uncorrelated $S = 1/2$ entities which give rise to a Curie-Weiss law with a Curie-Weiss temperature of $-1.5(2)$ K.

Reprinted (adapted) with permission from A. Golubev, R. E. Dinnebier, A. Schulz, R. K. Kremer, H. Langbein, A. Senyshyn, J. M. Law, T. C. Hansen, H.-J. Koo, M.-H. Whangbo, *Structural and Magnetic Properties of the Trirutile-type 1D-Heisenberg Anti-Ferromagnet CuTa_2O_6* , *Inorg. Chem.* **56(11)**, 6318-6329 (2017). Copyright (2017) American Chemical Society.

This experimental data can be well fitted to the $S = 1/2$ Heisenberg chain with the antiferromagnetic nearest-neighbour spin-exchange interaction model described by Eq.(4-3):

$$H = -J \sum_i \vec{S}_i \vec{S}_{i+1}, \quad (4-3)$$

where:

J is the antiferromagnetic spin-exchange interaction between the neighbouring Cu spins in the chain;

\vec{S}_i , and \vec{S}_{i+1} are the spin moments of the neighbouring Cu^{2+} cations.

The temperature dependence of the magnetic susceptibility of the $S = 1/2$ Heisenberg chain with antiferromagnetic nearest-neighbour spin-exchange interaction has been obtained using the Quantum Monte Carlo simulations and transfer-matrix density-matrix renormalization group calculations to high precision. Johnston *et al.* in 2000 encoded these results into a Padé approximant, the coefficients thereof are tabulated. [4-19] In order to allow for inter-chain spin-exchange interactions, which generally induce a long-range magnetic order at low temperatures, the following molecular field extension for the susceptibility in the paramagnetic regime was utilized:

$$\chi_{mol}(T) = \frac{(1 - C_{imp}) \chi_{mol}^{chain}(T)}{1 + \frac{zJ'}{N_A g^2 \mu_B^2} \chi_{mol}^{chain}(T)} + \frac{C_{imp}}{T - \Theta_{imp}} + \chi_0, \quad (4-4)$$

where:

$\chi_{mol}^{chain}(T)$ is the molar magnetic susceptibility of the antiferromagnetic Heisenberg chain;

χ_0 is the sum of the diamagnetic susceptibilities of the closed shells (Larmor diamagnetism);

Θ_{imp} is the Curie-Weiss temperature of the impurity moments;

J' is the inter-chain spin-exchange interaction to z neighbours. [4-20]

The second term in Eq. (4-4) is added to allow for the modelling of the susceptibility of the non-correlated impurity moments. This gives rise to the Curie-Weiss type susceptibility with the Curie-Weiss temperature θ_{imp} which takes care of minute exchanges between the impurity moments *e.g.* in impurity clusters. θ_{imp} may be expected to be very small compared to the intra-chain spin-exchange interaction. The blue dashed line in Figure 4-15 represents the chain susceptibility corresponding to the first term in Eq. (4-4) with the antiferromagnetic intra-chain spin-exchange interaction of $-49.8(2)$ K and a g -factor of $1.95(1)$. The value of $-0.1(1)$ K for the product $z'J'$ indicates a very small to vanishing inter-chain spin-exchange interaction. θ_{imp} amounted to $-1.5(2)$ K and the impurity fraction contributing to the Curie-Weiss tail at low temperatures is fitted to 7.5%. The temperature independent term χ_0 (Larmor diamagnetism) represents the sum of the diamagnetic susceptibilities of the closed shells. From the element increments χ_0 was estimated to -111×10^{-6} cm³/mol according to: Cu²⁺: -11×10^{-6} cm³/mol ; Ta⁵⁺: -14×10^{-6} cm³/mol ; O²⁻: -12×10^{-6} cm³/mol. [4-21] The fit yields a value of $-115(12) \times 10^{-6}$ cm³/mol, being in good agreement with the theoretical expectation. The rather large fraction of the uncorrelated spins was surprising since a substantial crystalline impurity phase could not be detected in the neutron diffraction experiment. In view of the fluffy morphology of the sample flakes, it can be tentatively attributed to positional disorder or to amorphous impurities disrupting antiferromagnetic correlations.

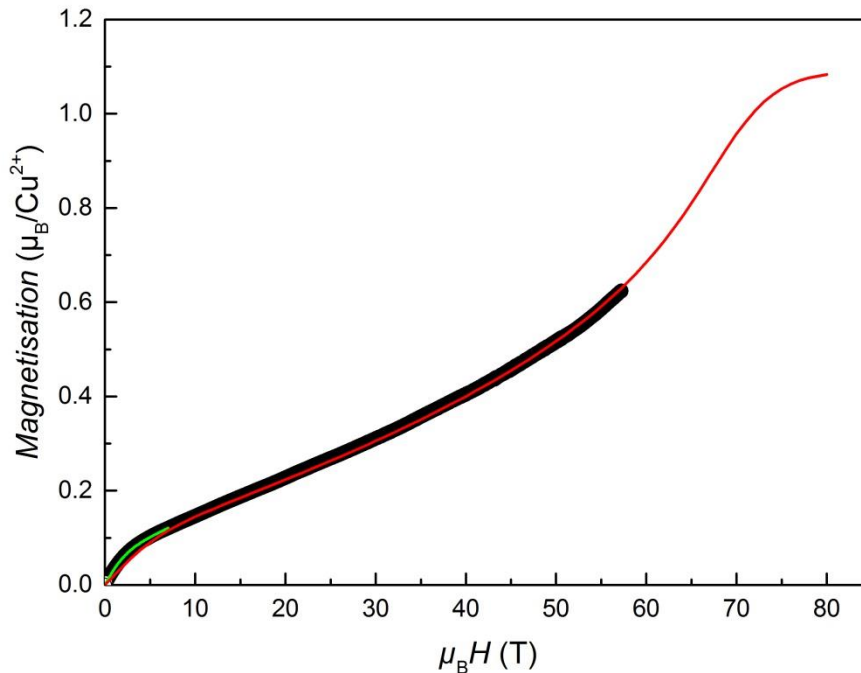


Figure 4-16. (black circles) Isothermal magnetization of polycrystalline CuTa_2O_6 at 2 K measured with the pulsed field magnetometer. Data represented by the green solid line have been collected on same sample with a SQUID magnetometer (see text). The red solid line represents the result of the QMC calculation of the magnetization with an antiferromagnetic nearest-neighbor spin-exchange of $J = 49$ K and a g-factor of 2.2.

Reprinted (adapted) with permission from A. Golubev, R. E. Dinnebier, A. Schulz, R. K. Kremer, H. Langbein, A. Senyshyn, J. M. Law, T. C. Hansen, H.-J. Koo, M.-H. Whangbo, *Structural and Magnetic Properties of the Trirutile-type 1D-Heisenberg Anti-Ferromagnet CuTa_2O_6* , *Inorg. Chem.* **56**(11), 6318-6329 (2017). Copyright (2017) American Chemical Society.

The result of the isothermal magnetization measurement at 2 K collected at the Hochfeld-Magnetlabor (Dresden) is shown in Figure 4-16 in comparison to the theoretical curve. Theoretical calculations of the magnetization $M(H, T)$ for the Heisenberg antiferromagnetic spin $S = 1/2$ chain with the nearest-neighbour interaction were performed with a Quantum Monte Carlo (QMC) algorithm employing the path integral method of the loop code incorporated within the ALPS (Algorithms and Libraries for Physics Simulations) project. [4-22, 4-23]

1.5×10^5 Monte Carlo steps were taken for the initial thermalization and 1.5×10^5 steps were subsequently carried out after the thermalization ensuring low

statistical error. Taking 250 spins and imposing periodic boundary conditions was found to be sufficient to approximate an infinite system at 2 K. The calculated magnetizations reproduce the experimental data very well and indicate saturation above ~75 T. In these calculations magnetization of 7.5 wt% of uncorrelated $S = 1/2$ entities as indicated by the fit of the low field magnetic susceptibility were included.

According to Affleck and Oshikawa [4-24] the saturation field H_{sat} of the antiferromagnetic spin $S = 1/2$ Heisenberg chain is connected to the spin-exchange and the g -factor as:

$$H_{\text{sat}} = -\frac{4J S}{g\mu_B}. \quad (4-5)$$

Using the spin-exchange of $J = -49$ K derived from the analysis of the low temperature magnetic susceptibility and the average g -factor obtained from the EPR spectroscopy (see Figure 4-17), a saturation field of ~66 T was found consistent with the experimental observations.

4.8 Electron paramagnetic resonance

A typical EPR spectrum of CuTa_2O_6 collected at room temperature is shown in Figure 4-17. It consists of a single broad resonance line with a g -factor very close to the average g -factor observed for Cu^{2+} in $\text{Zn}(\text{Mg})_{1-x}\text{Cu}_x\text{Sb}_2\text{O}_6$. [4-18] The rather broad (peak-to-peak linewidth $\Delta H_{pp} \approx 1$ kOe) almost symmetric resonance line can be well fitted to the derivative of a single Lorentzian-type absorption line with negligible ($\alpha \rightarrow 0$) admixture of a dispersive signal given by:

$$\frac{dP_{abs}}{dH} \propto \frac{d}{dH} \left[\frac{\Delta H + \alpha(H - H_{res})}{(H - H_{res})^2 + (\Delta H)^2} + \frac{\Delta H + \alpha(H + H_{res})}{(H + H_{res})^2 + (\Delta H)^2} \right], \quad (4-6)$$

where:

H_{res} is the resonance field;

ΔH the linewidth (half-width at half-maximum (HWHM)).

ΔH is of the same order of magnitude as the resonance field, and consequently positive and negative circular components of the exciting linearly polarized microwave field have to be included by adding the resonance at negative magnetic fields centered at $-H_{res}$. A slight asymmetry observed close to the minimum at the r.h.s. of the resonance position could be accounted for by adding an additional narrower absorption line of significantly smaller intensity (< 1 %). This line can be ascribed to impurity spins as also detected in the magnetic susceptibility experiments.

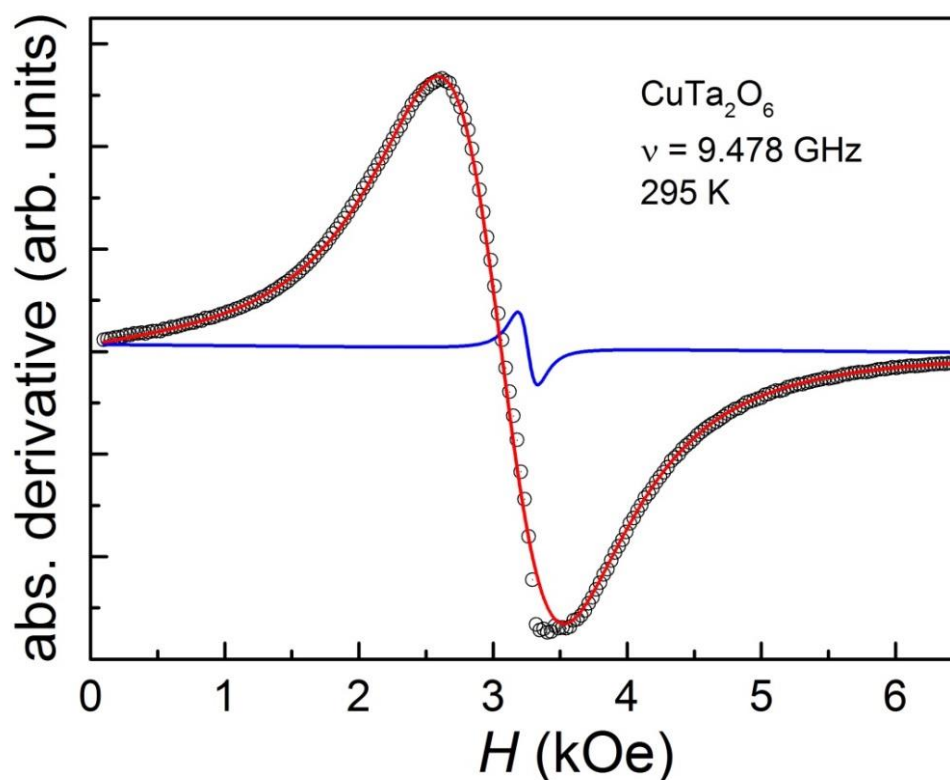


Figure 4-17. (circles) EPR absorption spectrum of polycrystalline sample of CuTa_2O_6 measured at room temperature at a microwave frequency of 9.478 GHz. The red solid line displays a Lorentzian absorption resonance line fitted to the experimental data. The blue solid line represents a second absorption line ascribed to free impurity centers.

Reprinted (adapted) with permission from A. Golubev, R. E. Dinnebier, A. Schulz, R. K. Kremer, H. Langbein, A. Senyshyn, J. M. Law, T. C. Hansen, H.-J. Koo, M.-H. Whangbo, *Structural and Magnetic Properties of the Trirutile-type 1D-Heisenberg Anti-Ferromagnet CuTa_2O_6* , *Inorg. Chem.* **56(11)**, 6318-6329 (2017). Copyright (2017) American Chemical Society.

The temperature dependent spectra were analysed on the basis of a single resonance line according to Eq.(4-6). The temperature dependence of the g -factor and the intensity of the EPR signal are shown in Figure 4-18.

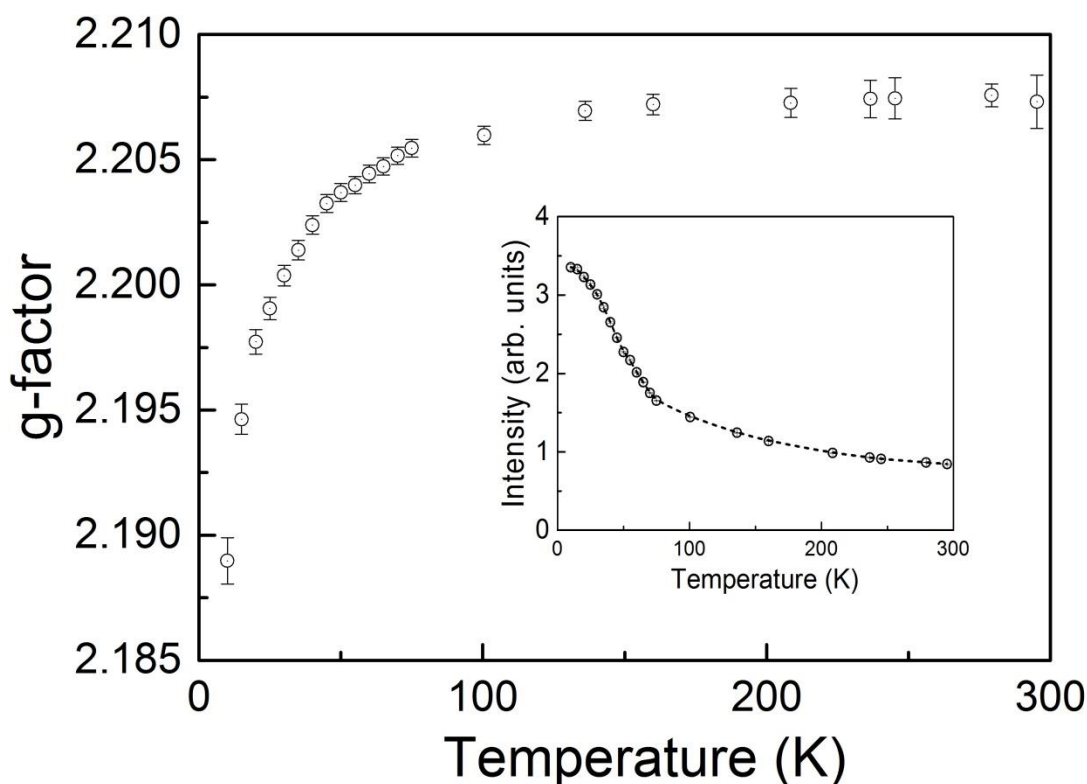


Figure 4-18. (main frame) g -factor of the EPR line for CuTa_2O_6 versus temperature. (inset) Integrated intensity of the EPR line.

Reprinted (adapted) with permission from A. Golubev, R. E. Dinnebier, A. Schulz, R. K. Kremer, H. Langbein, A. Senyshyn, J. M. Law, T. C. Hansen, H.-J. Koo, M.-H. Whangbo, *Structural and Magnetic Properties of the Trirutile-type 1D-Heisenberg Anti-Ferromagnet CuTa_2O_6* , *Inorg. Chem.* **56(11)**, 6318-6329 (2017). Copyright (2017) American Chemical Society.

From room temperature down to ~ 100 K, the g -factor is almost temperature independent and it amounts to

$$g = 2.2070 \pm 0.0005. \quad (4-7)$$

Below ~ 100 K the g -factor decreases i.e. the resonance field grows with decreasing temperature indicating the built-up of antiferromagnetic short-range correlations. By lowering the temperature the integrated intensity decreases following a Curie-Weiss-type temperature dependence. The g -factor signaled short-range correlations, the intensity bends over and tends to saturation at the lowest temperatures. The linewidth starts from ~ 800 Oe at room temperature,

decreases linearly with the decreasing temperature and saturates at the value of 450 Oe below 100 K.

4.9 Specific heat capacity

Anomalies in the heat capacity indicate magnetic short and long-range ordering. A polycrystalline sample of CuTa_2O_6 was measured in the temperature range from 0.4 to 100K. The result is shown in Figure 4-19.

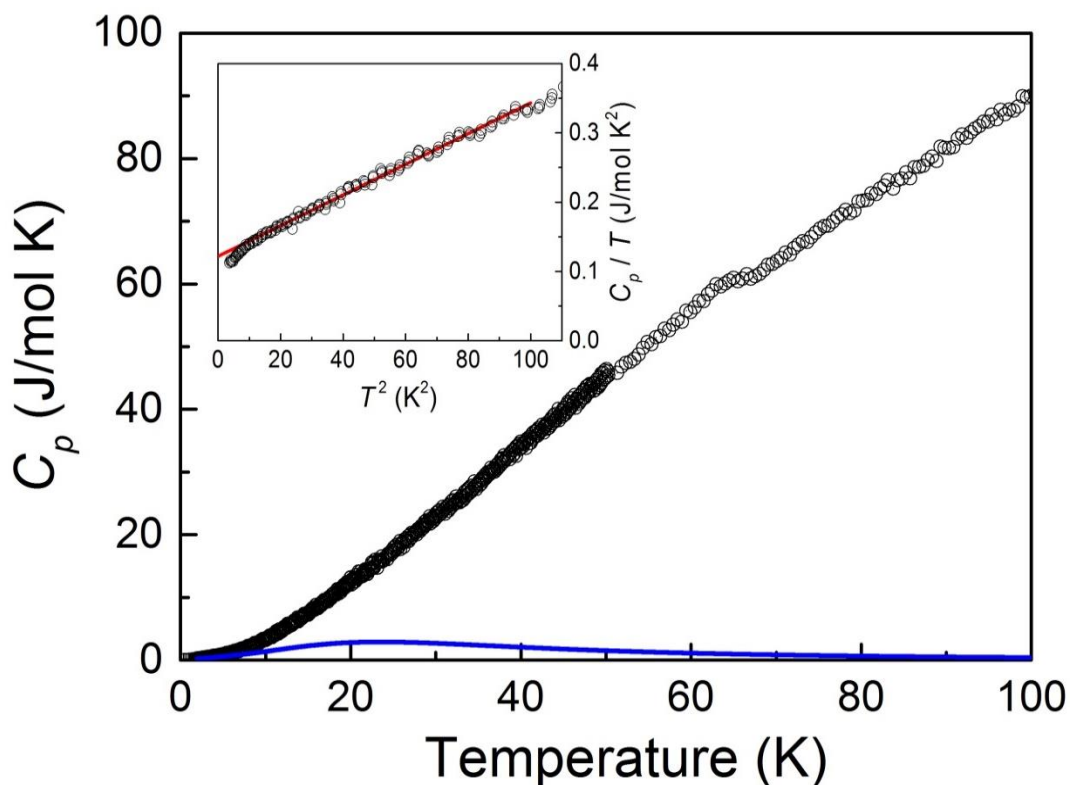


Figure 4-19. Specific heat capacity of CuTa_2O_6 . No apparent anomaly is seen at low temperatures. The feature at ~ 65 K is ascribed to magnetic impurities (for more details see text). The inset displays a Sommerfeld-type plot of the heat capacity divided by temperature versus T^2 . The red solid line is a linear least-squares fit to the data points between 10 and 90 K^2 intersecting the ordinate at a value of $0.122(3) \text{ J/molK}^2$.

Reprinted (adapted) with permission from A. Golubev, R. E. Dinnebier, A. Schulz, R. K. Kremer, H. Langbein, A. Senyshyn, J. M. Law, T. C. Hansen, H.-J. Koo, M.-H. Whangbo, *Structural and Magnetic Properties of the Trirutile-type 1D-Heisenberg Anti-Ferromagnet CuTa_2O_6* , *Inorg. Chem.* **56(11)**, 6318-6329 (2017). Copyright (2017) American Chemical Society.

At low temperatures no apparent anomalies could be detected. The blue solid line in Figure 4-19 represents the magnetic heat capacity of the spin $S = 1/2$ Heisenberg chain with the nearest-neighbour spin-exchange of -49 K [4-19] The maximum of 2.7 J/molK at ~ 25 K adds only 20% to the total heat capacity. Above

the maximum, the heat capacity decreases with $1/T^2$ and the magnetic heat capacity of the chain cannot account for the small hump at ~ 65 K. The entropy involved in this hump amounts to 0.3 J/molK or $\sim 3.5\%$ of the magnetic entropy $R \ln(2S+1) = R \ln 2$ expected to be removed by the ordering of the spin $S = 1/2$ chain system. This anomaly has no correspondence in the magnetic susceptibility. Judging from the magnitude of the entropy it is ascribed to a magnetic impurities. The low temperature (i.e. $k_B T \ll J$) magnetic heat capacity of the spin $S = 1/2$ Heisenberg chain with nearest neighbour antiferromagnetic spin-exchange is linear in temperature and inversely proportional to the intra-chain spin-exchange J according to [4-19]

$$C_{mag}(t \rightarrow 0) = \frac{2}{3} R t, \quad (4-8)$$

where:

$t = \frac{k_B T}{J}$ is the reduced temperature;

$R = 8.31446 \frac{J}{mol K}$ is the molar gas constant.

Assuming that the lattice contribution to the total heat capacity at low temperatures follows the Debye - T^3 power law, a Sommerfeld-type plot of the heat capacity divided by the temperature versus T^2 was used to extract C_{mag}/T ($T \rightarrow 0$) according to:

$$\frac{C_p(T)}{T} = \frac{2}{3} R \frac{k_B}{J} + \beta T^2. \quad (4-9)$$

The inset in Figure 4-19 displays the experimental data together with the fit of Eq.(4-9), to the low-temperature experimental data. The intercept with the ordinate amounts to 0.122(3) J/mol K² indicating an intra-chain spin-exchange of -45.4(7) K according to Eq.(4-9). This value is in good agreement with the results of the fits of the magnetic susceptibility and the isothermal magnetization measurements. Below ~ 3 K, $C_p(T)/T$ falls below the linear fit possibly due to the

built-up of long-range magnetic correlations which may have been masked in the magnetic susceptibility by the substantial Curie-tail contribution from the free spin entities. However, experimental data taken down to 0.4 K exhibit a leveling off towards lowest temperatures rather than an anomaly characteristic for the antiferromagnetic ordering at ~ 3 K indicating an absence of long-range order above 0.4K.

5. CuV_2O_6 ⁴

5.1. Introduction

Some years ago, the structural and magnetic properties of $\alpha\text{-CuV}_2\text{O}_6$ have been attracting a lot of interest. $\alpha\text{-CuV}_2\text{O}_6$ has been described as a one-dimensional spin $S = 1/2$ Heisenberg AFM chain with nearest-neighbor antiferromagnetic spin-exchange coupling ~ 80 K. [5-1, 5-2, 5-3]

AFM resonance experiments, [5-1] neutron diffraction, NMR, [5-2] and specific heat capacity measurements [5-3] showed a long-range magnetic order below ~ 22.5 K.

Recently, $\alpha\text{-CuV}_2\text{O}_6$ has attracted special attention as a possible active material for primary and rechargeable lithium batteries. [5-4, 5-5, 5-6] The catalytic and photocatalytic activity and mechanism for lithium intercalation into $\alpha\text{-CuV}_2\text{O}_6$ were investigated by Ghiyasiyan-Arani *et al.* [5-7]

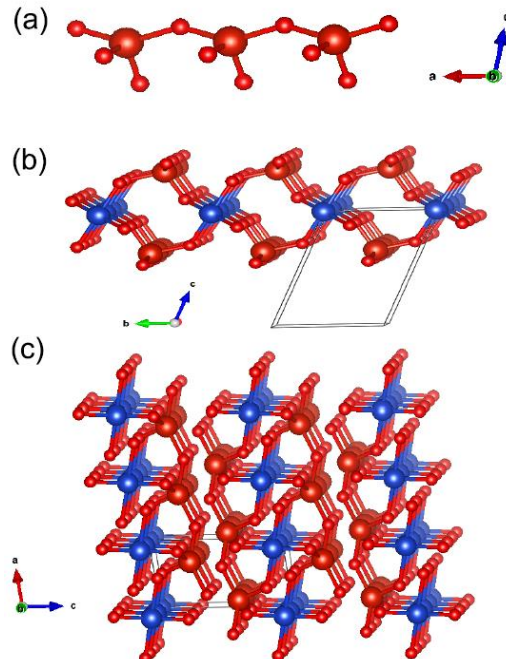


Figure 5-1. (color online) Crystal structure of $\alpha\text{-CuV}_2\text{O}_6$: (a) VO_3 chain of corner-sharing VO_4 tetrahedra. (b) CuV_2O_6 layer made up of stacks of CuO_4 square planes corner-shared with VO_3 chains. (c) Stacking of CuV_2O_6 layers in $\alpha\text{-CuV}_2\text{O}_6$.

⁴ This work has been prepared for publication

α -CuV₂O₆ crystallizes with a triclinic structure (space group $P\bar{1}$, no. 2) shown in Figure 5-1. [5-8] Lattice and atom positional parameters are listed in Table 5-1.

The crystal structure of α -CuV₂O₆ is composed of square planar CuO₄ units containing Cu²⁺ (d^9 , $S = 1/2$) ions and VO₄ tetrahedra containing V⁵⁺ (d^0 , $S = 0$) ions. [5-8] The VO₄ tetrahedra share their corners to form VO₃ chains shown in Figure 5-1(a). The square planar CuO₄ units stack along the a -direction and they share corners with four different VO₃ chains to form a CuV₂O₆ layer parallel to the ab -plane, as it shown in Figure 5-1(b). Such CuV₂O₆ layers are stacked along the c -direction (Figure 5-1(c)) to form α -CuV₂O₆.

As it is shown in Figure 5-1, there are no spin-exchange paths of the Cu – O – Cu type ('super exchange'). Cu²⁺ ions of α -CuV₂O₆ have uniform chain arrangements along three different directions (a -, ($a+b$)-, b -directions with nearest-neighbor Cu · · · Cu distances equal to 3.56, 4.87, 4.97 Å, respectively) within each CuV₂O₆ layer and one along the b -direction (with nearest-neighbor Cu · · · Cu distance equal to 6.485 Å) between the CuV₂O₆ layers.

5.2. Preparation

Polycrystalline samples of α - CuV_2O_6 were synthesized by firing a stoichiometric mixture of CuO (99.999%, Alfa Aesar) and V_2O_5 (99.999%, Alfa Aesar) in a porcelain crucible. In a first step, the thoroughly mixed powder was annealed to 540°C , then ground again in an agate mortar and heated up to 610°C .

Single crystals of α - CuV_2O_6 were grown from the powder using the chemical vapor phase transport (CVT) in a temperature gradient from 600°C to 500°C using TeCl_4 (30 mg) as a transport agent. [5-9]

5.3. Sample characterization

A large polycrystalline sample was prepared for the neutron scattering experiments to determine the magnetic structure. The phase purity of the sample was studied by X-ray powder diffraction (with Mo $K_{\alpha 1}$ radiation) at room temperature and by high-resolution neutron powder diffraction patterns collected on the high-resolution two-axis diffractometer D2B installed at the Institut Laue-Langevin (ILL, Grenoble) (with 1.594 Å wavelength) at low temperatures. For neutron experiments, the sample of ~9 g was filled into an 8 mm outer diameter thin-walled vanadium tubular container. Rietveld profile refinements were performed in the triclinic space group $P-1$ (no. 2) using the FullProf software [5-10] assuming a pseudo-Voigt peak profile (FullProf NPR = 5). Isotropic and anisotropic displacement parameters were tested in the refinements of the X-ray and neutron diffraction patterns, respectively. The background was modeled by a higher-order Chebychev polynomials. The refinements typically converged to Bragg- and R_f -reliability factors of ~ 2% or less. χ^2 -values better than 1 were achieved for the X-ray patterns. For the neutron diffraction, these factors were a bit larger. Table 5-1 summarizes our experimental data in comparison with the data published by Calvo and Manolescu. [5-8]

Table 5-1. Structural parameters (space group $P-1$) of α - CuV_2O_6 as obtained from the Rietveld profile refinement (FullProf) [5-10] of the XRD pattern collected with Mo $K_{\alpha 1}$ radiation and high-resolution NPD patterns ($\lambda = 1.594\text{\AA}$) at $T = 1.5$ K. The respective site occupancies were not refined. The rightmost column lists the structural parameters after Calvo and Manolescu. [5-8] Their data were given with respect to the space group setting $C-1$ and have been transformed into $P-1$ setting. In case anisotropic displacement factors were refined or available (columns, NPD, Calvo) isotropic displacement factors B were calculated using the program VESTA. Conventional reliability indicators are given in the bottom lines.

T (K)	RT(XRD)	1.5 (NPD)	RT (Calvo)
a (Å)	3.5503(2)	3.55643(2)	3.543(3)
b (Å)	4.9638(3)	4.95627(5)	4.968(3)
c (Å)	6.4737(4)	6.45485(5)	6.478(7)
α (deg)	107.836(2)	108.363(5)	107.861(7)
β (deg)	92.312(3)	92.4767(5)	92.25(8)
γ (deg)	112.708(3)	112.7108(5)	112.757(8)

Cu(1a)			
x	0	0	0
y	0	0	0
z	0	0	0
$B_{iso}(\text{Å}^2)$	0.67	0.23	0.64
V(2i)			
x	0.2059(3)	0.196(6)	0.2055(1)
y	0.3859(3)	0.372(5)	0.3856(2)
z	0.6547(2)	0.652(3)	0.65463(6)
$B_{iso}(\text{Å}^2)$	0.39	0.29	0.36
O1(2i)			
x	0.6974(f)	0.6974(4)	0.6961(5)
y	0.3847(f)	0.3847(3)	0.3866(8)
z	0.5677(f)	0.5677(2)	0.5684(3)
$B_{iso}(\text{Å}^2)$	0.8(f)	0.26	0.53
O2(2i)			
x	0.0312(f)	0.0312(5)	0.0331(5)
y	0.0554(f)	0.0554(4)	0.0608(8)
z	0.7207(f)	0.7207(3)	0.5684(3)
$B_{iso}(\text{Å}^2)$	0.8(f)	0.28	0.66
O3(2i)			
x	0.3939(f)	0.3939(4)	0.3908(6)
y	0.6846(f)	0.6846(3)	0.6852(9)
z	0.8905(f)	0.8905(2)	0.8896(3)
$B_{iso}(\text{Å}^2)$	0.8(f)	0.30	0.77

In order to re-determine the crystal structure at low temperature, and also to characterize the polycrystalline sample used for the neutron powder diffraction magnetic structure determination, a series of high-resolution neutron and X-ray powder diffraction measurements were carried out. The results are shown in Figure 5-2. The refined structural parameters are summarized in Table 5-1. These parameters are in good agreement with the data reported before by Calvo and Manolescu. [5-8] Neutron powder diffraction data provided more precise atom positions for the light atoms like oxygen. Anisotropic displacement factor shows a good agreement of neutron powder diffraction and single crystal X-ray diffraction

data. Striking anomalous displacement ellipsoids could not be seen. Therefore only isotropic displacement parameters are listed.

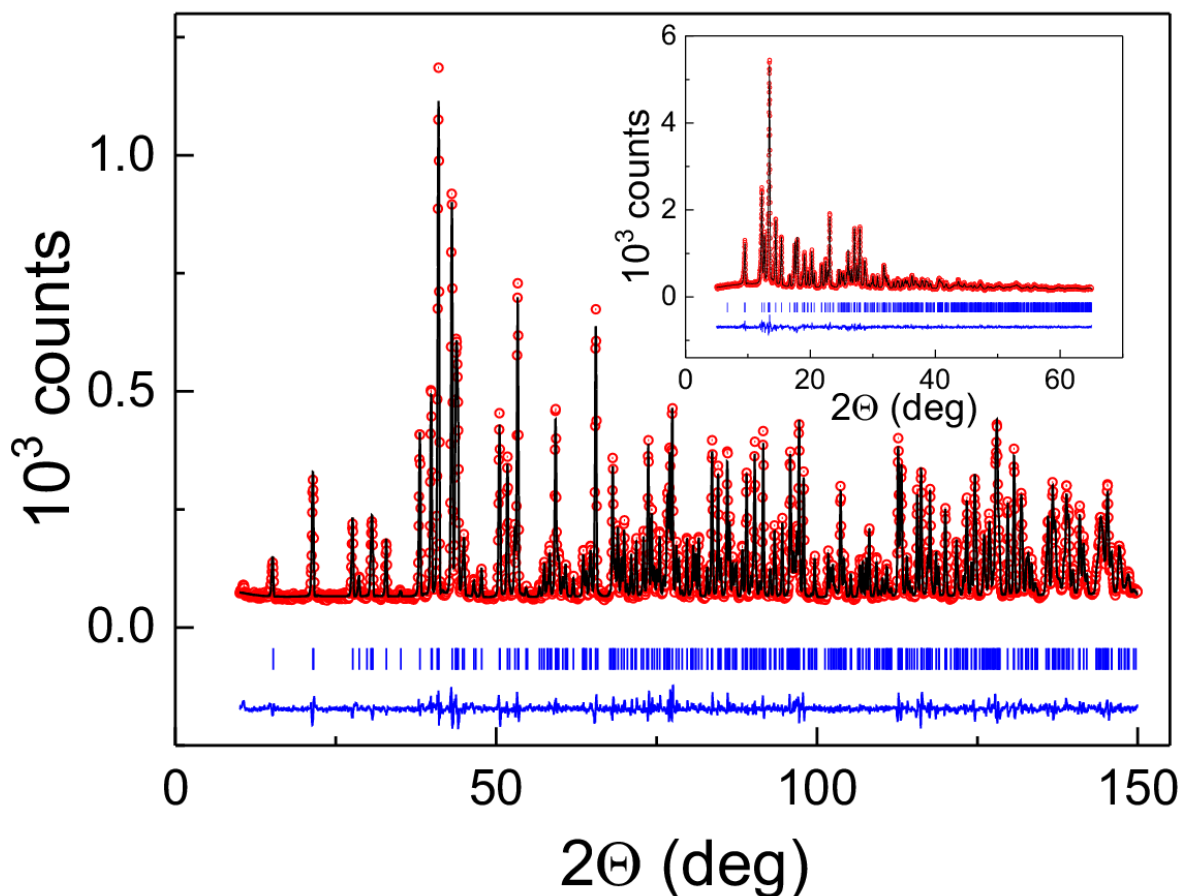


Figure 5-2. Neutron powder diffraction pattern of α - CuV_2O_6 collected at 1.5 K using neutrons with a wavelength of $\lambda = 1.594 \text{ \AA}$ (ILL D2B). The inset displays a room-temperature x-ray diffraction pattern collected using $\text{Mo K}_{\alpha 1}$ radiation together with a Rietveld profile refinement. In the plot, the red circles represent the measured data; the black solid line is the result of the refinement. The blue solid lines at the bottom of the graphs show the difference between the observed and calculated patterns. Vertical tics (blue) mark the angles of the Bragg reflections used to simulate the refined patterns. The refined structure parameters are summarized in Table 5-1.

5.4. Crystal structure

Cirilli *et. al.* [5-11] reported a peritectic decomposition of $\alpha\text{-CuV}_2\text{O}_6$ above $\sim 640^\circ\text{C}$. In order to confirm this observation and to investigate the decomposition reaction in more detail, DTA and high temperature XRD measurements around the decomposition temperature were carry out on a polycrystalline sample of $\alpha\text{-CuV}_2\text{O}_6$. Figure 5-3 displays a DTA trace of $\alpha\text{-CuV}_2\text{O}_6$, which reveals an exothermic peak with maximum at $\sim 637^\circ\text{C}$. A small precursor peak centered at 615°C is also seen.

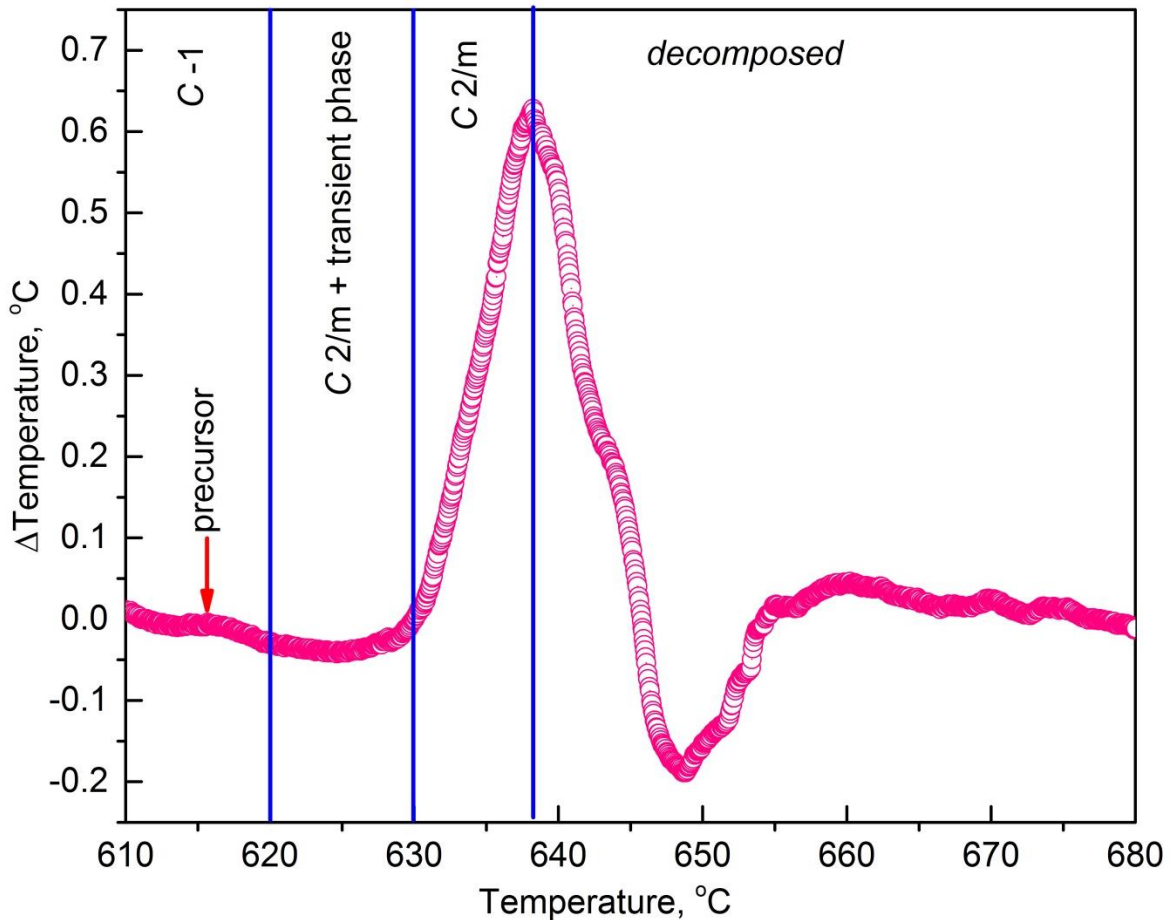


Figure 5-3. The DTA trace of $\alpha\text{-CuV}_2\text{O}_6$ (after subtraction of a suitable linear background) reveals an exothermic transformation above 637°C .

Figure 5-4 displays a contour plot composed of X-ray diffraction patterns collected with $\text{Mo K}_{\alpha 1}$ radiation between 500°C and 660°C .

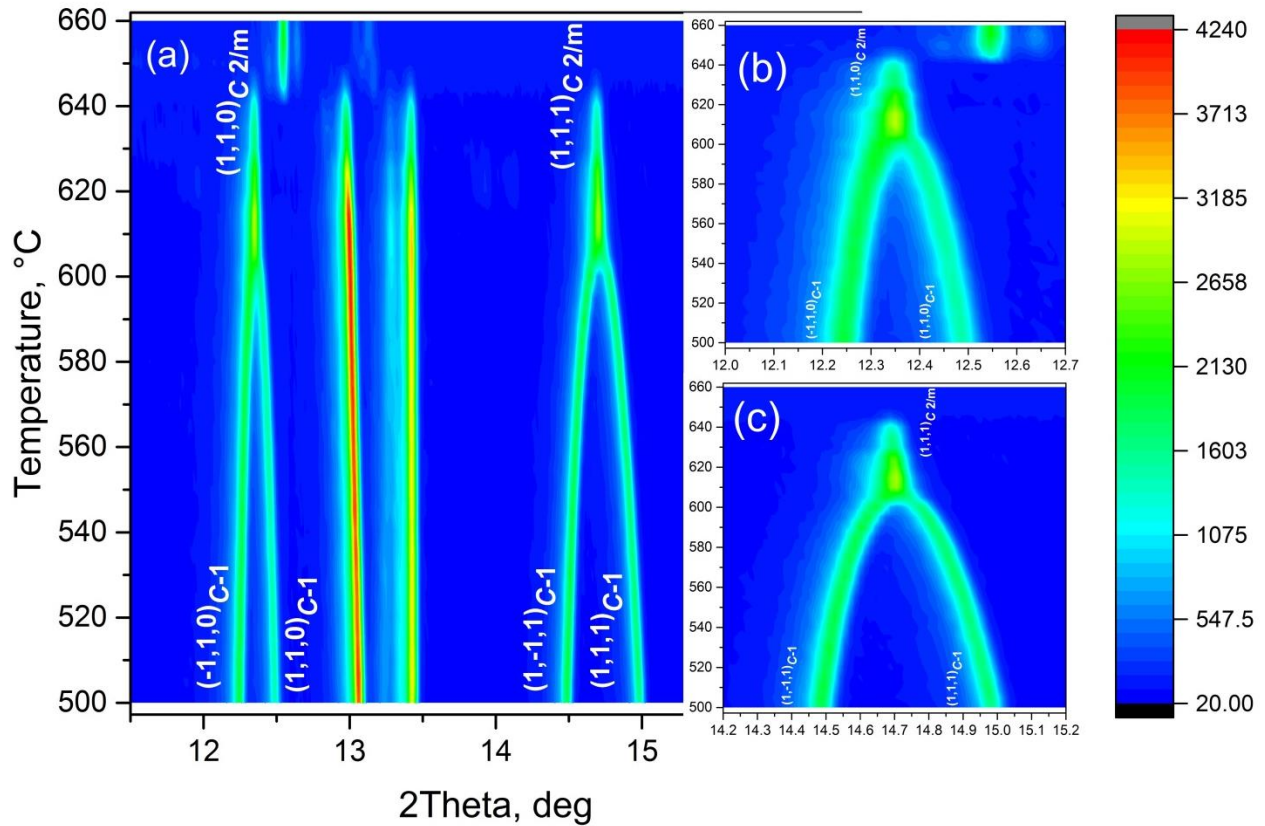


Figure 5-4. Contour plot of X-ray diffraction patterns of α - CuV_2O_6 sample collected with $\text{Mo K}\alpha_1$ radiation between 500 °C and 660 °C. Indexes of the Bragg reflections are given.

The contour plot reveals a structural phase transition starting at ~ 615 °C corresponding to the precursor peak detected in the DTA trace (see Figure 5-3).

Figure 5-5 displays the merging of two characteristic Bragg reflection indexed as $(-1,1,0)$, $(1,1,0)$ and $(1,-1,1)$, $(1,1,1)$ in $C-1$ space group and $(1,1,0)$ and $(1,1,1)$ in $C2/m$ space group. The solid line shows a fit of the Bragg angle with a critical power law $2\theta \propto t^{-\beta}$, where $t = \frac{T}{T_c} - 1$ is the reduced temperature and β is the critical exponent. From a least-squares fit of the Bragg positions the critical temperature for the structure phase transition $T_c = 615$ °C and critical exponent $\beta = 0.30$ were obtained.

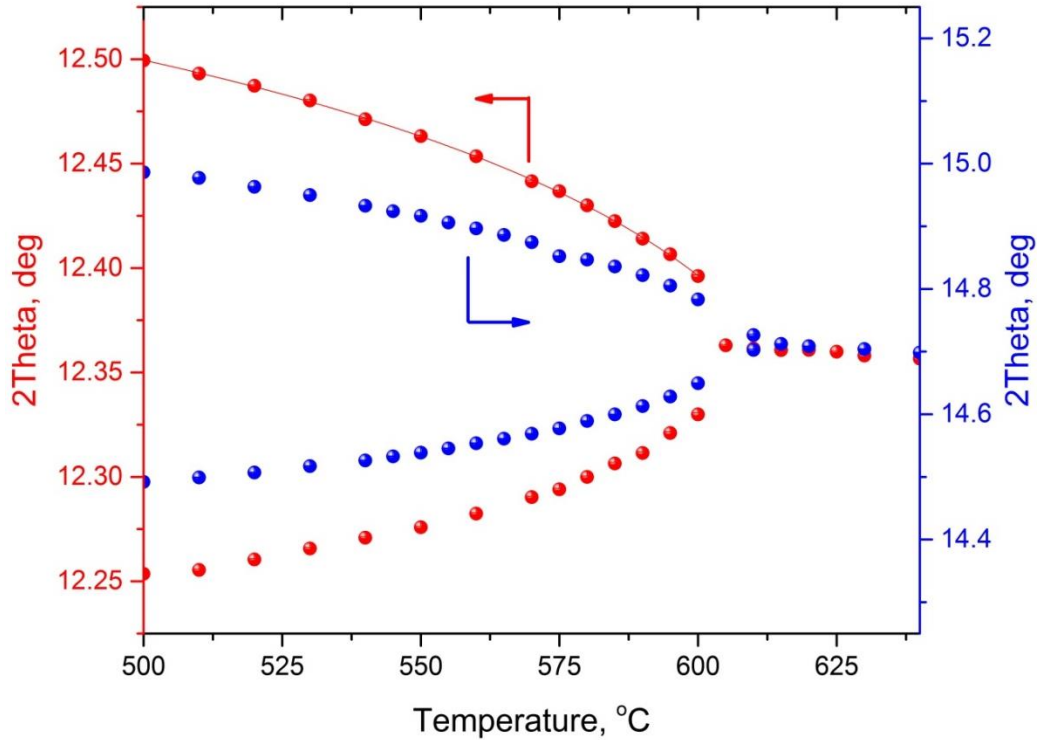


Figure 5-5. Splitting of $(1,1,0)_{C 2/m}$ and $(1,1,1)_{C 2/m}$ Bragg's peaks of $\alpha\text{-CuV}_2\text{O}_6$ below $\sim 615^\circ\text{C}$. X-ray powder diffraction pattern were collected using $\text{Mo K}\alpha_1$ radiation.

Figure 5-6 highlights two Bragg peaks that appear between 620°C and 630°C .

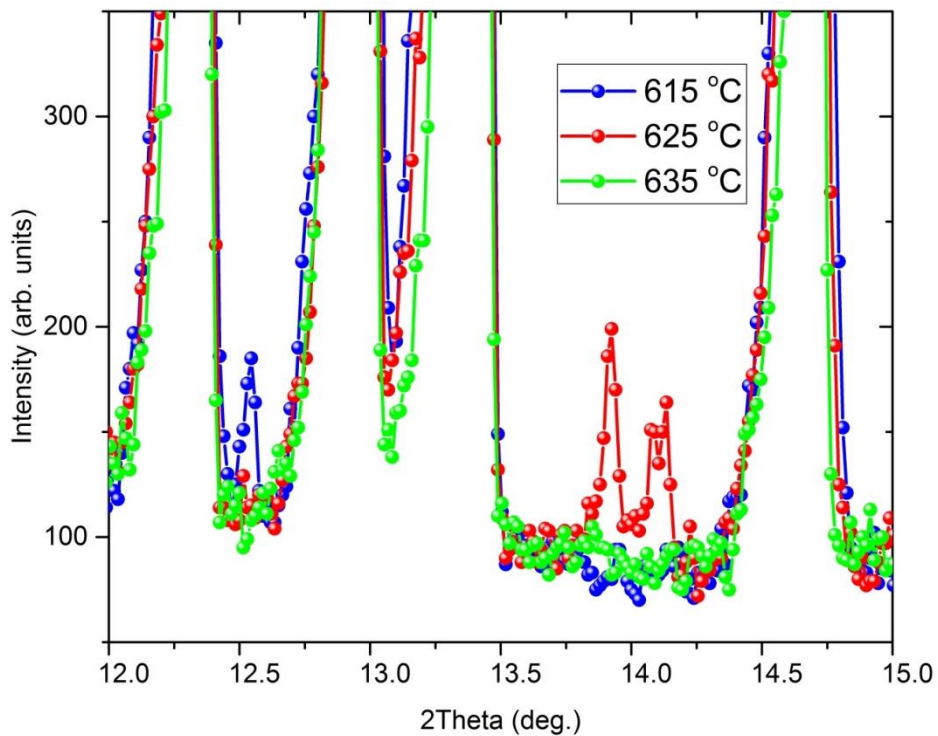


Figure 5-6. X-ray diffraction patterns ($\text{Mo K}\alpha_1$ radiation) of $\alpha\text{-CuV}_2\text{O}_6$ collected between 615°C and 635°C

Above ~615 °C the diffraction patterns can be well refined assuming the space group $C 2/m$ (see Figure 5-7). At ~620 °C small additional Bragg peaks appeared, which disappeared again above ~630 °C (see Figure X+3 and insert of Figure 5-7). Their Bragg positions and d-values are summarized in Table 5-2.

Table 5-2. Positions of the small Bragg peaks not indexable in $C 2/m$

2θ (deg)	d (Å)
7.01	5.80119
9.02	4.51031
9.68	4.20345
11.94	3.40993
13.9	2.93099
14.1	2.88963
15.58	2.61659
20.32	2.01057
21.04	1.9425
21.25	1.92352
21.46	1.90492
25.78	1.58983

These small extra peaks cannot be indexed based on space group $C 2/m$ with the lattice parameter listed in Table 5-3. Efforts to index them based on maximal subgroups of $C 2/m$ were not successful, so far. Currently, I ascribe these Bragg peaks to a transient phase, possibly with a multiple of the $C 2/m$ unit cell refined at 620 °C. An incommensurate transient phase can also not be excluded.

Table 5-3. Lattice parameters and atom positions of α - CuV_2O_6 between 615 °C and 635 °C

Temperature	615 °C	625 °C	625 °C	635 °C
Space group	$C -1$ (no.2)	$C -1$ (no.2)	$C 2/m$ (no.12)	$C 2/m$ (no.12)
a , Å	9.28670(14)	9.28873(19)	9.28773(17)	9.29198(14)
b , Å	3.55222(5)	3.55237(6)	3.55186(6)	3.55278(5)
c , Å	6.53004(9)	6.53102(11)	6.53081(11)	6.53389(8)
α , deg	90.06477(157)	90.04752(216)	90	90
β , deg	108.95452(72)	108.93539(94)	108.94194(118)	108.89532(91)
γ , deg	90.07244(157)	90.07401(205)	90	90

Cu				
x	0	0	0	0
y	0	0	0	0
z	0	0	0	0
V				
x	0.19760(23)	0.19839(33)	0.19825(31)	0.19742(28)
y	-0.00084(151)	-0.00219(231)	0	0
z	0.66101(32)	0.66191(45)	0.66174(44)	0.66212(38)
O1				
x	0.03919(68)	0.03923(95)	0.03855(97)	0.03627(86)
y	-0.00020(507)	-0.00528(762)	0	0
z	0.73127(98)	0.73231(141)	0.73324(145)	0.72772(127)
O2				
x	0.34269(75)	0.34055(106)	0.34102(97)	0.34653(85)
y	-0.03260(423)	0.02475(701)	0	0
z	0.88992(118)	0.88875(168)	0.88846(153)	0.89070(133)
O3				
x	0.30178(71)	0.30284(100)	0.30354(93)	0.30282(83)
y	-0.00905(508)	0.00452(768)	0	0
z	0.42759(113)	0.42796(162)	0.42762(151)	0.42858(130)

Figure 5-7 displays X-ray diffraction patterns and Rietveld profile refinements of α -CuV₂O₆ (Mo K _{α 1} radiation) between 500 °C and 640 °C. At temperatures $T \leq 620$ °C, refinements assuming the space group *C*-1 showed two of the triclinic angles (α and β) approaching 90° indicating that a monoclinic cell being an appropriate description for the phase for $T > 620$ °C. The space groups *C* 2 and *C* 2/m were tested to refine the patterns. It was found, that the reliability indicators are close to each other. Guided by observations by Bouloux *et. al.* for CdV₂O₆ (ICSD Code 15926) [5-12], Markkula *et. al.* for CoV₂O₆ (ICSD Code 263001) [5-13] and Andreetti *et. al.* for ZnV₂O₆ (ICSD Code 30880) [5-14] the description in space group *C* 2/m, including a mirror plane as an additional symmetry element was chosen for the description of the new phase of α -CuV₂O₆ between 615 °C and 640 °C.

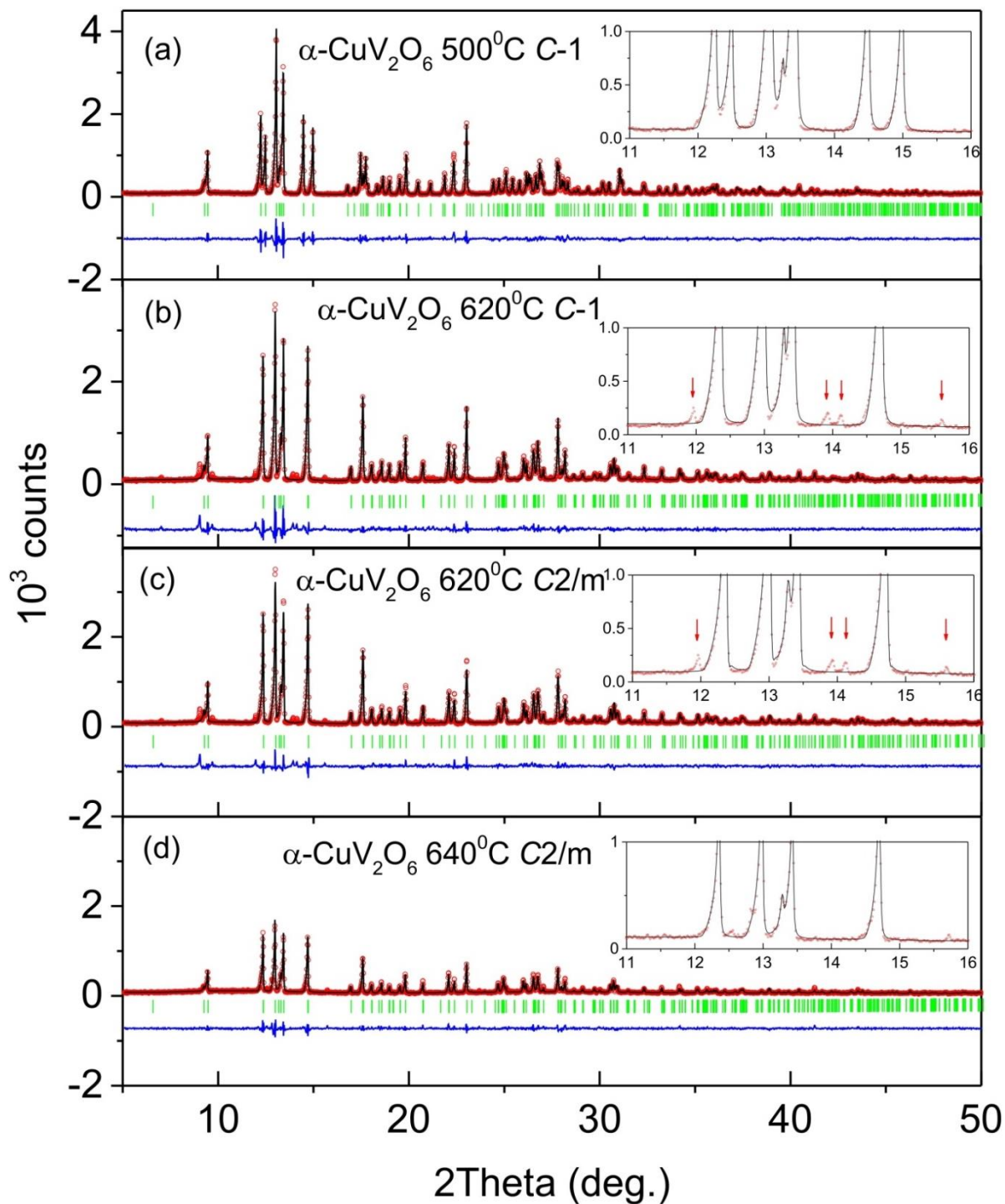


Figure 5-7. X-ray diffraction patterns (Mo $K_{\alpha 1}$ radiation) of α - CuV_2O_6 collected at high temperatures. At 500 °C (a) α - CuV_2O_6 is triclinic. (b) and (c) show refinements at 620 °C either by assuming the space group C-1 (no.2) (b) with angles $\alpha \approx \gamma \approx 90^\circ$ or in space group C2/m (no.12) (c), which both fit the pattern equally well. However, a closer inspection (see inserts) revealed additional Bragg peaks (red arrows) at angles given in Table 5-2. These Bragg peaks appear between $\sim 620^\circ\text{C}$ and $\sim 630^\circ\text{C}$ and disappear above (d). Pattern (d) was collected on the decomposed sample.

5.5. Spin-exchange parameters⁵

Considering the crystal structure, $\alpha\text{-CuV}_2\text{O}_6$ has no spin-exchange paths of the Cu–O–Cu type ('super-exchange'). $\alpha\text{-CuV}_2\text{O}_6$ rather has uniform chain arrangements along four different directions with super-super exchange character. To identify which one of these four chain arrangements accounts for the low dimensional AFM behavior observed experimentally, the Cu–O···O–Cu spin-exchanges, $J_1 - J_4$ (corresponding to Cu···Cu distances of = 3.556, 4.870, 4.972 and 6.485 Å, respectively) (Figure 5-8), were evaluated. The geometrical details (distances and angles) associated with the $J_1 - J_4$ exchange paths are summarized in Table 5-4. Results of medium resolution high intensity neutron powder diffraction on the ILL's diffractometer D20 (at a wavelength of 2.42 Å) were used as input parameters for DFT calculations.

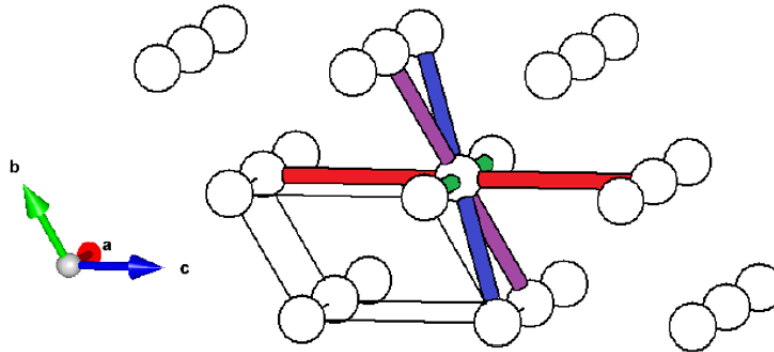


Figure 5-8. Spin-exchange paths of $\alpha\text{-CuV}_2\text{O}_6$. For simplicity, only the Cu^{2+} ions are shown, and the $J_1 - J_4$ correspond to the NN Cu···Cu distances of = 3.556, 4.870, 4.972 and 6.485 Å, respectively) spin-exchange paths are represented by colored cylinders: J_1 = green, J_2 = blue, J_3 = purple, J_4 = red.

Table 5-4. Cu···Cu and O···O distances and Cu–O···O and O···O–Cu angles associated with the Cu–O···O–Cu spin-exchange paths of $\alpha\text{-CuV}_2\text{O}_6$ (defined with colored cylinders in Figure. 5-8).

path	color	direction	$d_{\text{Cu}\cdots\text{Cu}}$, Å	$d_{\text{O}\cdots\text{O}}$, Å	$\angle_{\text{Cu-O}\cdots\text{O}}$, deg	$\angle_{\text{O}\cdots\text{O-Cu}}$, deg
J_1	green	a	3.556	3.039	100.74	53.38
J_2	blue	(a+b)	4.870	2.686	131.98	96.29
J_3	purple	b	4.972	4.431	92.07	78.82
J_4	red	c	6.485	2.757	161.07	161.07

⁵ The DFT calculations were performed by Prof. Myung-Hwan Whangbo from North Carolina State University (Raleigh, North Carolina 27695-8204, USA).

The energies of different spin states were expressed in terms of a Heisenberg spin-exchange Hamiltonian:

$$\mathcal{H} = - \sum_{i < j} J_{ij} \vec{S}_i \vec{S}_j, \quad (5-1)$$

where:

$J_{ij} = J_1 - J_4$ are parameters for the spin-exchange interaction between the spin sites i and j , as defined in Figure 5-8;

\vec{S}_i and \vec{S}_j are the spin angular momentum operators at the spin sites i and j , respectively.

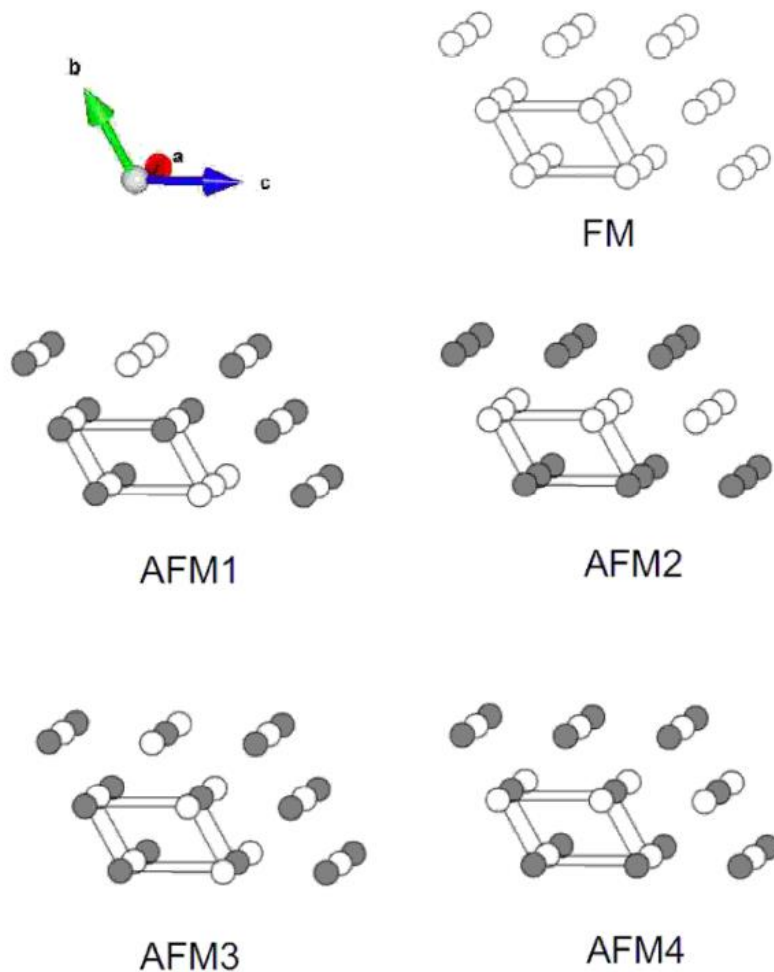


Figure 5-9. Ordered spin states of α -CuV₂O₆ employed to extract the values of $J_1 - J_4$ by the energy-mapping analysis based on DFT+U calculations.

To determine four spin-exchanges $J_1 - J_4$, spin-polarized DFT+U calculations for five ordered collinear spin states (one FM and four AF1 - AF4 states) defined using a 2×2×2 supercell (Figure 5-9) that contains eight formula units (FUs) were performed.

These calculations were performed with the Vienna ab initio Simulation Package (VASP) [5-15] with the projector augmented wave method, [5-16] the generalized gradient approximation (GGA) for the exchange and correlation functional [5-17] the tetrahedron method and Blöchl corrections. [5-18] The cut-off energy was set to 520 eV, and 4×4×3 k-point mesh was employed. The effect of electron correlations associated with the Cu 3d orbitals was taken into consideration by performing DFT plus the on-site repulsion (DFT+U) calculations with $U_{eff} = 4, 5, 6$ eV. [5-19]

In terms of the spin Hamiltonian Eq.(5-1), the energies of these five states per supercell can be expressed as:

$$\begin{aligned}
 E_{FM} &= \frac{-8J_1 - 8J_2 - 8J_3 - 8J_4}{4} \\
 E_{AFM1} &= \frac{+8J_1 + 8J_2 - 8J_3 - 8J_4}{4} \\
 E_{AFM2} &= \frac{-8J_1 + 8J_2 + 8J_3 - 8J_4}{4} \\
 E_{AFM3} &= \frac{+8J_1 + 8J_2 - 8J_3 + 8J_4}{4} \\
 E_{AFM4} &= \frac{+8J_1 - 8J_2 + 8J_3 - 8J_4}{4}
 \end{aligned} \tag{5-2}$$

The relative energies of the five ordered spin states calculated by DFT+U calculations are summarized in Table 5-5.

Table 5-5. Relative energies per eight f.u. (in meV per supercell) of the five collinear spin configurations used in the DFT+ U calculations for $U_{eff} = 4, 5, 6$ eV.

Spin configuration	Energy of eight f.u. in meV		
	$U_{eff} = 4\text{eV}$	$U_{eff} = 5\text{eV}$	$U_{eff} = 6\text{eV}$
FM	0	0	0
AFM1	-28.69	-22.71	-17.89
AFM2	-29.91	-24.10	-19.41
AFM3	-54.95	-43.98	-33.94
AFM4	-0.38	+0.13	+0.48

All five ordered spin states are magnetic insulating states with magnetic moments largely residing on Cu^{2+} ions (see Table 5-6).

Table 5-6. Magnetic moments on the Cu, V and O atoms in the FM states of $\alpha\text{-CuV}_2\text{O}_6$ from the DFT+ U calculations for $U_{eff} = 4, 5, 6$ eV.

atom	μ_B/atom		
	$U_{eff} = 4\text{eV}$	$U_{eff} = 5\text{eV}$	$U_{eff} = 6\text{eV}$
Cu	0.68	0.71	0.74
V	0.03	0.03	0.02
O	0.04	0.04	0.03

By mapping the relative energies of the five ordered spin states obtained from DFT+ U calculations onto the corresponding relative energies obtained from the Heisenberg spin-exchange Hamiltonian, values of $J_1 - J_4$ were determined (see Table 5-7)

Table 5-7. $J_1 - J_4$ spin-exchange parameters of $\alpha\text{-CuV}_2\text{O}_6$ determined by the energy-mapping analyses based on the DFT+ U calculations for $U_{eff} = 4, 5, 6$ eV.

Spin-exchange parameter	Spin-exchange(meV)		
	$U_{eff} = 4\text{eV}$	$U_{eff} = 5\text{eV}$	$U_{eff} = 6\text{eV}$
J_1	0.03	-0.07	-0.14
J_2	7.41	5.99	4.83
J_3	0.07	0.04	-0.03
J_4	6.30	4.93	3.79

Two AFM spin-exchanges J_2 and J_4 are dominated in $\alpha\text{-CuV}_2\text{O}_6$. The spin-exchange along the shortest $\text{Cu} \cdot \cdot \cdot \text{Cu}$ (J_1) is negligible. The dominant J_2 and J_4 constitute a

two-dimensional (2D) AFM anisotropic square spin lattice with an anisotropy ratio J_x/J_y of ~ 0.7 .

It is evident that the previously proposed [5-1, 5-2, 5-3] a 1D Heisenberg uniform AFM chain model is inappropriate to describe the magnetic parameters of α - CuV_2O_6 . In terms of magnetic orbitals of a CuO_4 square plane, the $3d_{x^2-y^2}$ orbital of Cu is combined with the $2p$ orbitals of the O ligands as depicted in Figure 5-10(a). Thus, the strength of the $\text{Cu}(1) - \text{O} \cdots \text{O} - \text{Cu}(2)$ AFM spin-exchange depends on how strongly the magnetic orbital of $\text{Cu}(1)\text{O}_4$ overlaps with that of $\text{Cu}(2)\text{O}_4$ square plane (Figure 5-10 (b)). This, in turn depends on how strongly the O $2p$ orbital of the $\text{Cu}(1)\text{O}_4$ magnetic orbital overlaps with that of the $\text{Cu}(2)\text{O}_4$ magnetic orbital. A strong Cu – O · · O – Cu spin-exchange occurs when the O · · O distance is shorter than the van der Waals distance between the two O atoms of the O · · O contact (3.04 Å). [5-20] As can be seen from Table 5-4, the O · · O distances are much longer in J_1 and J_3 than those in J_2 and J_4 spin-exchange paths. This allows to understand why J_2 and J_4 are stronger than J_1 and J_3 .

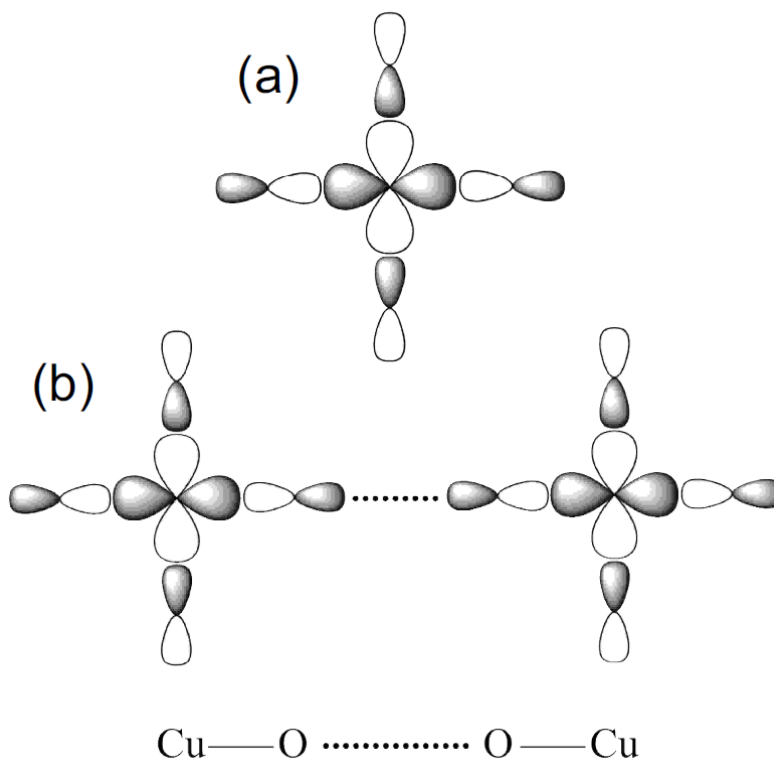


Figure 5-10. (a) Magnetic orbital of a CuO_4 square plane containing a Cu^{2+} (d^9 , $S = 1/2$) ion. (b) Interactions between two magnetic orbitals associated with a $\text{Cu}-\text{O} \cdots \text{O}-\text{Cu}$ spin-exchange. For simplicity, the case for $\text{Cu} - \text{O} \cdots \text{O} = 180^\circ$ is presented.

5.6. Magnetic properties

The magnetic susceptibility of a polycrystalline sample of α -CuV₂O₆ has been reported and discussed before by Vasilev *et al.*, Kikuchi *et al.* and Prokofiev *et al.* [5-1, 5-2, 5-3]

They reported a Néel temperature of 24 K. A first measurement of the heat capacity by Prokofiev *et al.* [5-3] found a λ -type anomaly in the heat capacity indicating long-range magnetic ordering at 22.7 K. This is close to what Vasilev *et al.* and Kikuchi *et al.* had found from susceptibility and NMR measurements. They found a good agreement of their experimental data with the theoretical prediction for a Heisenberg spin $S=1/2$ chain using Bonner-Fisher results. However, Prokofiev *et al.* reported some discrepancies. For example, the g -factor obtained from their fit of the susceptibilities measured with the magnetic field along with the needles (b -axis in $C-1$ setting, a -axis in $P-1$ setting) amounted to 2.44, remarkably larger compared to what is typically found for Cu²⁺ in Jahn-Teller elongated octahedral environment. [5-21] These inconsistencies triggered us to reinvestigate the magnetic properties of α -CuV₂O₆.

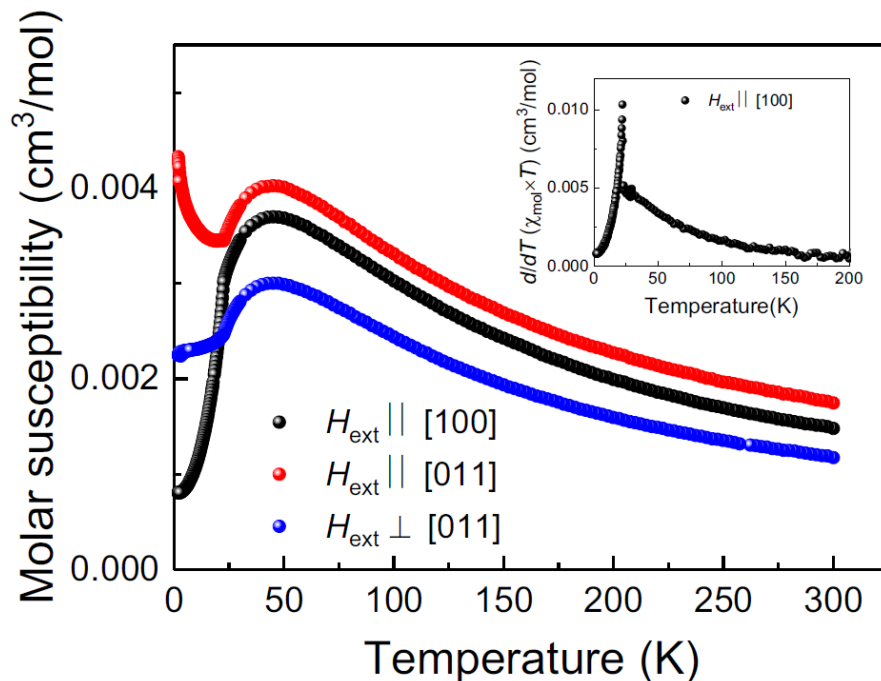


Figure 5-11. Anisotropy of the magnetic susceptibilities of a crystal of an α -CuV₂O₆ observed with magnetic field applied parallel [100] (along the crystal needle) and perpendicular as indicated.

A DC magnetization measurements *versus* magnetic field and temperature were performed in a Magnetic Property Measurement System (Quantum Design, MPMSXL) employing the RSO option. Figure 5-11 displays the temperature dependence of the magnetic susceptibilities of a needle-shaped crystal of α - CuV_2O_6 with the external field oriented parallel $\parallel a$ (in *P*-1 setting, parallel $\parallel b$ in *C*-1 setting) and perpendicular to the crystal needle, as indicated. The susceptibilities are characterized by a broad maximum centered at about 43 K indicates short-range AFM ordering, followed by a Curie-Weiss type hyperbolic decrease at high temperatures. The Curie-Weiss temperature amounts to ~ -70 K, (Figure 5-11) indicating a predominant antiferromagnetic spin-exchange. There is a large anisotropy of the magnetic susceptibilities. The susceptibility with field applied along [100] continuously decreases to lowest temperatures, whereas the susceptibilities with field applied perpendicular to [100] (perpendicular to the crystal needles) initially drop and after a kink at ~ 22.5 K either level off or slightly increase again. This behavior is typical for a uniaxial antiferromagnet with the easy axis aligned along or close to the [100] direction. At the kink temperature, a change of the slope for $\chi_{\text{mol}}([100])$ is observed.

Heat capacity measurements were performed in a Physical Property Measurement System (Quantum Design, PPMS) in magnetic fields up to 9 T with the field oriented perpendicular to the crystal needles. The quantity $d/dT (\chi_{\text{mol}} \times T)$ ('Fisher's heat capacity') [5-22] exhibits a sharp peak centered at ~ 22 K similar to the λ -shaped anomaly observed at this temperature in the heat capacity (see Figure 5-12 and also Ref. [5-3]).

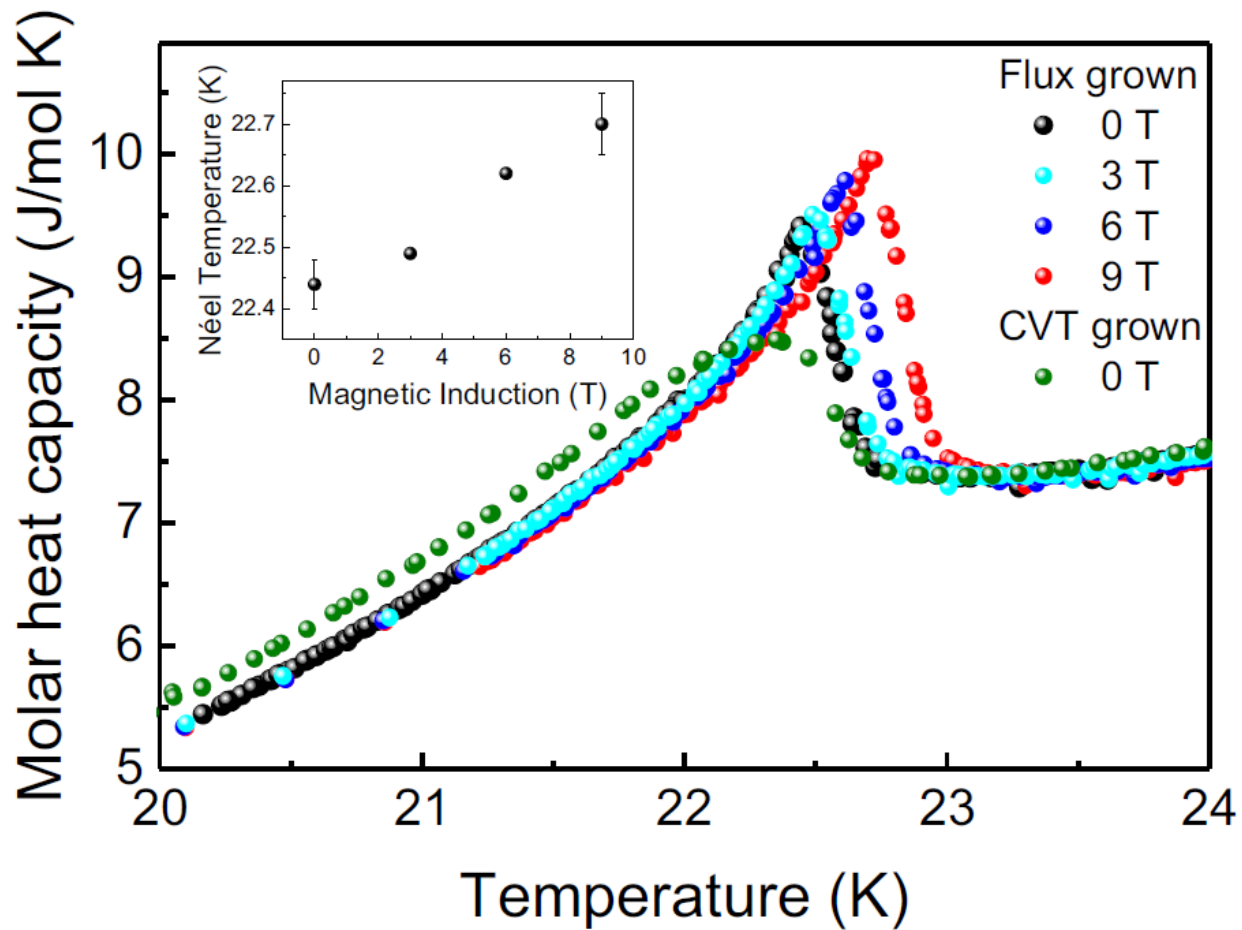


Figure 5-12. Heat capacity versus magnetic field of flux grown (crystals obtained from A.V. Prokofiev) and a CVT grown crystal near the Néel temperature. The λ -shaped anomaly shifts to higher temperature with increasing field applied perpendicular to the crystal needle. The anomaly of the CVT grown crystal is somewhat smeared out, however with the same onset temperature as the flux-grown crystal. The magnetic entropy contained in the anomaly amounts to $\sim 2\%$ of $R \ln 2$ expected for a spin $S=1/2$ system implying that almost all magnetic entropy is removed by short-range AFM ordering above the Néel temperature.

The insert in Figure 5-12 highlights the transitional temperature as a function of the external field.

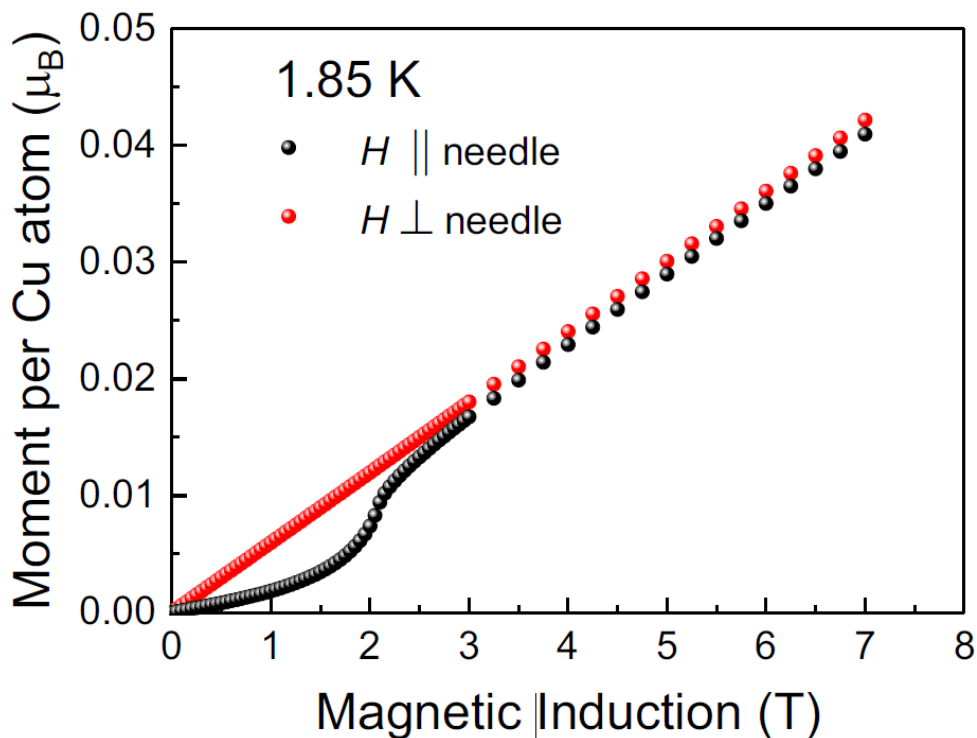


Figure 5-13. Magnetization of an α - CuV_2O_6 crystal at 1.85 K with the magnetic field applied parallel and perpendicular the crystal needle as indicated.

Figure 5-13 shows the magnetization of a needle-shaped α - CuV_2O_6 crystal at 1.85 K. The external field is oriented parallel ($\parallel a$ in P -1 setting, $\parallel b$ in C -1 setting) and perpendicular to the needle axis. With the latter orientation, the magnetization increases linearly with the field, whereas with the field oriented along the needle a typical spin-flop of the magnetization is observed. This finding indicates that the easy axis is close to $[100]$ as already found in the low-field susceptibility measurements. The spin-flop field *versus* temperature determined from the derivatives of the isothermal magnetization $M_{\text{mol}}(T,H)$, $(dM_{\text{mol}}(H,T)/dH)_T$ is displayed in Figure 5-14. The inset highlights the temperature dependence of the peaks. The spin-flop shifts toward to the higher fields with increasing temperature and disappears above the Néel temperature. The λ -anomaly in the heat capacity of the crystal grown from the flux is well-shaped and sharp at zero field peaks at 22.44(4) K. Applying a magnetic field slightly increases the Néel temperature (see inset Figure 5-12) but does not effect on the shape of the anomaly. The magnetic anomaly in the heat capacity of the CVT crystal is broadened indicating some

inhomogeneity. However, the onset of the anomaly coincides with the onset measured on the flux-grown crystal.

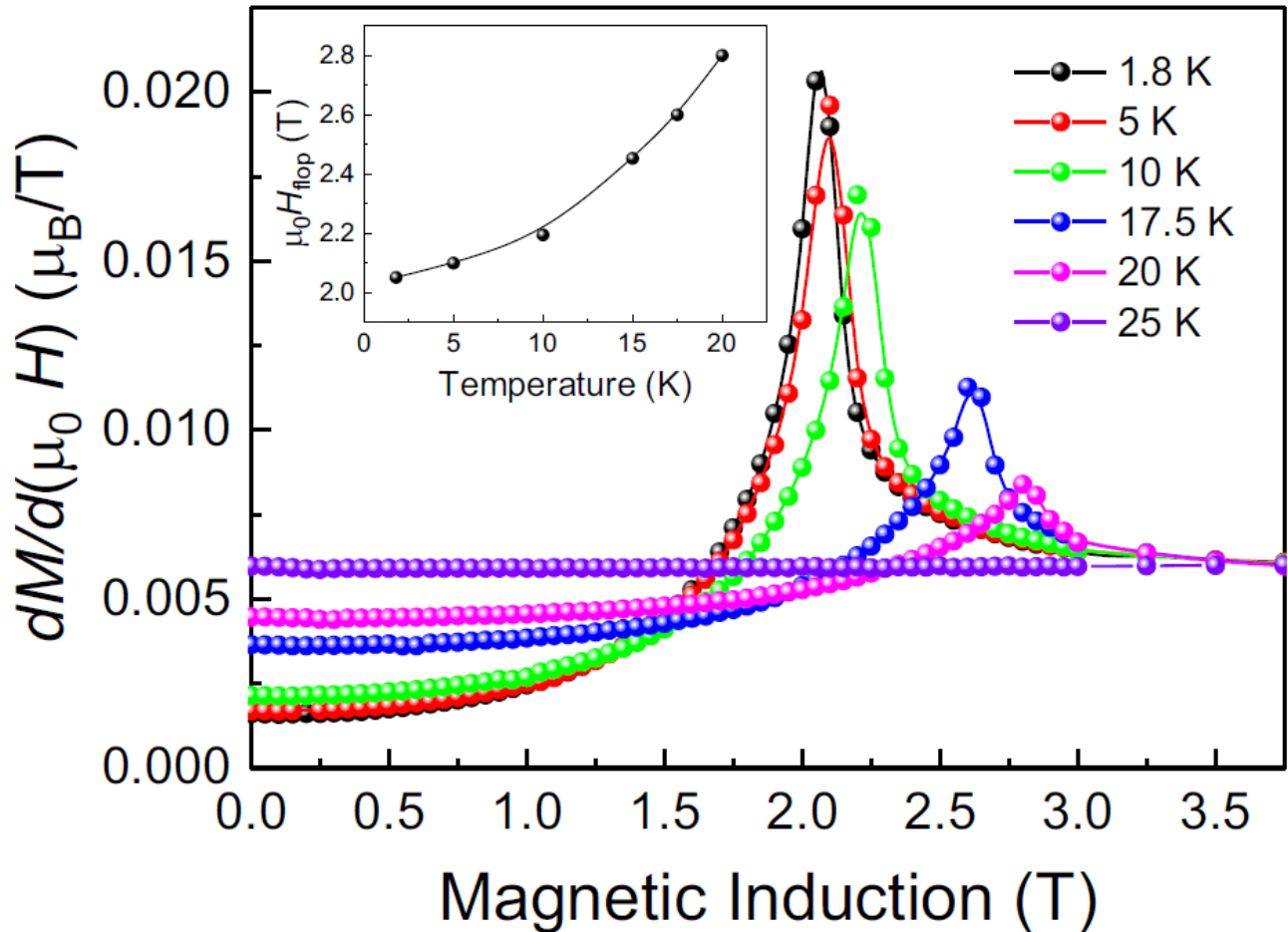


Figure 5-14. Derivative of the isothermal magnetization (per Cu atom) versus the magnetic field indicating the position of the spin-flop. The inset displays the spin-flop field versus measuring temperature.

5.7. Magnetic structure

The determination of the magnetic structure of α -CuV₂O₆ was performed from high-intensity medium-resolution neutron powder diffraction patterns collected at the two-circle diffractometer D20 installed at the Institut Laue-Langevin (ILL) in Grenoble, France.

Figure 5-15 displays the powder diffraction pattern taken at 1.5 K together with a Rietveld profile refinement of the nuclear structure. Atom and lattice parameters are in good agreement with data from the high-resolution neutron data (see Table 5-1). At $2\Theta = 16.14^\circ$ ($d = 8.61 \text{ \AA}$) and $2\Theta = 28.14^\circ$ ($d = 4.98 \text{ \AA}$) extra Bragg reflections are observed. They disappear above $\sim 22 \text{ K}$. Consequently, they were attributed to magnetic reflections.

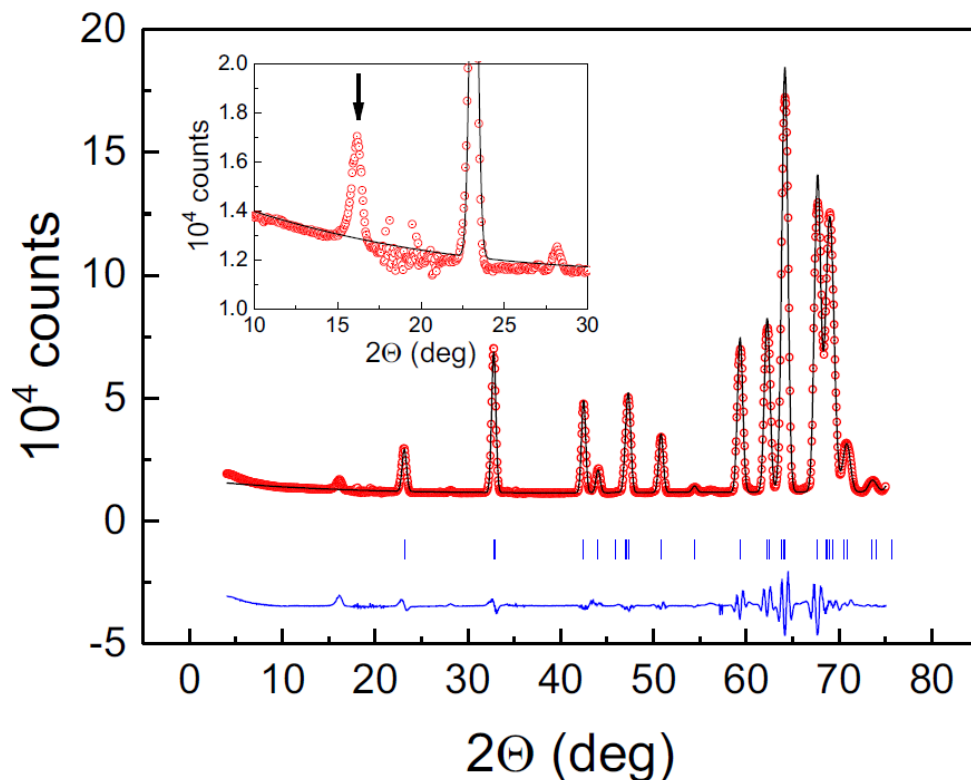


Figure 5-15. Neutron powder diffraction pattern of α -CuV₂O₆ collected at 1.5 K using neutrons with a wavelength of $\lambda = 2.424 \text{ \AA}$ on ILL's medium-resolution high-intensity powder diffractometer D20 shown together with a Rietveld profile refinement (solid black line). The red circles represent the measured counts, the blue solid lines at the bottom of the graphs show the difference between the observed and calculated patterns. Vertical ticks (blue) mark the Bragg angles of the reflections used to simulate the refined patterns. The inset displays the range with the strongest magnetic Bragg reflection at $d = 8.61 \text{ \AA}$ in an enlarged scale.

The plot of the integrated intensity of the $2\Theta = 16.14^\circ$ magnetic Bragg reflection *versus* temperature (see Figure 5-16) confirms the second order nature of the phase transition.

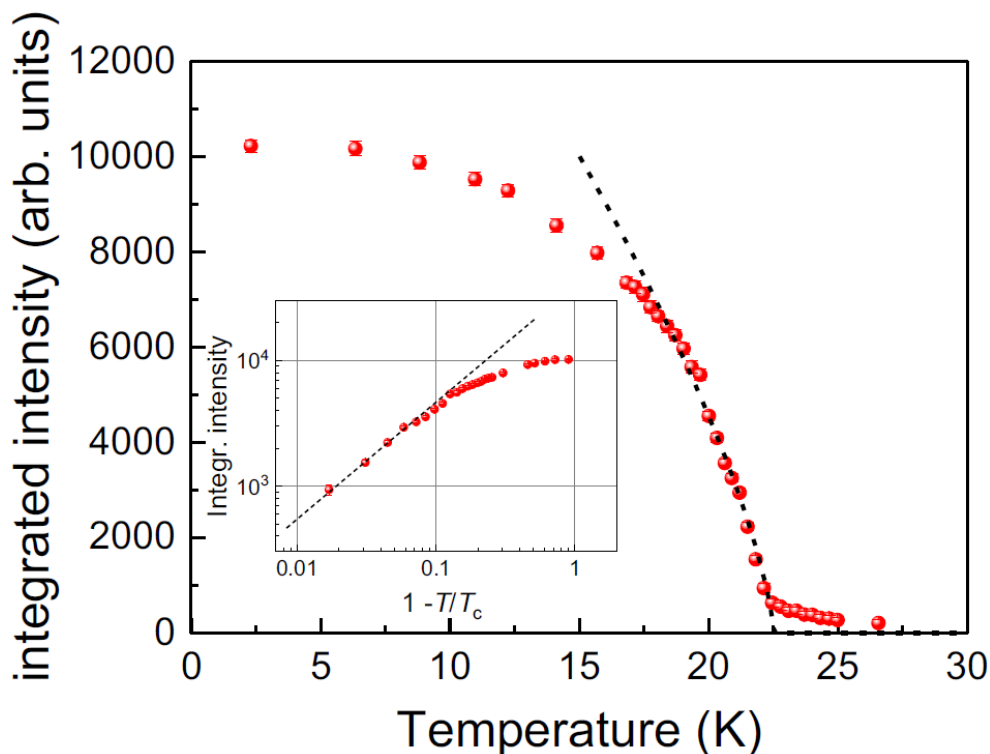


Figure 5-16. (red) circles Integrated intensities of the magnetic Bragg reflection at $2\Theta = 16.14^\circ$. The dashed line is a fit of the data close to $T_c = 22.37$ K with a critical power law according to Eq.(5-3) assuming a critical exponent $\beta = 0.36$.

A fit of the integrated intensity $I(T)$ to a power law (Eq.(5-3)) assuming a critical exponent $\beta = 0.36$ gave a critical temperature of $T_c = 22.37(7)$ K. It is in good agreement with the critical temperature found from magnetization and heat capacity experiments.

$$I(T) \propto \left(1 - \frac{T}{T_c}\right)^{2\beta}, \quad (5-3)$$

where:

β is the critical exponent. $\beta = 0.36$ is typical for the 3D-Heisenberg universality class [5-24]

T_c is the critical temperature.

In order to search for more magnetic Bragg reflections, a heat map of the difference diffraction patterns collected with acquisition time 1h per pattern while slowly (0.5K/min) ramping up the temperature from 1.5 K to 30 K was plotted at Figure 5-17 (30 K pattern is subtracted).

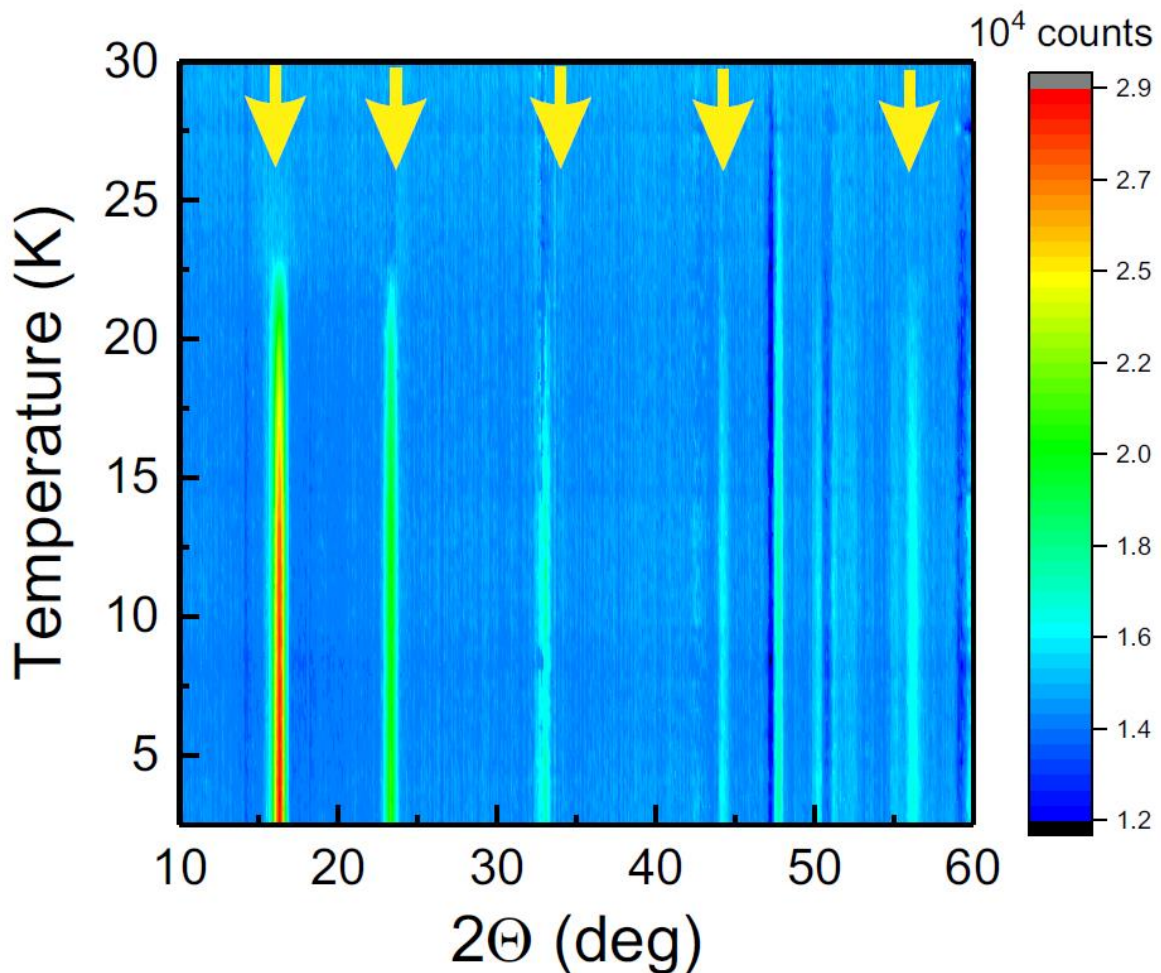


Figure 5-17. Plot of the difference intensity (30 K data set subtracted) versus Bragg angle and temperature of the D20 neutron powder diffraction patterns ($\lambda = 2.424 \text{ \AA}$) highlighting the magnetic Bragg reflections marked by (yellow) vertical arrows. They disappear above ~ 23 K.

Five additional Bragg peaks were identified. They disappear above ~ 23 K. Using the program k-search from the FullProf suite [5-10] and the lattice parameters refined from the diffractometer D20 (ILL) at 1.5 K, nuclear pattern of the magnetic

Bragg reflection could be readily indexed based on the propagation vector ($P-1$ setting of space group no. 2) $(0, 0.5, 0.5)$.

A symmetry analysis using the program Baslreps [5-10] yielded two equivalent one-dimensional irreducible representations with real basis vectors along a , b , and c . A full least-squares refinement of the magnetic structure was done based on the difference pattern $I(1.5\text{ K}) - I(30\text{ K})$ augmented by a constant offset to avoid small negative differences. Figure 5-18 shows the refined difference pattern and Figure 5-19 displays the magnetic structure.

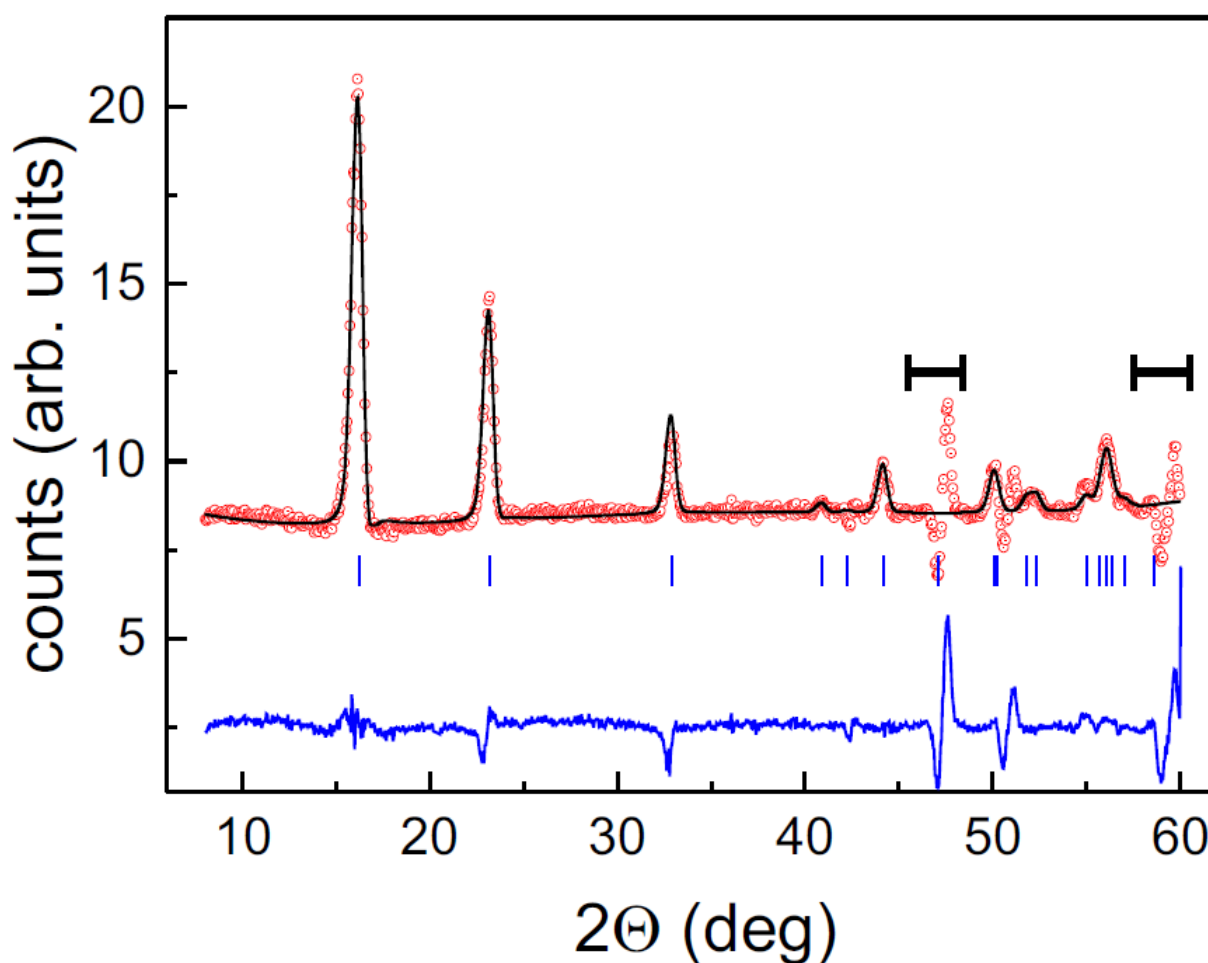


Figure 5-18. Rietveld profile refinement of the difference pattern, $I(1.5\text{ K}) - I(30\text{ K})$. (red) Circles indicate the difference counts $I(1.5\text{ K}) - I(30\text{ K})$, the (black) solid line shows the theoretical pattern calculated using the Bragg angles of the magnetic reflections indicated by the (blue) vertical bars. The (blue) solid line marks the difference between measured and calculated intensity. The two horizontal (black) short bars indicate regions that were excluded in the refinement.

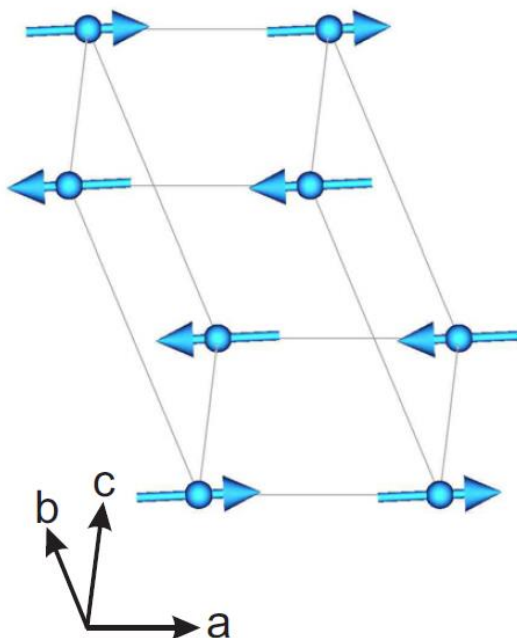


Figure 5-19. Magnetic structure of α - CuV_2O_6 . The moments point essentially along the a -axis (P-1 setting of space group no. 2). A primitive unit cell is outlined.

As already implied by the propagation vector, one finds a doubling of the nuclear cell along b and c . The magnetic moments align essentially along the a -axis with vanishing component along b . The refined components of the ordered moment are:

$$\mu(a) = 0.65(1)\mu_B,$$

$$\mu(b) = 0.0,$$

$$\mu(c) = 0.12(3)\mu_B,$$

and the magnitude of ordered moment amounted to

$$\mu = 0.66(2)\mu_B.$$

Based on one weak magnetic Bragg reflection, Kikuchi *et al.* in 2000 have proposed two possible AFM magnetic structure solutions. [5-2] Their saturation moment for both structures was found close to $0.7 \mu_B$ in good agreement with our results of the DFT calculations and neutron powder diffraction data. My magnetic structure solution based on a total of five magnetic Bragg reflections confirms

Kikuchi *et al.*'s second magnetic structure proposal shown as Figure 9(B) in Ref. [5-2]. The magnetic structure is characterized by parallel alignment of the Cu moments along [100] ($P-1$ setting) i.e. the direction of the shortest Cu - Cu distance. Cu moments in neighboring chains in the $a - b$ plane and moments in neighboring chains along [001] align antiparallel.

This magnetic structure solution is not immediately obvious from the DFT+ U calculations reported above. The total energy of three more magnetic structures (Figure 5-20) was calculated. For these calculations, the size of the chosen test cells has been increased to comprise 32 formula units. The AFM7 configuration corresponds to our best magnetic structure solution. Table 5-8 summarizes the total energies for these three additional test magnetic configurations in addition to the total energies estimated from the exchange parameters listed in Table 5-5.

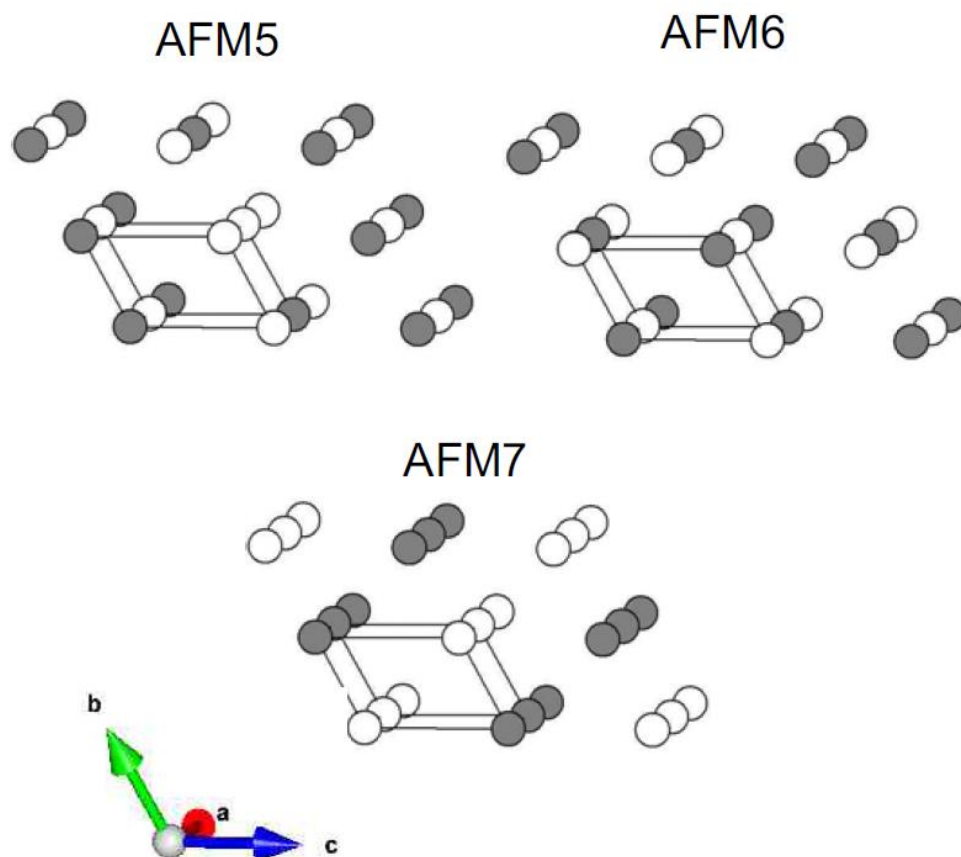


Figure 5-20. Three extra antiferromagnetic spin lattices, AFM5, AFM6, AFM7, used for a consistency check of the DFT+ U results of the spin-exchange parameters listed in Table 5-5. The total energies are summarized in Table 5-8. The configuration AFM7 corresponds to the magnetic structure found from our neutron diffraction data.

Table 5-8. Total energies per eight f.u. (in meV) relative to the ferromagnetic setting for the three extra antiferromagnetic collinear test configurations using $U_{eff} = 4, 5, 6$ eV. The configuration AFM7 corresponds to our best magnetic structure solution. Values in brackets have been calculated using the spin-exchange parameters listed in Table 5-5.

Spin configuration	energy for eight f.u. in meV		
	$U_{eff} = 4\text{eV}$	$U_{eff} = 5\text{eV}$	$U_{eff} = 6\text{eV}$
FM	0	0	0
AFM5	-41.86(-41.28)	-32.99(-32.57)	-25.78(-25.47)
AFM6	-25.37(-25.56)	-19.53(-19.59)	-14.75(-14.68)
AFM7	-57.53(-55.10)	-45.62(-43.82)	-35.91(-34.58)

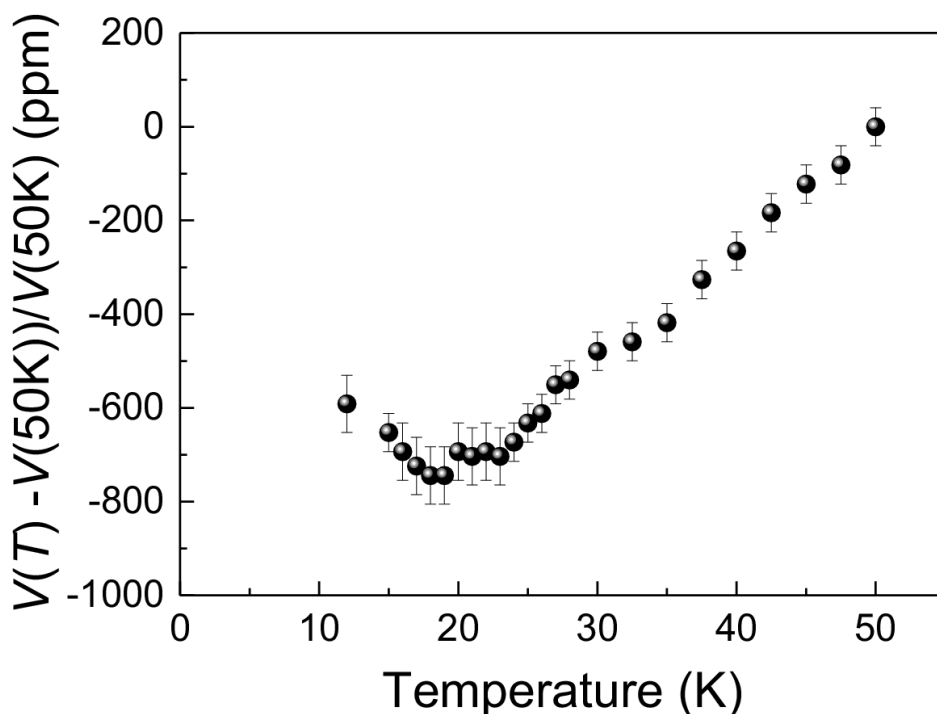


Figure 5-21. Temperature dependence of the unit cell volume relative to its value at 50K.

A series of low-temperature X-ray powder diffraction measurements revealed magnetoelastic distortions associated with AFM long-range ordering. Figures 5-21 and 5-22 display the temperature dependence of the cell volume and the lattice parameters relative to their 50 K values. With decreasing temperature, the cell volume undergoes a contraction but exhibits anomalous behavior with an upturn below ~ 20 K, approximately coinciding with the Néel temperature. The upturn in the cell volume is essentially due to anomalous thermal expansion of the c lattice

parameter, and some slight expansion of the b lattice parameter below ~ 20 K whereas a expands over the whole temperature range and passes through a shallow maximum at ~ 20 K. A broad rounded maximum is also visible for the angle α with a downturn below the Néel temperature whereas the temperature dependence of the angles β and γ remains rather unremarkable.

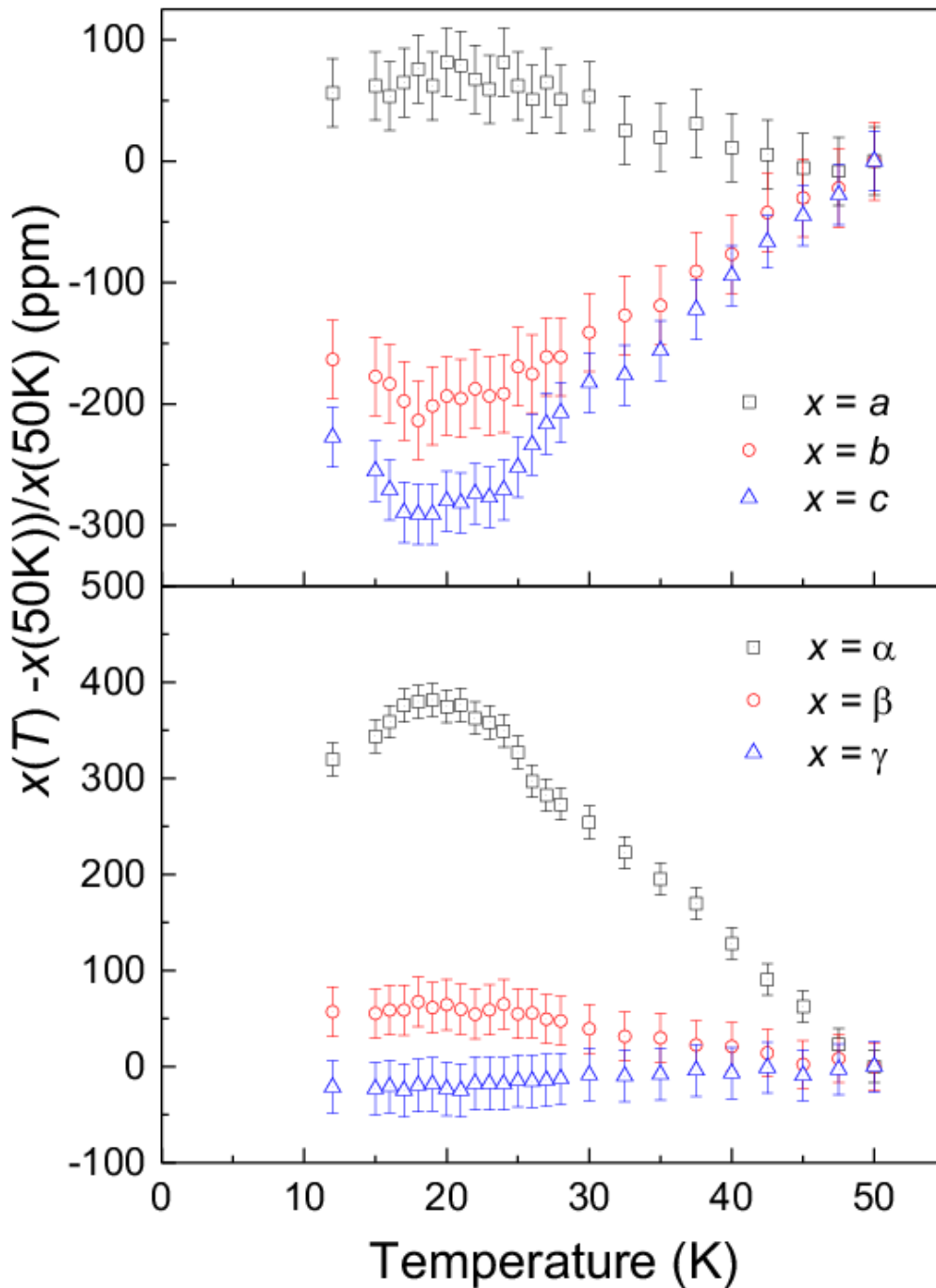


Figure 5-22. Temperature dependence of the lattice parameters relative to their values at 50 K.

5.8. Quantum Monte Carlo calculations ⁶

The magnetic structure determination provides strong support to the results of our DFT+*U* calculations, which suggested an anisotropic 2D model on a square planar spin lattice. This result questions all fits of the magnetic susceptibility data carried out so far, assuming a linear Heisenberg chain with uniform antiferromagnetic nearest-neighbour spin-exchange interaction. [5-1, 5-2, 5-3]

A straightforward analytical relationship for the magnetic susceptibilities of anisotropic spin $S = 1/2$ Heisenberg square lattices is not available in the literature. Therefore Quantum Monte Carlo (QMC) calculations of the magnetic susceptibility and the heat capacity for the anisotropic $S = 1/2$ square lattices as a function of the ratio $\alpha = J_y/J_x$ from $0.5 \leq \alpha \leq 1$ were carried out.

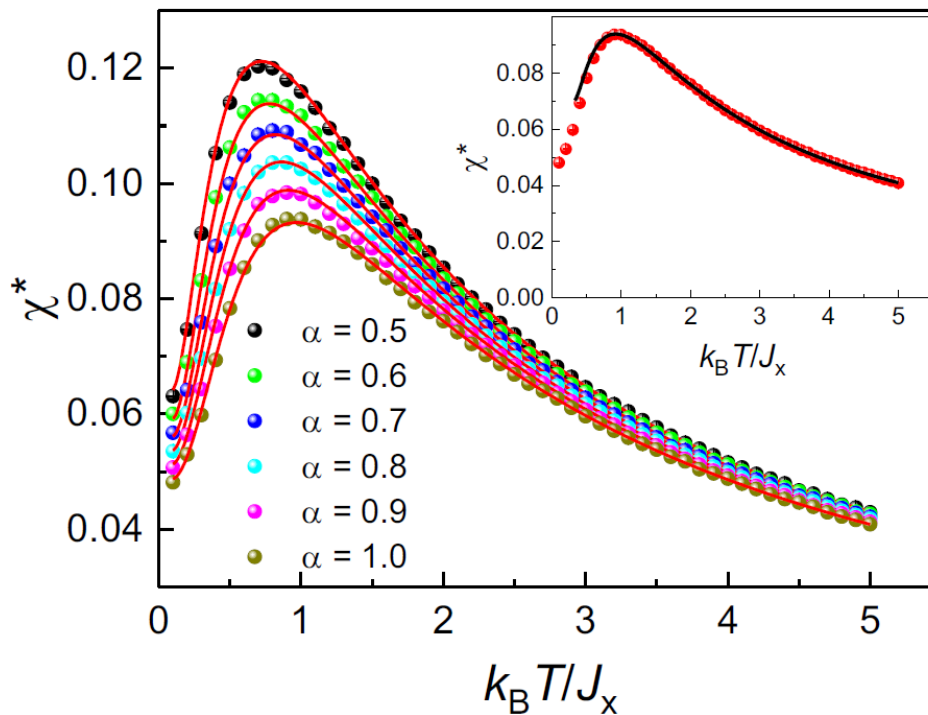


Figure 5-23. Reduced magnetic susceptibility, $\chi^* = \frac{\chi J_x}{N_A g^2 \mu_B^2}$, of the anisotropic square planar Heisenberg lattice with nearest-neighbour spin-exchange interaction, J_x and J_y for ratios $0.5 \leq \alpha = J_y/J_x \leq 1$. The (red) solid lines are fits with a Padé approximant according to Eq.(5-5). The inset shows the comparison of the isotropic ($J_x = J_y$) square planar $S = 1/2$ lattice with Rushbrooke's and Wood's series expansion results. The dots represent the results of Monte Carlo calculations. [5-24]

⁶ The Monte Carlo calculations were carried out by L. Webber in the group of Prof. S. Wessel at the Institute for Theoretical Solid State Physics at RWTH Aachen.

These calculations were based on the stochastic series expansion method with operator-loop updates. [5-25, 5-26, 5-27]

Figure 5-23 represents the results of Monte Carlo calculations *versus* the reduced temperature obtained for six discrete ratios α . They were obtained on systems with $N = L^2$ lattices sites and a linear extend up to $L = 64$. Using the procedure and definitions as detailed in Ref. [5-29] the reduced magnetic susceptibilities (Eq.(5-5)) were approximated by a Padé approximant according to Eqns. (5-4)-(5-9) for each value of α separately.

The reduced magnetic susceptibilities defined according to:

$$\chi^* = \frac{\chi J_x}{N_A g^2 \mu_B^2} \quad (5-4)$$

The Padé approximant fitted to the Monte Carlo results is given by:

$$\chi^* = \frac{1}{4t} P_{(3)}^{(2)}(\alpha, t) \quad (5-5)$$

where:

$$P_{(3)}^{(2)}(\alpha, t) = \frac{\sum_{n=0}^2 \frac{N_n}{t^n}}{\sum_{n=0}^3 \frac{D_n}{t^n}} \quad (5-6)$$

and

$$t = \frac{T}{J_x} \text{ and } \alpha = J_y/J_x \quad (5-7)$$

The Padé coefficients, N_n and D_n are

$$N_0 = D_0 = 1 \quad (5-8)$$

and

$$N_n = \sum_{m=0}^3 N_{nm} \alpha^m \quad (5-9)$$

$$D_n = \sum_{m=0}^3 D_{nm} \alpha^m \quad (5-10)$$

The results for N_{nm} and D_{nm} are compiled in Table 5-9.

Table 5-9. Coefficients of the polynomial in α acc. to Eqns. (5-9) and (5-10) used to calculate the Padé coefficients in Eq. (5-6).

n	N_{n0}	N_{n1}	N_{n2}	N_{n1}
1	0.42517227	-1.94996503	2.45481936	-1.01710032
2	-0.00672101	0.04844110	0.05435803	0
n	D_{n0}	D_{n1}	D_{n2}	D_{n1}
1	0.39562457	0.56572425	0	0
2	0.32766975	0.28347657	-1.01436893	0.68899462
3	0	-0.07080594	0.53091006	0

From performing a finite-size analysis, it was shown that these results represent the thermodynamic limit behavior.

In order to fit the experimental susceptibilities, the Padé coefficients of Table 5-9 were fitted to polynomial of up to the 4th degree. This polynomial allows a continuous variation of the susceptibilities on the anisotropy parameter α .

Figure 5-24 represents the magnetic susceptibilities of a crystal of α -CuV₂O₆ measured with a field of 0.1 Tesla applied along the crystal needle (a -axis in P-1 setting) and a fit of the magnetic susceptibility to the prediction of an anisotropic Heisenberg-type square lattice. To get a good agreement with an experiment, in addition to the ratio α and the g -factor, weak inter-planar exchange interactions, J_{inter} , were taken into account by a mean field approach according to

$$\chi^*(\alpha, g, T) = \frac{\chi_{sq}(\alpha, g, T)}{1 + \chi_{sq}(\alpha, g, T) \frac{z_{inter} J_{inter}}{N_A g^2 \mu_B^2}}, \quad (5-11)$$

where:

z_{inter} is the number of neighboring moments seen by a Cu moment in an adjacent plane;

J_{inter} represents the spin-exchange interaction between planes;

N_A is the Avogadro's constant. [5-29]

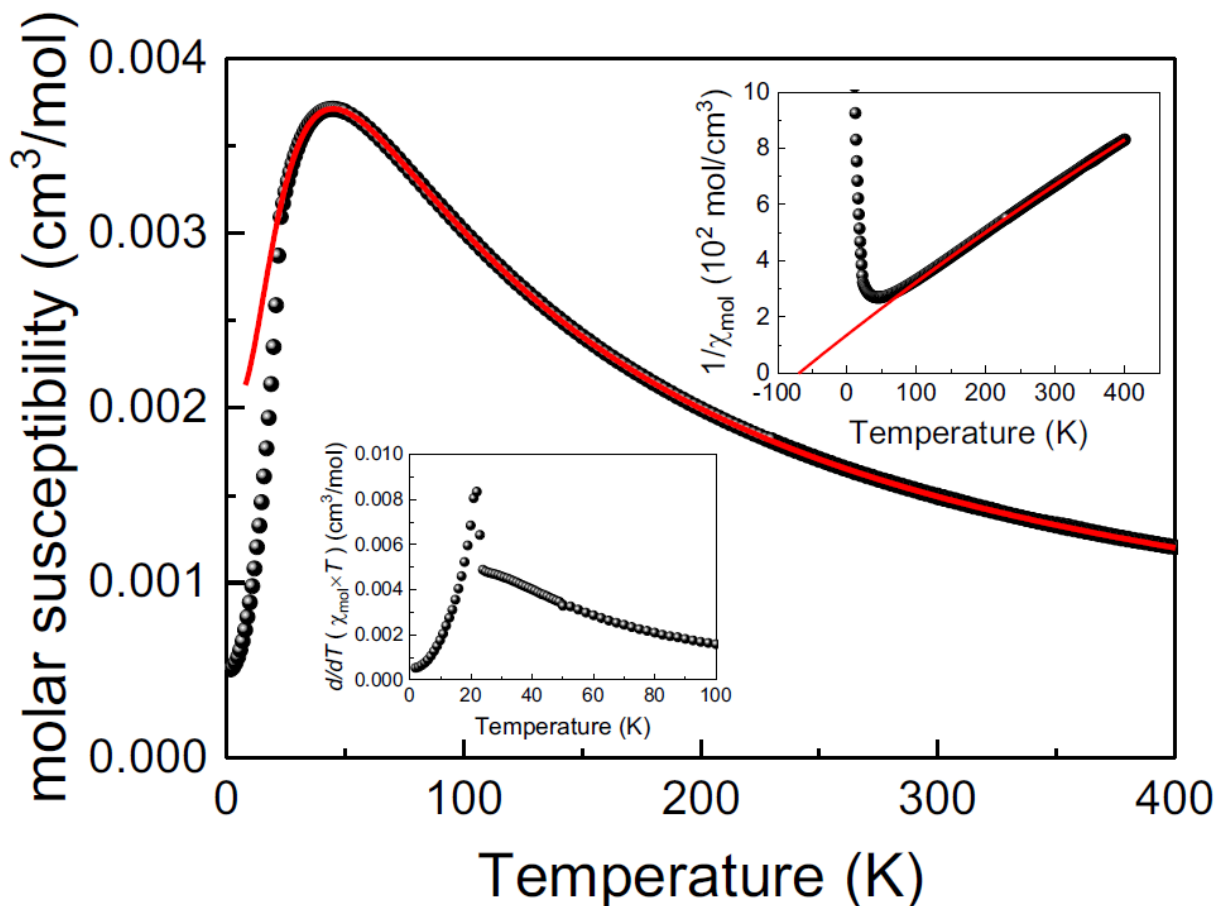


Figure 5-24. Magnetic susceptibility of a crystal of α - CuV_2O_6 measured with a field of 0.1 Tesla applied parallel to the crystal needle (a-axis in P-1 setting). The (red) solid line is a fit of the magnetic susceptibilities ($T \geq 30$ K) to the prediction of an anisotropic Heisenberg-type square lattice with parameters indicated in the text. The upper inset displays the inverse susceptibility with a fit to a Curie-Weiss law ($T \geq 30$ K) indicating a Curie-Weiss temperature of $-70(2)$ K. The lower inset shows 'Fisher's heat capacity' obtained by taking the derivative with respect to temperature of the quantity $\chi_{\text{mol}} \times T$ showing the ordering peak at $22.2(1)$ K.

The inter-planar spin-exchange product $z_{\text{inter}}J_{\text{inter}}$ represents an effective inter-planar coupling strength. Positive $z_{\text{inter}}J_{\text{inter}}$ is pointing to predominant AFM spin-exchange coupling between the planes.

$$z_{\text{inter}}J_{\text{inter}} = 2.9(1)\text{K}.$$

It is comparable to the inter-planar spin-exchange parameters J_1 and J_3 obtained from the DFT calculations (see Table 5-5).

Finally the experimental susceptibility data were fitted against

$$\chi_{mol}(T) = (1 - \chi_{imp})\chi^*(\alpha, g, T) + \frac{\chi_{imp}C_{imp}}{T - \Theta} + \chi_0, \quad (5-12)$$

where:

$(1 - \chi_{imp})\chi^*(\alpha, g, T)$ represents the susceptibility of the anisotropic square planar model including inter-planar coupling;

$\frac{\chi_{imp}C_{imp}}{T - \Theta}$ represents the susceptibility of paramagnetic impurities;

χ_0 is the temperature independent susceptibility.

The temperature independent susceptibility takes care of the diamagnetic contributions from the electrons in the closed shells and a van Vleck contribution.

The diamagnetic contribution can be estimated from for the respective elements in their appropriate oxidation state using tabulated increments and for CuV_2O_6 it amounts to $-91 \times 10^{-6} \text{ cm}^3/\text{mol}$. [5-30]

The van Vleck contribution for Cu^{2+} cations depends on the direction of the magnetic field with respect to the crystal axes and amounts to about $+100 \div +120 \times 10^{-6} \text{ cm}^3/\text{mol}$ and thus often overcompensates the negative diamagnetic contribution. [5-31]

The temperature independent susceptibility contribution was refined to

$$\chi_0 = 130(2) \times 10^{-6} \text{ cm}^3/\text{mol}.$$

The fit of the crystal susceptibilities with the developed Padé approximant converged to an anisotropy ratio $\alpha_{padé} \approx 0.7$, confirming nicely the DFT+*U* results. It also strongly support the description of $\alpha\text{-CuV}_2\text{O}_6$ in form of a 2D anisotropic $S=1/2$ AFM Heisenberg system.

5.9. Electron paramagnetic resonance

During the fitting procedure of the magnetic susceptibilities, it was found indispensable to reduce the number of free parameters. Especially the g -factor turned out to be critical to obtain meaningful results. In order to determine the g -factor, a series of angular and temperature dependent electron paramagnetic resonance (EPR) measurements on the same single crystal used for the anisotropic susceptibility measurements (see Figure 5-11) were performed. The spectra were collected with a Bruker X-band ($\nu = 9.4803\text{GHz}$) spectrometer with an EMX premiumX bridge and ERC73 electromagnet. Symmetric ESR resonance lines were observed and analyzed by fitting a Lorentzian absorption line. Figure 5-25 shows the angular dependence of the g -factor when the needle-shaped crystal was rotated around [011] in the plane of the external field. This orientation allows to measure g -factors, parallel ($g_{||}$) and perpendicular (g_{\perp}) to [011] (see Figure 5-25).

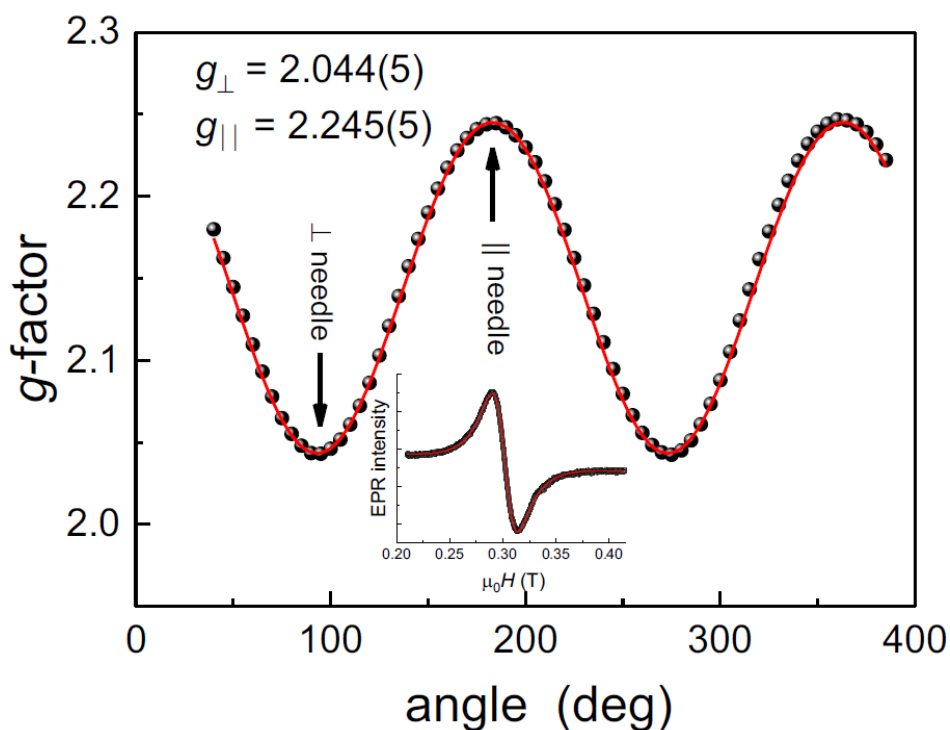


Figure 5-25. Angular dependence of the g -factor of an $\alpha\text{-CuV}_2\text{O}_6$ needle-shaped crystal at room temperature. The crystal was oriented such that the needle direction could be aligned along the external field. The spectra were collected at a microwave frequency of 9.4803 GHz. The insert displays a typical EPR spectrum (dots). The red solid line represents a fit with a Lorentzian absorption line.

The angular dependence of the g -factor was fitted to the general angular dependence of the g -factor for an axial system given by [5-21]

$$g^2(\varphi) = g_{[100]}^2 \cos^2(\varphi - \varphi_0) + g_{\perp[011]}^2 \sin^2(\varphi - \varphi_0), \quad (5-13)$$

where

φ is the angle between the external field and the direction of the principal axes

φ_0 is a phase factor.

The g -factor along [100] (in P -1 setting) was determined to be

$$g_{[100]} = 2.243(4).$$

The g -factors are in the range of what is typically found for Cu^{2+} spin $S = 1/2$ systems in an elongated octahedral environment. [5-21] A slight decrease less than 0.13% of $g_{[100]}$ is observed between room temperature and the Néel temperature. The linewidth of the EPR resonance line exhibits a critical divergence very close to the Néel temperature (see inset Figure 5-26).

Using $g_{[100]}$ restricted to 2.297(2), close to the value observed in the ESR experiments, experimental magnetic susceptibility measured with the magnetic field applied along the needle (see Figure 5-11) was fitted. Following parameters for J_x and the ratio α were obtained:

$$J_x = 54.6(5)\text{K}$$

$$\alpha = J_y/J_x = 0.71(1)$$

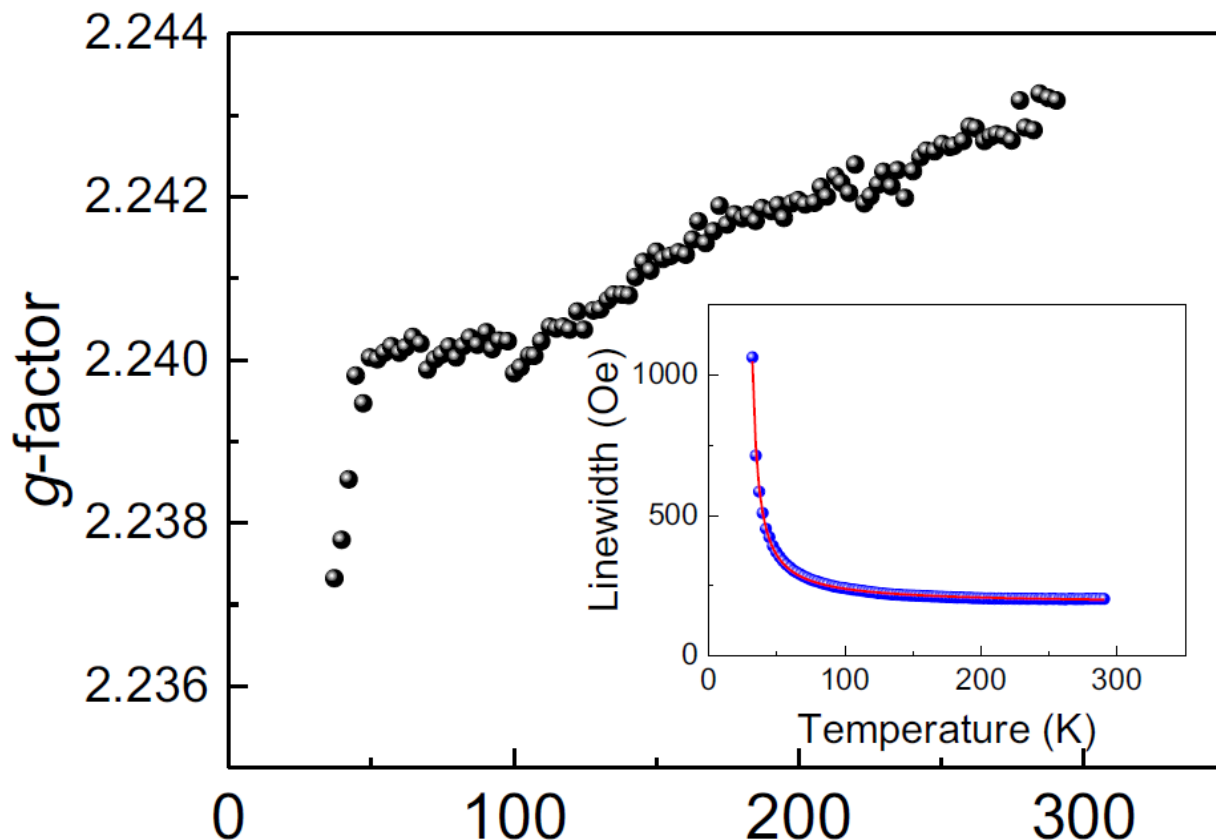


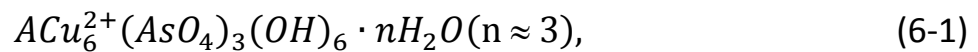
Figure 5-26. Temperature of the g -factor of $\alpha\text{-CuV}_2\text{O}_6$ measured at a microwave frequency of 9.4803 GHz with the external magnetic field along the needle axis (a-axis in P-1 setting). The inset displays the temperature dependence of the EPR linewidth (FWHM). The (red) solid line is a fit of the temperature dependence with $\Delta H \propto 1/(T - T^*) + \Delta H^\infty$ with $T^* = 27.6(2)$ K and $\Delta H^\infty = 185(1)$ Oe.

6. Rare-earth mixite and agardite minerals⁷

6.1. Introduction

Recently, in the scope of low-dimensional quantum magnets, several Cu^{2+} natural minerals like azurite, malachite, green, and black diopside, to name a few, attracted attention in search for systems with unusual magnetic ground states. [6-1] The immediate advantage of natural mineral samples is that very often large and well grown crystals are readily and cheaply available. However, increasingly systems have been investigated with more complex crystal structures. Moreover, they often contain several magnetic entities in different crystallographic positions hampering sample characterization, e.g. of the magnetic and thermal bulk properties. In addition, these minerals often contain crystal water molecules or also hydroxyl groups with hydrogen bonds leaving an assignment of the relevant spin exchange pathways sometimes highly difficult. [6-2]

Mixite and agardite form a group of copper rare-earth minerals with the chemical composition:



where:

A is a trivalent rare-earth cation.

Depending on the trivalent cation A, these minerals have different names, referring to the mineralogist who first described them. In this work, the following systems were studied:

- Mixite with the composition $\text{BiCu}_6(\text{OH})_6(\text{AsO}_4)_3 \cdot n\text{H}_2\text{O} (n \approx 3)$,
- Goudeyite with the composition $\text{YCu}_6(\text{OH})_6(\text{AsO}_4)_3 \cdot n\text{H}_2\text{O} (n \approx 3)$,
- La-Agardite with the composition $\text{LaCu}_6(\text{OH})_6(\text{AsO}_4)_3 \cdot n\text{H}_2\text{O} (n \approx 3)$,

⁷ This work has been published in ZAAC 644(24), 1782-1790 (2018) DOI: 10.1002/zaac.201800344 and Zeitschrift für Naturforschung B, Zeitschrift für Naturforschung B, Volume 75, Issue 1-2, 191–199

- Lu-Agardite with the composition $\text{LuCu}_6(\text{OH})_6(\text{AsO}_4)_3 \cdot n\text{H}_2\text{O}$ ($n \approx 3$).

Mixites and agardite minerals crystallize with a zeolite-type structure (see Figure 6-1) with a honeycomb arrangement of rings composed of six CuO_4 ribbon chains which are interconnected by slightly distorted $(\text{AsO}_4)^{3-}$ tetrahedra (see Figure 6-2) to form regular ‘six-rings’. Cu in these compounds is divalent with one hole in the $3d$ shell ($3d^9$ configuration) with a spin $S=1/2$ magnetic moment. The pronounced one-dimensional character of the crystal structure suggests that low-dimensional quantum magnetic properties with extended short-range correlation regimes may be observed.

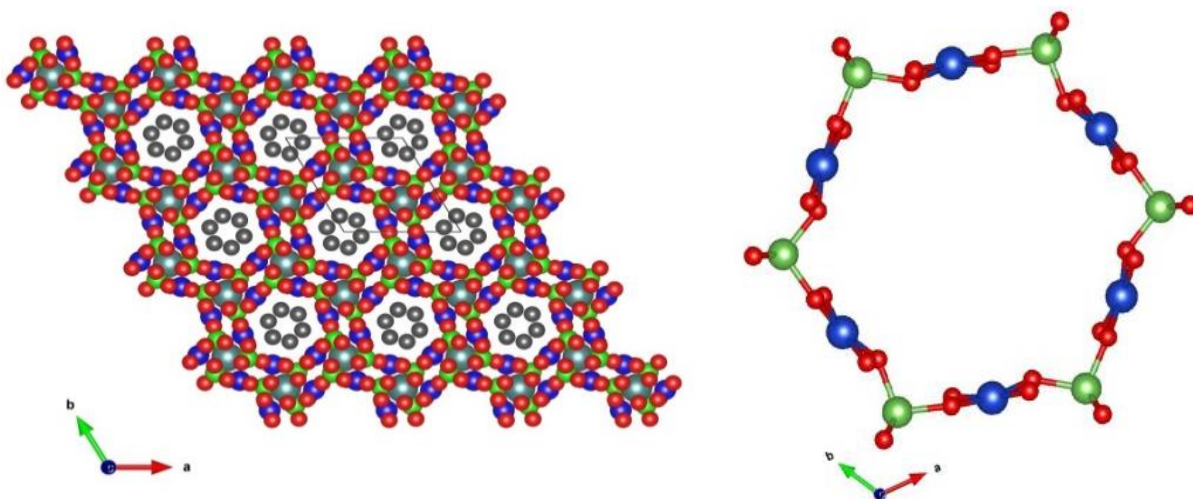


Figure 6-1. Crystal structure of mixite (space group $P6_3/m$ (no. 176)) projected along $[0001]$. The blue, green and grey spheres represent the Cu, As and A atoms, respectively. Red and black spheres depict oxygen atoms. The (black) O atoms in the zeolite-type channels represent the oxygen atoms of the 3 water molecules. They have been placed at Wyckoff position 6h ($x, y, \frac{1}{4}$) and but also be located at two neighboring partially occupied positions. [6-3]

In CuO_4 ribbon chains (see Figure 6-2), nearest-neighbor spin-exchange interaction takes place via $\text{Cu} - \text{O} - \text{Cu}$ bonds with bridging angles close to 90° . This configuration often results in small ferromagnetic or antiferromagnetic spin-exchange to the nearest-neighbors. With nearest-neighbor exchange being small or even negligible, next-nearest neighbor spin-exchange becomes important or even dominant. Irrespective of the sign of the nearest-neighbor spin-exchange, the inherent magnetic frustration in such so-called J_1 - J_2 chains often order with

incommensurate helicoidal ground states [6-4, 6-5, 6-6, 6-7, 6-8] including type-II multiferroicity. [6-9, 6-10, 6-11, 6-12]

Lately, Mourigal *et al.* and Orlova *et al.* demonstrated that in J_1 - J_2 chains, exposed to a magnetic field, bond or spin nematic behavior can be observed. [6-13, 6-14]

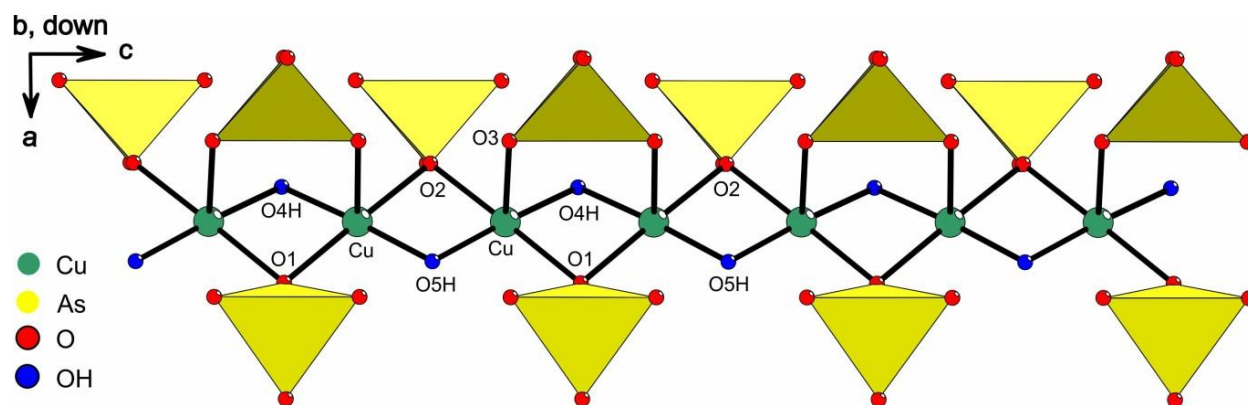


Figure 6-2. Chain of edge-sharing CuO_5 square-pyramids with the $(\text{AsO}_4)^{3-}$ groups attached to oxygen atoms O1, O2, and O3, as indicated. Due to the 6_3 screw symmetry operation, the As atoms (Wyckoff site 6h, $z_{\text{As}} = \frac{1}{4}$) connect only to every second oxygen atom along the chains. Cu, As, O, and O (of OH) atoms are depicted by green, yellow, red and blue spheres, respectively.

The crystal structure of natural mixite $(\text{Bi}, \text{Ca})\text{Cu}_6(\text{OH})_6(\text{AsO}_4)_3 \cdot n\text{H}_2\text{O}$ ($n \approx 3$) was initially determined by Mereiter and Preisinger. [6-3] They detected a mixed occupation of the trivalent site with Bi and Ca atoms in a ratio of 0.66 to 0.34. The honeycomb arrangement of rings composed of six CuO_4 ribbons interconnected by $(\text{AsO}_4)^{3-}$ anions form infinite channels which can accommodate up to three 'zeolite'-type water molecules. The water molecules were found to be highly disordered. The crystal structure of synthetic mixite $\text{BiCu}_6(\text{OH})_6(\text{AsO}_4)_3 \cdot 3\text{H}_2\text{O}$ was refined from single-crystal data by Miletic, Zemann and Nowak in 1997. [6-15] Synthetic goudeyite where the trivalent site is occupied by Y^{3+} was studied by Aruga and Nakai in 1985. [6-16] The Bi/Ca or the Y atoms and the Cu and As atoms occupy single Wyckoff sites in the crystal structure. For the oxygen atoms of the water molecules in the hexagonal tube, a total of five partially occupied sites were refined. Frost *et al.* [6-17] have synthesized and investigated $\text{RECu}_6(\text{OH})_6(\text{AsO}_4)_3 \cdot n\text{H}_2\text{O}$ ($\text{RE} = \text{Y}, \text{La}, \text{Ce}, \text{Pr}, \text{Sm}, \text{Eu}; n \approx 3$) samples by Raman spectroscopy and determined the lattice parameters by the X-ray powder diffraction. They reported a linear correlation of the lattice parameter a on the

ionic radii of the *RE* elements with a variation from Y to La of about 1.1%. The dependence of the *c* lattice parameters on the ionic radii was less clearly pronounced.

6.2. Preparation

Polycrystalline samples of natural mixite were separated from mineral specimens from various sources (Wittichen, Germany, Jáchymov, Czech Republic)⁸. The samples were rinsed in demineralized water and dried in ambient air.

Polycrystalline samples with of $RECu_6(OH)_6(AsO_4)_3 \cdot nH_2O$ (RE = Y, Bi, La, Lu; $n \approx 3$) were prepared following the recipes described in literature. [6-15, 6-18]

Stoichiometric mixtures of $RE(NO_3)_3 \cdot mH_2O$ ($3.5 < m < 6$), $Cu(NO_3)_2 \cdot 2.5H_2O$ and $Na_2HAsO_4 \cdot 7H_2O$ (all from Alfa Aesar; purity 99.99% or better) were dissolved in demineralized water and precipitated by slowly dripping in 1 molar NaOH while stirring until completion of the reaction. The fluffy precipitates were rinsed repeatedly in demineralized water and dried in ambient conditions. X-ray diffraction patterns collected on such powders showed a diffuse broad background but no coherent Bragg reflections. In order to improve the crystallinity, the precipitates were stirred into 10 ml demineralized water and filled into a Teflon lined stainless steel autoclave and heated up to 175 °C for two days. Adjusting the pH to ~8.5, before the autoclave treatment, gave the best results and low amounts of impurity phases.

⁸ Some of the natural mixite samples were kindly provided by Franz X. Schmidt from the Staatliches Museum für Naturkunde (Rosenstein 1, 70191 Stuttgart, Germany)

6.3. Sample characterization

Figure 6-3 displays a SEM picture of a piece of the natural mixite separated from the sample originated from Wittichen mine. Mixite has a fibrous morphology. As previously reported by Frost *et al.* for natural mixite samples from other sources, the fibers are several hundred μm long and up to $5\ \mu\text{m}$ wide. [6-19]

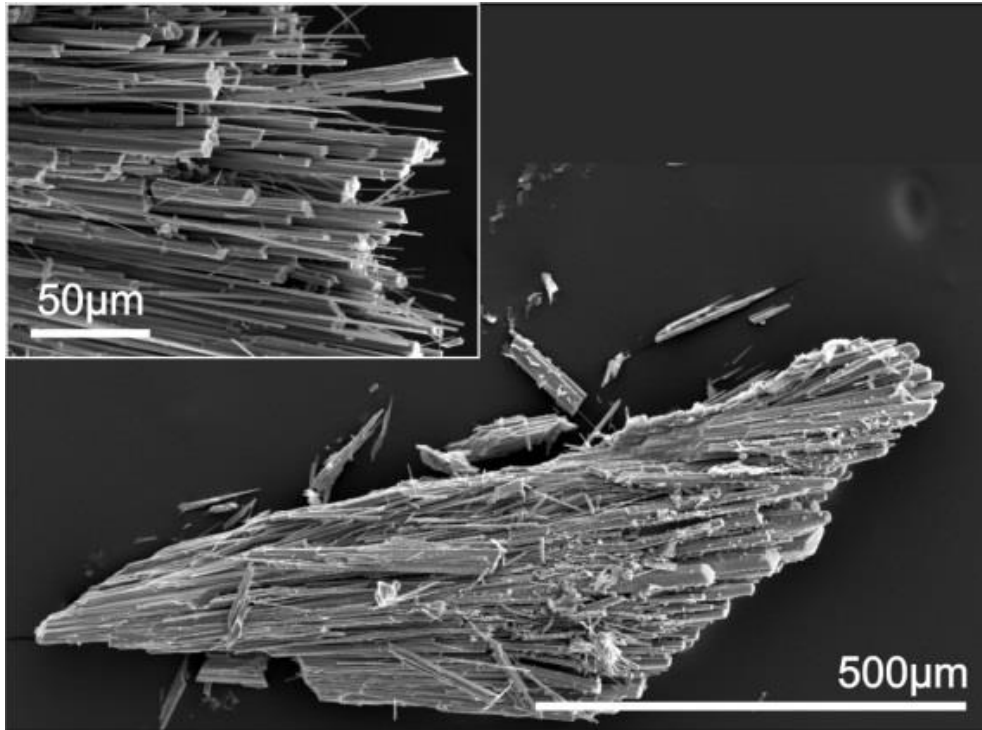


Figure 6-3. SEM image of a piece of natural mixite sample from Wittichen

Energy dispersive X-ray (EDX) microprobe analysis was done to determinate the chemical composition of the natural samples. Figure 6-4 shows an EDX spectrum of natural mixite sample (Wittichen) revealing that besides the expected elements Bi, Ca, Cu, As and O, the sample contains also traces of Si. These can be ascribed to an impurity barite and quartz base material the crystals grow upon. The sample from Jáchymov contains substantial amounts of Fe and therefore was discarded from the subsequent magnetic characterization.

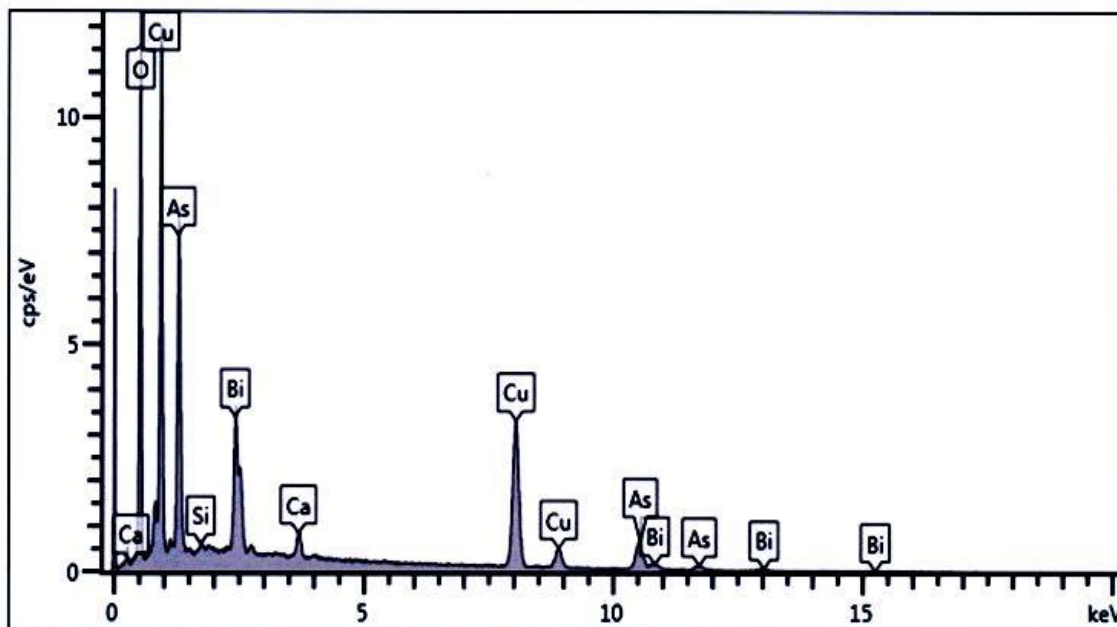


Figure 6-4. EDX spectrum of our natural mixite sample originating from Wittichen.

Table 6-1 summarizes the results of the EDX analysis averaged over five independently collected spectra collected from the Jáchymov and the Wittichen samples.

Table 6-1. Results of the EDX analysis (in atom %) of the Wittichen mixite sample no. 2. The expected values have been calculated from the ideal composition $\text{BiCu}_6(\text{OH})_6(\text{AsO}_4)_3 \cdot 3\text{H}_2\text{O}$.

Element	expected	Jáchymov	Wittichen
Bi	3.23	2.46 ± 0.08	2.42 ± 0.21
Ca	-	0.56 ± 0.03	1.21 ± 0.16
Cu	19.35	20.78 ± 0.44	19.02 ± 1.84
As	9.68	8.25 ± 0.13	10.90 ± 0.20
Si	-	0.90 ± 0.26	0.35 ± 0.27
Fe	-	0.24 ± 0.10	-
P	-	1.40 ± 0.03	-
O	67.74	65.05 ± 0.48	66.1 ± 2.2

The composition of the Wittichen natural mixite sample amounts to $\text{Bi}_{0.76\pm 0.07}\text{Ca}_{0.38\pm 0.05}\text{Cu}_6\text{As}_{3.44\pm 0.06}\text{O}_{20.85\pm 0.70}\text{Si}_{0.11\pm 0.08}$ which is in good agreement with the expected values, except for the As content which is about 10% larger than expected.

All samples (except the sample from Jáchymov) were investigated for its phase purity by X-ray powder diffraction using Mo $K_{\alpha 1}$ radiation ($\lambda = 70.9300$ pm). In Figure 6-5, the diffraction patterns are shown in comparison with the results of the Rietveld profile refinements of the diffraction patterns. The refined lattice parameters are compiled in Table 6-2. [6-15, 6-16, 6-18]

Table 6-2. Room-temperature lattice parameters of the samples under investigation in comparison to literature data (space group P63/m, no. 176)

sample	Composition	$a, b/\text{pm}$	c/pm	reference
Wittichen mixite	$(\text{Bi,Ca})\text{Cu}_6(\text{OH})_6(\text{AsO}_4)_3 \cdot 3\text{H}_2\text{O}$	1362.970(9)	592.077(7)	this work
synthetic mixite	$\text{BiCu}_6(\text{OH})_6(\text{AsO}_4)_3 \cdot 3\text{H}_2\text{O}$	1362.794(19)	592.221(12)	this work
goudeyite	$\text{YCu}_6(\text{OH})_6(\text{AsO}_4)_3 \cdot 3\text{H}_2\text{O}$	1353.128(17)	588.176(11)	this work
goudeyite	$\text{YCu}_6(\text{OH})_6(\text{AsO}_4)_3 \cdot 3\text{H}_2\text{O}$	1358.3(2)	589.5(1)	Aruga [6-16]
synthetic mixite	$\text{BiCu}_6(\text{OH})_6(\text{AsO}_4)_3 \cdot 3\text{H}_2\text{O}$	1363.3(2)	591.3(2)	Miletich [6-15]

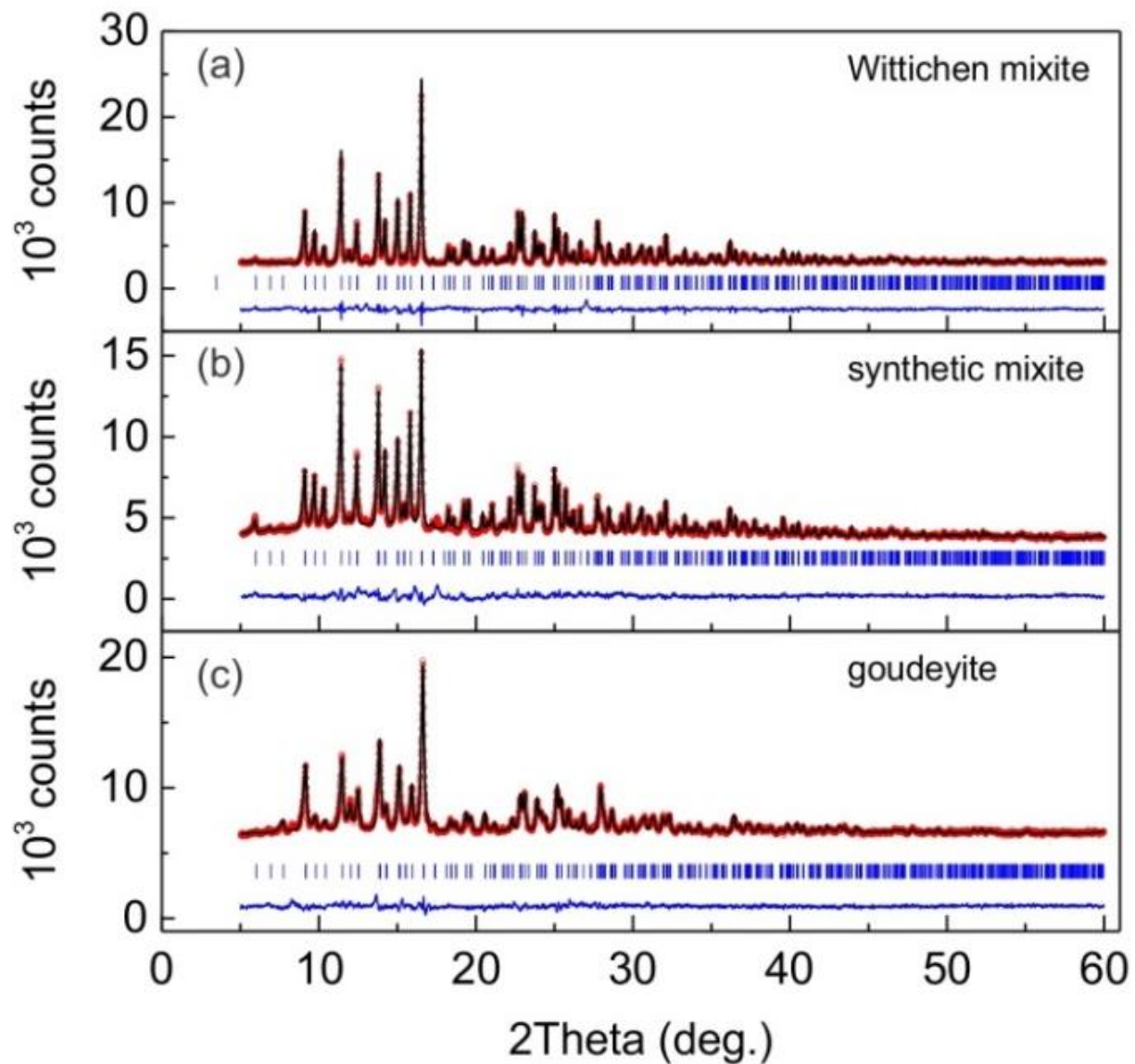


Figure 6-5. X-ray powder diffraction patterns (red circles) of mixite and goudeyite Mo $K_{\alpha 1}$ radiation ($\lambda = 70.9300$ pm) plotted in comparison with the patterns obtained from the Rietveld profile refinement (black solid line). The differences are shown in the lower part by the blue solid lines. The positions of the Bragg reflections used to simulate the patterns are indicated by the blue vertical bars in the lower part of the figure.

Figure 6-6 shows the X-ray diffraction patterns of $RECu_6(OH)_6(AsO_4)_3 \cdot nH_2O$ ($RE = Y, La, Lu; n \approx 3$) together with the Rietveld refinement starting from the atom positional parameters listed by Mereiter et al. [6-3] For goudeyite $YCu_6(OH)_6(AsO_4)_3 \cdot nH_2O$ ($n \approx 3$) the Rietveld refinement assured phase purity, whereas for $RECu_6(OH)_6(AsO_4)_3 \cdot nH_2O$ ($RE = La, Lu; n \approx 3$) impurity Bragg reflections were detected. For La- Agardite, they can be attributed to a 5.1% weight fraction of the CuO ($C 2/c$, Ref. [6-20]). And for Lu- Agardite, these impurities are a 1.9% weight fraction of the CuO and an 11.5% weight fraction of the $LuAsO_4$ ($ZrSiO_4$ structure type, Ref. [6-21]).

Tables 6-3 and 6-4 compile the lattice parameters and the positional parameters of the Cu and As atoms, at the Wyckoff position 12i and 6h, respectively. The RE atoms at Wyckoff position 2d with coordinates $2/3, 1/3, 3/4$ are coordinated by a tri-capped trigonal prism with a 6+3 oxygen coordination (as shown in Figure 6-7).

Table 6-3. Lattice parameters and cell volumes of $RECu_6(OH)_6(AsO_4)_3 \cdot nH_2O$ ($RE = Y, La, Lu; n \approx 3$)

RE	$a(\text{\AA})$	$c(\text{\AA})$	$V_{\text{cell}}(\text{\AA}^3)$
Y	13.5313(2)	5.8818(1)	932.653(24)
La	13.7069(1)	5.9545(1)	968.853(15)
Lu	13.5058(2)	5.8608(1)	925.817(30)

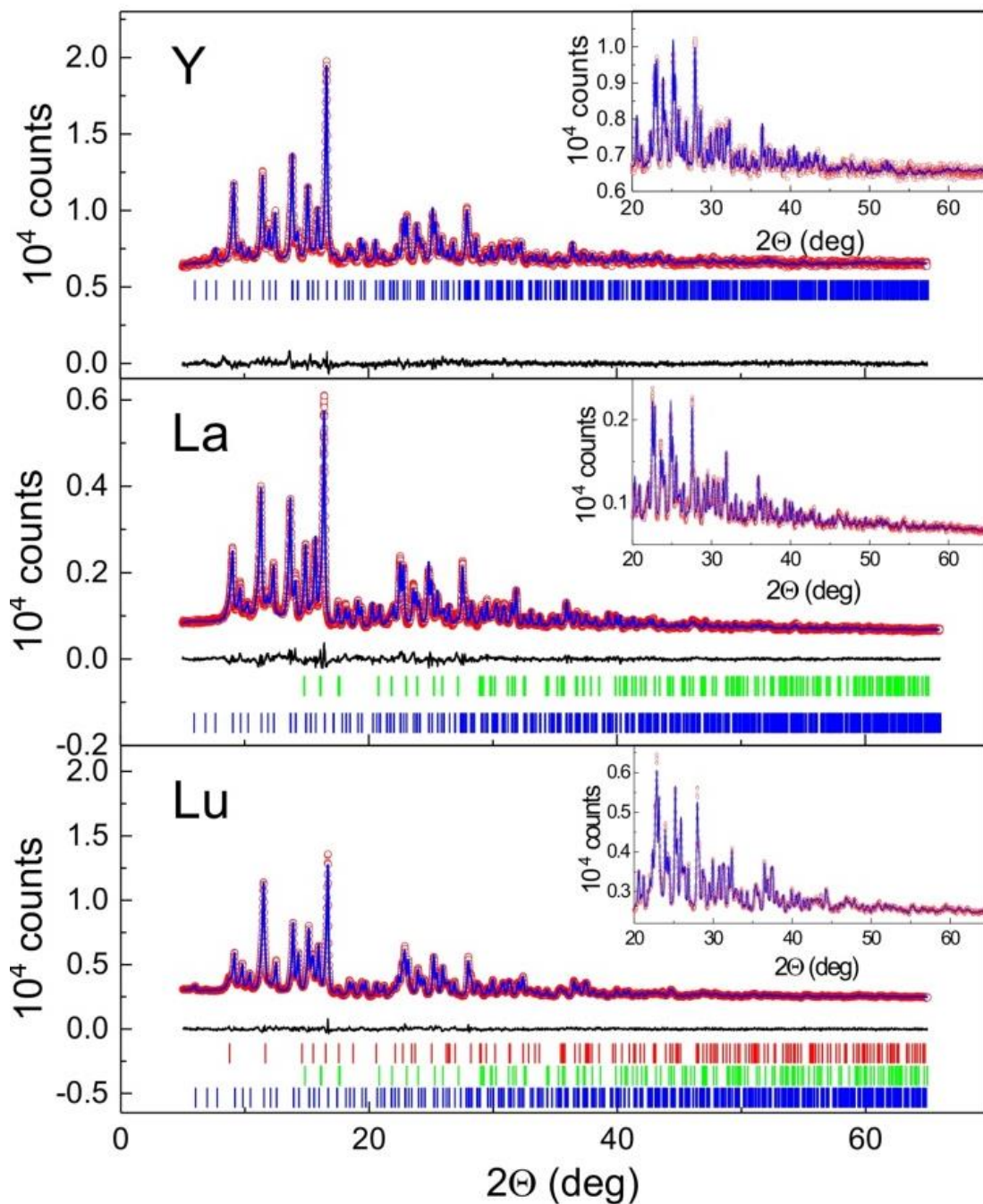


Figure 6-6. X-ray diffraction patterns of $RECu_6(OH)_6(AsO_4)_3 \cdot nH_2O$ ($RE = Y, La, Lu; n \approx 3$), from top to bottom. The red dots mark the measured counts, the (blue) solid lines the results of the Rietveld refinement. The (black) solid lines underneath represent the differences between measured and calculated pattern. The vertical bars mark the Bragg angles of the reflections used to simulate the pattern. The (blue) bars relate to the phases $RECu_6(OH)_6(AsO_4)_3 \cdot nH_2O$ ($RE = Y, La, Lu; n \approx 3$); the green and red vertical bars mark the Bragg positions of CuO and $LuAsO_4$ impurity phases (for more details see text). The insets display the high-angle regions in an enlarged scale.

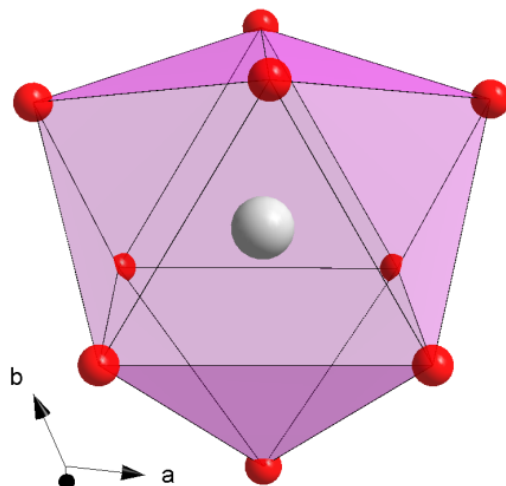


Figure 6-7. Tri-capped trigonal prism oxygen atom coordination of the RE atoms in $RECu_6(OH)_6(AsO_4)_3 \cdot nH_2O$ ($RE = Y, La, Lu; n \approx 3$). The red spheres represent the oxygen atoms, the RE atoms are shown by the light grey spheres.

The lattice parameters and the cell volume exhibit a continuous decrease from La via Y to Lu which mirrors the ionic radii of the RE ions. Whereas for the a lattice parameter a clear linear dependence on the ionic radius [6-22] is observed, c deviates noticeably from a linear dependence for small ionic radii i.e. for $LuCu_6(OH)_6(AsO_4)_3 \cdot 3H_2O$ (see Figure 6-8).

Table 6-4. positional parameters of the Cu and As atoms of $RECu_6(OH)_6(AsO_4)_3 \cdot nH_2O$ ($RE = Y, La, Lu; n \approx 3$)

RE	Cu			As		
	x	y	z	x	y	z
Y	0.41016(20)	0.09434(18)	0.49931(60)	0.65285(30)	0.15190(26)	1/4
La	0.41103(12)	0.09908(12)	0.50101(29)	0.65393(21)	0.14585(19)	1/4
Lu	0.41328(45)	0.09533(42)	0.51087(98)	0.64258(6)	0.14665(52)	1/4

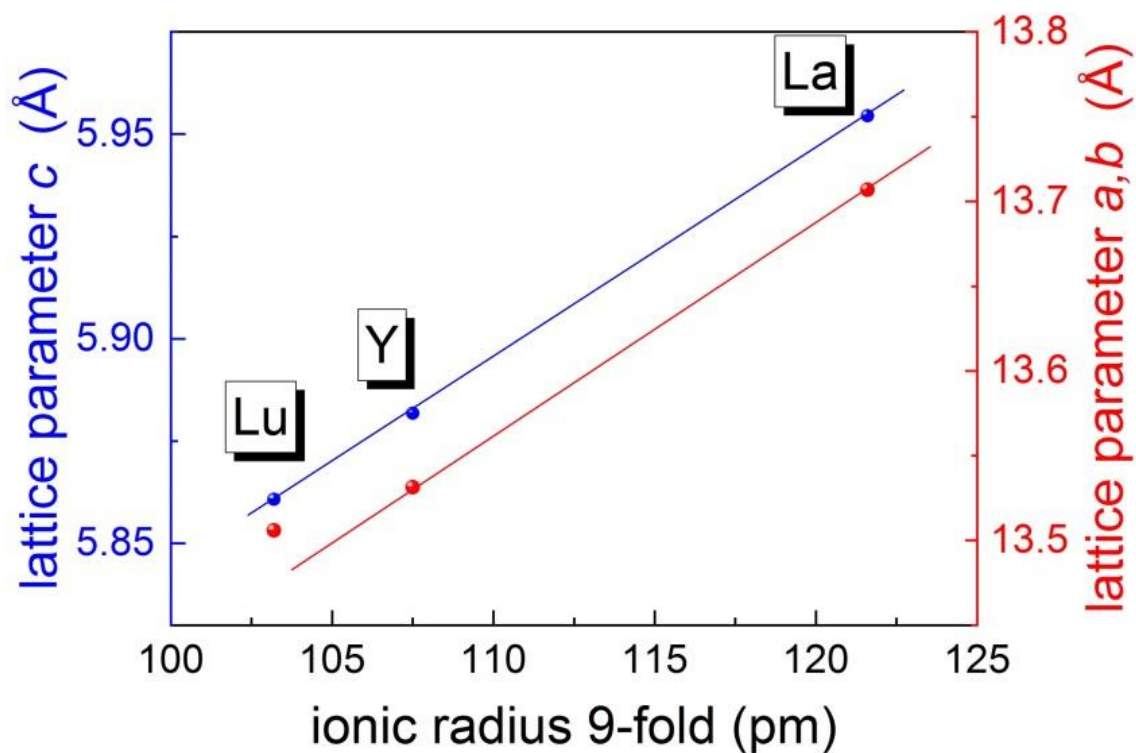


Figure 6-8. Lattice parameters of $RECu_6(OH)_6(AsO_4)_3 \cdot nH_2O$ ($RE = Y, La, Lu; n \approx 3$) as a function of the ionic radii of the RE ions in a 9-fold coordination (from [6-22]).

The Cu – O – Cu bonding angles relevant for sign and magnitude of the spin-exchange in and between the ribbon chains (see Figure 6-2) also varies with the ionic radius of the RE species (see Figure 6-9).

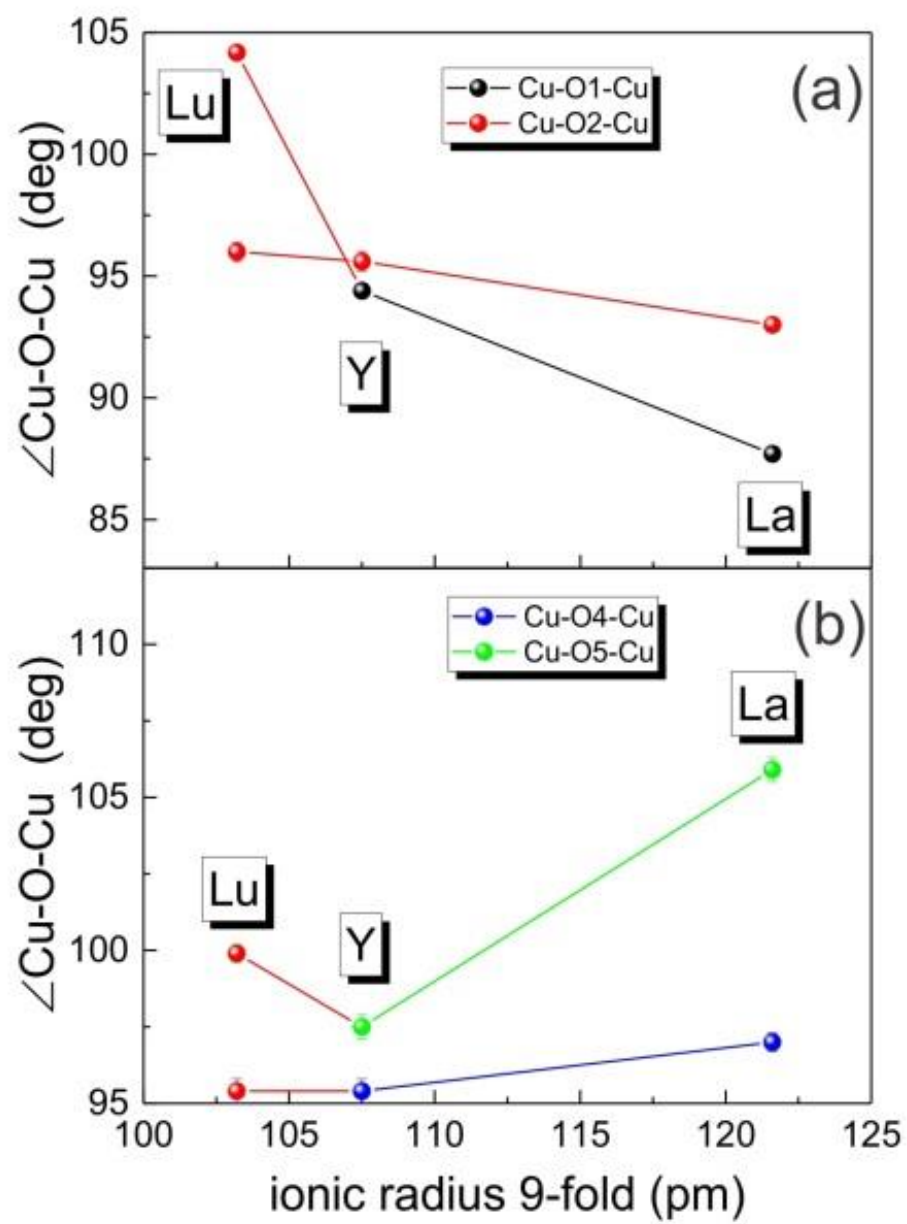


Figure 6-9. Cu- O – Cu bonding angles as a function of the ionic radii of the RE atoms as indicated. O1(a) and O2(b) atoms connect to AsO_4^{3-} groups.

6.4. Thermal gravimetric analysis

Timofejeva in 1965 [6-23], Dietrich *et al.* in 1969 [6-24] and Miletich *et al* in 1997 [6-15] investigated de- and re-hydration of mixite samples. Several dehydration steps were found. Our studies were done in a Netzsch TGA setup with heating rates of 2°C/min in an Argon atmosphere. The samples were placed in Al crucibles. Figure 6-10 shows the results collected on the artificial samples of Mixite and on $RECu_6(OH)_6(AsO_4)_3 \cdot nH_2O$ ($RE = Y, La, Lu; n \approx 3$) samples in comparison with the TGA trace reported by Miletich artificial Mixite.

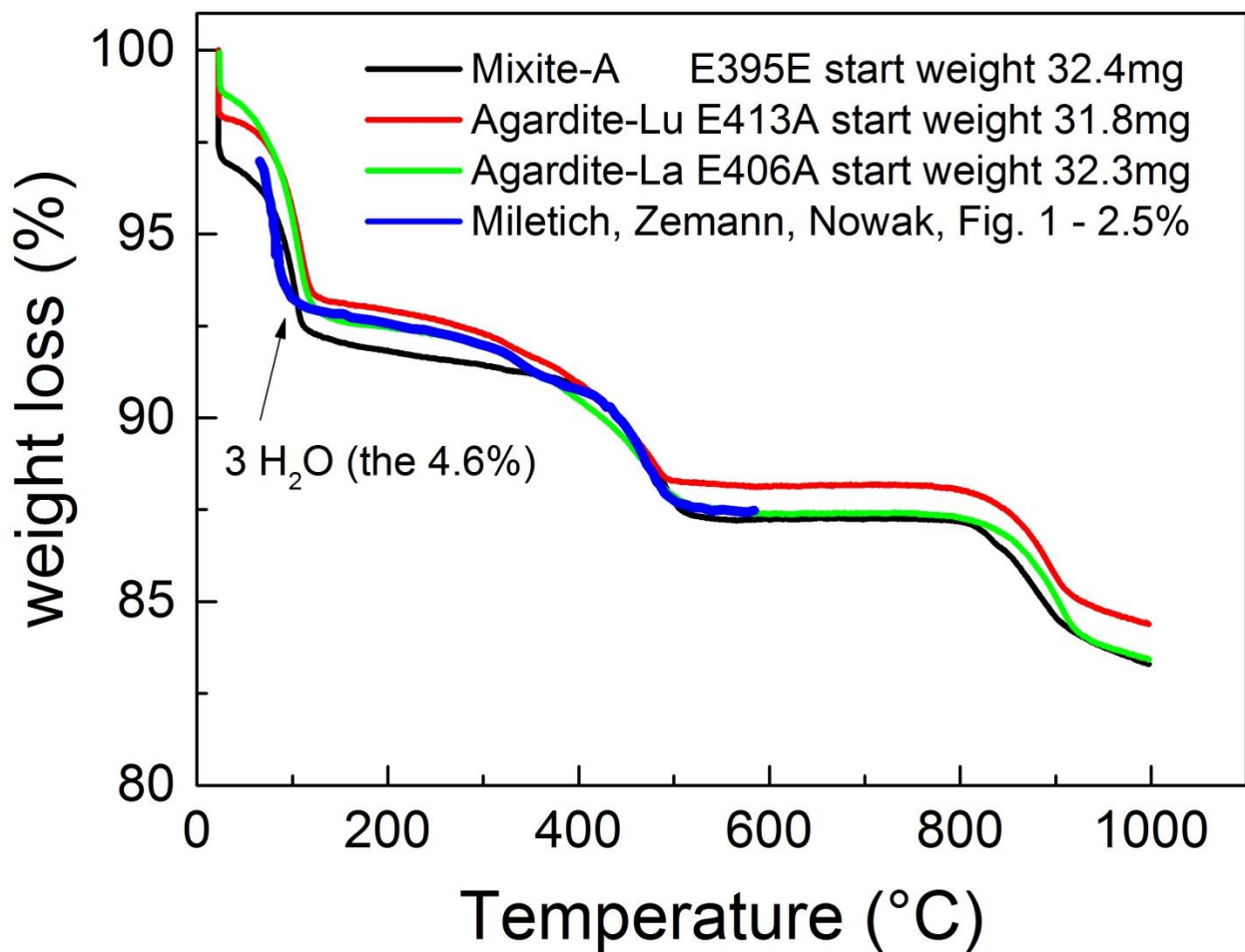


Figure 6-10. TGA analysis of dehydration of mixite. Black, red and green solid lines are artificial mixite, artificial Lu-agardite and artificial La-agardite respectively prepared as described in chapter 5.2, blue solid line is a data published as a Fig.1 by R. Miletich, J. Zemann, and M. Nowak, Phys. Chem. Minerals 1997, 24: 411–422 shifted by -2.5% weight loss and +35°C in temperature.

The weight loss induced by raising the temperature is characterized by 4 distinct steps, an initial weight decrease by approximately 3% at about 26 °C, a second ridge at about 93°C, a third and somewhat broader step between 390 °C and 510°C and a final step of approximately of ~3% at 820°C. The first step close to room temperature has not been seen by Miletich and is ascribed to some residual moist in our sample. The second and the third steps at $90\pm 30^\circ\text{C}$ and $450\pm 60^\circ\text{C}$, characterized by weight losses of 4.5% and 3%, respectively, have also been detected by Miletich et al., Dietrich *et al.* and Timofejeva. The second slope has been assigned to the complete depletion of the water molecules (zeolitic-type water, 4.6% expected for $n \approx 3$) and the third step to irreversible thermal decomposition of the samples, probably with the loss of H₂O from the (OH)⁻ groups. The fourth step, centered at about 840°C, is assigned to evaporation of the decomposition products.

6.5. Spin-exchange parameters⁹

Structural parameters refined by Mereiter and Preisinger in 1986 [6-3, 6-25] were used as initial input parameters for the DFT calculations of the total energy. Six ordered spin configurations were evaluated using the Vienna *ab initio* simulation package (VASP) with the projected augmented-wave method employing the generalized gradient approximation (GGA) of Perdew, Burke, and Ernzerhof for the exchange and correlation functionals. The plane wave cut-off energy was set to 400 eV and the irreducible Brillouin zone was sampled at 32 k -points. The GGA+ U calculations were carried out by varying the on-site repulsion energy between 4 and 6 eV suitable for Cu^{2+} . The energies of the six ordered spin states were mapped on the Heisenberg spin-exchange Hamiltonian:

$$\mathcal{H} = - \sum_{i < j} J_{ij} \vec{S}_i \vec{S}_j, \quad (6-2)$$

where:

$J_{ij} = J_1, J_2, \dots, J_5$ are the parameters for the spin-exchange interaction between the spin sites i and j , as defined in Figure 6-11;

\vec{S}_i and \vec{S}_j are the spin angular momentum operators at sites i and j , respectively.

⁹ The DFT calculations were performed by Prof. Myung-Hwan Whangbo from North Carolina State University (Raleigh, North Carolina 27695-8204, USA).

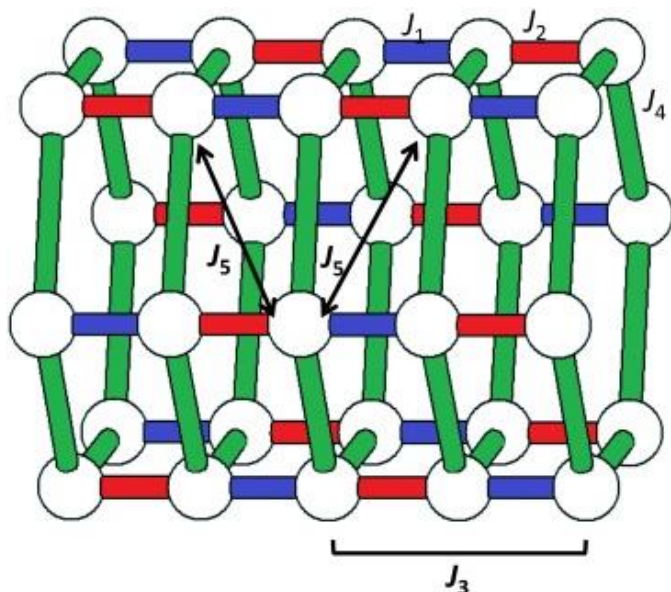


Table 6-5. Distances between the Cu atoms within and between the hexagonal rings.

spin-exchange	distance/pm
J_1 (blue)	293.040
J_2 (red)	298.960
J_3	592.000
J_4 (green)	511.030
J_5	590.558

Figure 6-11. Definition of the various exchange parameters J_i used to map the total energies from the DFT + U calculations onto the Heisenberg Hamiltonian eq. (19).

The mapping reveals that the dominant spin-exchange couples Cu moments along the c axis (J_2). In addition to the nearest-neighbor spin-exchange (J_2), much smaller, almost negligible, competing next-nearest-neighbor spin-exchange (J_1) is also found (see Table 6-6).

Table 6-6. Spin-exchange parameters J_i , as defined in Figure 6-11, obtained from the total energies DFT calculations assuming six ordered spin configurations.

spin-exchange	$U = 4$ eV	$U = 5$ eV	$U = 6$ eV
J_1 (blue), meV	-1.76	-0.81	-0.09
J_2 (red), meV	-58.54	-47.61	-38.35
J_3 , meV	-4.95	-4.09	-3.39
J_4 (green), meV	-8.21	-7.01	-5.93
J_5 , meV	-0.19	-0.11	-0.05

The spin-exchange coupling between the Cu moments in six-rings (J_4) is by a factor of six smaller than the exchange between the Cu moments along the c axis (J_2). The $(\text{AsO}_4)^{3-}$ arsenate molecules connect to every other oxygen atom pair in

the ribbon chains (see Figure 6-2). J_2 and the considerably smaller J_4 alternate in the links between the six rings. J_3 is by a factor of ten smaller than J_2 and frustration due to next-nearest-neighbor spin-exchange can be ignored in a first approach.

The following simplified exchange coupling scheme (Figure 6-12) results if only the two dominating spin-exchange interactions J_2 and J_4 are taken into consideration.

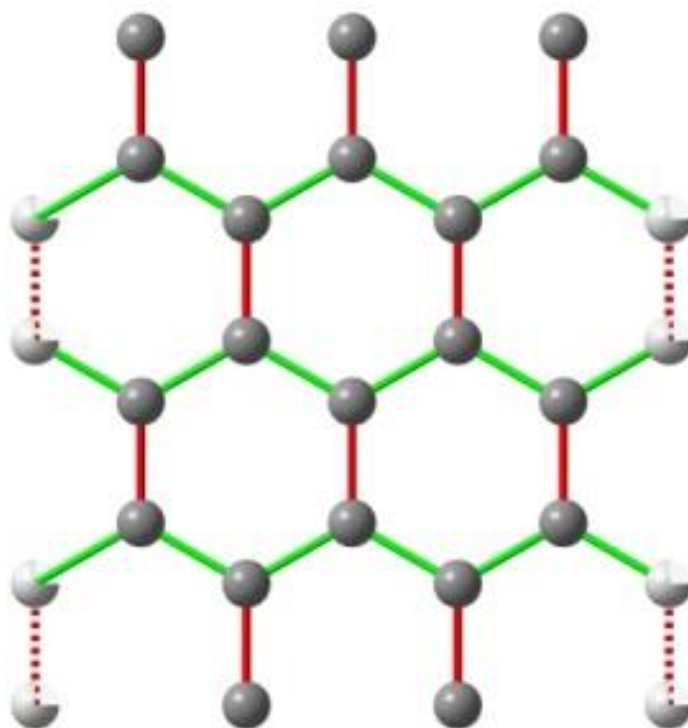


Figure 6-12. Reduced spin-exchange coupling scheme of an 'unfolded' six-ring. Spheres represent Cu atoms; spheres with an octant cut out are identical. In the six-fold ring structure The two dominating spin-exchange paths J_2 (red) and J_4 (green) are highlighted (color code as in Figure 6-11). Dotted bonds are identical.

6.6. Raman Scattering

Miletich *et al.* [6-15] proposed that the hydrogen atoms that connect O4H and O5H (see Figure 6-2) form hydrogen bonds within the same six-rings ($d_{O4H-O5H}=2.89 \text{ \AA}$) and the hydrogen atom coordinating to O4H establish a hydrogen bond to O3 ($d_{O3-O4H}= 2.83 \text{ \AA}$) interconnecting to the oxygen network of a neighbor six-ring. In order to identify and trace compositional and hydrogen-bonding network variations, Frost and collaborators in a series of reports investigated the lattice vibrations of mixite samples from various geological origins. [6-18 ,6-19, 6-26, 6-27]

They observed Raman bands between 800 and 830 cm^{-1} and assigned them to stretching vibrations of the $(\text{AsO}_4)^{3-}$ groups. Possible formation of protonated $(\text{HAsO}_4)^{2-}$ and $(\text{H}_2\text{AsO}_4)^-$ anions were discussed in detail. Their stretching vibrations should show up as broad sidebands at the high energy shoulder of the $(\text{AsO}_4)^{3-}$ Raman modes, the latter being centered between 800 and 900 cm^{-1} . The Raman bands at around 470 cm^{-1} were assigned to the ν_4 $(\text{AsO}_4)^{3-}$ bending modes whereas the ν_2 bending modes of $(\text{AsO}_4)^{3-}$ and possible $(\text{HAsO}_4)^{2-}$ anions show up between $\sim 324 \text{ cm}^{-1}$ and $\sim 423 \text{ cm}^{-1}$. Hydroxyl stretching bands are seen near 3300 cm^{-1} . Weak water Raman bands may be expected between ~ 1600 and $\sim 1700 \text{ cm}^{-1}$. [6-18]

Figure 6-13 displays a comparison of the Raman spectra of our natural and synthetic mixite and goudeyite samples. The overall structure of the spectra is quite similar proving that fine microscopic structural details of our samples which could not be discerned by the powder X-ray diffraction measurements, e. g. oxygen site positions and occupancies are very well preserved. Above 1000 cm^{-1} the spectra are rather featureless. The $(\text{OH})^-$ stretching vibrations are observed for natural mixite and synthetic goudeyite samples between 3400 and 3500 cm^{-1} . Clear indications of water molecules modes have not been seen (see insets in Figure 6-13)

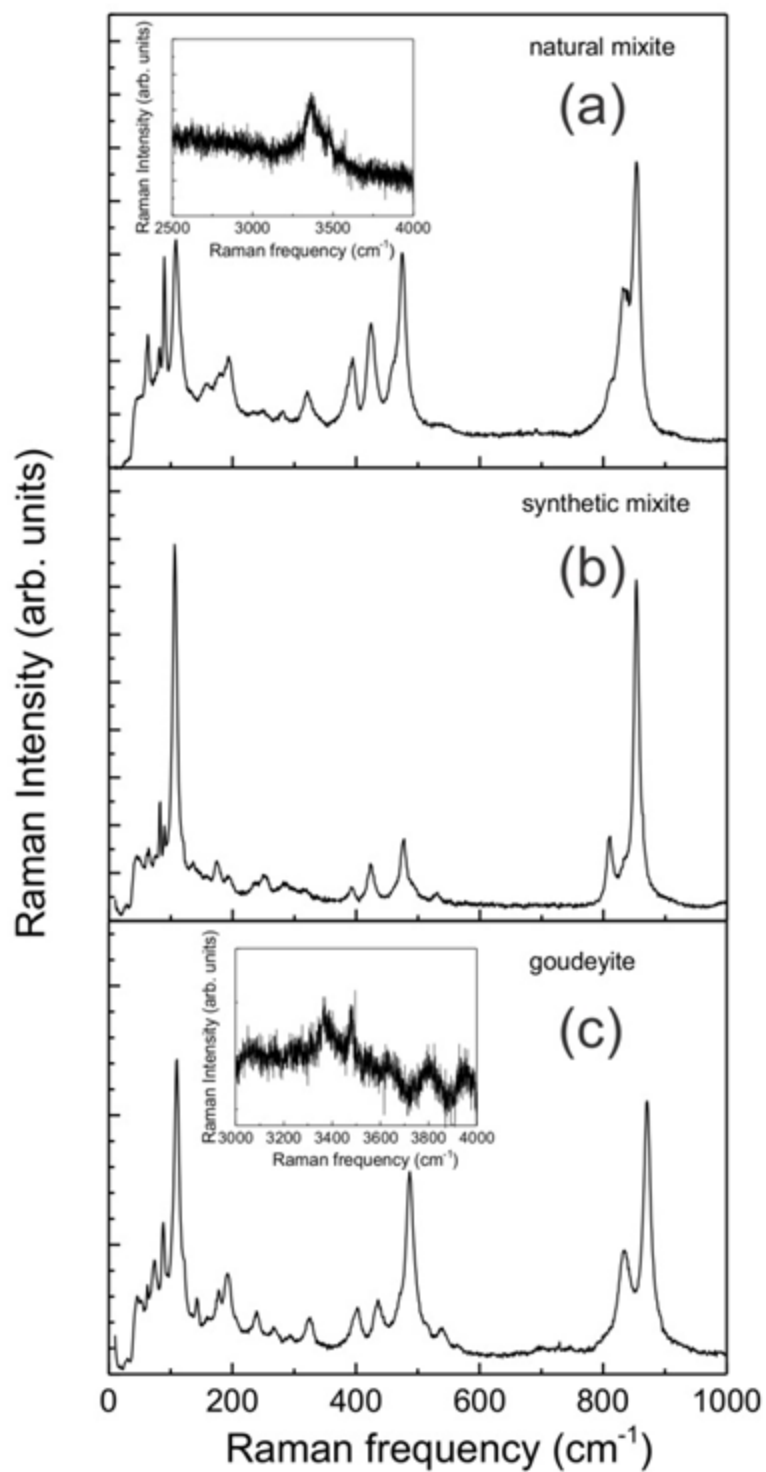


Figure 6-13. Comparison of the Raman spectra of (from top to bottom) our natural mixite, the synthetic mixite, and the synthetic goudeyite samples. The inserts display the energy range where OH⁻ stretching vibrations are expected.

Previously, Frost and collaborators defined three different regions below 1000 cm^{-1} in Raman spectra of mixite and goudeyite:

- a set with several sharp peaks below 200 cm^{-1} ,
- a set of four bands between 300 and 500 cm^{-1} ,
- the region between 800 and 900 cm^{-1} with two very sharp bands associated with $(\text{AsO}_4)^{3-}$ stretching vibrations, some of them with faint broad shoulders at the high energy side. [6-18, 6-19, 6-26, 6-27]

The peak positions of our natural and synthetic mixite samples agree very well. For synthetic goudeyite sample, the $(\text{AsO}_4)^{3-}$ vibrations and the peaks in the center of the spectrum are shifted to higher frequencies by $\sim 20\text{ cm}^{-1}$ whereas the Raman frequencies of the peaks below 200 cm^{-1} coincide fairly well.

Figure 6-14 displays the splitting and a deconvolution of the $(\text{AsO}_4)^{3-}$ -related bands between 800 and 900 cm^{-1} . As already stated above, the bands of synthetic goudeyite are shifted to higher Raman frequencies reflecting the shorter As – O bond length. This can be proven by comparing the lattice parameters of goudeyite with mixite (see Table 6-2).

Two weaker bands at the low energy side of the spectra are clearly resolved for both mixite samples. Goudeyite has only one band at $\sim 835\text{ cm}^{-1}$, which is about twice as broad as the main peak at $\sim 871\text{ cm}^{-1}$. It can be due to an overlay of the two separate low energy peaks observed for the mixite. Very weak shoulders at the high energy slopes of the main As – O stretching bands could be associated with the stretching vibrations of the HAsO_4^{2-} and the H_2AsO_4^- groups. Their relative intensities amount at best to 5 % or less of the total intensity of the $(\text{AsO}_4)^{3-}$ stretching modes. The remaining peaks compare fairly well in all Raman spectra emphasizing good crystalline quality of our synthetic samples as already indicated by the X-ray results.

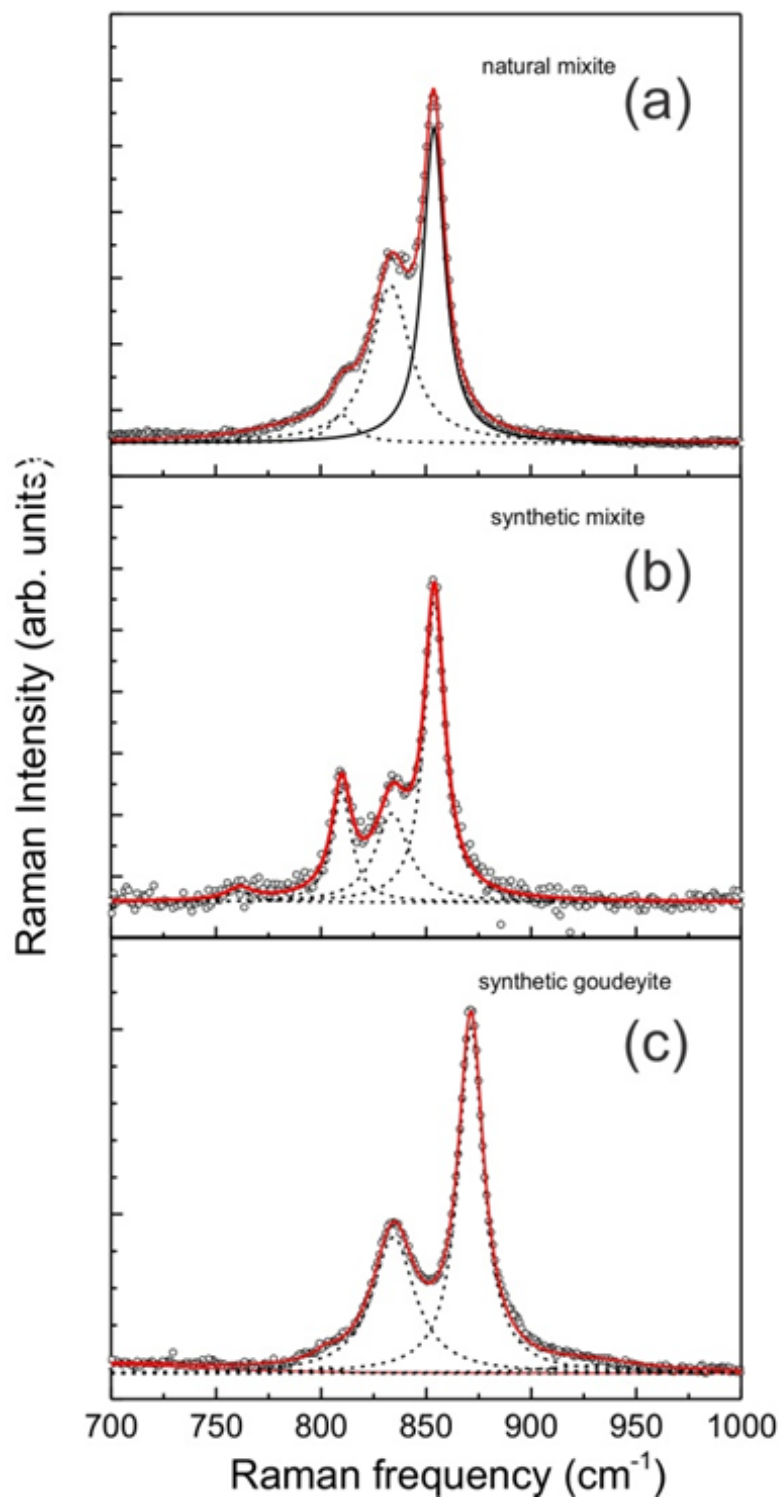


Figure 6-14. Raman spectra of natural and synthetic mixite and synthetic goudeyite (from top to bottom) in the energy range where $(\text{AsO}_4)^{3-}$ related stretching vibrations are expected. The solid black lines represent a deconvolution of the spectra with several Lorentz lines given by the dashed lines. The resonance positions of the individual modes are compiled in Table 6-7.

Table 6-7. Results of the deconvolution of the As – O stretching bands observed in the Raman spectra between 800 and 900 cm^{-1} of natural and synthetic mixite and synthetic goudeyite.

natural mixite		synthetic mixite		synthetic goudeyite	
cm^{-1}	rel. %	cm^{-1}	rel. %	cm^{-1}	rel. %
785(4)	5.6(0.9)	761.4(2.0)	2.6(1.5)	--	--
810.1(0.4)	4.9(0.9)	809.8(0.2)	18.9(1.9)	802.0(1.3)	0.7(0.3)
833.3(0.1)	42.5(1.1)	833.8(0.4)	25.6(2.0)	834.5(0.1)	37.2(0.5)
853.9(0.1)	47.0(0.6)	853.0(0.2)	52.9(1.2)	871.3(0.1)	56.9(0.3)
--	--	--	--	~930	5.2(1.0)

Figure 6-15 displays a compilation of the room-temperature Raman spectra of $RE\text{Cu}_6(\text{OH})_6(\text{AsO}_4)_3 \cdot n\text{H}_2\text{O}$ ($RE = \text{Y, La, Lu}; n \approx 3$) together with the spectrum for $\text{YCu}_6(\text{OH})_6(\text{AsO}_4)_3 \cdot n\text{H}_2\text{O}$ ($n \approx 3$) (see Figure 6-13). The inset displays the energy range where OH^- stretching vibrations are expected. Qualitatively, these spectra are very similar indicating the same structure type in support of our X-ray structure solutions. One can easily identify three different regions similar to those described before. Some modes are more pronounced due to the difficulties of focusing the laser spot on polycrystalline particles. Quantitatively, there are slight shifts e.g. for the pronounced mode just below 500 cm^{-1} which up-shifts from La to Lu from 475 to 488 cm^{-1} which follows the decreasing lattice parameters on-going from La to Lu. Similarly, the modes near 900 cm^{-1} , which have been attributed to stretching vibrations of the $(\text{AsO}_4)^{3-}$ group exhibit an up-shift from 871 to 876 cm^{-1} , for La and Lu, respectively. Some extra splitting is discerned, e.g. of the 876 cm^{-1} mode of $\text{LuCu}_6(\text{OH})_6(\text{AsO}_4)_3 \cdot 3\text{H}_2\text{O}$. The $(\text{OH})^-$ stretching vibrations are broad but well resolved for La and Lu. The Y and Lu exhibit a slight downshift of about 15 to 20 cm^{-1} .

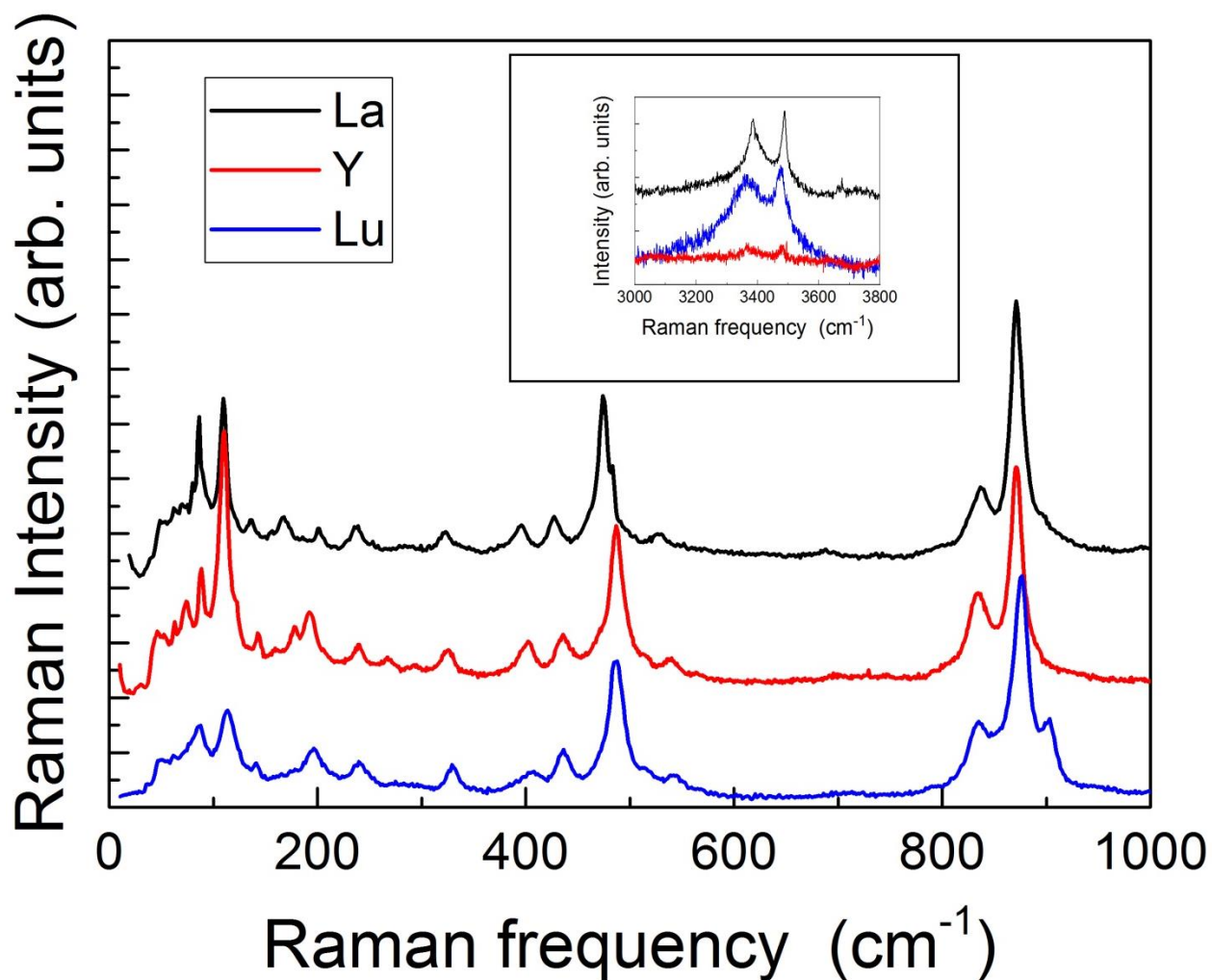


Figure 6-15. Raman spectra of $RECu_6(OH)_6(AsO_4)_3 \cdot nH_2O$ ($RE = Y, La, Lu; n \approx 3$) collected at room temperature. The spectra have been up-shifted for clarity.

6.7. UV-VIS spectroscopy¹⁰

Figure 6-16 highlights the powder reflectance spectrum of $\text{LaCu}_6(\text{OH})_6(\text{AsO}_4)_3 \cdot 3 \text{H}_2\text{O}$ in the NIR/vis/UV range. Two bands at $\tilde{\nu} = 13700 \text{ cm}^{-1}$ (1.70 eV) and $\tilde{\nu} = 31900 \text{ cm}^{-1}$ (3.94 eV) and a significantly weaker band centered at approximately 5100 cm^{-1} were observed. The former clearly originate from $d-d$ electronic transitions on the $[\text{Cu}^{\text{II}}\text{O}_5]$ chromophore. The insert in Figure 6-16 highlights the weak mode in the NIR range. This band is similar to that reported by Frost *et al.* and has been ascribed to HOH overtone vibrations. [6-17]

For the $[\text{Cu}^{\text{II}}\text{O}_5]$ chromophore pyramids, strong radial and angular distortions of the ligand field are expected. Angular overlap model (AOM) calculations were performed to understand the correlation between the geometric distortion (Jahn-Teller elongation) n of the chromophore and its d -electron energies. [6-29, 6-30, 6-31]

An advantage of the AOM model is its ability to employ the actual geometry of the chromophores, as determined from the crystal structure analysis. With the AOM model, only one σ - and two π -interactions for each ligand with the five $3d$ -orbitals of the central cation (in total 15 bonding parameters for a square-pyramidal chromophore) are used for the fitting between calculated and observed transition energies instead of the global ligand field parameters ($10Dq$ or Δ_o). The decomposition of the global ligand field parameter into σ and π components permits also accounting for the effects of the second coordination sphere, e.g. anisotropic π -bonding of ligands. [6-32] Moreover, mixing between the $4s$ - and $3d$ -orbitals of copper (d - s mixing [6-31, 6-33]) is taken into account

¹⁰ Experiments and angular overlap model calculations have been performed by Prof. R. Glaum (Rheinische Friedrich-Wilhelms-Universität Bonn)

using the *eds* parametrization in the CAMMAG program package.[6-34, 6-35, 6-36]

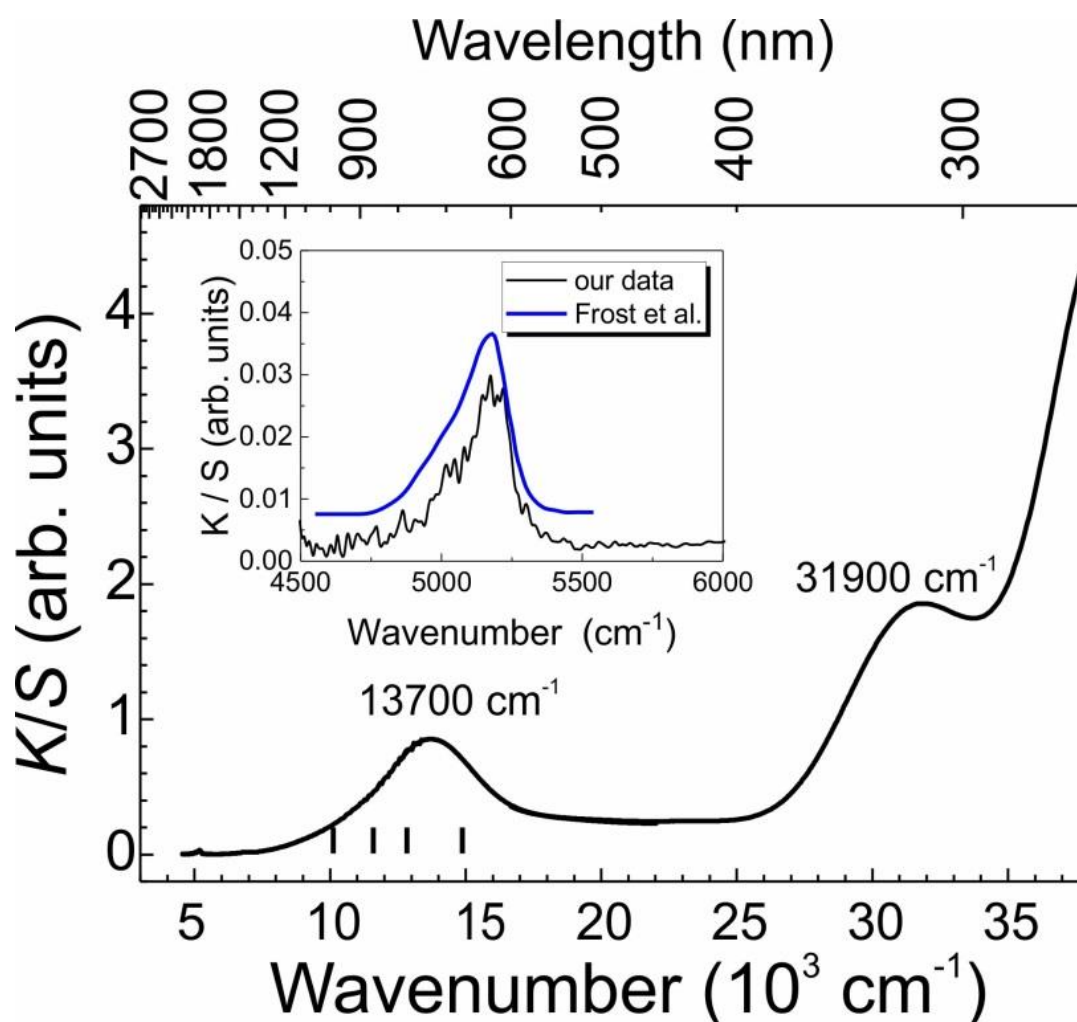


Figure 6-16. Powder reflectance spectrum of $\text{LaCu}_6(\text{OH})_6(\text{AsO}_4)_3 \cdot 3 \text{H}_2\text{O}$. Black vertical bars mark the ligand-field transition energies, for the square-pyramidal $[\text{Cu}^{\text{II}}\text{O}_5]$ chromophore, obtained from AOM calculations. The ordinate axis displays the Kubelka-Munk relation, $K/S = (1 - R_f)^2 / (2R_f)$, where $R_f = I(\text{LaCu}_6(\text{OH})_6(\text{AsO}_4)_3 \cdot 3 \text{H}_2\text{O}) / I(\text{BaSO}_4)$. $I(\text{LaCu}_6(\text{OH})_6(\text{AsO}_4)_3 \cdot 3 \text{H}_2\text{O})$ and $I(\text{BaSO}_4)$ are the reflected light intensities of the sample and the BaSO_4 used as white standard, respectively. [28] The inset displays our NIR spectrum given by the (black) solid line. For comparison, we also show the spectrum for $\text{LaCu}_6(\text{OH})_6(\text{AsO}_4)_3 \cdot 3 \text{H}_2\text{O}$ reported by Frost *et al.* (blue solid line). [6-17]

With additional constraints, the number of independent bonding parameters can be reduced. For the energy $e_\sigma(\text{Cu}^{\text{II}}-\text{O})$, proportionality to the distance $1/(d_{\text{Cu-O}})^5$ is assumed. [6-37] Usually, the e_π parameter can be taken as 1/4 of the

corresponding energies e_σ (in the case of “undisturbed” π -interaction). [6-31, 6-32]

In the case of $\text{LaCu}_6(\text{OH})_6(\text{AsO}_4)_3 \cdot 3 \text{H}_2\text{O}$, with all oxygen atoms coordinating to Cu^{2+} in the pyramidal plane showing $\text{c.n.}(\text{O}^{2-}) = 4$ (see Figure 6-2) a reduction of π -bonding has been assumed. This is similar to the AOM parametrization for chains of edge-sharing $[\text{M}^{\text{III}}\text{O}_6]$ octahedra e.g. in phosphates MPO_4 (CrVO_4 structure type; $\text{M} = \text{Ti}, \text{V}, \text{Cr}$). [6-38, 6-39, 6-40]

Thus, $e_{\pi,x}$, the π -interaction within the (Cu, O, Cu) plane was set to zero, while for the π -interaction perpendicular to this plane $e_{\pi,y} = 1/4 e_\sigma$ was assumed.

Inter-electronic repulsion is introduced into the AOM calculations via the Racah parameters B and C , spin-orbit coupling by parameter ξ . For the angular overlap modelling, the free ion ratio $C_0/B_0 = 3.8$ (Cu^{2+}) was taken and kept constant during the calculations. [6-31] Covalent contributions to the Cu–O interaction in the chromophore were considered by the nephelauxetic ratio β [$\beta = B/B_0$; $B_0(\text{Cu}^{2+}) = 1240 \text{ cm}^{-1}$]. [6-31] The spin-orbit coupling parameter ξ was also assumed to be reduced relative to the free ion value $\xi_0(\text{Cu}^{2+}) = 830 \text{ cm}^{-1}$ by the nephelauxetic ratio β . The best fit of the optical spectrum of $\text{LaCu}_6(\text{OH})_6(\text{AsO}_4)_3 \cdot 3 \text{H}_2\text{O}$ obtained with the following AOM parameters: $B = 992 \text{ cm}^{-1}$ ($\beta = 0.80$), $C = 3770 \text{ cm}^{-1}$, $\xi = 664 \text{ cm}^{-1}$, $e_\sigma(\text{Cu–O}) \sim d(\text{Cu–O})^{-5}$ and $e_\sigma(\text{Cu–O})_{\text{max}} = 7200 \text{ cm}^{-1}$ (for O3). Using a Stevens orbital reduction parameter of $k = 0.8$ [6-31, 6-41] leads to an effective magnetic moment of $\mu/\mu_B = 1.87$ and the components $g_x = 2.05$, $g_y = 2.12$, and $g_z = 2.27$ ($g_{\text{averaged}} = 2.15$) of the g -tensor for the $[\text{Cu}^{\text{II}}\text{O}_5]$ chromophore corresponding to a Curie constant of $0.44 \text{ cm}^3\text{K/mol}$, is in good agreement with the experimental observation (see Table 6-9).

6.8. Magnetic properties

A comparison of the magnetic susceptibilities of natural and synthetic mixite and goudeyite (Y-agardite) is shown in Figure 6-17. The characteristic feature of all susceptibilities is a broad maximum. The position of this maximum depends on the compound such is found of ~ 120 K, ~ 93 K and ~ 50 K for natural mixite, synthetic mixite and synthetic goudeyite, respectively. At temperatures above the maximum, the susceptibilities fall off with temperature with a Curie-Weiss law. Towards the lowest temperatures, the susceptibilities increase again with amounts different for the three compounds. This increase is ascribed to the magnetism of the single-ion impurities, *e.g.* defects in the crystal structure or some co-substitution. The defects and the magnetic impurities, though not traceable within the resolution of microprobe technique, are uncorrelated with the magnetism of the bulk and diverge hyperbolically with a Curie law. The different magnitude of the low-temperature Curie-type increase supports this presumption. The much lower magnitude for the synthetic samples indicating that the natural mixite sample – though probably better crystallized – contains other magnetic impurities (*e. g.* Fe cations) which do not couple to the Cu subsystem.

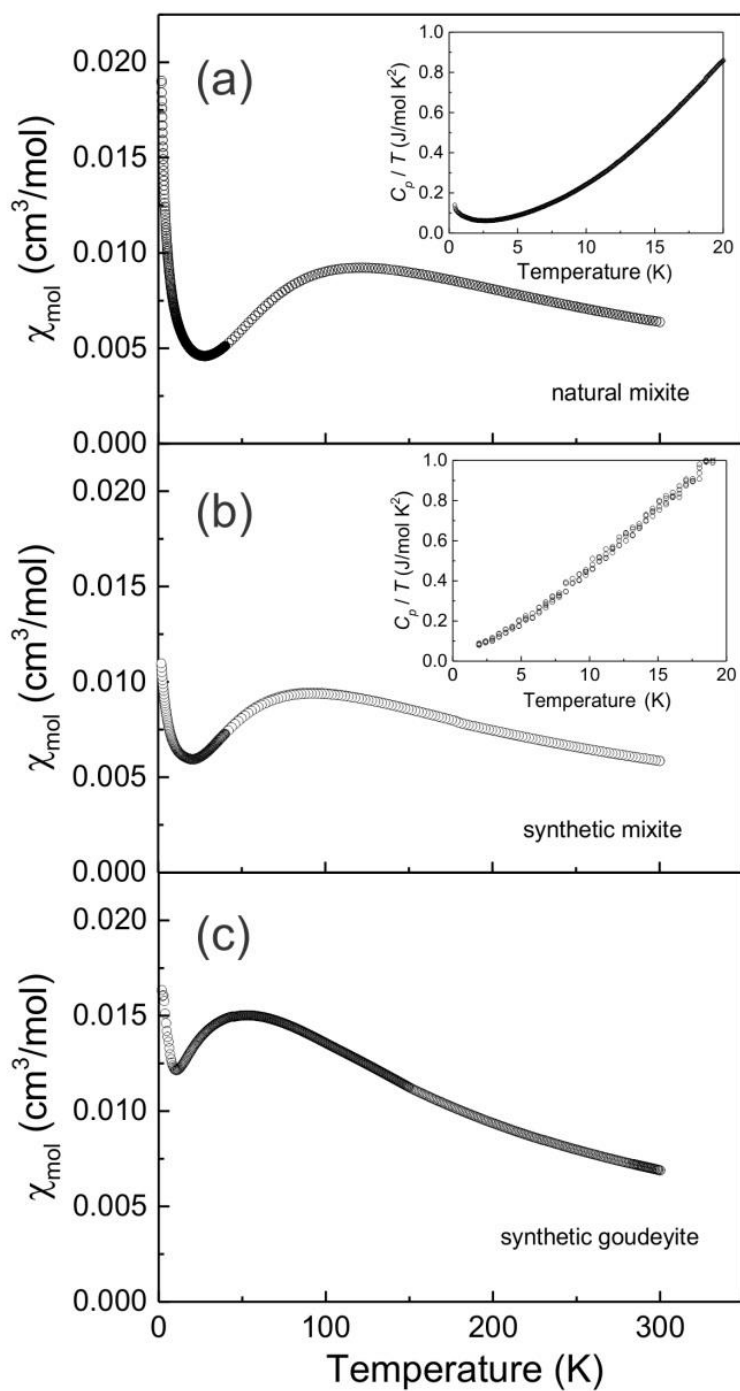


Figure 6-17. Comparison of the magnetic susceptibilities (per one Cu atom) of (a) natural and (b) synthetic mixite and (c) synthetic goudeyite. Measuring magnetic fields were 1T for natural mixite and synthetic goudeyite and 0.1 T for synthetic mixite. The inset in panels (a) and (b) display the heat capacity divided by temperature showing no long-range magnetic ordering down to 0.4 K.

The broad maxima in the magnetic susceptibilities indicate antiferromagnetic correlations within the Cu^{2+} cation system. Such broad anomalies are usually found within low-dimensional or dimer magnetic systems. [6-42] In order to analyze the susceptibility data and to extract characteristic spin-exchange parameters the following fitting procedures were carried out:

- 1) The magnetic contribution from the magnetic impurities or defects were quantified by fitting the low temperature ($T < 10$ K) susceptibilities to a Curie-Weiss law.
- 2) Their contribution was subtracted from the experimental data (see Figure 6-18).

Theoretical susceptibility data, for example, from exact diagonalization or Quantum Monte Carlo(QMC) calculations for the connected six-ring $S=1/2$ configuration are not available in the literature. However, rather convincing agreements could be found by fitting the difference susceptibility data to the theoretical susceptibilities of a $S=1/2$ Heisenberg chain with alternating spin-exchange interaction described by the following Hamiltonian,

$$\mathcal{H} = J_A \sum_i \vec{S}_{2i-1} \vec{S}_{2i} + J_B \sum_i \vec{S}_{2i} \vec{S}_{2i+1} = J_A \sum_i (\vec{S}_{2i-1} \vec{S}_{2i} + \alpha \vec{S}_{2i} \vec{S}_{2i+1}), \quad (6-3)$$

where:

J_A and J_B represent the alternating spin-exchange interactions along the chain;

$\alpha = J_B/J_A$ is the alternation parameter.

$\alpha = 1$ describes the Heisenberg chain with uniform nearest-neighbor coupling. $\alpha = 0$ describes a system of spin dimers. Attempts to fit these data with a uniform chain or a plain dimer model, even allowing for a molecular field-type inter-chain or inter-dimer spin-exchange, did not converge.

Quantum Monte Carlo calculations for the magnetic susceptibilities of the alternating chains with discrete ratios $0 \leq \alpha \leq 1$ are available in literature, and they have been fitted to a Padé approximant allowing to access also general ratios for the alternation parameter α . [6-43] The difference susceptibility data were finally fitted to the general equation

$$\chi(T) = C \cdot \chi_{spin}(T) + \chi_0. \quad (6-4)$$

The first term describes the spin susceptibility of the alternating chain and χ_0 allows for temperature independent terms from the diamagnetic contributions of the electrons in the closed shells and positive van Vleck contributions due to excitations to excited electronic states of the Cu^{2+} cations. The latter can be substantial and often do over-compensate the diamagnetic contributions. Using Pascal's increments for the cations and a van Vleck contribution of $\sim 100 \times 10^{-6} \text{ cm}^3/\text{mol}$ per Cu^{2+} cation, χ_0 was fixed to $\sim 200 \times 10^{-6} \text{ cm}^3/\text{mol}$ per formula unit. Additional fitting parameters were the g-factor, the alternation parameter α , and the exchange parameter J_A . Table 6-8 summarizes the relevant fit parameters, and Figure 6-18 displays the experimental data corrected for impurities in comparison with the fits to the alternating chain model.

Table 6-8. Relevant fit parameters as obtained by fits of Eq. (6-4) to the magnetic susceptibility data. The letter f added in brackets indicates that this parameter was fixed in the fitting procedures.

compound	g	$J_A \times k_B^{-1}$ [K]	α	χ_0 [$10^{-6} \text{ cm}^3/\text{mol}$]	C
nat. mixite	2.09(1)	206(2)	0.52(1)	200(f)	6(f)
syn. mixite	2.14(1)	169(2)	0.79(1)	200(f)	6(f)
syn. goudeyite	2.125(f)	127(2)	0.75(1)	200(f)	5.1(f)

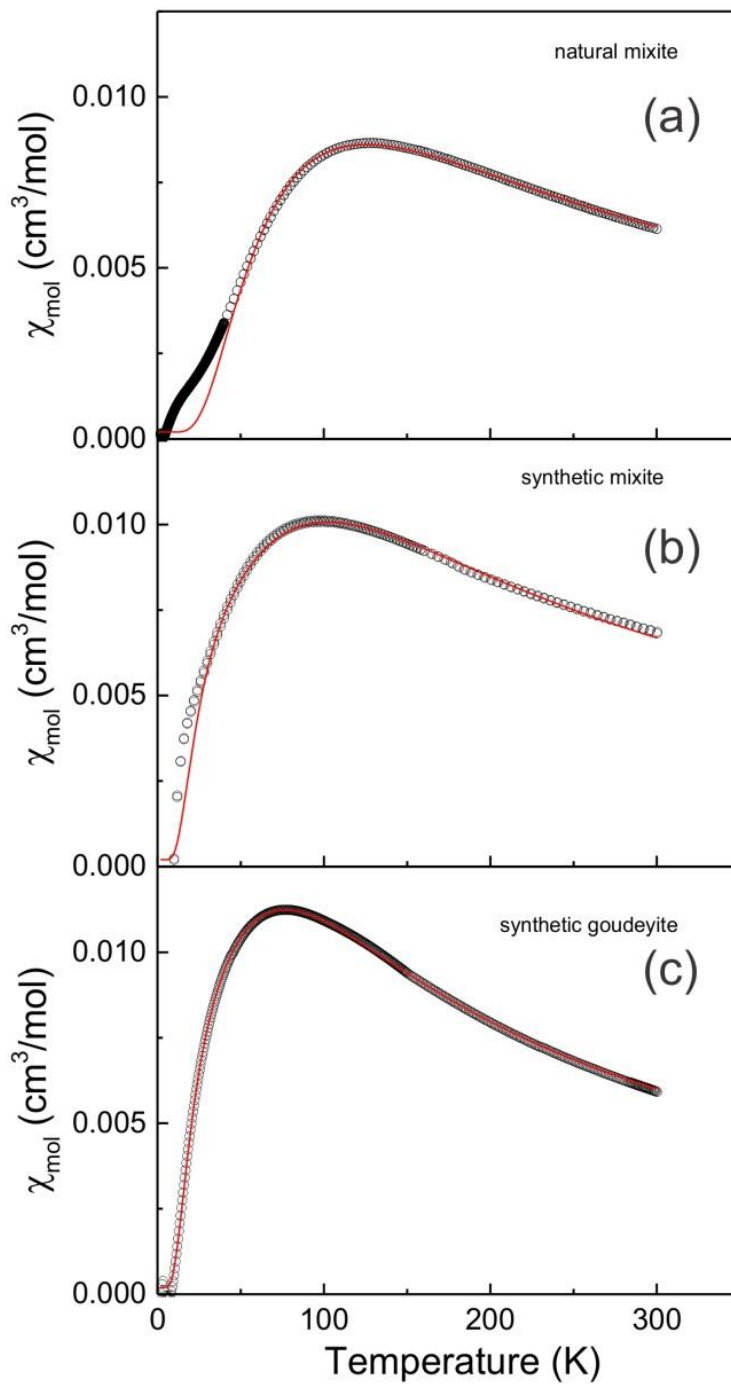


Figure 6-18. Comparison of the magnetic susceptibilities (for one formula unit) of (a) natural $(\text{Bi,Ca})\text{Cu}_6(\text{OH})_6(\text{AsO}_4)_3 \cdot 3\text{H}_2\text{O}$ and (b) synthetic $(\text{BiCu}_6(\text{OH})_6(\text{AsO}_4)_3 \cdot 3\text{H}_2\text{O})$ mixite and (c) synthetic goudeyite $(\text{YCu}_6(\text{OH})_6(\text{AsO}_4)_3 \cdot 3\text{H}_2\text{O})$ corrected for magnetic impurities (see text) in comparison to the results of the fits to the theoretical susceptibilities of an alternating Heisenberg $S=1/2$ spin chain. The fit parameters are summarized in Table 6-8.

The good agreement of the magnetic susceptibility with that of the antiferromagnetic Heisenberg spin $S = 1/2$ chain with alternating exchange coupling is also found for $\text{LaCu}_6(\text{OH})_6(\text{AsO}_4)_3 \cdot 3 \text{H}_2\text{O}$ (Figure 6-20(a)). The magnetic susceptibilities of $\text{LaCu}_6(\text{OH})_6(\text{AsO}_4)_3 \cdot 3\text{H}_2\text{O}$ can also be well fitted with the alternating chain model. The magnetic susceptibility of $\text{LuCu}_6(\text{OH})_6(\text{AsO}_4)_3 \cdot 3\text{H}_2\text{O}$ shares some similarities with those of mixite, and $\text{RECu}_6(\text{OH})_6(\text{AsO}_4)_3 \cdot 3\text{H}_2\text{O}$ ($\text{RE}=\text{La}, \text{Y}$) but could not be fitted to the alternating exchange Heisenberg chain model Eq. (6-3). However, a trend that immediately becomes apparent from the experimental data is the decrease of the magnitude of the overall antiferromagnetic spin exchange from $\text{LaCu}_6(\text{OH})_6(\text{AsO}_4)_3 \cdot 3\text{H}_2\text{O}$ to $\text{LuCu}_6(\text{OH})_6(\text{AsO}_4)_3 \cdot 3\text{H}_2\text{O}$. This is already signaled by the downshift of the broad short range order maximum and also by the decrease of the Curie Weiss temperature (see Table 6-9) obtained from fits of high temperature susceptibilities ($175 \text{ K} \leq T \leq 300 \text{ K}$) to the Curie-Weiss law,

$$\chi_{\text{mol}}(T) = C/(T - \Theta_{CW}) + \chi_0, \quad (6-5)$$

where:

Θ_{CW} is the Curie Weiss temperature.

Compared to $\text{LaCu}_6(\text{OH})_6(\text{AsO}_4)_3 \cdot 3\text{H}_2\text{O}$, the temperature position of the susceptibility maxima of $\text{YCu}_6(\text{OH})_6(\text{AsO}_4)_3 \cdot 3\text{H}_2\text{O}$ and $\text{LuCu}_6(\text{OH})_6(\text{AsO}_4)_3 \cdot 3\text{H}_2\text{O}$ decrease by a factor of two and five, respectively. The Curie-Weiss temperatures, which measure the sum of the spin exchange to the interacting magnetic neighbor, drop by a factor of two.

Table 6-9. Spin exchange parameters of $RECu_6(OH)_6(AsO_4)_3 \times 3 H_2O$ according to eq. (1) and Curie-Weiss temperature Θ_{CW} .

RE	J_A (K)	α	Θ_{CW} (K)	Ref.	C (cm ³ K/Cu-mol)
La	213(3)	0.56(2)	-202(3)	this work	0.448(3)
Y	128(1)	0.76(1)	-97(1)	[6-44]	0.393(2)
Lu	-	-	-92(1)	this work	0.415(3)
nat. Mixite	206(2)	0.52(1)	-176(2)	[6-44]	0.488(5)

As already observed for the mixite samples [6-44] heat capacity data of $RECu_6(OH)_6(AsO_4)_3 \cdot 3H_2O$ ($RE = La, Y$) showed no indication of long-range magnetic order down to 0.4K.

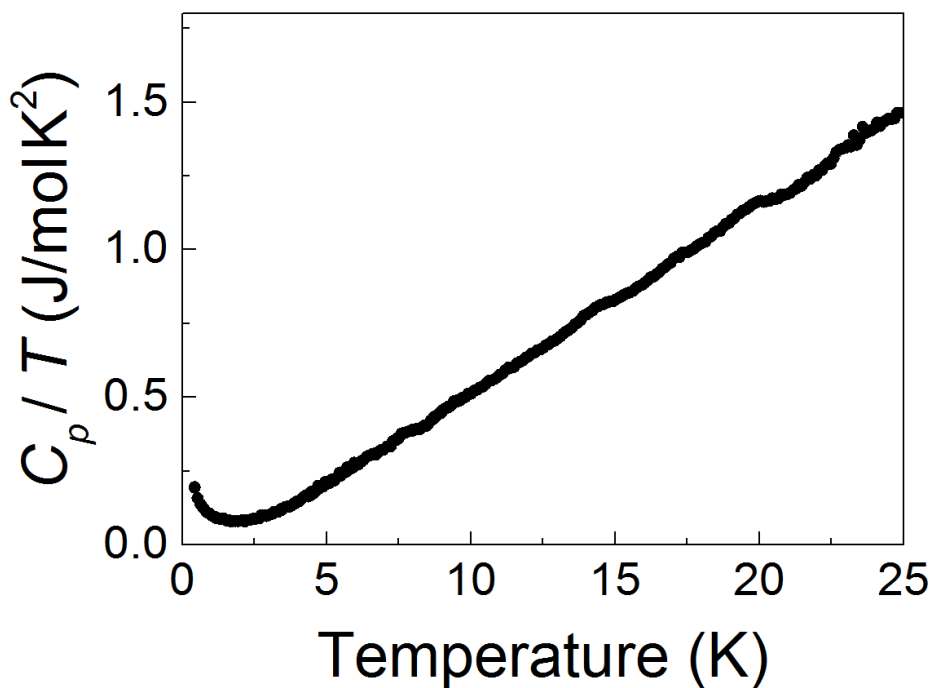


Figure 6-19. Specific heat capacity of $LaCu_6(OH)_6(AsO_4)_3 \cdot 3 H_2O$. No apparent anomaly is seen at low temperatures

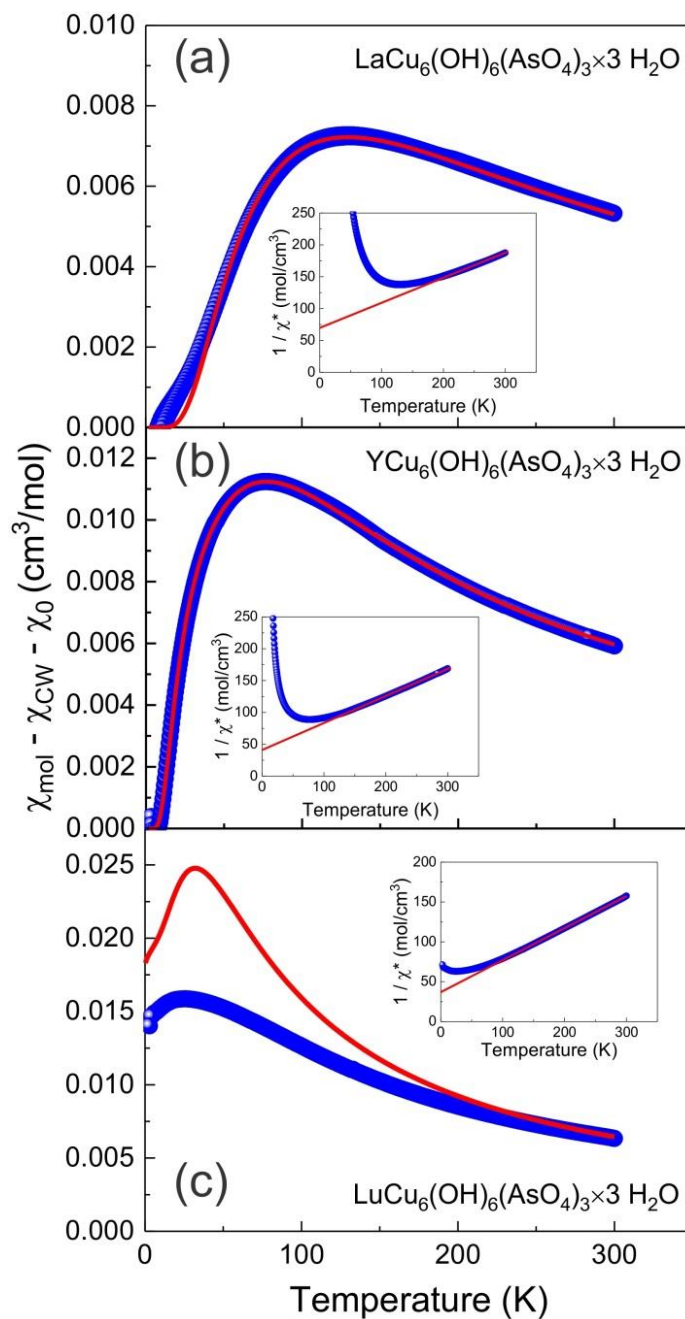


Figure 6-20. Magnetic susceptibilities of $RECu_6(OH)_6(AsO_4)_3 \cdot 3 H_2O$ corrected for a temperature independent contribution and a Curie-tail at low temperatures due to single-ion magnetic species. The (red) solid lines in case of La and Y represents a fit with a spin $S=1/2$ Heisenberg chain with alternating antiferromagnetic spin exchange according to Eq. (6-3) with parameters listed in Table 6-9. The (red) solid line in (c) represents the susceptibility of a spin $S=1/2$ Heisenberg chain with uniform nearest-neighbor antiferromagnetic spin exchange of 50 K calculated according to Ref. [6-43]. The insets display the inverse susceptibility together with a fit of the Curie-Weiss law (Eq. (6-5)) to the data for $T > 175$ K. The fitted parameters are listed in Table 6-9.

7. Summary and Conclusion

This thesis is focused on the experimental investigation into the chemical, structural, magnetic and vibrational properties of low-dimensional quantum antiferromagnets. All investigated compounds contain Cu cations in the oxidation state +2 as magnetically active species.

Detailed X-ray and neutron powder diffraction measurements proved that samples of CuTa_2O_6 prepared by low-temperature precursor decomposition, initially reported to crystallize with the tetragonal trirutile structure type at room temperature exhibit a slight monoclinic distortion that is removed at a temperature above 503(3) K. The space group of the high temperature phase is $P4_2/mnm$. At room temperature the crystal structure of CuTa_2O_6 is similar to that of CuSb_2O_6 and can be described in space group $P2_1/c$. The structural phase transition effects a noticeable rearrangement of the oxygen environments of the Cu and the Ta cations. At room temperature the apical Cu – O distances all range above 2 Å with the Cu – O3 distance due to a Jahn-Teller elongation being by about 5 % larger than the Cu distances to O1 and O2. For the high temperature tetragonal phase, the Cu - O distances are markedly shorter than 2 Å. The opposite configuration is observed for the Ta coordination polyhedra. The Ta – O distances are being smaller in the low temperature phase and larger in the high temperature phase. Density functional calculations predict CuTa_2O_6 to constitute a 1D antiferromagnetic linear chain with intra-chain spin-exchange interaction along diagonals in the *ab* planes (in tetragonal setting). The inter-chain spin-exchange interaction is found to be smaller by a factor of five. The theoretical results are confirmed by magnetic susceptibility and isothermal magnetization measurements which both follow very well the theoretical prediction for a 1D antiferromagnetic Heisenberg chain with nearest-neighbour spin-exchange interaction. Low temperature magnetic susceptibility, heat capacity and high-intensity neutron diffraction experiments could not detect any long-range magnetic order down to temperatures of 0.4 K. To understand why the magnetic properties of CuTa_2O_6 exhibit a strong 1D character, it is important to examine the magnetic orbitals of the axially-elongated CuO_6 octahedra: the strength of spin-

exchange between two magnetic ions is determined by the overlap between their magnetic orbitals, i.e. not only the distance but also the angular orientation of the orbitals becomes essential. With the four short Cu-O bonds of the CuO_6 octahedron, the Cu $3d_{x^2-y^2}$ orbitals undergo σ^* antibonding with the $2p$ orbitals of the four O ligands. Consequently, the magnetic properties of CuTa_2O_6 are not defined by Cu-O-Cu spin-exchanges (super exchanges), but rather by strong super-super exchanges via collinear Cu-O \cdots O-Cu pathways.

About two decades ago $\alpha\text{-CuV}_2\text{O}_6$ had been described as a one-dimensional spin $S=1/2$ Heisenberg chain with nearest-neighbor spin exchange interaction. Density functional calculations of the spin-exchange parameters reported in this work raised serious doubts about these previous studies. The investigations reported in this thesis rather suggest a two-dimensional square lattice quantum antiferromagnet behavior. Single crystals and large polycrystalline samples of the $\alpha\text{-CuV}_2\text{O}_6$ were used for the re-characterization of the magnetic and structural properties. The crystal structure of $\alpha\text{-CuV}_2\text{O}_6$ was refined from detailed X-ray and neutron powder diffraction measurements. With increasing temperature $\alpha\text{-CuV}_2\text{O}_6$ exhibits a structural phase transition from a triclinic to a monoclinic at 620°C , before it decomposes at 637°C . *Ab initio*, density functional calculations and angular dependent magnetization and EPR measurements unequivocally determined the spin lattice of $\alpha\text{-CuV}_2\text{O}_6$. They also suggested that, the magnetic properties of $\alpha\text{-CuV}_2\text{O}_6$ should be described by an anisotropic Heisenberg-type spin $S = 1/2$ square lattice with weak inter-planar antiferromagnet spin-exchange interaction being by more than an order of magnitude smaller than the intra-planar spin-exchange. Quantum Monte Carlo calculations of the magnetic susceptibilities of an anisotropic square lattice Heisenberg spin $S=1/2$ system have been performed and encoded into a Padé approximant which were used to fit the experimental magnetization data. The anisotropy ratio J_y/J_x determined experimentally for $\alpha\text{-CuV}_2\text{O}_6$ amounts to 0.71, in best agreement with the results of the density functional calculations. Spin-exchange along the shortest Cu - Cu distance is minimal. According to the heat capacity, magnetization and neutron powder diffraction measurements $\alpha\text{-CuV}_2\text{O}_6$ undergo a long-range

antiferromagnetic order below ~ 22.5 K to a collinear magnetic structure with magnetic moments $\sim 0.7 \mu_B$, apparently reduced due to quantum fluctuation.

The natural minerals mixite, goudeyite and agardite are isotypic and contain Cu^{2+} cations in linear chain arrangement. Natural and synthetic mixites, goudeyite and agardites samples were used to investigate their chemical, structural, vibrational and magnetic properties in detail. Low-dimensional antiferromagnetic spin-exchange coupling between the spin moments on the Cu^{2+} cations was found. The magnetic properties are determined by substantial antiferromagnetic spin-exchange between the magnetic moments on the Cu^{2+} cations consistent with the density functional calculations. The temperature dependence of the magnetic susceptibilities is dominated by short-range antiferromagnetic correlations showing up as a characteristic broad hump which reflects the low-dimensional character of the spin lattice in the mixite type crystal structure. Long-range magnetic ordering could not be detected down to 0.4K. A first model approach of the magnetic properties of all three systems in terms of an alternating $S=1/2$ Heisenberg model describes the magnetic susceptibilities rather well. Susceptibility measurements indicate differences between the natural and the synthetic samples. Whereas the spin-exchange alternation parameters for the synthetic samples are very close to each other, those of the natural sample is by about 25% lower. It can be the result of the modification of spin-exchange pathway within the six rings due to substitution of Bi by about 30% of Ca in natural mixite sample. The fits of the magnetic susceptibilities clearly rule out a coupled $S=1/2$ dimer model which has lately been proposed for the magnetic properties of several other Cu^{2+} minerals.

7. Zusammenfassung und Schlussfolgerung

Die vorliegende Arbeit konzentriert sich auf die experimentelle Untersuchung der chemischen, strukturellen, magnetischen und gitterdynamischen Eigenschaften niedrigdimensionaler Quantenantiferromagnete. Alle untersuchten Verbindungen enthalten Cu-Kationen in der Oxidationsstufe +2 als magnetisch aktive Spezies.

Detaillierte Röntgen- und Neutronenpulverbeugungsmessungen zeigten, dass CuTa_2O_6 Proben, die durch Zersetzung von Vorläufern bei niedriger Temperatur hergestellt wurden und ursprünglich bei Raumtemperatur mit der tetragonalen Trirutile-Struktur kristallisierten, eine leichte monokline Verzerrung aufweisen, die bei einer Temperatur über 503 (3) K entfernt wird. Die Raumgruppe der Hochtemperaturphase ist $P42/mnm$. Bei Raumtemperatur ähnelt die Kristallstruktur von CuTa_2O_6 der von CuSb_2O_6 und kann in der Raumgruppe $P2_1/c$ beschrieben werden. Der strukturelle Phasenübergang bewirkt eine merkliche Umlagerung der Sauerstoffumgebung der Cu- und Ta-Kationen. Bei Raumtemperatur liegen die apikalen Cu-O-Abstände alle über 2 Å, wobei der Cu-O3-Abstand aufgrund einer Jahn-Teller-Streckung, die um etwa 5% größer ist als die Cu-Abstände zu O1 und O2. Für die tetragonale Hochtemperaturphase sind die Cu-O-Abstände deutlich kürzer als 2 Å. Die entgegengesetzte Konfiguration wird für die Ta-Koordinationspolyeder beobachtet. Die Ta-O-Abstände sind in der Niedertemperaturphase kleiner und in der Hochtemperaturphase größer. Dichtefunktionalrechnungen sagen voraus, dass CuTa_2O_6 eine 1D-antiferromagnetische lineare Kette mit Spin-Austausch-Wechselwirkung innerhalb der Kette entlang Diagonalen in den ab-Ebenen (in tetragonaler Umgebung) bildet. Die Spin-Austausch-Wechselwirkung zwischen den Ketten ist um den Faktor fünf kleiner. Die theoretischen Ergebnisse werden durch Messungen der magnetischen Suszeptibilität und der isothermen Magnetisierung bestätigt, die beide sehr gut der theoretischen Vorhersage für eine 1D-antiferromagnetische Heisenberg-Kette mit Spin-Austausch-Wechselwirkung zum nächsten Nachbarn folgen. Experimente zur magnetischen Suszeptibilität bei niedriger Temperatur, Wärmekapazität und Neutronenbeugung mit hoher

Intensität konnten keine magnetische Fernordnung bis zu Temperaturen von 0,4 K nachweisen. Um zu verstehen, warum die magnetischen Eigenschaften von CuTa_2O_6 einen starken 1D-Charakter aufweisen, ist es wichtig, die Magnetorbitale der axial verlängerten CuO_6 -Oktaeder zu untersuchen: die Stärke des Spinaustauschs zwischen zwei magnetischen Ionen wird durch die Überlappung zwischen ihren Magnetorbitalen bestimmt, d.h. nicht nur der Abstand, sondern auch die Winkelorientierung der Orbitale wird wesentlich. Mit den vier kurzen Cu-O-Bindungen des CuO_6 -Oktaeders bilden die Cu $3d_{x^2-y^2}$ Orbitale eine σ^* Antibindung mit den $2p$ Orbitalen der vier O-Liganden aus. Folglich werden die magnetischen Eigenschaften von CuTa_2O_6 nicht durch Cu-O-Cu-Spin-Austausche (Super-Austausche) definiert, sondern durch starke Super-Super-Austausche über kollineare Cu-O ... O-Cu-Pfade.

Vor etwa zwei Jahrzehnten wurde $\alpha\text{-CuV}_2\text{O}_6$ als eindimensionale Spin $S = 1/2$ Heisenberg-Kette mit Spinaustausch-Wechselwirkung zum nächsten Nachbarn beschrieben. Dichtefunktionalberechnungen der Spinaustauschparameter, die in dieser Arbeit berichtet sind, ließen ernsthafte Zweifel an diesen früheren Studien aufkommen. Die in dieser Arbeit beschriebenen experimentellen Untersuchungen legen eher ein zweidimensionales quadratisches Gitterquanten-Antiferromagnetverhalten nahe. Einkristalle und große polykristalline Proben des $\alpha\text{-CuV}_2\text{O}_6$ wurden zur erneuten Charakterisierung der magnetischen und strukturellen Eigenschaften verwendet. Die Kristallstruktur von $\alpha\text{-CuV}_2\text{O}_6$ wurde anhand detaillierter Röntgen- und Neutronenpulverbeugungsmessungen verfeinert. Mit zunehmender Temperatur zeigt $\alpha\text{-CuV}_2\text{O}_6$ bei 620°C einen strukturellen Phasenübergang von einer triklinen zu einer monoklinen Struktur, bevor es sich bei 637°C zersetzt. Ab initio, Dichtefunktionsberechnungen und winkelabhängige Magnetisierungs- und EPR Messungen bestimmten eindeutig das Spin-Gitter von $\alpha\text{-CuV}_2\text{O}_6$. Sie belegen, dass die magnetischen Eigenschaften von $\alpha\text{-CuV}_2\text{O}_6$ durch ein anisotropes Spin $S = 1/2$ Quadratgitter vom Heisenberg-Typ beschrieben werden sollten, wobei die schwache interplanare Antiferromagnet-Spin-Austausch-Wechselwirkung um mehr als eine Größenordnung kleiner ist als die intraplanarer Spinaustausch. Quanten-Monte-Carlo-Berechnungen der magnetischen Suszeptibilitäten eines anisotropen

quadratischen Heisenberg Spin $S = 1/2$ Systems wurden durchgeführt und in ein Padé-Approximanten kodiert, der zur Anpassung der experimentellen Magnetisierungsdaten verwendet wurde. Das experimentell ermittelte Anisotropieverhältnis J_y/J_x für $\alpha\text{-CuV}_2\text{O}_6$ beträgt 0,71, sehr gut mit den Ergebnissen der Dichtefunktionsberechnungen übereinstimmend. Der Spinaustausch entlang des kürzesten Cu-Cu-Abstands ist minimal. Entsprechend der Wärmekapazität, belegen Magnetisierungs- und Neutronenpulverbeugungsmessungen von $\alpha\text{-CuV}_2\text{O}_6$ eine antiferromagnetische Fernordnung unter $\sim 22,5$ K zu einer kollinearen magnetischen Struktur mit magnetischen Momenten $\sim 0,7 \mu_B$, die aufgrund von Quantenfluktuation gegenüber dem erwarteten Wert von $1 \mu_B$ verringert sind.

Die natürlichen Mineralien Mixit, Goudeyit und Agardit sind isotyp und enthalten Cu^{2+} Kationen in linearer Kettenanordnung. Natürliche und synthetische Mixit-, Goudeyit- und Agarditproben wurden verwendet, um ihre chemischen, strukturellen, gitterdynamischen und magnetischen Eigenschaften im Detail zu untersuchen. Es wurde eine niedrigdimensionale antiferromagnetische Spin-Austausch-Kopplung zwischen den Spinmomenten an den Cu^{2+} Kationen gefunden. Die magnetischen Eigenschaften werden durch einen wesentlichen antiferromagnetischen Spinaustausch zwischen den magnetischen Momenten an den Cu^{2+} Kationen in Übereinstimmung mit den Dichtefunktionsberechnungen bestimmt. Die Temperaturabhängigkeit der magnetischen Suszeptibilitäten wird von kurzreichweitigen antiferromagnetischen Korrelationen dominiert, die sich als charakteristischer breiter Buckel in der magnetischen Suszeptibilität zeigen, der den niedrigdimensionalen Charakter des Spin-Gitters in der Mixit-Kristallstruktur widerspiegelt. Eine magnetische Fernordnung konnte bis zu 0,4 K nicht nachgewiesen werden. Ein erster Modellansatz zur Modellierung der magnetischen Eigenschaften aller drei Systeme anhand eines alternierenden $S = 1/2$ Heisenberg-Modells beschreibt die magnetischen Suszeptibilitäten relativ gut. Suszeptibilitätsmessungen zeigen Unterschiede zwischen den natürlichen und den synthetischen Proben. Während die Spinaustausch-Wechselparameter für die synthetischen Proben sehr nahe beieinander liegen, sind die der natürlichen Probe um etwa 25% niedriger. Dies kann das Ergebnis der Modifikation des

Spinaustauschweges innerhalb der sechs Ringe aufgrund der Substitution von Bi durch etwa 30% Ca in einer natürlichen Mixitprobe sein. Die Anpassungen der magnetischen Suszeptibilitäten schließen ein gekoppeltes $S = 1/2$ Dimer-Modell eindeutig aus, das kürzlich für die magnetischen Eigenschaften mehrerer anderer Cu^{2+} Mineralien vorgeschlagen wurde.

Bibliography

1. Introduction

- [1-1] J. G. Bednorz, K. A. Müller, *Zeitschrift für Physik B*, **64**, 189–193(1986).
- [1-2] E. Ising, *Zeitschrift für Physik A*, **31**, 253 (1925).
- [1-3] L. Onsager, *Physical Review*, **65**, 117 (1944).
- [1-4] J. C. Bonner and M. E. Fisher, *Physical Review*, **135**, A640 (1964).
- [1-5] X. Wang and T. Xiang, *Physical Review B*, **56**, 5061 (1997).
- [1-6] T. Xiang, *Physical Review B*, **58**, 9142 (1998).
- [1-7] T. Xiang and X. Wang, *Lecture Notes in Physics: Density-matrix renormalization*, vol. 528 (Springer, 1999).
- [1-8] D. C. Johnston, R. K. Kremer, M. Troyer, X. Wang, A. Klümper, S. L. Bud'ko, A. F. Panchula, and P. C. Canfield, *Physical Review B*, **61**, 9558 (2000).
- [1-9] J. M. Law, H. Benner, and R. K. Kremer, *Journal of Physics: Condensed Matter*, **25**, 065601 (2013).
- [1-10] N. D. Mermin and H. Wagner, *Physical Review Letters*, **17**, 1133 (1966).
- [1-11] V. L. Berezinskii, *Soviet Physics - Journal of Experimental and Theoretical Physics*, **32**, 493 (1971)
- [1-12] J. des Cloizeaux, J.J. Pearson, *Physical Review*, **128**, 2131 (1962)

2. Theory

- [2-1] URL <https://www.mlz-garching.de/spodi>
- [2-2] URL <https://www.ill.eu/users/instruments/instruments-list/d20/description/instrument-layout/>
- [2-3] URL [<https://www.nist.gov/pml/nist-x-ray-form-factor-attenuation-and-scattering-tables-database-cont>
- [2-4] URL <https://www.nist.gov/ncnr/neutron-scattering-lengths-list>
- [2-5] P. Hohenberg, W. Kohn, *Physical Review. B*, **136**, 864–871 (1964).

- [2-6] W. Kohn, L.J. Sham, *Physical Review A*, **140**, A1133–A1138 (1965)
- [2-7] J.P. Perdew, A. Ruzsinszky, J. Tao, V.N. Staroverov, G. Scuseria, G.I. Csonka, *Journal of Chemical Physics*, **123 (6)**, 062201 (2005).
- [2-8] A.D. Becke, *The Journal of Chemical Physics*, **140 (18)**, A301 (2014).
- [2-9] J.P. Perdew, J.A. Chevary, S. H. Vosko, K. A. Jackson, M. R. Pederson, D. I. Singh, C. Fiolhais, *Physical Review B*, **46 (11)**, 6671 (1992).
- [2-10] A. D. Becke, *Physical Review A*, **38 (6)**, 3098–3100 (1988).
- [2-11] D. C. Langreth, M. J. Mehl, *Physical Review B*, **28 (4)**, 1809 (1983).

3. Experimental methods

- [3-1] URL <http://worldsciencereport.blogspot.com/2018/05/neutron-scattering.html>
- [3-2] URL <https://www.stoe.com/product/stoe-stadi-p/>
- [3-3] URL <https://www.bruker.com/products/x-ray-diffraction-and-elemental-analysis/x-ray-diffraction/d8-advance/technical-details.html>
- [3-4] URL <http://www.crismat.ensicaen.fr/spip.php?article478&lang=fr>
- [3-5] URL <https://www.ill.eu/users/instruments/instruments-list/d20/description/instrument-layout/>
- [3-6] URL <https://www.mlz-garching.de/spodi>
- [3-7] URL <https://www.isis.stfc.ac.uk/Pages/Quantum-Design-MPMS-XL7.aspx>
- [3-8] Quantum Design, “QDMPS 5XL manual”, 1998.
- [3-10] R. L. Fagaly, “*SQUID Instruments and Applications*”, Tristan Technologies San Diego, 2005
- [3-11] J. Weil, J. Bolton, J. Wertz, “*Electron Paramagnetic Resonance: Elementary Theory and Practical Applications*” (Wiley-Interscience publication, 1994).

- [3-12] URL <http://www.hzdr.de/db/Cms?pNid=2687>
- [3-14] S. A. Zvyagin, E. Čížmár, M. Ozerov, J. Wosnitza, R. Feyerherm, S. R. Manmana, F. Mila, *Physical Review B*, **83**, 060409 (2011).
- [3-15] URL <http://www.bruker.com/products/mr/epr.html>
- [3-16] P. Rieger, “*Electron Spin Resonance*”, (Brown University)
- [3-17] B. M. Weckhuysen, R. Heidler, R. A. Schoonheydt, “*Characterization I*”, pp. 295–335 (Springer, 2004).
- [3-18] J. M. Law, Ph.D. thesis, Loughborough University (2011).
- [3-19] URL <https://www.bruker.com/products/mr/epr/emxplus.html>
- [3-20] V. L. Berezinskii, *Soviet Physics - Journal of Experimental and Theoretical Physics*, **32**, 493 (1971)
- [3-21] E. S. R. Gopal, “*Specific Heats at Low Temperatures*”, (Plenum Press, 1966).
- [3-22] S. J. Joshua, *Australian Journal of Physics*, **37**, 305 (1984).
- [3-23] F. Han, “*A Modern Course in the Quantum Theory of Solids*” (World Scientific, 2013).
- [3-24] J. M. Coey, “*Magnetism and Magnetic Materials*” (Cambridge University Press, 2010).
- [3-25] M. G. Banks, Ph.D. thesis, Loughborough University (2007).
- [3-26] M. Evangelisti, Ph.D. thesis, University of Leiden (2001).
- [3-27] F. Pobell, “*Matter and Methods at Low Temperatures*” (Springer, 2007).
- [3-28] Quantum Design, “*Physical Property Measurement System: Heat Capacity Option User’s Manual*”, 1085-1150 (2004).
- [3-29] J. C. Lashley, M. F. Hundley, A. Migliori, J. L. Sarrao, P. G. Pagliuso, T. W. Darling, M. Jaime, J. C. Cooley, W. L. Hults, L. Morales, *Cryogenics*, **43**, 369 (2003).

- [3-30] J. S. Hwang, K. J. Lin, and C. Tien, *Review of Scientific Instruments*, **68**, 94 (1997).
- [3-31] D.J. Gardiner, “*Practical Raman spectroscopy*”, (Springer-Verlag, 1989).
- [3-32] URL https://en.wikipedia.org/wiki/Raman_scattering
- [3-33] URL <https://images.app.goo.gl/pSFsnE5a1aQRFWVB7>
- [3-34] URL https://www.horiba.com/en_en/products/detail/action/show/Product/labram-hr-evolution-1083/
- [3-35] B. Wunderlich, in “*Encyclopedia of Materials: Science and Technology*”, (Pergamon, 2001).
- [3-36] URL https://www.netzsch-thermal-analysis.com/media/thermal-analysis/brochures/STA_449_F5_Jupiter_en_web.pdf

4. $CuTa_2O_6$

- [4-1] G. J. Bayer, *Journal of the American Ceramic Society*, **43**, 495-496 (1960).
- [4-2] O. von Heidenstam, *Arkiv för kemi, mineralogi och geologi*, **28**, 375-387 (1968).
- [4-3] S. M. Eicher. PhD Thesis . McMaster University **1984**.
- [4-4] V. Propach, *Zeitschrift für anorganische und allgemeine Chemie*, **435**, 161-171 (1977).
- [4-5] H. Vincent, B. Bochu, J. J. Aubert, J. C. Joubert, M. Marezio, *Journal of Solid State Chemistry*, **24**, 245-253 (1978).
- [4-6] P. N. Wa llunga, *Acta Chemica Scandinavica*, **37**, 117-123 (1983).
- [4-7] C. T. Prewitt, A. W. Sleight, *Materials Research Bulletin*, **vol. 5**, 207-211 (1970).

- [4-8] J. M. Longo, A. W. Sleight, *Materials Research Bulletin*, **Vol. 10**, 1273-1278 (1975).
- [4-9] I. Krabbes, H. Langbein, *Zeitschrift für Naturforschung B*, **51**, 1605-1610 (1996).
- [4-10] H. Langbein, M. Bremer, I. Krabbes, *Solid State Ionics*, **101**, 579-584 (1997).
- [4-11] A.M. Nakua, H. Yun, J.E. Greedan, J.N. Reimers, C. Stager, *Journal of Solid State Chemistry*, **91**, 105-112 (1991).
- [4-12] H. Mueller-Buschbaum, R. Z. Wichmann, *Zeitschrift für anorganische und allgemeine Chemie*, **536**, 15-23 (1986).
- [4-13] J.N. Reimers, J.E. Greedan, C.V. Stager, R. Kremer, *Journal of Solid State Chemistry*, **83**, 20-30 (1989).
- [4-14] M.-H Whangbo, H.-J. Koo, D. Dai, *Journal of Solid State Chemistry*, **176**, 417-481 (2003).
- [4-15] URL <http://www.cryst.ehu.es/rep/sam.html>
- [4-16] E. Kroumova, M. I. Aroyo, J. M. Perez Mato, A. Kirov, C. Capillas, S. Ivantchev, H. Wondratschek, *Phase Transitions*, **76**, 155-170 (2003).
- [4-17] H. Haeuseler, *Spectrochimica Acta Part A*, **37**, 487-495 (1981).
- [4-18] E.-O Giere, A. Brahim, H. J Deiseroth, D. Reinen, *Journal of Solid State Chemistry*, **131**, 263-274 (1997).
- [4-19] D.C. Johnston, R. K. Kremer, M. Troyer, X. Wang, A. Klümper, L. Bud'ko, A. F. Panchula, P.C. Canfield, *Physical Review B*, **61**, 9558-9606 (2000).
- [4-20] R. L. Carlin, „*Magnetochemistry*“, (Springer Verlag, 1986).
- [4-21] P. W. Selwood, „*Magnetochemistry*“, 2nd ed., (Interscience, 1956).

[4-22] S. Todo, K. Kato, *Physical Review Letters*, **87**, 1–4 (2001).

[4-23] A.F. Albuquerque , F. Alet, P. Corboz, P. Dayal, A. Feiguin, S. Fuchs, L. Gamper, E. Gull, S. Gürtler, A. Honecker, R. Igarashi, M. Körner, A. Kozhevnikov, A. Läuchli, S.R. Manmana, M. Matsumoto, I.P. McCulloch, F. Michel, R.M. Noack, G. Pawłowski, L. Pollet, T. Pruschke , U. Schollwöck, S. Todo, S. Trebst, M. Troyer, P. Werner, S. Wessel, *Journal of Magnetism and Magnetic Materials*, **310**, 1187–1193, (2007).

[4-24] I. Affleck, M. Oshikawa, *Physical Review B*, **60**, 1038–1056 (1999).

5. CuV_2O_6

[5-1] A. N. Vasilev, L. A. Ponomarenko, A. L. Smirnov, E. V. Antipov, Yu. A. Velikodny, M. Isobe, Y. Ueda, *Physical Review B*, **60**, 3021 (1999).

[5-2] J. Kikuchi, K. Ishiguchi, K. Motoya, M. Itoh, K. Inari, N. Eguchi, J. Akimitsu, *Journal of the Physical Society of Japan*, **69**, 2660 (2000).

[5-3] A. V. Prokofiev, R. K. Kremer, W. Assmus, *Journal of Crystal Growth*, **231**, 498 (2001).

[5-4] Y. Sakurai, H. Ohtsuka, J. Yamaki, *Journal of the Electrochemical Society*, **135**, 32 (1988).

[5-5] H. Ma, S. Zhang, W. Ji, Z. Tao, J. Chen, *Journal of the American Chemical Society*, **130**, 5361 (2008).

[5-6] F. Cheng, J. Chen, *Journal of Materials Chemistry*, **21**, 9841 (2011).

[5-7] M. Ghiyasiyan-Arani, M. Masjedi-Arani, M. Salavati-Niasari, *Journal of Materials Science*, **27** 4871 (2016)

[5-8] C. Calvo , D. Manolescu, *Acta Crystallographica Section B*, **29**, 1743 (1973).

- [5-9] P. Becker-Bohatý, cited after M. Binnewies, R. Glaum, M. Schmidt, P. Schmidt, *Chemical Vapor Transport Reactions*, de Gruyter, Berlin/Boston, p.311 (2012).
- [5-10] J. Rodríguez-Carvajal, *Physica B*, **192**, 55 (1993).
- [5-11] V. Cirilli, A. Burdese, C. Bristi, *Atti della Reale accademia della scienze di Torino*, **95**, 15 (1961).
- [5-12] J.C. Bouloux, J. Galy, *Bulletin de la Societe Chimique de France* 1969, p736-p740, (1969)
- [5-13] M. Markkula, A.M. Arevalo-Lopez, J.P. Attfield, *Journal of Solid State Chemistry*, **192**, p390-p393 (2012).
- [5-14] G.D. Andreetti, G. Calestani, A. Montenero, M. Bettinelli, *Zeitschrift fuer Kristallographie*, **168**, p53-p58 (1984).
- [5-15] G. Kresse, J. Furthmüller, *Physical Review B*, **54**, 11169 (1996).
- [5-16] G. Kresse, D. Joubert, *Physical Review B*, **59**, 1758 (1999).
- [5-17] J. P. Perdew, A. Ruzsinszky, G. I. Csonka, O. A. Vydroz, G. E. Scuseria, L. A. Constantin, X.L. Zhou, K. Burke, *Physical Review Letters*, **100**, 136406 (2008).
- [5-18] P. E. Blöchl, *Physical Review B*, **50**, 17953 (1994).
- [5-19] S. L. Dudarev, G. A. Botton, S. Y. Savrasov, C. J. Humphreys, A. P. Sutton, *Physical Review B*, **57**, 1505 (1998).
- [5-20] M. Whangbo, H. Koo, D. Dai, *Journal of Solid State Chemistry*, **176**, 417 (2003).
- [5-21] A. Abragam, B. Bleaney, "*Electron Paramagnetic Resonance of Transition Ions*", (Oxford University Press, 1970).
- [5-22] M. E. Fisher, *Philosophical Magazine*, **7**, 1731 (1962)

- [5-23] J. C. LeGuillou, J. Zinn-Justin, *Physical Review Letters*, **39**, 95 (1977).
- [5-24] G.S. Rushbrooke, P.J. Wood, *Molecular Physics*, **1**, 257 (1958)
- [5-25] A. W. Sandvik, *Physical Review B*, **59**, R14157 (1999).
- [5-26] O. F. Syljuasen, A. W. Sandvik, *Physical Review E*, **66**, 046701 (2002).
- [5-27] F. Alet, S. Wessel, M. Troyer, *Physical Review E*, **71**, 036706 (2005).
- [5-28] D.C. Johnston, R. K. Kremer, M. Troyer, X. Wang, A. Klümper, L. Bud'ko, A. F. Panchula, P.C. Canfield, *Physical Review B*, **61**, 9558-9606 (2000).
- [5-29] R. L. Carlin, "*Magnetochemistry*", (Springer Verlag, 1986).
- [5-30] P. W. Selwood, "*Magnetochemistry*" 2nd ed. (Interscience, 1956).
- [5-31] M. G. Banks, R. K. Kremer, C. Hoch, A. Simon, B. Ouladdiaf, J.-M. Broto, H. Rakoto, C. Lee, M.-H. Whangbo, *Physical Review B*, **80**, 024404 (2009).

6. Rare-earth mixite and argadite minerals

- [6-1] D. S. Inosov, *Advances in Physics*. **2018**, 67, 149-252.
- [6-2] H. J. Xiang, C. Lee, H.-J. Koo, X. G. Gong and M.-H. Whangbo, *Dalton Transactions*, **42**, 823 (2013).
- [6-3] K. Mereiter, A. Preisinger, *Sitzungsberichte und Anzeiger - Österreichische Akademie der Wissenschaften, Mathematisch-Naturwissenschaftliche Klasse*, **123**, 79–81 (1986).
- [6-4] B. J. Gibson, R. K. Kremer, A. V. Prokofiev, W. Assmus, G. J. McIntyre, *Physica B*, **350**, e253 – e256 (2004).
- [6-5] M. Enderle, C. Mukherjee, B. Fåk, R. K. Kremer, J.-M. Broto, H. Rosner, S.-L. Drechsler, J. Richter, J. Malek, A. Prokofiev, W. Assmus, S. Pujol, J.-L.

- Raggazzoni, H. Rakoto, M. Rheinstädter, H. M. Rønnow, *Europhysics Letters*, **70**, 237-243 (2005).
- [6-6] L. Capogna, M. Mayr, P. Horsch, M. Raichle, R. K. Kremer, M. Sofin, A. Maljuk, M. Jansen, B. Keimer, *Physical Review B*, **71**, 140402–1 (2005).
- [6-7] M. G. Banks, R. K. Kremer, C. Hoch, A. Simon, B. Ouladdiaf, J.-M. Broto, H. Rakoto, C. Lee, M.-H. Whangbo, *Physical Review B*, **80**, 024404–1 – 024404-15 (2009).
- [6-8] C. Lee, Jia Liu, M.-H. Whangbo, H.-J. Koo, R. K. Kremer, A. Simon, *Physical Review B*, **86**, 060407-1 – 060407-5 (2012).
- [6-9] Y. Naito, K. Sato, Y. Yasui, Y. Kobayashi, Y. Kobayashi, M. Sato, *Journal of the Physical Society of Japan*, **76**, 023708-1 – 023708-3 (2007).
- [6-10] S. Seki, T. Kurumaji, S. Ishiwata, H. Matsui, H. Murakawa, Y. Tokunaga, Y. Kaneko, T. Hasegawa, Y. Tokura, *Physical Review B*, **82**, 064424-1 - 064424-1 (2010).
- [6-11] L. Zhao, T.-L. Hung, C.-C. Li, Y.-Y. Chen, M.-K. Wu, R. K. Kremer, M. G. Banks, A. Simon, M.-H. Whangbo, C. Lee, J. S. Kim, I. Kim, K. H. Kim, *Advanced Materials*, **24**, 2469–2473 (2012).
- [6-12] J. M. Law, P. Reuvekamp, R. Glaum, C. Lee, J. Kang, M.-H. Whangbo, R. K. Kremer, *Physical Review B*, **84**, 014426-1 - 014426-8 (2011).
- [6-13] M. Mourigal, M. Enderle, B. Fåk, R. K. Kremer, J. M. Law, A. Schneidewind, A. Hiess, A. Prokofiev, *Physical Review Letters*, **109**, 027203-1 - 027203-5 (2017).
- [6-14] A. Orlova, E. L. Green, J. M. Law, D. I. Gorbunov, G. Chanda, S. Krämer, M. Horvatić, R. K. Kremer, J. Wosnitza, G. L. J. A. Rikken, *Physical Review Letters*, **118**, 247201-1- 247201-5 (2017).
- [6-15] R. Miletich, J. Zemmann, M. Nowak, *Physics and Chemistry of Minerals*, **24**, 411–422 (1997).

- [6-16] A. Aruga, I. Nakai, *Acta Crystallographica, Section C*, **41** 161-163 (1985).
- [6-17] R. L. Frost, A. R. McKinnon, P. A. Williams, K. A. Erickson, M. L. Weier, P. Leverett, *Neues Jahrbuch für Mineralogie Abhandlungen*, **181**, 11 – 19 (2005).
- [6-18] R. L. Frost, M. Weier, W. Martens, *Spectrochimica Acta A*, **63**, 685–689 (2006).
- [6-19] R. L. Frost, M. Weier, W. Martens, L. Duong, *Mineralogical Magazine*, **69(2)**, 169-177 (2005).
- [6-20] S. Asbrink, L. J. Norrby, *Acta Crystallographica Section B*, **26**, 8-15. (1970).
- [6-21] G. Lohmueller, G. Schmidt, B. Deppisch, V. Gramlich, C. Scheringer, *Acta Crystallographica Section B*, **29**, 141-142 (1973).
- [6-22] The ionic radii for a 9-fold coordination have been taken from URL <http://abulafia.mt.ic.ac.uk/shannon/ptable.php>.
- [6-23] T.S. Timofejeva , Proceedings of the Russian Mineralogical Society, **94**, 698–703 (1965).
- [6-24] J.-E. Dietrich, M. Orliac , F. Permingeat, *Bulletin de la Société Française de Minéralogie et de Cristallographie*, **92**, 420–434 (1969).
- [6-25] see also cif file ICSD 70117
- [6-26] R. L. Frost, J. Čejka, J. Sejkora, J. Plášil, S. Bahfenne, S. J. Palmer, *Journal of Raman Spectroscopy*, **41**, 566 – 570 (2010).
- [6-27] J. Čejka, J. Sejkora, J. Plášil, E. C. Keefe, S. Bahfenne, S. J. Palmer, and R. L. Frost, *Journal of Raman Spectroscopy*, **412**, 1154 – 1159 (2011).
- [6-28] G. Kortüm, „*Reflexionsspektroskopie*“, (Springer-Verlag, 1969).

- [6-29] C. K. Jørgensen, R. Pappalardo, H. H. Schmidtke, *Journal of Chemical Physics*, **39**, 1422-1430 (1963).
- [6-30] D. E. Richardson, *Journal of Chemical Education*, **70**, 372-380 (1993).
- [6-31] B. N. Figgis, M. A. Hitchman, "*Ligand Field Theory and Its Applications*", (Wiley-VCH, 2000).
- [6-32] D. Reinen, M. Atanasov, S. L. Lee, *Coordination Chemistry Reviews*, **175**, 91-158 (1998).
- [6-33] M. J. Riley, *Inorganica Chimica Acta*, **268**, 55-62 (1998).
- [6-34] D. A. Cruse, J. E. Davies, J. H. Harding, M. Gerloch, D. J. Mackey, R. F. McMeeking, "*CAMMAG, a FORTRAN program*", (Cambridge, 1980).
- [6-35] M. Gerloch, "*Magnetism and Ligand-Field Analysis*", Cambridge University Press, 1983).
- [6-36] M. Riley, "*CAMMAG for PC, v4.0*", (University of Queensland, 1997).
- [6-37] M. Bermejo, L. Pueyo, *Journal of Chemical Physics*, **78**, 854-857 (1983).
- [6-38] R. Glaum, M. A. Hitchman, *Australian Journal of Chemistry*, **49**, 1221-1228 (1996).
- [6-39] R. Glaum, „*Neue Untersuchungen an wasserfreien Phosphaten der Übergangsmetalle* (in German)“, thesis of habilitation, Univ. of Gießen, Germany **1999**.
- [6-40] R. Glaum, H. Thauern, *Inorganic Chemistry*, **46**, 2057-2066 (2007).
- [6-41] K. W. H. Stevens, *Proceedings of the Royal Society A*, **219**, 542-555 (1953).
- [6-42] L. J. de Jongh, A. R. Miedema, *Advances in Physics*, **23**, 1-260 (1974).

[6-43] D. C. Johnston, R. K. Kremer, M. Troyer, X. Wang, A. Klümper, L. Bud'ko, A. F. Panchula, P. C. Canfield, *Physical Review B*, **61**, 9558-9606 (2000).

[6-44] A. Golubev, E. Bruecher, A. Schulz, R. K. Kremer, F. X. Schmidt, E.E. Gordon, M.-H. Whangbo, *Zeitschrift für anorganische und allgemeine Chemie*, **644(24)**, 1782-1790 (2018).

Curriculum Vitae

PERSONAL INFORMATION

Golubev Aleksandr

 Moscow (Russia)

 +4915735946753  +79776547275

 a.golubev@fkf.mpg.de

golubev.m.alexander@yandex.ru

Sex Male | Date of birth 27/04/1988 | Nationality Russian

EDUCATION AND TRAINING

15/04/2016–Present

PhD in Chemistry

Max Planck Institute for Solid State Research
Heisenbergstraße 1, 70569 Stuttgart (Germany)

01/09/2013–05/05/2015

Master in materials science exploring large scale facilities (Erasmus mundus program)

Université Montpellier 2 (01/09/2012–30/08/2013)
Place Eugène Bataillon, 34095 Montpellier (France)
<http://www.english.univ-montp2.fr/>

Technical University of Munich (01/09/2013–05/05/2015)
Arcisstraße 21, 80333 Munich (Germany)
<http://www.tum.de/>

Ludwig Maximilian University of Munich (01/09/2013–05/05/2015)
Geschwister-Scholl-Platz 1, 80539 Munich (Germany)
<http://www.uni-muenchen.de/index.html>

01/09/2005–01/07/2011

MSc Mechanical Engineer

Bauman Moscow State Technical University (Special-Purpose Engineering department)
2-nd Baumanskaya, 5, 105005 Moscow (Russia)

Acknowledgements

Firstly, I would like to thank Prof. Dr. Robert Dinnebier for enabling me to carry out my doctoral work at the Max Planck Institute for Solid State Research. I would like to thank Dr. Hans-Georg and Fr. Birgit King for their assistance in the many administrative questions.

I am grateful to Prof. Dr. Robert Dinnebier, Prof. Dr. Rainer Niewa and Prof. Dr. Joris van Slageren for participating in my thesis committee.

Above all, I would like to say that it was an honor to have Dr. Reinhard K. Kremer as my scientific advisor. His experimental expertise and vast knowledge were critical factors in the completion of this thesis. The experimental and the technical assistance from the technicians in his group Fr. Eva Brücker, Fr. Gisela Siegle and Hr. Stefan Höhn helped me a lot in solving many of the challenges presented in this work. It is difficult to overestimate the density functional theory calculations performed by Prof. M. H. Whangbo and Prof. H.J. Koo, which were essential in understanding properties of studied compounds. I would like to thank my collaborators, which I meet during these years. Hr. A. Schultz for the excellent high-precision Raman scattering measurements, Dr. A. Senyshyn, Dr. V. Baran and Dr. C. Ritter for their help at neutrons facilities, Dr. J. M. Law for the pulsed magnetic field measurements performed for CuTa_2O_6 , Dr. H. Langbein and Dr. by F. X. Schmidt for providing samples for my study. I am deeply thankful to Fr. Eléonore Reinéry for proof-reading of this thesis. Without their support, this thesis would not have been possible.

Lastly, I would like to thank my family and friends especially Fr. Anna Dauriskikh for constant encouragement and support along my long educational journey, my beloved wife Maria and my daughter Christina for giving an aim in my life.